Journeys Beyond the Standard Model

by

Gilly Elor

A dissertation submitted in partial satisfaction of the

requirements for the degree of

Doctor of Philosophy

in

Physics

in the

Graduate Division

of the

University of California, Berkeley

Committee in charge:

Professor Lawrence J. Hall, Chair
Professor Raphael Bousso
Professor Chung-Pei Ma

Spring 2013

Journeys Beyond the Standard Model

Abstract

Journeys Beyond the Standard Model

by

Gilly Elor

Doctor of Philosophy in Physics

University of California, Berkeley

Professor Lawrence J. Hall, Chair

The much anticipated era of the Large Hadron Collider is finally upon us, making today an extremely interesting time to be doing theoretical particle physics. The recent Higgs-like signal is certainly the most exciting particle physics discovery in decades. However with this discovery comes the reminder that we are now, more than ever, in need of theoretical work to understand new physics. The Standard Model is incomplete; it does not accommodate the experimental observation of dark matter, or the baryon asymmetry of the Universe. In addition, the SM has aesthetic or fine-tuning problems, like the gauge hierarchy problem and the strong CP problem. The task of model builders centers around addressing these and other issues by constructing new physics models that may be tested experimentally.

To Aviva and Arye Dror,

# Contents

## III   Origins of the Matter - Antimatter Asymmetry   101

## 6  Bubble Baryogenesis   102

# List of Figures

# List of Tables

# Acknowledgments

I would like to thank my collaborators Piyush Kumar, Hock-Seng Goh, Alex Dahlen, Joshua T. Ruderman, and David Pinner. I would especially like to thank Yasunori Nomura, Clifford Cheung, and Tomer Volansky for collaboration and guidence. Above all I would like to thank my advisor, Lawrence J. Hall, without whom this work would not be possible.

# Chapter 1

# Introduction

The Standard Model (SM) of Particle Physics is an extremely well tested theory that describes the electromagnetic, weak and strong nuclear forces and the elementary particles on which these forces act. The SM is well described by the local gauge group

$$G = SU(3)_C \times SU(2)_L \times U(1)_Y. \tag{1.1}$$

The group $SU(2)_L \times U(1)_Y$ describes the unified weak and electromagnetic interactions; $SU(2)_L$ is the weak isospin group, acting on left-handed spin one-half fermions, and $U(1)_Y$ is the abelian hypercharge group. At low scales the $SU(2)_L \times U(1)_Y$ symmetry is spontaneously broken to a residual group $U(1)_{em}$ whose corresponding gauge boson is the massless photon and the associated electromagnetic coupling is $\alpha_e \sim 1/137$. The remaining three gauge bosons, the $W^{\pm}$ and the neutral $Z$, become massive upon symmetry breaking via the Higgs mechanism.

Quantum Chromodynamics (QCD) is the theory of the strong interactions described by the $SU(3)_C$ "color" gauge group. The strong interactions are mediated by eight vector bosons, the gluons, and act on quarks – the elementary constituents of hadrons (mesons and baryons.) Unlike the electroweak interactions the strong force between quarks actually increases with separation distance. As a consequence isolated quarks do not exist in nature, rather they are always bound together in the form of hadrons. To summarize the elementary particle content of the SM

- Six spin 1/2 leptons: e (electron), $\mu$ (muon), $\tau$ (tau), and the corresponding neutrinos $\nu_e$, $\nu_\mu$, and $\nu_\tau$

- Six flavors of spin 1/2 quarks: d (down), u (up), s (strange), c (charm), b (bottom), t (top)

- Four spin one electroweak vector bosons; $W^+$, $W^-$, $Z$, and $\gamma$ (photon)

- Eight colors of spin one QCD vector bosons; the gluons

- One complex scalar Higgs

The above fermions are all taken to be four component Dirac fields. Fermions can be decomposed in terms of two component left and right handed Weyl spinors. For instance the leptons form three right handed $SU(2)_L$ singlets $e_R$, $\mu_R$, $\tau_R$, and three left handed doublets $(e^-, \nu_e)_L$, $(\mu^-, \nu_\mu)_L$ $(\tau^-, \nu_\tau)_L$ implying that members of each doublet will mix under a $SU(2)_L$ transformation.

While the SM successfully describes the interactions and properties of the known elementary particles it is still incomplete; it does not accommodate such things as the experimental observation of dark matter, or the matter - antimatter asymmetry of the Universe. In addition, the SM has aesthetic or fine-tuning problems, like the gauge hierarchy problem and the strong CP problem. To address these and other issues, model builders propose new "beyond the SM" models and mechanisms that are inspired by top-down considerations, such as string theory, and are potentially experimentally testable.

## 1.1   The Gauge Hierarchy Problem

One of the most outstanding questions in particle physics is why the weak force is orders of magnitude stronger then gravity. Alternatively this may be phrased as "why is the weak scale, $M_W \sim 80$ GeV, so much less than the planck scale $m_{\mathrm{Pl}} \sim 10^{19}$ GeV?"

The electrically neutral component of the SM higgs field has a classical scalar potential of the form

$$V_H = m_H^2 |H|^2 + \lambda |H|^4. \tag{1.2}$$

For the SM particles to acquire a mass via the Higgs Mechanism, the higgs must develop a non-vanishing vacuum expectation value at the minimum of its potential. This is possible if $\lambda > 0$ and $m_H^2 < 0$ in 1.2, resulting in $\langle H \rangle = \sqrt{-m_H^2/2\lambda}$. Experimental measurements of the properties of the weak interactions can be used to deduce that $\langle H \rangle \sim 174$GeV, and therefore the higgs mass must be close to the weak scale. Recently the ATLAS [2] and CMS [27] experiments have seen evidence for a higgs like particle with a mass of $\sim 125$ GeV. While this is certainly the most exciting particle physics discovery in decades, the lack of any hints of new physics is cause for worry. The problem is that $m_H^2$ receives enormous quantum corrections from every particle that couples, directly or indirectly, to the higgs field. The physical observed value of $m_H^2$ is comprised of a bare contribution, $m_0^2$, which is modified by quantum corrections and can be written as follows,

$$m_H^2 = m_0^2 + \Delta m_H^2 \sim (125 \text{ GeV})^2. \tag{1.3}$$

For instance the contribution due to a SM top quark loop is roughly given by

$$\Delta m_H^2 = -\frac{|y_t|^2 \Lambda_{UV}^2}{8\pi^2}, \tag{1.4}$$
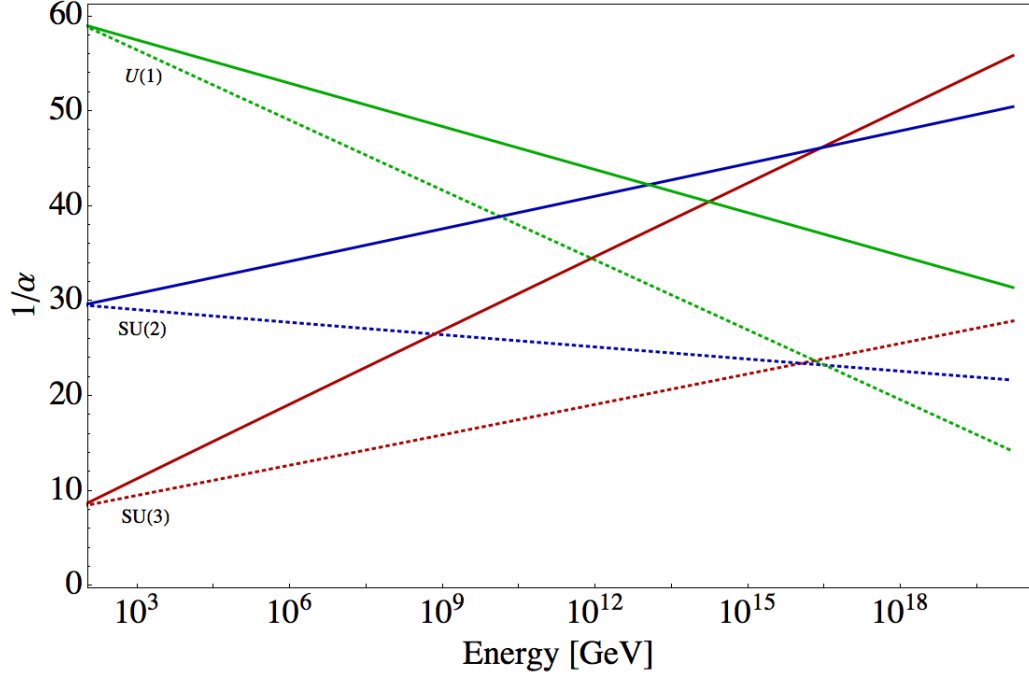
Figure 1.1: An example illustrating the improvement in gauge coupling unification in a SUSY theory over the SM. The running coupling constants $1/\alpha_i = 4\pi/g_i^2$ are plotted verses energy scale. The (red, blue, green) lines correspond to the coupling constant of the $i = (SU(3), SU(2), U(1))$ gauge groups. The solid (dotted) lines correspond to $1/\alpha_i$ in the SM (MSSM). The superpartners in the MSSM are all taken to have masses approximately at 1TeV

where the higgs yukawa coupling to fermions goes as $-y_f H \bar{f} f$, and $\Lambda_{UV}$ is a momentum cutoff used to regulate the divergence coming from the loop integral. From an effective theory perspective $\Lambda_{UV}$ is interpreted as the energy scale at which new physics enters the theory. If there is no new physics between the weak and the planck scale then $\Lambda_{UV} \sim m_{\rm Pl}$. If this is really the case then $\Delta m_H^2 \propto -10^{19}$ GeV, and the only way to explain the observed higgs mass in Eq. 1.3 is if there is a miraculous cancelation at the level of many orders of magnitudes. Such a "fine-tuning" of fundamental parameters has been deemed unnatural and a great problem. The quarks and leptons and the electroweak gauge bosons of the SM all obtain masses from $\langle H \rangle$, so that the entire mass spectrum of the SM is directly or indirectly sensitive to the cutoff $\Lambda_{UV}$. A popular resolution is to hope that there exists some new physics, entering at a low scale $\Lambda_{UV} \sim M_W$, with some kind of symmetry property to justify the vanishing of all divergent contributions.

### 1.1.1 Supersymmetry

If there exists a heavy complex scalar particle with mass $m_s$ that couples to the Higgs through $-\lambda_s|H|^2|S|^2$, the higgs mass is modified through a scalar loop by the positive contribution

$$\Delta m_H^2 = \frac{\lambda_s \Lambda_{UV}^2}{16\pi^2} + ....$$ (1.5)

For the dangerous divergent term of 1.4 to cancel we would therefore require that $m_s = m_f$ and $y_t \sim \lambda_s^2$, which can arise naturally if there exists a symmetry between fermions and bosons [1]. This supersymmetry (SUSY) is in fact desirable from a top-down perspective, since string theory requires SUSY at some scale in order to have any hope of producing the spectrum of SM particles at low energies.

For SUSY to be a symmetry between fermions and bosons means that a SUSY transformation acting on a fermion will turn it into a boson and vise verse. From a group theory perspective this means that a particle and its "superpartner" (fermion and boson pairs) will belong to a single irreducible representation of the SUSY algebra, called a supermultiplet.

The Minimal Supersymmetric Standard Model (MSSM) is the simplest supersymmetric extension of the SM. In the MSSM every SM boson field has a fermion superpartner and visa verse. In terms of two component spinors the superpotential [2] for the MSSM is

$$W_{MSSM} = \bar{u}y_u Q H_u - \bar{d}y_d Q H_d - \bar{e}y_e L H_d + \mu H_u H_d,$$ (1.6)

here the $y_i$'s are yukawa couplings and $(Q, L, H_u, H_d)$ are superfields corresponding to chiral supermultiplets. For instance the squark and quark fields are parametrized by $Q(x^\mu, \theta) = \tilde{q}(x^\mu) + \theta q(x^\mu) + \theta^2 F_q$. [3] The MSSM Higgs doublets can be written $H_u = (H_u^+, H_u^0)$ and $H_d = (H_d^0, H_d^-)$[4]. Where again each field is interpreted as a superfield with scalar higgeses and fermion higgsinos. A second complex scalar higgs field is required to ensure the cancellation of the gauge anomaly and the proper mass generation of the fermions. The neutral scalar that corresponds to the physical SM

---

[1]Another class of potentially natural solutions to the gauge hierarchy problem are composite higgs models, in which the higgs is not a fundamental particle. However such proposals are plagued with theoretical difficulties and experiments have placed severe restrictions on them.

[2]The holomorphic function of the scalar fields from which the Lagrangian is deduced. For a review see [115].

[3]Here $\theta$ is a two-component anti-commuting grassmann variable which can be thought of as a coordinate of superspace. In the language of superspace SUSY is given a geometric interpretation as a manifold obtained by addition four anti-commuting (fermionic) coordinates to the usual (bosonic) spacetime coordinates $x^\mu$. Points in superspace are therefore parametrized by $(x^\mu, \theta_\alpha, \theta_{\dot{\alpha}}^\dagger)$. $F_q$ is an auxiliary field introduced solely to allow the SUSY algebra to close off-shell. For further details on superspace see [115].

[4]There is an implied asymmetric epsilon tensor in the contracted two component fields of Eq. 1.6.

higgs boson is then a linear combination of neutral components of the MSSM higgses $h_u^0$ and $h_d^0$.

Another appealing aspect of SUSY theories is the great improvement in gauge coupling unification. The values of the fundamental coupling constants of the SM receive scale dependent loop corrections resulting in an energy dependent variation of their strengths. At high scales $M_{\mathrm{GUT}} \sim 10^{16}$ GeV, the three couplings appear to unify. The unification is not perfect, but this may be due to the fact that the calculation has yet to take into account the effects of new particles coming in at the grand unifying (GUT) scale. This is illustrated in Fig1.1 where the (red, blue, green) solid lines correspond to the running coupling constant $1/\alpha_i = 4\pi/g_i^2$ of the SM gauge group $i = (3, 2, 1)$. The dashed lines correspond to the same couplings whose running is modified by loops of MSSM superpartners The unification is significantly improved in the MSSM.

If SUSY is unbroken members of the same supermultiplet will have the same mass. Since the superpartners have yet to be observed, susy must be broken at a scale higher than that which has been experimentally probed. The higher the scale of SUSY breaking the larger the superpartner masses are, and the greater the required tuning in Eq. (1.3) will be. As the LHC experiments place ever higher bounds on the masses of the superparticles this natural solution to the hierarchy problem becomes less and less appealing.

By the Goldstone theorem, the breaking of a non-abelian symmetry results in the appearance of new particles. The goldstone fermion associated with susy breaking, the gravitino, leads to a well known cosmological problem: thermal production of light gravitinos will overclose the Universe unless the reheating temperature $(T_R)$ [99] after inflation is constrained to be small. Therefore there exists a tension between susy and theories such as thermal leptogenesis [54] which require a high $T_R$. In Chap. 4 we discuss this "Cosmological Gravitino Problem" in more detail, analyze the effects of different SUSY mass spectrums, and study additional implications for cosmology.

## 1.1.2 Calling Naturalness into Question

There are many situations in nature where small variations of a physical observable would have had catastrophic consequences for the existence of observers. This beckons the question; can we build new physics models in which parameters have tuned values because those are the values most compatible with the formation of observers such as ourselves? For a parameter to be "environmentally selected" there must be a large ensemble of possible values of that parameter. Such an ensemble is provided within the context of String Theory, in which there exists an enormous "Landscape" of possible vacua, each corresponding to a different possible dimensional compactification with its own values for the fundamental constants of nature. Additionally Eternal Inflation [62] provides a mechanism for physically realizing different vacua in the landscape via quantum tunnelings. The string landscape or "Multiverse" has lead

to a new philosophy for model building; instead of relying on naturalness and symmetry arguments to explain the values of observables, we allow for observables to have be tuned if they represent "environmentally selected" values in the string landscape that are highly compatible with the formation of observers such as ourselves.

This idea was first applied by Weinberg as the solution to the Cosmological Constant (CC) problem [114]. The CC Problem can be rephrased by asking the question "Why is the CC smaller then several known contributions to it?" Writing Einstein's equations with a cosmological constant term

$$R_{\mu\nu} - \frac{1}{2}Rg_{\mu\nu} + \Lambda g_{\mu\nu} = 8\pi G T_{\mu\nu}, \qquad (1.7)$$

here $R_{\mu\nu}$ is the Ricci curvature tensor, R is the scalar curvature, $g_{\mu\nu}$ is the metric tensor, $\Lambda$ is the CC, G is Newtons gravitational constant, and $T_{\mu\nu}$ is the matter stress-energy tensor. The vacuum should be Lorentz invariant which implies that $\langle T^{vac}_{\mu\nu}\rangle = -\rho^{vac}g_{\mu\nu}$, where $\rho$ is the energy density. Therefore $\Lambda$ can be identified with the vacuum energy density which has been determined observationally to have an incredibly small and yet nonzero value. The issue is that there are large (divergent) field theory contributions to the vacuum energy density arising from particle fluctuations in the vacuum. These contributions have different signs and can in principle cancel off one another in order to explain the value of the CC. However such a cancelation represents a tuning of many orders of magnitude. In particular

$$\frac{\rho^{obs}_{vac}}{\rho_{vac}} \sim \left(\frac{10^{-12}\text{GeV}}{10^{3-18}\text{GeV}}\right)^4 \sim 10^{-60} - 10^{-120}. \qquad (1.8)$$

There is no known way to explain the very small value of $\Lambda$ by invoking symmetries. Weinberg explanation [114] was to assume that $\Lambda$ took on different values in different domains in the Universe, and to place anthropic bounds on its value based on compatibility with the formation of observers. The existence of observers would require, at zeroth order, the successful formation of galaxies. In particular a large positive $\Lambda$ would cause the Universe to expand to quickly for galaxies to have time to form. Alternatively a large negative value of $\Lambda$ would cause the universe to quickly collapse [5] Similar arguments may be used to address the gauge hierarchy problem. From this anthropic perspective, the weak scale much be muss less then the Planck scale since increasing the weak scale too much could prevent the formation of the complex nuclei required for our existence. Therefore with this anthropic viewpoint weak scale supersymmetry is no long required [6].

---

[5]In actuality Weinberg's argument may be viewed as a little outdated since it relays too heavily on assumptions about actual observers. Instead current methods select out "typical" values using various geometric measures [21, 20, 111] to regulate the infinite volume (and therefore probabilities) of eternal inflation. This therefore eliminates the need to really posit the exact (and debatable) conditions for observers to form. These recent approaches give a a better prediction the Weinberg.

[6]String theory of course still requires SUSY, however SUSY need not be at the weak-scale. For

## 1.2 Dark Matter

Studies of galactic rotation curves, velocity dispersion relations of galaxies, gravitational lensing, and the Cosmic Microwave Background (CMB) are just some of the observations that provide unequivocal evidence for the existence of Dark Matter (DM); gravitationally interacting non-SM particles that have yet to be directly observed but are surmised to account for the majority of the matter in the Universe. Since the SM does not contain a successful DM candidate [7] new physics is required to explain its nature, origin and associated relic abundance. Meanwhile the lack of any definitive signal of the non-gravitational interactions of DM constrain its mass and interactions, thereby excluding many models. Constructing a working, testable model of dark matter is not a trivial task.

### 1.2.1 Thermal Freeze-Out

Measurements from WMAP [68] indicate that the relic abundance of dark matter is approximately

$$\Omega_{DM}h^2 \sim 0.11, \tag{1.9}$$

where $\Omega = \rho/\rho_c$ is the ratio of DM energy density to critical energy density of the Universe. In the early Universe temperatures are very high and the SM particles are thermalized. Assuming there exist non-gravitational interactions between the SM and the DM, these interactions will initially keep the DM particles in thermal equilibrium with the SM bath. As the universe expands and cools the SM-DM interactions become less effective and eventually the DM will decouple. Roughly speaking the DM particles will stay in thermal equilibrium with the early Universe bath as long as their interaction rate exceeds the Hubble expansion rate

$$H(T) < n(T)\langle \sigma v \rangle, \tag{1.10}$$

where $H(T)$ is the temperature dependent Hubble expansion, $n(T)$ is the number density and $\langle \sigma v \rangle$ is the thermally averaged interaction cross section. The time evolution of the number density is given by the Boltzmann equation [86] as

$$\frac{dn}{dt} + 3Hn = -(n^2 - n_{eq}^2)\langle \sigma v \rangle, \tag{1.11}$$

string theory's purposes SUSY may appear at any scale below the $m_{Pl}$. Additionally it is shown [8, 9] that for the dramatic improvement in gauge coupling unification the entire MSSM is not required at the low scales. In fact the authors of [8, 9] considered a theory in which only the scalars where made light, and showed that with this "split" spectrum unification is comparable to that of the MSSM as it is the fermions the dominate the renormalization group running of the couplings

[7]Neutrinos have been considered as a DM candidate since they interact so little with ordinary matter. However neutrinos are very light and are produced at relativistically speeds. Such a "hot" DM candidate is essentially ruled out by free-streaming constraints on galactic structure formation [110].
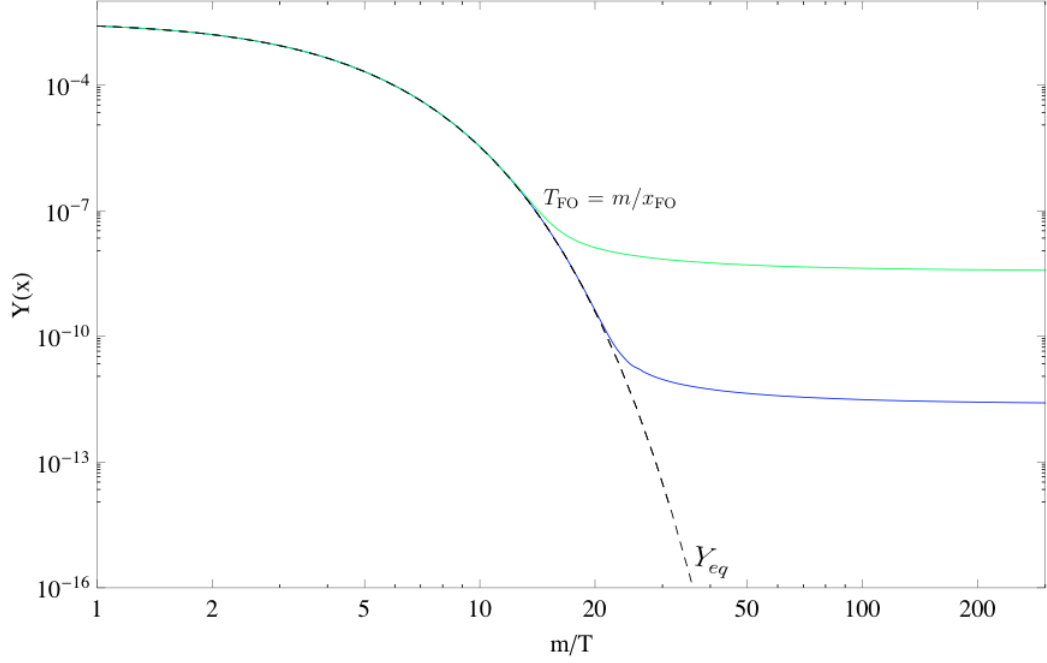
Figure 1.2: Example illustrating the thermal Freeze-Out of a particle. The green and blue curves correspond to the yield of particles with the same mass but with higher/lower interaction rates $\langle \sigma v \rangle$ respectively. The dotted curve corresponds to the equilibrium yield which becomes Boltzmann suppressed once $T < m$. Initially the particles track their equilibrium rate until a temperature $T_{FO} \sim m/25$ at which point Eq. (1.10) is no longer true and the particle abundance "Freezes-Out" since $dY/dx \sim 0$. The FO yield of the particle with the greater interaction rate (blue) is lower then that of the particle with the lower interaction rate (green) since a larger interaction rate means the particle will track equilibrium longer and thus be more greatly affected by the Boltzmann depletion.

so that DM particle production is sourced by the interactions on the right hand side of Eq. (1.11), while on the left hand side the Hubble expansion acts to damp out this production. Eventually the two terms will become comparable $H(T) \sim n(T)\langle \sigma v \rangle$ and the co-moving number density will become fixed. In Eq. (1.11) $n_{eq}(T)$ is the number density of a particle in equilibrium which goes as $T^3$ at early times when the particle is relativistic, but become exponentially Boltzmann suppressed once temperatures fall below the particle mass.

It is convenient to re-write Eq. (1.11) in terms of co-moving (or yield) variables; $Y = n/s$ and $x = m/T$, where $s \propto T^3$ is the co-moving entropy density, and $m$ is the particle mass. Changing variables Eq. (1.11) becomes:

$$\frac{dY}{dx} = -\frac{s\langle \sigma v \rangle}{Hx} \left( Y^2 - Y_{eq}^2 \right). \tag{1.12}$$

Fig. 1.2 illustrates an example of this thermal DM production mechanism. The green (blue) curves correspond to the yield of particles with the same mass but with higher

(lower) interaction rates. The dotted curve corresponds to the equilibrium yield which becomes Boltzmann suppressed once $T < m$. Initially the particles track their equilibrium rate until a temperature $T_{FO} \sim m/25$ at which point Eq. (1.10) is no longer true and the particle abundance Freezes-Out (FO) with a yield approximately given by

$$Y_{\text{FO}} \simeq \frac{1}{M_{\text{Pl}} \langle \sigma v \rangle} \frac{1}{T_{FO}}. \tag{1.13}$$

This is the standard "WIMP" paradigm [86] whereby DM initially in thermal equilibrium with the SM bath undergoes FO yielding approximately the correct DM relic abundance for weak scale DM mass and interactions cross-sections. The corresponding relic abundance is $\Omega \propto m Y_{FO}$, and so satisfying Eq. (1.9) corresponds to $m Y_{FO} \simeq 4 \times 10^{-10}$ GeV.

The FO yield in 1.13 is inversely proportional to the interaction rate since the greater $\langle \sigma v \rangle$ the longer the particle tracks its equilibrium value, and therefore the more it will be effected by the non-relativistic Boltzmann depletion. Eq. (1.13) is in principle "reconstructable" meaning that it depends only on low scale or infra-red (IR) quantities that can in principle be measured.

## 1.2.2 Dark Matter Candidates

A famous DM candidate exist in SUSY theories; it is the neutral LSP whose stability is ensured by an R-parity (a residual symmetry between particles and their superpartners which is often evoked to ensure, for instance, that the proton decay rate is not too fast to conflict with observations.) In the MSSM the potential DM candidates are the $\tilde{b}$, $\tilde{w}$, $\tilde{h}$, and $\tilde{\nu}$. For natural and experimentally allowed LSP masses the FO abundance of the bino overproduces, while the FO abundance of the wino, higgsino, and sneutrino underproduces. One possible solution is the Well-Tempered Neutralino [7], in which the LSP is a neutralino with a $\tilde{b} - \tilde{w} - \tilde{h}$ mixture tuned just right to get the correct relic abundance. Another possible resolution is to imagine that the lightest SUSY particle is actually a LOSP (lightest observable sector particle) which undergoes FO and subsequently decays to Gravitino DM [50] - [51]. In this case the DM abundance goes as

$$\Omega_{\tilde{G}} = \frac{m_{\tilde{G}}}{m_{LOSP}} \Omega_{LOSP}. \tag{1.14}$$

Since the bino overproduces it is a possible LOSP candidate. In addition since the LOSP need not be electrically neutral it may just as well be the slepton which also overproduces. A problem with this resolution is that for sub-TeV LOSP masses these late decays may result in harmful effects during the era of Big Bang Nucleosynthesis (BBN) and are so excluded.

### 1.2.3 Alternatives Production Mechanisms

In Chap. 2 we consider a scenario where DM is very weakly coupled to the SM (observable) sector, but has strong couplings to particles in its own (hidden) sector so that in the early Universe it is in thermal equilibrium with a hidden sector bath. Such hidden or sequestered sector scenarios are well motivated from top-down considerations. We analyze all possible cosmological origins of weak-scale DM in this framework. In the traditional single sector scenario, DM is produced via the thermal FO mechanism discussed above. While DM will still undergo FO in its own sector, a handful of other production mechanism are also active in the two sector setup. In particular the inter-sector couplings will ensure that the LOSP is unstable and will decay to particles in the hidden sector. Depending on the size of these couplings the LOSP decay will occur at different eras during the thermal evolution, resulting in cosmological histories where various DM production mechanisms dominate the final abundance. In Chap. 3 we show that each dark matter production mechanism is associated with a distinctive window of lifetimes and cross-sections for particles which may be produced at the LHC. In all cases, the losp is relatively long-lived on collider time scales, leading to events with displaced vertices and other exotic tracks such as "kinks".

## 1.3 The Strong CP Problem

The QCD lagrangian allows a charge-parity (CP) violating term of the form

$$\mathcal{L} = \frac{\theta}{16\pi^2} F^a_{\mu\nu} \tilde{F}^{\mu\nu a}, \tag{1.15}$$

where the duel field strength is $\tilde{F}^a_{\mu\nu} = \epsilon_{\mu\nu\rho\sigma} F^{\rho\sigma a}/2$. The operator in Eq. (1.15) violates CP and contributes, for instance, to the neutron electric dipole moment $d_n$ which has been constrained to be small by experiments. This then places a bound on the $\theta$-term of about $\theta << 10^{-10}$. Why is $\theta$ so small and yet non-zero? This is the origin of the strong CP problem. Although CP violation exists in the SM weak interactions, it does not (beyond the $\theta$ term of course) exist in the strong interactions. So physics beyond the SM is required to explain the non-zero value of $\theta$.

The Peccei-Quinn (PQ) resolution to the strong CP problem is to postulate the existence of a new global $U(1)_{PQ}$ symmetry [100]. The $\theta$ parameter is promoted from a constant value to a dynamic field. The potential of this field can naturally have a value that makes $\theta$ small. The vev of this field will spontaneously breaks the PQ symmetry, and the new particle, the pseudo-goldstone boson associated with this breaking, is dubbed the axion. The axion can interact with the SM in various ways [84, 46] once PQ is broken at some new scale $f_a << m_{\text{Pl}}$, where $f_a$ is the axion decay constant.

If supersymmetry is embraced as the solution to the gauge hierarchy problem than this implies that the axion has a fermionic "axino" superpartner which couples to the gravitino. In Chap. 5 we will show that a general operator analysis implies that in the absence of unnatural fine-tuning the axino has a mass greater than or equal to the mass of the gravitino. As a consequence, bounds from thermal gravitino and axino production are complementary in parameter space and the result is a very stringent limit on $T_R$. Generically we will show that these combined cosmological gravitino and axino problems lead to a bound of $T_R < 10^3 - 10^6$ GeV, essentially eliminating the entire parameter space of high $T_R$ models.

## 1.4 Baryogenesis

New physics is required to explain the dynamic origin of the observed matter-antimatter asymmetry of the Universe,

$$\eta = \frac{n_B - \bar{n}_B}{s} \sim \frac{n_B}{s} \sim 6 \times 10^{-10}. \tag{1.16}$$

here $n_B$ ($\bar{n}_B$) is the baryon (antibaryon) number density. Since no matter antimatter asymmetry is expected to have been produced during the Big Bang, it is not satisfactory to simply impose the asymmetry as an initial condition in the early Universe. Rather the non-zero asymmetry must be dynamically generated from an initially baryon symmetric Universe. A mechanism that does this must satisfy the Sakharov conditions [104];

- Baryon number (B) violation

- CP violation

- Departure from thermal equilibrium

The first Sakharov condition is obvious; clearly a mechanism that generates baryons must violate baryon number associated with a re-phasing symmetry $U(1)_B$. The CP violation requirement may seem a little less obvious but turns out to be crucial. Without CP violation baryon violating interactions would occur at the same rate as their conjugate interactions, so although baryons would be produced, an equal number of anti-baryons would also be produced leading to a net zero asymmetry. The final criteria; that the B and CP violating interactions occur out of thermal equilibrium is also straightforward and is simply the statement that the baryon asymmetry would average to zero if these interactions would equilibrate. There are many proposal mechanisms for explaining the observed asymmetry in Eq. 6.50, some examples are electroweak baryogenesis [109], thermal leptogenesis [54], and Affleck-Dine baryogenesis [71, 92].

Consider a complex scalar field parameterized in terms of the polar fields $(r, \theta)$.

$$\phi(x,t) = r(x,t)e^{i\theta(x,t)}. \tag{1.17}$$

The corresponding Noether current associated with the $U(1)_B$ re-phasing is given by

$$J_\mu = i(\phi\partial_\mu\phi^\dagger - \phi^\dagger\partial_\mu\phi). \tag{1.18}$$

The associated scalar field charge density is identified with the baryon number density

$$n_B = J_0 = r^2\dot{\theta}. \tag{1.19}$$

So there exists a mechanical analog in which baryon number can be thought of as an "angular momentum" in field space. A non-zero baryon number therefore requires first that $r \neq 0$; the field must be displaced from the origin, and second that $\dot{\theta} \neq 0$ so that there is an angular velocity in field space. This can be achieved if the potential has explicated B violating terms, since the re-phasing symmetry of $\phi$ corresponds to a shift symmetry of $\theta$. The requirement of B violation therefore leeds to a potential of the scalar field such that $dV/d\theta \neq 0$. CP violation can be accommodated via complex phases in the scalar potential.

Constraints on baryon number violation today means that at late times the field must be in a B conserving region of phase space. So to generate a non-zero asymmetry the $\phi$ must be displaced from the B conserving vacua in the early universe. The B and CP violating terms in the potential will ensure that the baryon asymmetry will be dynamically generated as the $\phi$ journeys from a B-violating region of the potential in the early universe to the B-symmetric origin today. If there exists a classically allowed trajectory connecting the two vacua (that is the phase transition between the B-violating phase in the early Universe and the B-symmetric phase today is second order or higher) then the field will simply rolls to the origin. The result is a curved trajectory through field space. The end product of this is a homogeneous scalar condensate that can eventually decay to SM fields. This scenario is Affleck-Dine Baryogenesis and has been greatly studied. Realistic models where the scalar field is an MSSM scalar superpartner have been proposed. In these models the reason for the scalar baryon to be initially displaced from the B violating vacua must be justified. This is done by assuming the scalar baryon lives along a MSSM flat direction (directions where the scalar potential vanishes but is lifted by SUSY breaking effects) [93].

In Chap. 6 we discuss a proposal for a new mechanism of baryogenesis dubbed Bubble Baryogenesis, in which a complex scalar baryon undergoes a percolating first-order phase transition in the early Universe. Tunneling from a metastable vacua is described by Coleman's instanton solution, and in Minkowski space corresponds to a bubble nucleation event. As in Affleck-Dine, B and CP violating terms exist in the scalar baryons's potential and in this case they act to torque the instanton solution in

field space. The corresponding bubbles will carry an asymmetry in their walls, ultimately resulting in a spatially inhomogeneously distributed asymmetry. The bubbles nucleate expand and eventually collide, percolation occurs, and the entire universe is converted to true vacua. Bubble collision dynamics will also add to the asymmetry yield. After the collision, the bubbles thermalize; the asymmetry spreads and can migrate to the SM via decays. The bubble collisions open up a variety of well studied and potentially observable phenomenological consequences; for instance the production of gravitational waves and the creation and evaporation of black holes. Additionally our bubble collisions produce Q-balls and oscillons: non-topological solitions, which depending on the specifics of the model, may be stable or long lived and potentially observable today.

## 1.5  Published Work

The majority of the dissertation is based upon published work. Information on Hidden Sector Dark Matter can be found in [30, 32]. Our work on gravitino dark matter can be found in [30]. The Cosmological Axino Problem and gravitino dark matter in the presence of axinos have been studied in [31]. Finally for our proposal of a new mechanism for baryogenesis see [29].

# Part I

# Dark Matter

# Chapter 2

# Hidden Sector Dark Matter

Top-down considerations have recently motivated the exploration of "parallel sectors" comprised of their own particles and interactions but "hidden" from us (the visible sector) due to the weakness of the couplings connecting the hidden and visible sector particles. Phenomenologically viable models of SUSY breaking require the addition of a hidden sector where SUSY is broken. SUSY breaking is communicated to the visible sector, which contains for instance the MSSM fields, by some form of messenger interactions. For example these can be gravitational-strength interactions at the Planck scale [95], or the ordinary gauge interactions (as in Gauge Mediated Supersymmetry Breaking) [47]. It is also possible to take the separation of the visible and SUSY breaking sectors as geographic. This fits in well with string theory's predictions for the existence of six extra compact dimensions. Thus it is actually a physical distance separates the visible and hidden sectors [102].

In addition to providing new avenues for model-building, this broad framework opens up a range of new possibilities for the origin of DM. A priori, there is no reason for DM to couple to the visible sector with interactions other than gravity. The inclusion of a weak-scale hidden sector, complete with its own set of particles, dynamics, and thermal history, substantially expands the allowed space of mechanisms for DM generation. If DM shares size-able interactions with visible sector particles, then thermal equilibrium will be efficiently maintained until FO results in a thermal relic abundance of DM. Alternatively, it may be that DM couples extremely weakly to the visible sector and to itself, as is the case for superWIMPs [50, 51] and FIMPs [63, 14]. A third and final possibility is that DM is very weakly coupled to the visible sector, but has substantial couplings to a hidden sector to which it is thermally equilibrated. In general, this hidden sector will contain its own set of particles and interactions and will have a temperature different from that of the visible sector[1]. What then are all the various possible origins of DM in this enormous class of theories?

The DM will be assumed to be stable due to a symmetry shared by the visible and

---

[1]If the temperature of the two sectors are the same, the sectors have equilibrated implying that there is only one sector.

hidden sectors, for example R-symmetry in SUSY theories. For now we will remain agnostic about the choice of model. We simply denote the lightest visible and hidden sector particles charged under some stabilizing symmetry by $X$ and $X'$, which have masses $m$ and $m'$ taken to be broadly of order the weak scale such that $m > m'$. By definition, $X'$ is the DM particle. We also assume the existence of a weak coupling which bridges the visible and hidden sector and mediates the decay

$$X \rightarrow X' + \ldots, \tag{2.1}$$

where the ellipses denote what are typically visible decay products.

The cosmological evolution of this setup is entirely fixed by only a handful of parameters. This is analogous to standard single sector FO, where the DM abundance is solely determined by the DM annihilation cross-section in Eq. (1.13). Here we find that DM relic abundance is in general fixed by the following set of parameters:

$$\{m, m', \langle \sigma v \rangle, \langle \sigma v \rangle', \xi, \tau, \epsilon\}, \tag{2.2}$$

where $\langle \sigma v \rangle$ and $\langle \sigma v \rangle'$ are the thermally averaged annihilation cross-sections for $X$ and $X'$, respectively, $\xi = T/T'$ is the ratio of the visible and hidden sector temperatures, $\tau$ is the lifetime of $X$, and $\epsilon$ is a measure of the CP-phase in $X$ decays. In particular cases, the relic abundance depends on only a subset of the above parameters.

We evolve the cosmological history of the visible and hidden sectors over the parameter space defined in Eq. (2.2) in order to systematically identify all possible origins of hidden sector DM. Of course, the simplest possibility is that DM undergoes hidden sector Freeze-Out (FO'), yielding a thermal relic abundance. This has been considered in many hidden sector models, and was studied systematically in [53]. On the other hand, the remaining possibilities for the origin of DM fall into two very broad categories:

- **Freeze-Out and Decay (FO&D).** $X$ undergoes FO and then decays out of equilibrium, yielding an abundance of $X'$. As we will see later, the final abundance of $X'$ goes as

$$\Omega \propto \frac{m'}{m \langle \sigma v \rangle}. \tag{2.3}$$

- **Freeze-In (FI).** $X$ decays while still in thermal equilibrium with the visible sector, yielding an abundance of $X'$. As we will see later, the final abundance of $X'$ goes as

$$\Omega \propto \frac{m'}{m^2 \tau}. \tag{2.4}$$

Within the categories of FO&D and FI exist a number of distinct variations. For example, if FO&D or FI happen to produce an abundance of $X'$ particles exceeding a particular critical value, then the $X'$ particles will promptly undergo an era of "re-annihilation." During this time the $X'$ particles will efficiently annihilate within a
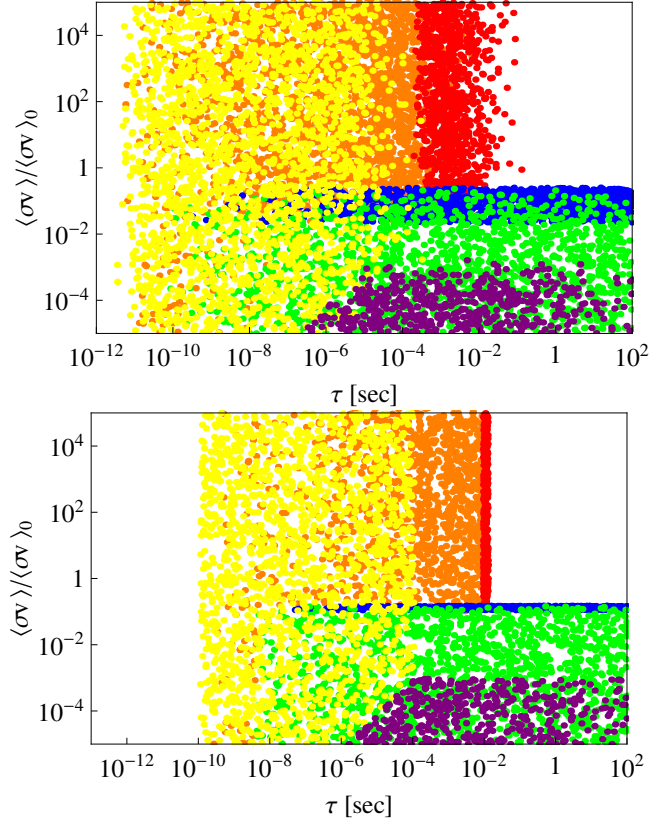
Figure 2.1: Hidden sector DM can originate via a handful of production mechanisms, each corresponding to a distinctive window in the $\tau - \langle\sigma v\rangle$ plane. Aside from hidden sector FO′, these mechanisms are {FO&D, FO&D$_r$, FO&D$_a$, FI, FI$_r$, FI$_a$}, denoted by {blue, green, purple, red, orange, yellow}. Each point corresponds to $\Omega h^2 = 0.11$, where we have scanned over a very inclusive parameter space defined by $10^{-5} < \langle\sigma v\rangle/\langle\sigma v\rangle_0, \langle\sigma v\rangle'/\langle\sigma v\rangle_0 < 10^5$, $10^{-3} < \xi < 10^{-1}$, $10^{-8} < \epsilon < 10^{-3}$, where $\langle\sigma v\rangle_0 = 3 \times 10^{-26}$ cm$^3$/s. In the left panel, the masses have been scanned over a broad region 10 GeV $< m <$ 1 TeV and $1/20 < m'/m < 1/2$, while in the right panel, the masses have been fixed to a narrow region $m = 100$ GeV and $1/4 < m'/m < 1/3$.

Hubble time despite the fact that $X'$ is no longer thermally equilibrated with the hidden sector. Because the final DM abundance changes accordingly, we refer to this mechanism of DM production as FO&D$_r$ and FI$_r$. Another variation arises if $X$ decays are CP-violating, in which case FO&D and FI may produce an abundance of DM endowed with a particle anti-particle asymmetry. Such an effect is possible because although the visible and hidden sectors are separately in thermal equilibrium, they are not in equilibrium with each other. We denote these asymmetric modes of DM production by Asymmetric Freeze-Out and Decay (FO&D$_a$) and Asymmetric Freeze-In (FI$_a$). These mechanisms are entirely distinct from the framework of Asymmetric DM [77], in which the DM particle anti-particle asymmetry is inherited from an already existent baryon asymmetry.

As seen in Eqs. 2.3 and 2.4, each of these DM production mechanisms maps to a distinctive window in the parameter space spanned by $\tau$ and $\langle\sigma v\rangle$—and where *all* other parameters, $m$, $m'$, $\langle\sigma v\rangle'$, $\xi$, and $\epsilon$, are scanned over an inclusive range of values. This is remarkable because $\tau$ and $\langle\sigma v\rangle$ can, in principle, be measured at the LHC since they are attributed to X, which is a visible sector field. For example, see the left panel of Figure 2.1, where each point corresponds to $\Omega h^2 = 0.11$, and each color denotes the dominant mechanism of DM production at that particular point in parameter space. Even though all parameters but $\tau$ and $\langle\sigma v\rangle$ have been scanned over a generous range, one sees that FO&D corresponds to a narrow band in $\langle\sigma v\rangle$ while FI corresponds to a narrow band in $\tau$.

On the other hand, it is also very likely that $m$, and perhaps even $m'$, might be measured at colliders, for instance if the visible decay products of $X \to X' + \ldots$ can be used to kinematically reconstruct the event. In the event that $m$ and $m'$ are indeed measured, the boundaries between DM production mechanisms in the $\tau - \langle\sigma v\rangle$ plane become even more distinct, as shown in the right panel of Figure 2.1. Because each production mechanism lies in a distinctive region in the $\tau - \langle\sigma v\rangle$ plane, there is a possibility that the origin of DM might be successfully reconstructed at the LHC even in this much broader framework compared to that of standard single sector FO.

## 2.1   Two-Sector Cosmology

Our setup is comprised of a visible and hidden sector, each with sizeable self-interactions which serve to maintain thermal equilibrium in each sector at temperatures $T$ and $T'$, respectively. We assume that these sectors couple to one other only through portal interactions which are extremely feeble, so these temperatures are not equal, i.e. $T \neq T'$. To begin, we limit the present discussion as well as that of Sections 2.1.1 and 2.1.2 to the case in which the visible and hidden sectors are entirely decoupled but for gravitational effects. In Section 2.1.3 and onwards we introduce portal interactions connecting the visible and hidden sectors and study the significant impact of these couplings on the cosmological history.

Throughout, we assume that the visible and hidden sectors enjoy a symmetry, discrete or continuous, that keeps DM cosmologically stable. The lightest visible sector particle charged under this stabilizing symmetry is denoted by $X$, and likewise in the hidden sector, $X'$, which we take to be lighter than $X$. In the limit in which the visible and hidden sectors are decoupled, $X$ and $X'$ are, of course, simultaneously stable. However, as portal interactions are switched on, $X$ becomes unstable and decays with a width $\Gamma$ into particles which ultimately yield an $X'$ in the final state. We will study the cosmological evolution of the number densities $n$ and $n'$ of $X$ and

$X'$, which obey the coupled Boltzmann equations

$$\frac{d}{dt}n + 3Hn = -(n^2 - n_{\text{eq}}^2)\langle \sigma v \rangle - \Gamma n \tag{2.5}$$

$$\frac{d}{dt}n' + 3Hn' = -(n'^2 - n_{\text{eq}}'^2)\langle \sigma v \rangle' + \Gamma n, \tag{2.6}$$

where $n_{\text{eq}}$ and $n_{\text{eq}}'$ are the thermal equilibrium abundances and it is understood that here $\Gamma$ is thermally averaged and we work in a regime in which the effects of the corresponding inverse decays are negligible. Here we take the thermally averaged annihilation cross-sections, $\langle \sigma v \rangle$ and $\langle \sigma v \rangle'$, to be independent of temperature. A primary aim of this paper is to study the most general cosmological evolution which follows from these equations, subject only to the requirement that $\langle \sigma v \rangle$ and $\langle \sigma v \rangle'$ are large enough that both $X$ and $X'$ undergo freeze-out. Note that we take the masses of $X$ and $X'$, $m$ and $m'$, both to be broadly of order the weak scale.

The relative size of $T$ and $T'$ can have a drastic impact on the cosmological history. To see why this is so, let us define the ratio of temperatures to be

$$\xi \equiv \frac{T'}{T}. \tag{2.7}$$

If we assume the standard picture of slow-roll inflation, then the inflaton can, in principle, couple with different strengths to the visible and hidden sectors. As a consequence, the decay of the inflaton reheats each sector to a different temperature, corresponding to an initial condition for $\xi$ given by $\xi_{\text{inf}} = T'_{\text{inf}}/T_{\text{inf}}$, the ratio of temperatures in each sector immediately after the decay of the inflaton, which we take to be less than 1. Naively $\xi = \xi_{\text{inf}}$ for all time. However, interactions between the sectors can change $\xi$ from $\xi_{\text{inf}}$. For example, scatterings between the sectors which are generically dominated in the UV, can increase the high temperature value of $\xi$ to $\xi_{\text{UV}}$, which is taken to be a free parameter. In addition, there can be IR contributions to $\xi$ as well. These contributions are discussed in more detail in Section 2.1.7.

Even ignoring interactions between the two sectors, $\xi$ actually varies as a function of temperature due to the separate conservation of the co-moving entropies, $S = g_{*S}T^3$ and $S' = g_{*S}'T'^3$, in each sector. Specifically, this implies that $\xi$ varies as a function of temperature to the extent to which the numbers of degrees of freedom in the visible and hidden sectors vary with temperature:

$$\xi(T) \propto \left(\frac{g_{*S}(T)}{g_{*S}'(T)}\right)^{\frac{1}{3}}, \tag{2.8}$$

where $g_{*S}(T)$ and $g_{*S}'(T)$ are the number of relativistic degrees of freedom in the visible and hidden sectors, respectively, when the visible sector is at a temperature $T$. A change in $g_{*S}(T)$ or $g_{*S}'(T)$ by an order of magnitude only affects $\xi$ at the level

of a factor of two; hence, when comparing DM production from processes at different temperatures, this effect may be justifiably ignored.

In general, the energy density in the hidden sector affects the expansion rate of the universe during BBN, which places an important, albeit weak constraint on $\xi$. In particular, any hidden sector particles which are relativistic at BBN contribute an effective number of extra neutrino species

$$\Delta N_\nu = \frac{4}{7} \, g'_*(T_{\text{BBN}}) \, \xi(T_{\text{BBN}})^4. \tag{2.9}$$

The present bound from experiment is $\Delta N_\nu < 1.4$ [48], which is surprisingly mild: that is, for $g'_*(T_{\text{BBN}}) = 100$, this is satisfied by taking $\xi(T_{\text{BBN}}) = 1/3$. Furthermore, according to Eq. (2.8), at higher temperatures $\xi$ can be close to unity even if $g'_* > 100$ [53].

## 2.1.1 Visible Sector Freeze-Out (FO)

In the early universe, visible sector particles reside in a thermal bath at temperature $T$ with abundances fixed accordingly by equilibrium thermodynamics. As $T$ drops below the mass of $X$, $m$, the number density of $X$ particles, $n$, remains in thermal equilibrium and undergoes the usual Boltzmann suppression. The $X$ particles undergo FO as the rate of annihilations, $n\langle \sigma v \rangle$, drops below the expansion rate $H$, which occurs at a temperature $T_{\text{FO}} \simeq m/x_{\text{FO}}$. The parameter $x_{\text{FO}}$ depends only logarithmically on $\langle \sigma v \rangle$, and for roughly weak scale cross-sections $x_{\text{FO}} \approx 20 - 25$. Defining the yield, $Y = n/s$ where $s$ is the entropy of the visible sector, we obtain the familiar expression for the yield at FO,

$$Y_{\text{FO}} \simeq \frac{3}{2\pi} \sqrt{\frac{5}{2}} \frac{\sqrt{g_*}}{g_{*S}} \frac{1}{M_{\text{Pl}} \langle \sigma v \rangle} \frac{1}{T_{\text{FO}}}. \tag{2.10}$$

In the decoupled limit, $X$ is stable and will account for the totality of DM in the universe if $m Y_{\text{FO}} \simeq 4 \times 10^{-10}$ GeV. This corresponds to a critical cross-section of $\langle \sigma v \rangle_0 \simeq 3 \times 10^{-26}$ cm$^3$/s.

Because we have thus far assumed that the visible and hidden sectors only interact gravitationally, the only effect of the hidden sector on FO in the visible sector is through its contribution to the energy density of the universe. However, this effect is tiny and can be accounted for in Eq. (2.10) by increasing $g_*$ by a factor

$$1 + \frac{7}{43} \Delta N_\nu \left( \frac{g_*(T_{\text{FO}})}{g_*(T_{\text{BBN}})} \right)^{\frac{1}{3}} \left( \frac{g'_*(T_{\text{BBN}})}{g'_*(T_{\text{FO}})} \right)^{\frac{1}{3}}, \tag{2.11}$$

where we have ignored the difference between $g_*$ and $g_{*S}$. For $T_{\text{FO}} < M_W$ this increases $Y_{\text{FO}}$ by at most 17% for $\Delta N_\nu = 1$. Thus the BBN constraint implies that the standard relation between the DM abundance and the DM annihilation cross-section is preserved to a good accuracy.
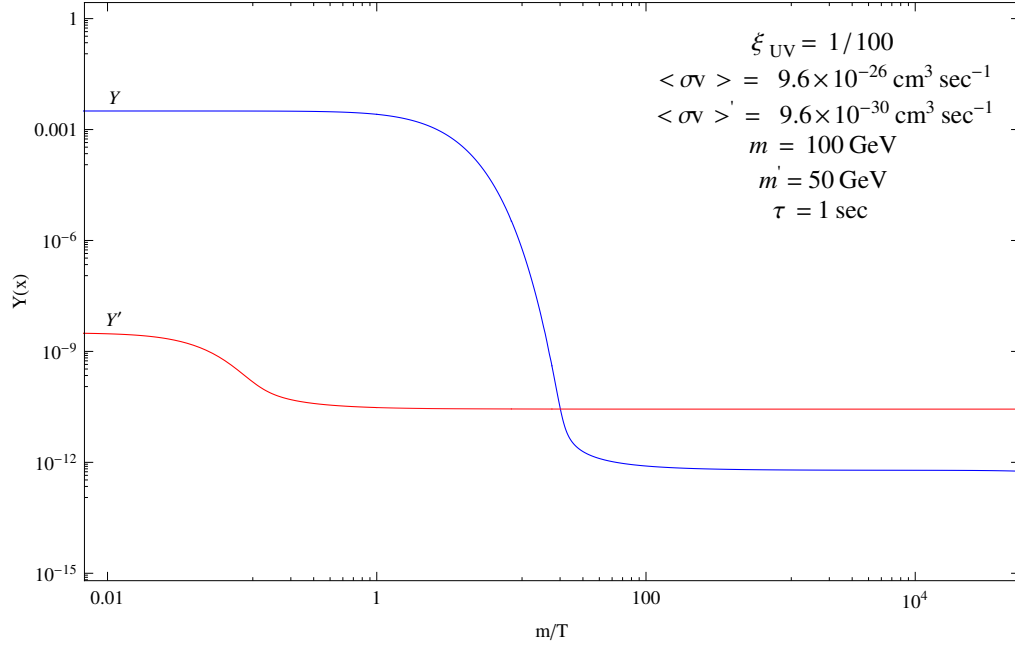
Figure 2.2: $X$ and $X'$ yields as a function of $m/T$ for a particular choice of parameters. The visible and hidden sectors separately undergo FO and FO$'$, respectively. At high temperatures $Y'/Y \sim \xi_{\mathrm{UV}}^3 = 10^{-6}$. Since $m'$ is not much less than $m$, a cool hidden sector, $\xi \ll 1$, implies that FO$'$ occurs before FO. A cool hidden sector tends to make $Y'_{\mathrm{FO}'} < Y_{\mathrm{FO}}$, but this is more than compensated by having $\langle \sigma v \rangle' \ll \langle \sigma v \rangle$. Using the quoted parameters in Eq. (2.13) gives $Y'_{\mathrm{FO}'} \simeq 200\, Y_{\mathrm{FO}}$.

## 2.1.2   Hidden Sector Freeze-Out (FO$'$)

As the temperature $T'$ of the hidden sector falls below $m'$, the number density of $X'$ particles, $n'$, tracks the equilibrium distribution and becomes exponentially suppressed. Ultimately, the $X'$ particles undergo FO$'$ once the hidden sector drops to a temperature $T'_{\mathrm{FO}'} = m'/x'_{\mathrm{FO}'}$, just as $X$ undergoes FO at $T_{\mathrm{FO}} = m/x_{\mathrm{FO}}$. Here the prime on $T'$ indicates that the temperature is that measured in the hidden sector, while the prime on FO$'$ indicates that this temperature is being evaluated at the time of FO$'$, *not* FO. Thus, the ratio of visible sector temperatures at FO$'$ compared to FO is

$$\frac{T_{\mathrm{FO}'}}{T_{\mathrm{FO}}} = \frac{1}{\xi_{\mathrm{FO}'}} \frac{m'}{m}, \tag{2.12}$$

where we took $x'_{\mathrm{FO}'} \simeq x_{\mathrm{FO}}$. Consider the parametric scaling of the above expression. Reducing $m'/m$ tends to shift FO$'$ to a later time than FO, while reducing $\xi_{\mathrm{FO}'}$ tends to do precisely the opposite. While in principle either ordering is possible, we focus on a scenario in which FO$'$ occurs before FO, as this leads to a richer set of cosmological histories once portal interactions between the sectors are included.

First, consider the case $\langle \sigma v \rangle' = \langle \sigma v \rangle$. Because $n'$ at FO$'$ is fixed by $H$ at $T_{\mathrm{FO}'}$

and $T_{\text{FO}'} > T_{\text{FO}}$, there is naively a greater number of $X'$ particles yielded by FO' than $X$ particles yielded by FO. However, because FO' occurs earlier, there is also a commensurately greater amount of entropy dilution, so the total $X'$ yield actually turns out to be less than the $X$ yield. To see this, let us define $Y' = n'/s$ to be the $X'$ yield normalized to the *visible sector entropy*, which will be useful for comparing with the $X$ yield. We find that for arbitrary $\langle\sigma v\rangle'/\langle\sigma v\rangle$

$$\frac{Y'_{\text{FO}'}}{Y_{\text{FO}}} \simeq \frac{T_{\text{FO}}}{T_{\text{FO}'}} \frac{\langle\sigma v\rangle}{\langle\sigma v\rangle'} \simeq \xi_{\text{FO}'} \frac{m}{m'} \frac{\langle\sigma v\rangle}{\langle\sigma v\rangle'}. \tag{2.13}$$

Hence, the yield of $X'$ from FO' is subdominant to the yield of $X$ from FO as long as the hidden sector is sufficiently cool or if its annihilations are sufficiently strong. See Figure 2.2 for a plot of the evolution of $X$ and $X'$ abundances as a function of $x = m/T$, for a choice of parameters making the contribution from FO' greater than that from FO.

### 2.1.3   The Portal

Until now, we have not considered the effect of direct, albeit tiny couplings which might directly connect the visible and hidden sectors. Consider a portal operator $\mathcal{O}$ which connects $X$ and $X'$, thereby mediating the decay

$$X \to X' + \dots, \tag{2.14}$$

where the ellipses denote what is typically visible SM particles. For the moment, let us ignore the particulars of $\mathcal{O}$ and attempt to characterize the gross features of the cosmological history as a function of the $X$ lifetime, $\tau = 1/\Gamma$. As the lifetime is taken from cosmological scales to microscopic scales, the cosmology typically transitions through four broadly defined scenarios[2]:

- **Multi-Component Dark Matter.** $X$ is so long lived that it is stable over cosmological time scales. Thus $X$ and $X'$ comprise the DM of the universe.

- **Freeze-Out and Decay.** $X$ decays late, after leaving thermal equilibrium, yielding a contribution to the $X'$ abundance.

- **Freeze-In.** $X$ decays fast enough that it produces a substantial $X'$ abundance from decays occurring while $X$ is still in thermal equilibrium.

- **Thermalized at Weak Scale.** $X$ decays so quickly that the visible and hidden sectors are actually in thermal equilibrium at the weak scale. From the point of view of cosmology, the visible and hidden sectors are a single sector.

---

[2]This is only a rough sketch; a more precise understanding of the various possibilities is given in Section 2.2.
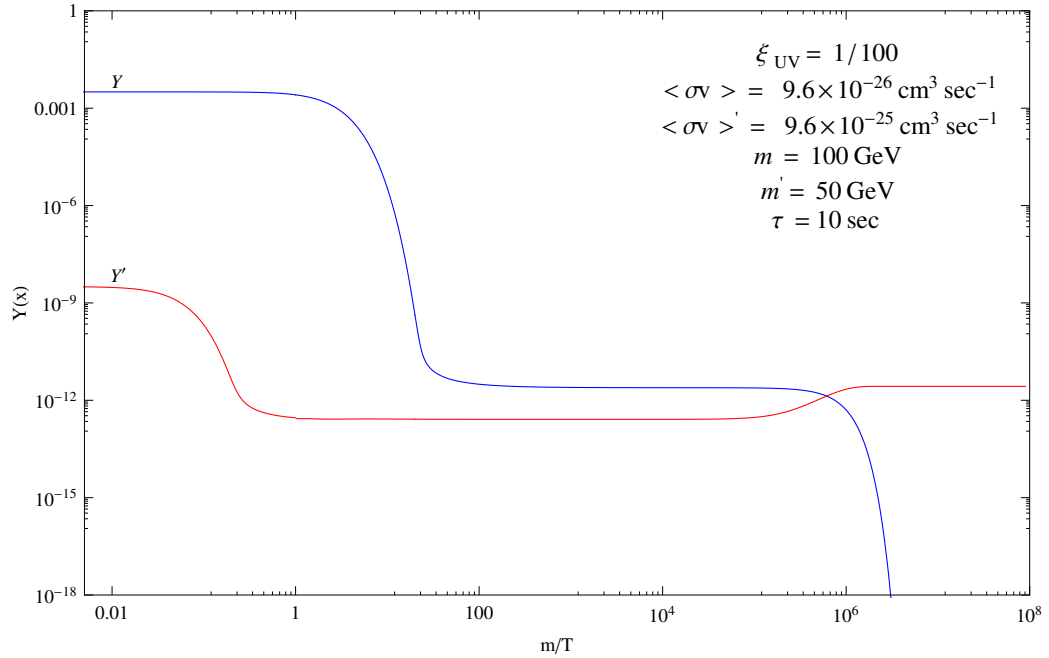
Figure 2.3: $X$ and $X'$ yields as a function of $m/T$ for DM production dominated by FO&D. The $X$ particles undergo FO and then later decay, yielding an $X'$ abundance that is larger than that which arises from FO'. The parameters $\xi, \langle \sigma v \rangle, m$ and $m'$ are the same as in Figure 2.2, but $\langle \sigma v \rangle'$ is increased giving $Y'_{\mathrm{FO}'} > Y_{\mathrm{FO}}$. For $\tau = 1$ second, $X$ decays are occurring at the MeV era.

While the first category is certainly a logical possibility, it has been well explored in the literature and is hard to test experimentally since the DM abundance depends on $\langle \sigma v \rangle'$, so we will ignore it. Moreover, we will not consider the last category because we are specifically interested in cosmological scenarios in which the visible and hidden sectors are not thermally equilibriated at the weak scale. Thus, our discussion will center on the FO&D and FI phases of the two-sector cosmology.

### 2.1.4 Freeze-Out and Decay (FO&D)

In the presence of the portal operator, $\mathcal{O}$, $X$ is no longer stable. Thus, after $X$ undergoes FO, it eventually decays into $X'$ particles; we call this DM production mechanism "Freeze-Out and Decay" (FO&D). The resulting $X'$ may form the dominant contribution to the final yield of $X'$, as illustrated in Figure 2.3. Assuming the $X$ decay process, $X \to X' + \ldots$, produces exactly one $X'$ for each $X$, we find

$$Y'_{\mathrm{FO\&D}} = Y_{\mathrm{FO}}. \tag{2.15}$$

Consequently, the energy density produced by FO&D is suppressed relative to that of conventional FO by a factor of $m'/m$. If FO&D accounts for the total DM abundance
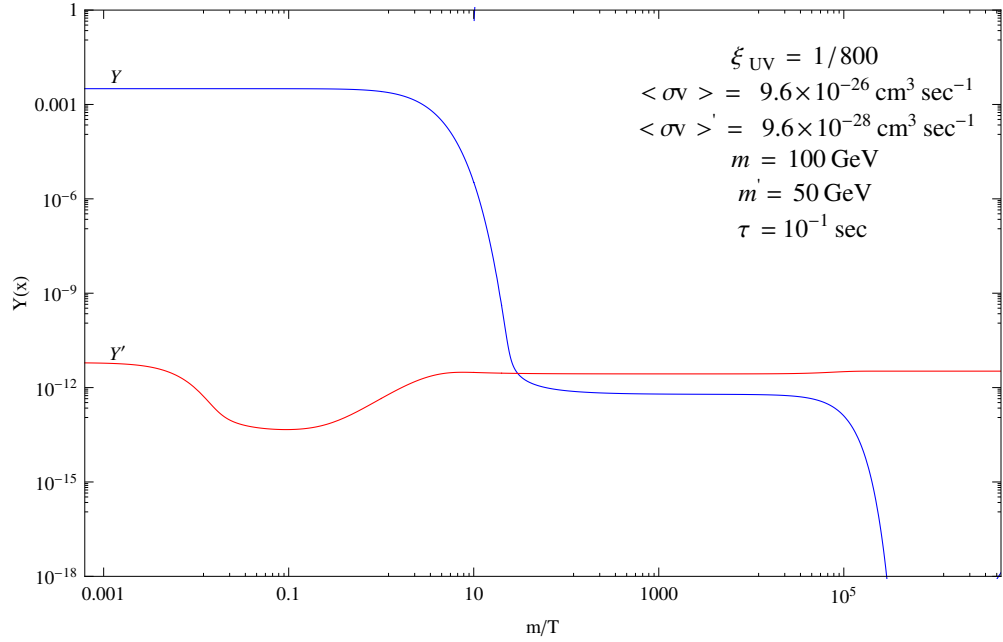
Figure 2.4: $X$ and $X'$ yields as a function of $m/T$ for DM production dominated by FI. While $X$ is relativistic and in thermal equilibrium, the small fraction of $X$ that decay yield an important contribution to the $X'$ abundance. As soon as $X'$ undergoes FO', the FI mechanism begins to effectively populate an $X'$ abundance that grows until $T$ drops below $m$, when the $X$ abundance becomes exponentially suppressed. Once the age of the universe reaches $\tau$, the relic $X$ particles from FO all decay but, for the parameter choice for this figure, the increase in $Y'$ from this FO&D process is sub-dominant to the FI contribution.

in the universe, then this implies that $\langle \sigma v \rangle = (m'/m)\langle \sigma v \rangle_0$, where recall that $\langle \sigma v \rangle_0$ is the annihilation cross-section needed to account for the measured DM abundance in standard single sector FO. This dilution factor is useful in theories in which FO normally produces an overabundance of DM, for instance as occurs in supersymmetric theories if the LSP is a bino.

Mechanisms similar to FO&D have been discussed extensively in the literature for a small subset of candidates for $X$ and $X'$ and operators $\mathcal{O}$. In particular, there is a large body of work [50, 51] concerning the so-called superWIMP scenario in which $X$ is effectively a bino or right-handed slepton and $X'$ is the gravitino. Axinos [13] and goldstini [36, 34] have also been studied as alternative choices for $X'$.

## 2.1.5 Freeze-In (FI)

As the $X$ decay rate is increased, at a certain point a new DM production mechanism, "Freeze-In" (FI), begins to dominate. Here $X'$ particles arise from decays of $X$ particles which are still in thermal equilibrium. As long as the $X'$ have already undergone FO', the $X'$ produced by FI can comprise the dominant source of DM, as

shown in Figure 2.4.

At any temperature $T > m$ the production of $X'$ by FI generates a yield which goes schematically as

$$Y'_{\text{FI}}(T) \propto \Gamma t \propto \frac{\Gamma M_{\text{Pl}}}{T^2}, \tag{2.16}$$

where $t$ is the total time that $X$ is relativistic. A key aspect of FI by decays is that it is IR dominated by low temperature dynamics; this is true independent of the dimensionality of the connector operator which mediates the decay. FI can also occur by two-to-two scattering via a marginal coupling (this is also IR dominated). However it turns out to be numerically subdominant compared to that from decays and inverse decays [63], so this will not be discussed from now on for simplicity. As $\Gamma$ becomes larger, FI plays an important role in increasing $\xi(T)$ as the temperature drops, as we will discuss in Section 2.1.7. Here we focus on the $X'$ produced after FO′. The FI yield from $X$ decay is dominated by contributions from $T \sim m$ and is the same as computed in [63] for FI from inverse decays. The precise formula for the FI yield is

$$Y'_{\text{FI}} = C_{\text{FI}}(x_{\text{FO}'})\,\frac{\Gamma M_{\text{Pl}}}{m^2}$$

$$C_{\text{FI}}(x_{\text{FO}'}) \simeq \frac{135}{2\pi^5}\sqrt{\frac{5}{2}}\frac{g_X}{g_{*S}\sqrt{g_*}}\int_{x_{\text{FO}'}}^{\infty} K_1(x)x^3 dx \tag{2.17}$$

$$\overset{x_{\text{FO}'}\to 0}{\longrightarrow}\quad C_{\text{FI}} = 1.64\frac{g_X}{g_{*S}\sqrt{g_*}},$$

where $g_X$ is the number of degrees of freedom of $X$ and $x_{\text{FO}'} \equiv m/T_{\text{FO}'}$. As shown in Eq. 2.12, in the limit in which the hidden sector is much cooler than the visible sector, $X'$ freezes out very early so $x_{\text{FO}'} \to 0$. Finally, note that if FI accounts for the total DM abundance today, then for weak scale masses this implies a range of lifetimes given by $\tau \simeq 10^{-4}$ s $- 10^{-1}$ s. If the decay of $X$ is mediated by a marginal operator with the dimensionless coefficient $\lambda$, then this range of lifetimes corresponds to $\lambda = 10^{-12} - 10^{-11}$. For decays mediated by a higher dimensional portal interaction, this range applies to $\lambda \equiv (m/M_*)^{d-4}$ where $d$ and $M_*$ are the dimension and scale of the higher dimension operator. Interestingly, for $d = 5$ operators, this corresponds to $M_* \simeq 10^{13} - 10^{15}$ GeV, which is roughly of order the GUT scale.

## 2.1.6   Re-Annihilation

For simplicity, we have ignored the effects of $X'$ annihilation on FO&D and FI. Naively, this is a justifiable omission, since both FO&D and FI occur only after the hidden sector has undergone FO′. However, even after FO′, the $X'$ abundance arising from non-equilibrium production may be so large that the $X'$ annihilation rate grows to exceeds the expansion rate, initiating a new era of $X'$ annihilation that we dub
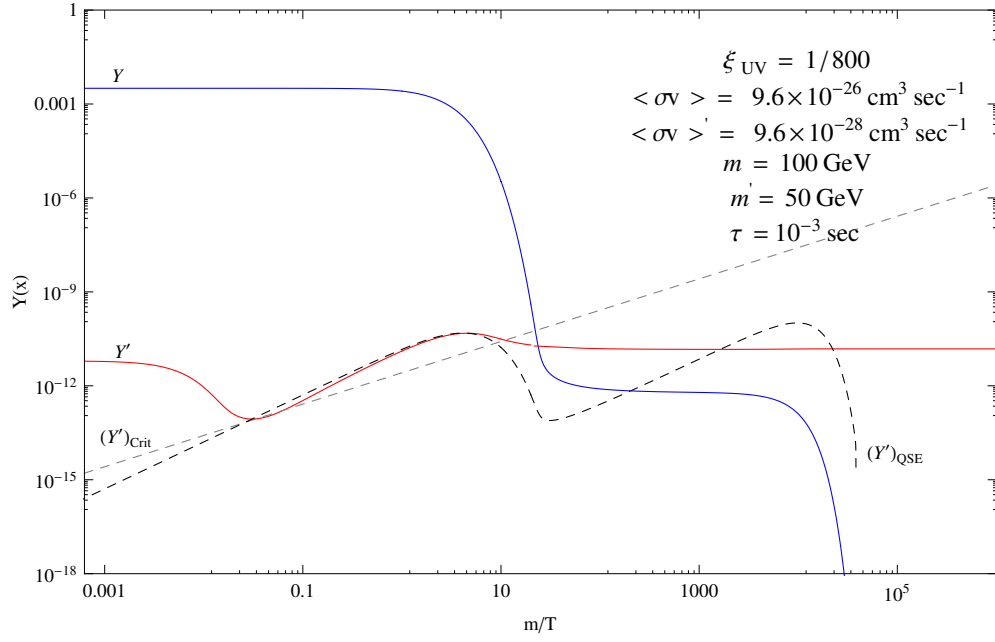
Figure 2.5: $X$ and $X'$ yields as a function of $m/T$ for DM production dominated by FI followed by re-annihilation. Re-annihilation occurs because the FI yield exceeds $Y'_{\text{crit}}$ at some temperature where $Y'_{\text{QSE}} > Y'_{\text{crit}}$. Once this happens, $Y'$ tracks $Y'_{\text{QSE}}$ until it dips below $Y'_{\text{crit}}$, which occurs as $Y$ drops rapidly at FO. The value of $Y'$ at this crossing point is the final yield of $X'$ particles.

re-annihilation. Re-annihilation and the resulting $X'$ abundance can be understood through a study of the Boltzmann equation, written in terms of yield variables and $x = m/T$,

$$x\frac{d}{dx}Y' \simeq -\frac{Y'^2}{Y'_{\text{crit}}} + \frac{\Gamma Y}{H}, \tag{2.18}$$

where

$$Y'_{\text{crit}} \equiv \frac{H}{\langle\sigma v\rangle' s}. \tag{2.19}$$

The first term on the right-hand side of Eq. 2.18 corresponds to $X'$ annihilation; since we are interested in times well after FO', $Y' \gg Y'_{\text{eq}}$ and we ignore inverse annihilations. The second term is effectively a source term for $X'$ production, corresponding to the decays of $X$ to $X'$. At $T \simeq m$ this is the source term which drives FI, while for $T \approx \sqrt{\Gamma M_{Pl}}$ this is the source term which drives FO&D. However, the analyses of FI and FO&D in the previous sections ignored the annihilation term.

The destruction and production of $X'$ occur faster than the Hubble rate if the first and second terms on the right-hand side of Eq. (2.18) are larger than $Y'$, respectively, that is if

$$Y' > Y'_{\text{crit}} \qquad \& \qquad \frac{\Gamma Y}{H} > Y'. \tag{2.20}$$
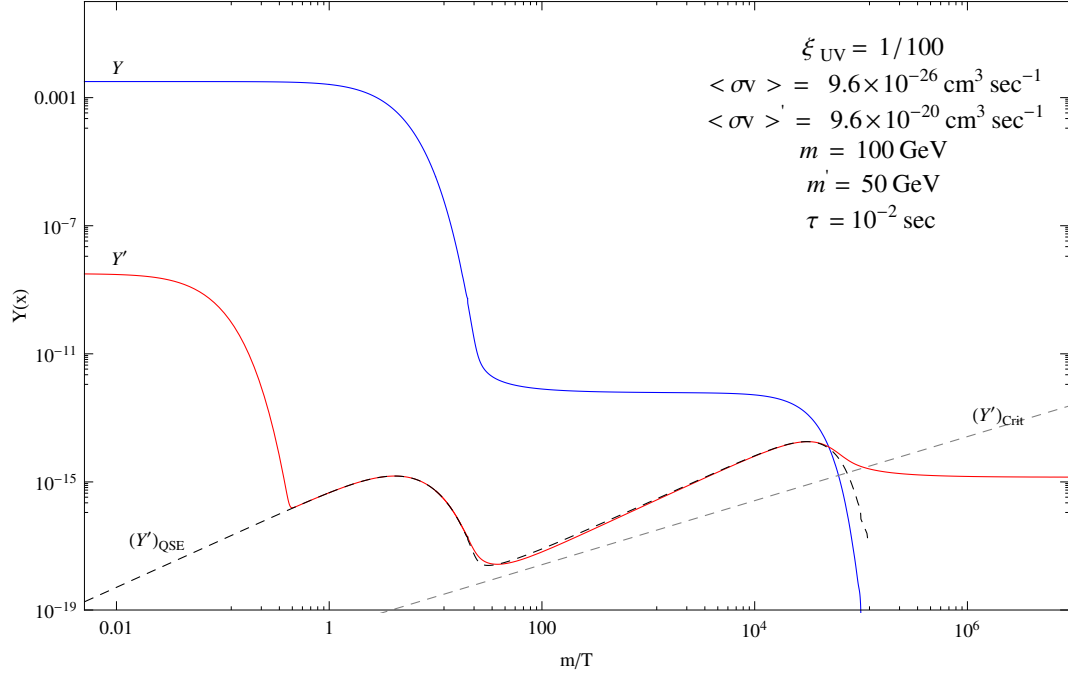
Figure 2.6: $X$ and $X'$ yields as a function of $m/T$ for DM production dominated by FO&D followed by re-annihilation. $Y'$ tracks $Y'_{\mathrm{QSE}}$ until it drops below $Y'_{\mathrm{crit}}$, which occurs when $Y$ drops sharply as $X$ decay.

In this case the $Y'$ abundance rapidly evolves to a Quasi-Static Equilibrium (QSE) in which the production of $X'$ particles is counter-balanced against depletion from the annihilation process. This causes the two terms on the right-hand side of Eq. (2.18) to cancel, so that $Y'$ becomes equal to $Y'_{\mathrm{QSE}}$, where

$$Y'^2_{\mathrm{QSE}} = \frac{\Gamma Y}{H} Y'_{\mathrm{crit}} = \frac{\Gamma Y}{\langle \sigma v \rangle' s}. \tag{2.21}$$

Setting $Y' = Y'_{\mathrm{QSE}}$ in the first equation of (2.20), one discovers that QSE is possible only during eras having

$$Y'_{\mathrm{QSE}} > Y'_{\mathrm{crit}}. \tag{2.22}$$

As $X'$ undergo FO$'$, the depletion of $X'$ will stop once $Y'$ drops to $Y'_{\mathrm{QSE}}$, provided Eq. (2.22) is satisfied, as shown in Figures 2.5 and 2.6 which were produced by numerically solving the exact Boltzmann equations. Subsequently $Y'$ tracks $Y'_{\mathrm{QSE}}$ until Eq. (2.22) is violated. This always eventually happens because $Y'_{\mathrm{crit}}$ grows linearly with $m/T$ and $Y'_{\mathrm{QSE}}$ drops as $Y$ is reduced by FO or $X$ decay. When QSE ends, i.e. when $Y'_{\mathrm{QSE}} = Y'_{\mathrm{crit}}$, the re-annihilation rate drops below the expansion rate so that QSE is lost and the $X'$ yield becomes constant. The final $X'$ abundance is fixed by the value of $Y'$ at this point. We will denote FO&D and FI which are subsequently

followed by re-annihilation by $FO\&D_r$ and $FI_r$. Note that re-annihilation did not occur in the examples shown in Figures 2.2-2.4 because Eq. (2.22) was violated at $FO'$ and all subsequent eras.

Figures 2.5 and 2.6 show yield plots for cases where DM is dominated by $FI_r$ and $FO\&D_r$, respectively. The dashed lines indicate $Y'_{\text{QSE}}$ and $Y'_{\text{crit}}$. In both plots, one sees that, once inverse annihilations of $X'$ can be neglected, QSE occurs during eras with $Y'_{\text{QSE}} > Y'_{\text{crit}}$, with $Y'$ accurately tracking $Y'_{\text{QSE}}$. Eventually, $Y'_{\text{QSE}}$ falls below $Y'_{\text{crit}}$ and QSE ends. The final DM abundance reflects the value of $Y'_{\text{QSE}}$ at the end of the QSE era, which we now study.

To analytically compute $Y'_{\text{FO\&D}_r}$ and $Y'_{\text{FI}_r}$, we must compute the temperature at the end of QSE, $T_r$, which is by definition the solution to the equation

$$Y'_{\text{QSE}}(T_r) = Y'_{\text{crit}}(T_r). \tag{2.23}$$

According to Eq. (2.21), $Y'_{\text{QSE}} \propto \sqrt{Y}$, so the solution to this equation depends on the expression for $Y$ during the era under consideration. Going from $T$ to $x$ variables, then for $FO\&D_r$ and $FI_r$ we must solve the transcendental equations

$$\begin{cases} x_{\text{FO\&D}_r}^{1/2}\, e^{-x_{\text{FO\&D}_r}} = \frac{1}{2}\left(\frac{5}{18\pi^2 g_\star}\right)^{1/4} \frac{1}{Y_{\text{FO}} M_{\text{Pl}}^{3/2} \Gamma^{1/2} \langle\sigma v\rangle'}, & \text{FO\&D}_r \\ x_{\text{FI}_r}^{5/2}\, e^{-x_{\text{FI}_r}} = \frac{\sqrt{2}\pi^{7/2}}{45} \frac{g_*}{g} \frac{m}{M_{\text{Pl}}^2 \Gamma\langle\sigma v\rangle'}, & \text{FI}_r \end{cases} \tag{2.24}$$

Hence, the final yields for FO&D and FI followed by re-annihilation are given by

$$Y'_{\text{FO\&D}_r} = Y'_{\text{crit}}(T_{\text{FO\&D}_r}) \qquad Y'_{\text{FI}_r} = Y'_{\text{crit}}(T_{\text{FI}_r}), \tag{2.25}$$

This result is very similar in structure to the yield obtained from standard $FO'$, namely $Y'_{\text{FO}'} = Y'_{\text{crit}}(T_{\text{FO}'})$. For $s$ wave annihilation $Y'_{\text{crit}} \propto 1/T$, so the re-annihilation yields obey the simple relation

$$T_{\text{FO\&D}_r} Y'_{\text{FO\&D}_r} = T_{\text{FI}_r} Y'_{\text{FI}_r} = T_{\text{FO}'} Y'_{\text{FO}'} \tag{2.26}$$

To be concrete, this implies that the DM yield for $FO\&D_r$ and $FI_r$ are given by the formulas

$$Y'_{\text{FO\&D}_r} \simeq \frac{3}{2\pi}\sqrt{\frac{5}{2}}\frac{\sqrt{g_*}}{g_{*S}}\frac{1}{M_{\text{Pl}}\langle\sigma v\rangle'}\frac{1}{T_{\text{FO\&D}_r}} \tag{2.27}$$

$$Y'_{\text{FI}_r} \simeq \frac{3}{2\pi}\sqrt{\frac{5}{2}}\frac{\sqrt{g_*}}{g_{*S}}\frac{1}{M_{\text{Pl}}\langle\sigma v\rangle'}\frac{1}{T_{\text{FI}_r}},$$

where $T_{\text{FI}_r} = m/x_{\text{FI}_r}$, and $T_{\text{FO\&D}_r} = T_{\text{Decay}}/\sqrt{x_{\text{FO\&D}_r}}$ so that the exponential in Eq. (2.24) goes simply as $e^{-x}$. Here $T_{\text{Decay}}$ is the temperature at which $X$ decays and $x_{\text{FI}_r}$ and $x_{\text{FO\&D}_r}$ are given by the solutions of Eq. (2.24). The DM yield from FO&D and FI can differ substantially from $FO\&D_r$ and $FI_r$. The condition for avoiding re-annihilation effects is $Y'_{\text{FI}} < Y'_{\text{crit}}(T = m)$ for FI and $Y_{\text{FO}} < Y'_{\text{crit}}(T = \sqrt{\Gamma M_{\text{Pl}}})$ for FO&D.

### 2.1.7  Sector Equilibration

Thus far we have ignored the effects of the connector operator $\mathcal{O}$ on the thermal properties of the visible and hidden sectors. Specifically, there is the danger that $\mathcal{O}$ couples the sectors so strongly that they actually come into thermal equilibrium. This scenario corresponds to the case where $\xi = T'/T \approx 1$ near the weak scale. In general, $\xi$ is temperature dependent and receives contributions from UV and IR-sensitive physics,

$$\xi^4(T) = \xi_{\mathrm{UV}}^4 + \xi_{\mathrm{IR}}^4(T). \tag{2.28}$$

The UV contribution to the hidden sector temperature, $\xi_{\mathrm{UV}}$, arises from two sources, so $\xi_{\mathrm{UV}}^4 = \xi_{\mathrm{inf}}^4 + \xi_R^4$. If the inflaton couples directly to the hidden sector, then $\xi_{\mathrm{inf}}$ is generated by an initial heating of the hidden sector from inflaton decays. This contribution is independent of the portal interactions, and was discussed in earlier sections. On the other hand, $\xi_R$ results from scattering processes mediated by $\mathcal{O}$ occurring at the reheat temperature, $T_R$. These processes are active if $\mathcal{O}$ is a higher-dimension operator. In this case, $\mathcal{O}$ contributes a 2-to-2 scattering cross-section, $\langle \sigma v \rangle_R$, which produces an $X'$ yield of

$$Y_R' \sim M_{\mathrm{Pl}} T_R \langle \sigma v \rangle_R. \tag{2.29}$$

The $T_R$ dependence of $\langle \sigma v \rangle_R$ depends on the dimensionality of $\mathcal{O}$. If $X'$ is inert, $Y_R'$ can easily overclose the universe unless $T_R$ is sufficiently small. For instance, in the case of gravitino LSP this is the origin of the well-known bounds on $T_R$ from overclosure [99]. On the other hand, our assumption is that $X'$ possesses self-interactions, so $X'$ particles produced by scattering at reheating will be efficiently thermalized via the $X'$ annihilation until the onset of FO'. Only after FO' can an abundance $X'$ particles be produced via FI. Consequently, in the presence of $X'$ annihilations, the FI abundance from the higher dimension operator $\mathcal{O}$ is given by Eq. 2.29, only with $T_R$ replaced by $T_{\mathrm{FO}'}$. Because $T_{\mathrm{FO}'}$ is not exceedingly far from the weak scale, this UV dominated FI contribution from 2-to-2 scattering will in general be subdominant to the IR dominated FI contribution from decays discussed in Section 2.1.5.

Since the $X$ particles are produced with energy $T_R$, the hidden sector is reheated by the visible sector to an energy density given by $T_R'^4 \sim Y_R' T_R^4$. Thus, the ratio of visible and hidden sector temperatures is given by

$$\xi_R \sim (M_{\mathrm{Pl}} T_R \langle \sigma v \rangle_R)^{1/4}, \tag{2.30}$$

in the case where there is 2-to-2 scattering processed mediated by higher dimension operators.

Finally, let us consider the IR contribution to $\xi$, which essentially arises from FI. For decays of $X$ at temperature $T$, FI produces a yield $Y_{\mathrm{FI}}'$ given by (2.16). The produced $X'$ particles have an energy distribution characteristic of temperature $T$. We assume that the interactions of the hidden sector are sufficient to rapidly

thermalize the energy of these $X'$ into distributions of all the hidden sector particles at temperature $T'$. As long as the hidden sector remains sufficiently cool, then FI will be mediated by decays and inverse decays can be ignored. From this point of view, FI leaks energy and entropy out of the visible sector into the hidden sector. This effect is especially important when the lifetime of $X$ is short, since the strength of this energy leakage is proportional to $\Gamma$. The contribution to $\xi_{\mathrm{IR}}$ from FI is

$$\xi_{\mathrm{IR}}^4(T) = A \, \frac{M_{\mathrm{Pl}}\Gamma}{T^2} \qquad (T > m), \qquad (2.31)$$

with an analytic estimate giving $A \approx 135\sqrt{5} \, g_X/(\pi^5 \sqrt{g_*}g_*')$. As $T$ drops below $m$ the FI process gets exponentially switched off, so

$$\xi_{\mathrm{IR}}(T) \simeq \xi_{\mathrm{IR}}(m) \qquad (T < m). \qquad (2.32)$$

As $\Gamma$ increases we reach a critical point where $\xi_{\mathrm{IR}}(T \simeq m) = 1$; the FI process is now so strong that the two sectors are equilibrated when $T \simeq m$. Since $m > m'$ the $X$ particles no longer undergo FO, and instead track their equilibrium abundance by decaying. Consequently, there is single thermalized sector and DM results from the single process of FO′. For $\xi_{\mathrm{UV}}^4 \ll 1$, the critical lifetime that leads to this equilibration scales as $m^{-2}$

$$\tau_{\mathrm{min}} \simeq 10^{-13} \text{ s } \left( \frac{100\,\mathrm{GeV}}{m} \right)^2 \left( \frac{100}{g_*'(T \simeq m)/g_X} \right), \qquad (2.33)$$

where the numerical coefficient has been extracted from our numerical results. Since the contribution to the heating of the hidden sector from FI is model-independent, we include its effects throughout our analysis. On the other hand, the UV-sensitive contributions are very model-dependent, so we take $\xi_{\mathrm{UV}}$ to be a free parameter which is small.

## 2.1.8   Summary of Results

Let us now summarize the results. We have show that in this setup the present day abundance of DM particles can originate only from a handful of cosmological production mechanisms. In the simplest case, the hidden sector undergoes FO′, yielding a thermal relic abundance of $X'$ particles. Alternatively, via the FO&D mechanism, an abundance of $X$ particles can FO in the visible sector, and then decay very late into $X'$ particles. The FI mechanism functions so that $X$ particles, while still in thermal equilibrium, provide an abundance of $X'$ particles through decays. Lastly, if the $X'$ yields from FO&D and FI exceed a certain critical yield, $Y'_{\mathrm{crit}}$, then the hidden sector enters an era of re-annihilation. The final abundances for FO&D$_{\mathrm{r}}$ and FI$_{\mathrm{r}}$ are controlled by the temperature at the end of this re-annihilation era. The analytic

| T | $x$ |
|---|---|
| $T_{\text{FO}} = \frac{m}{x_{\text{FO}}}$ | $x_{\text{FO}} \sim \ln\left[\frac{\sqrt{45}}{2}\frac{1}{\pi^{5/2}}\frac{g}{\sqrt{g_\star}}M_{\text{Pl}}m\langle\sigma v\rangle\right]$ |
| $T_{\text{FO}'} = \frac{1}{\xi_{\text{FO}'}}\frac{m'}{x'_{\text{FO}'}}$ | $x'_{\text{FO}'} \sim \ln\left[\frac{\sqrt{45}}{2}\frac{1}{\pi^{5/2}}\frac{g}{\sqrt{g_\star}}\xi^2_{\text{FO}'}M_{\text{Pl}}m'\langle\sigma v\rangle'\right]$ |
| $T_{\text{FO\&D}_{\text{r}}} = \frac{T_{\text{Decay}}}{\sqrt{x_{\text{FO\&D}_{\text{r}}}}} = \left(\frac{45}{2\pi^2 g_\star}\right)^{\frac{1}{4}}\sqrt{\frac{M_{\text{Pl}}\Gamma}{x_{\text{FO\&D}_{\text{r}}}}}$ | $x_{\text{FO\&D}_{\text{r}}} \sim \ln\left[\left(\frac{90}{\pi^2 g_\star}\right)^{\frac{1}{4}}\sqrt{2}x_{\text{FO}}\frac{\langle\sigma v\rangle'}{\langle\sigma v\rangle}\frac{\sqrt{\Gamma M_{\text{Pl}}}}{m}\right]$ |
| $T_{\text{FI}_{\text{r}}} = \frac{m}{x_{FI_r}}$ | $x_{\text{FI}_{\text{r}}} \sim \ln\left[\frac{45}{\sqrt{2}\pi^{7/2}}\frac{g}{g_\star}\frac{M^2_{\text{Pl}}\langle\sigma v\rangle'\Gamma}{m}\right]$ |

Table 2.1: Expressions for the various temperatures relevant for each DM production mechanism. The "$x''$" quantities employed in the first column are given approximate expressions in the second column. The quantity $\xi_{\text{FO}'}$ is computed in (2.40) below.

.

expressions for the DM yield are

$$Y'_{\text{FO\&D}} = C_{\text{FO}}\,\frac{1}{M_{\text{Pl}}\langle\sigma v\rangle}\frac{1}{T_{\text{FO}}}\ \propto\ \frac{1}{m\langle\sigma v\rangle} \tag{2.34}$$

$$Y'_{\text{FO}'} = C_{\text{FO}}\,\frac{1}{M_{\text{Pl}}\langle\sigma v\rangle'}\frac{1}{T_{\text{FO}'}}\ \propto\ \frac{\xi_{\text{FO}'}}{m'\langle\sigma v\rangle'} \tag{2.35}$$

$$Y'_{\text{FO\&D}_{\text{r}}} = C_{\text{FO}}\,\frac{1}{M_{\text{Pl}}\langle\sigma v\rangle'}\frac{1}{T_{\text{FO\&D}_{\text{r}}}}\ \propto\ \frac{\sqrt{\tau}}{\langle\sigma v\rangle'} \tag{2.36}$$

$$Y'_{\text{FI}_{\text{r}}} = C_{\text{FO}}\,\frac{1}{M_{\text{Pl}}\langle\sigma v\rangle'}\frac{1}{T_{\text{FI}_{\text{r}}}}\ \propto\ \frac{1}{m\langle\sigma v\rangle'} \tag{2.37}$$

$$Y'_{\text{FI}} = C_{\text{FI}}\,\frac{\Gamma M_{\text{Pl}}}{m^2}\ \propto\ \frac{1}{\tau m^2} \tag{2.38}$$

in the cases where the various mechanisms dominate the contribution to the total yield. Here we have defined the dimensionless constants $C_{\text{FO}} = \frac{3}{2\pi}\sqrt{\frac{5}{2}\frac{\sqrt{g_\ast}}{g_{\ast S}}}$ and $C_{\text{FI}} = 1.64\frac{g}{g_{\ast S}\sqrt{g_\ast}}$, and the various temperatures are defined in Table 2.1. The dimensionless values "$x$" defined in the second column of this table are determined in each case by solving a transcendental equation of the general form:

$$x^n\,e^{-x} = f(m, m', \langle\sigma v\rangle, \langle\sigma v\rangle', \xi, \tau) \tag{2.39}$$

for some rational number $n$ and where $f$ is a some function of the arguments. Here we have taken an approximate solution in which the effect of $x^n$ is neglected.

Note that only FO$'$ depends on $\xi$; in particular it depends on the value of $\xi$ at $T_{\text{FO}'}$ which is denoted in the Table 2.1 as $\xi_{\text{FO}'}$. From the analysis in Section 2.1.7, one notes that the quantity $\xi_{\text{FO}'} \equiv \xi(T_{\text{FO}'})$ has different forms depending on whether

$T_{\mathrm{FO'}}$ is greater or smaller than $m$. $\xi_{\mathrm{FO'}}$ can be computed as:

$$\xi_{\mathrm{FO'}} = \begin{cases} \left(\xi_{\mathrm{UV}}^4 + \frac{A\Gamma M_{\mathrm{Pl}}}{m^2}\right)^{1/4} & , \quad T_{\mathrm{FO'}} < m \\ \left(\frac{A\Gamma M_{\mathrm{Pl}} x_{\mathrm{FO}}^2}{2\,m'^2}\right)^{1/2}\left[1 + \left(1 + \frac{4\,\xi_{\mathrm{UV}}^4\,m'^4}{A^2\Gamma^2\,M_{\mathrm{Pl}}^2\,x_{\mathrm{FO}}^4}\right)^{1/2}\right]^{1/2} & , \quad T_{\mathrm{FO'}} > m \end{cases} \tag{2.40}$$

where $A$ is as defined after Eq. (2.31).

## 2.2 Cosmological Phase Diagrams

We have identified and characterized all possible mechanisms of DM production which can arise within a general two-sector framework. To this end, we have simulated the cosmological history of this system over a broad range of values for the relevant parameters:

$$\{m, m', \langle\sigma v\rangle, \langle\sigma v\rangle', \xi_{\mathrm{UV}}, \tau\}, \tag{2.41}$$

where $\xi_{\mathrm{UV}}$ is the UV initial condition for $\xi$ which receives contributions from the decay of the inflaton as well as scattering processes from higher-dimensional operators described in Eq. (2.28)[3]. As noted earlier, it is quite remarkable that the cosmology is determined solely by just a handful of quantities.

In this section we present a series of "cosmological phase diagrams" depicting the regions in parameter space in which each mode of DM production, i.e. FO&D, FI, etc., accounts for the dominant contribution to the present day DM abundance. For example, Figure 2.7 is a cosmological phase diagram in the $\tau - \frac{\langle\sigma v\rangle'}{\langle\sigma v\rangle}$ plane for particular values of $\{m, m', \langle\sigma v\rangle, \xi_{\mathrm{UV}}\}$, as explained in the caption. Each colored shaded region corresponds to a particular DM production mode which is dominant in that region. The boundaries of each phase have been computed analytically. The solid black contours correspond to the present day DM relic abundance, calculated numerically using the coupled Boltzmann equations in Eqs. (2.5). Let us consider some of the features of Figure 2.7 in detail.

First, note that the lifetime $\tau$ is constrained both from above and below as shown by the red vertical lines in Figure 2.7. The upper limit is easy to understand as it originates from the requirement the decay products of $X$ do not ruin the successful predictions of BBN [99]. While the precise constraint depends on the nature of $X$ and its decay products, here we use

$$\tau_{\mathrm{max}} \simeq 100 \text{ s}, \tag{2.42}$$

as depicted by the red line at large $\tau$ in Figure 2.7. The lower limit on $\tau$ comes from demanding that the two sectors are *not* in thermal equilibrium with each other at

---

[3]Here we also take $\xi_{\mathrm{UV}}$ to include effects from additional sources of entropy dumping into either sector before the weak era, so that $\xi_{\mathrm{UV}}$ is effectively the weak scale value of $\xi$, modulo the contribution from $X$ decays in the IR.
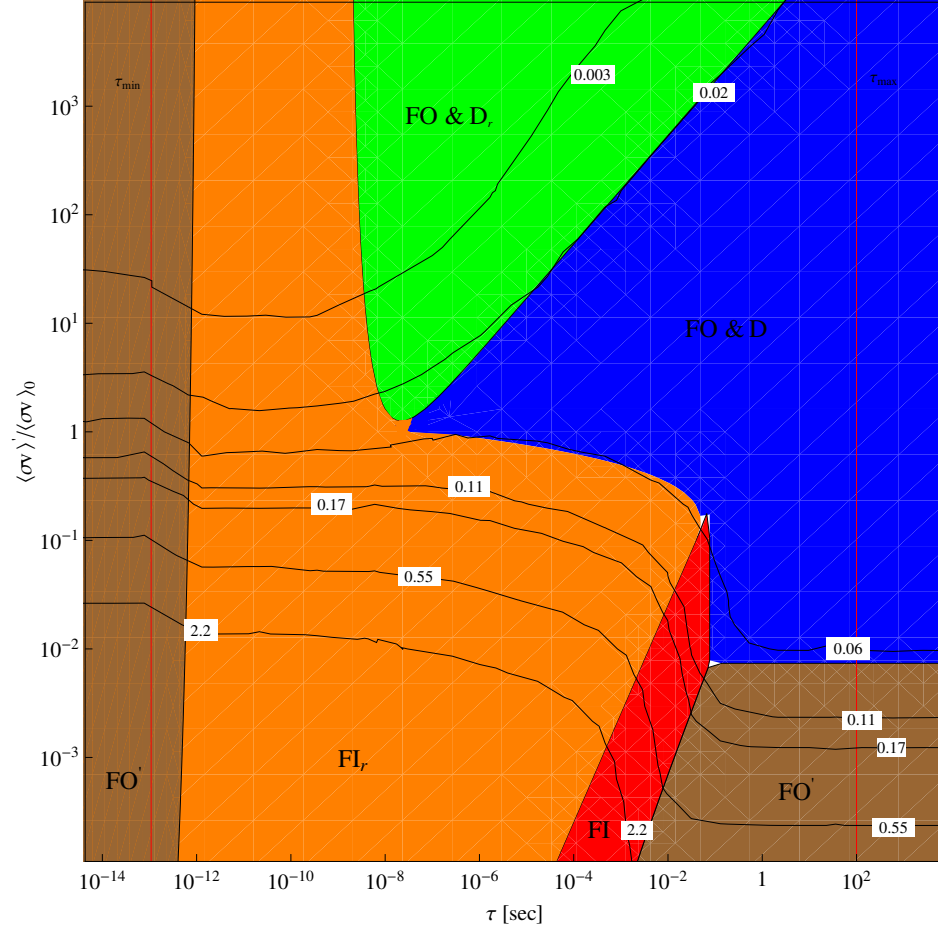
Figure 2.7: Cosmological phase diagram showing regions in the $\frac{\langle \sigma v \rangle'}{\langle \sigma v \rangle_0}$ versus $\tau$ plane where different mechanisms contributing to the relic abundance dominate. The values of the other relevant parameters are chosen as: $\xi_{\mathrm{UV}} = 0.01$, $m = 100\,\mathrm{GeV}$, $m' = 50\,\mathrm{GeV}$, $\langle \sigma v \rangle = \langle \sigma v \rangle_0 = 3 \times 10^{-26}\ \mathrm{cm^3/s}$. Contours of $\Omega h^2$, computed from a full numerical analysis for $Y'$ (numerical solution of Eq. (2.5) and Eq. (2.6)), are shown. Regions in which the various mechanisms dominate are shown in different colors. These regions are computed analytically and overlaid on the numerical plot. The agreement is quite good.

the weak scale. In Section 2.1.7 we found that for $\xi_{\mathrm{UV}}^4 \ll 1$, the two sectors becomes thermally equilibrated if the lifetime is shorter than

$$\tau_{\min} \simeq 10^{-13}\,\mathrm{s}\ \left( \frac{100\,\mathrm{GeV}}{m} \right)^2 \left( \frac{100}{g'_*(T \simeq m)/g_X} \right). \tag{2.43}$$

For $\tau \lesssim 10^{-13}$ s, the two sectors are, from a cosmological perspective, a single sector. As a consequence, there is no distinction between FO and FO′—the visible and hidden sectors together maintain thermal equilibrium until $X'$ undergoes single sector FO′. This is depicted by the *brown* region in the left in Figure 2.7. The yield $Y'_{\mathrm{FO'}}$ in this

region is independent of $\tau$ because $\xi_{\mathrm{FO'}} = 1$ in the expression for $Y'_{\mathrm{FO'}}$ in Table 2.1. Note that the *brown* region extends to $\tau$ larger than $\tau_{\mathrm{min}}$, as will be discussed soon.

Next, let us discuss the salient features of Figure 2.7 as we move from the largest to the smallest allowed values for $\tau$. Furthermore, for a given value of $\tau$, the dominant DM production mechanism changes as a function of $\frac{\langle\sigma v\rangle'}{\langle\sigma v\rangle}$. For example, for the choice of parameters in Figure 2.7, one finds that FO&D and FO' dominate over FI for $10^{-1}$ s $\lesssim \tau \lesssim 100$ s. This is because the lifetime is too long (the coupling is too weak) for the FI mechanism to set in, as shown in Section 2.1.5. For values of $\tau$ in the above range with $\frac{\langle\sigma v\rangle'}{\langle\sigma v\rangle} \gtrsim 10^{-1}$, corresponding to the *blue* shaded region, FO&D is the dominant mechanism. Indeed, from the shape of the contours one can see that in this region the relic abundance is independent of $\frac{\langle\sigma v\rangle'}{\langle\sigma v\rangle}$ and $\tau$ as dictated by the expression for $Y'_{\mathrm{FO\&D}}$ in Table 2.1. For $\frac{\langle\sigma v\rangle'}{\langle\sigma v\rangle} \lesssim 10^{-2}$, FO' starts to dominate over FO&D since the annihilation cross-section of $X'$ becomes sufficiently small. This is shown by the *brown* region in the right in the figure. For such long lifetimes, one finds that $\xi_{\mathrm{FO'}} \approx \xi_{\mathrm{UV}}$ from (2.28), implying that $Y'_{\mathrm{FO'}}$ is essentially independent of $\tau$ (see the expression for $Y'_{\mathrm{FO'}}$ in Table 2.1). Thus, the contour lines in this region are roughly horizontal. The boundary between the FO&D and FO' regions for this range of $\tau$ is given by :

$$Y'_{\mathrm{FO\&D}} = Y'_{\mathrm{FO'}} \implies \frac{\langle\sigma v\rangle'}{\langle\sigma v\rangle} = \xi_{\mathrm{FO'}} \frac{m}{m'} \frac{\langle\sigma v\rangle'}{\langle\sigma v\rangle} \propto \text{constant}$$

which in the $\frac{\langle\sigma v\rangle'}{\langle\sigma v\rangle} - \tau$ plane corresponds to $\frac{\langle\sigma v\rangle'}{\langle\sigma v\rangle} \approx$ constant, since $\xi_{\mathrm{FO'}} \approx \xi_{\mathrm{UV}}$.

For $10^{-8}$ s $\lesssim \tau \lesssim 10^{-4} - 10^{-1}$ s, FI and FI$_\mathrm{r}$ begin to dominate over FO&D and FO' because the portal interactions between sectors is growing stronger. In particular, FI is dominant in the narrow band shown by the *red* shaded region in Figure 2.7. For FI to be the dominant mechanism, the yield from FI must be larger than that from FO' but smaller than that from FI$_r$; hence the narrow band in which FI is the dominant mechanism. The boundary curves between the FI region and the FO' & FI$_r$ regions are given by:

$$Y'_{\mathrm{FI}} = Y'_{\mathrm{FI}_r} \implies \frac{\Gamma M_{\mathrm{Pl}}^2 \langle\sigma v\rangle'}{m} = \frac{C_{\mathrm{FO}}}{C_{\mathrm{FI}}} x_{\mathrm{FI}_r} \frac{\langle\sigma v\rangle'}{\langle\sigma v\rangle} \propto \tau \qquad (2.44)$$

$$Y'_{\mathrm{FI}} = Y'_{\mathrm{FO'}} \implies \frac{\Gamma M_{\mathrm{Pl}}^2 \langle\sigma v\rangle' m'}{\xi_{\mathrm{FO'}} m^2} = \frac{C_{\mathrm{FO}}}{C_{\mathrm{FI}}} x_{\mathrm{FO'}} \frac{\langle\sigma v\rangle'}{\langle\sigma v\rangle} \propto \tau$$

Both curves imply a linear relation between $\frac{\langle\sigma v\rangle'}{\langle\sigma v\rangle}$ and $\tau$, only with different coefficients depends on $\xi_{\mathrm{FO'}}$ as well, but in this region $\xi_{\mathrm{FO'}} \approx \xi_{\mathrm{UV}}$ is a constant. Also, note from Table 2.1 that $Y'_{\mathrm{FI}}$ does not depend on $\frac{\langle\sigma v\rangle'}{\langle\sigma v\rangle}$, hence the contour lines for the relic abundance are almost vertical. They are not completely vertical since it turns out that FI never fully dominates the contribution to the relic abundance.

For $10^{-8}$ s $\lesssim \tau \lesssim 10^{-4} - 10^{-1}$ s with $\frac{\langle \sigma v \rangle'}{\langle \sigma v \rangle} \lesssim 1$, the FI yield becomes so large that it exceeds the critical yield at $T_{\mathrm{FI}_r}$, implying that $X'$ starts to re-annihilate and the yield is given by $Y'_{\mathrm{FI}_r}$. This is shown by the *orange* region in the figure. From Table 2.1, one sees that contours for $Y'_{\mathrm{FI}_r}$ are essentially horizontal since the dependence on $\tau$ only arises from the logarithm. As one increases $\frac{\langle \sigma v \rangle'}{\langle \sigma v \rangle}$ above roughly unity, FO&D starts to dominate over FI$_r$ as shown by the *blue* region, since the annihilation cross-section of $X'$ becomes large enough that the yield $Y'_{\mathrm{FI}_r}$ becomes smaller than $Y'_{\mathrm{FO\&D}}$. The boundary curve between these two regions is defined by:

$$Y'_{\mathrm{FO\&D}} = Y'_{\mathrm{FI}_r} \implies \frac{\langle \sigma v \rangle'}{\langle \sigma v \rangle} = \frac{x_{\mathrm{FI}_r}}{x_{\mathrm{FO}}} \frac{\langle \sigma v \rangle'}{\langle \sigma v \rangle} \propto x_{\mathrm{FI}_r} \propto \ln \left[ \frac{\langle \sigma v \rangle'}{\langle \sigma v \rangle} \frac{1}{\tau} \right]$$

showing that $\frac{\langle \sigma v \rangle'}{\langle \sigma v \rangle}$ is essentially constant up to a logarithmic dependence.

If $\frac{\langle \sigma v \rangle'}{\langle \sigma v \rangle}$ is further increased, FO&D is eventually superseded by FO&D$_r$ as shown by the *green* region. In this case the $X'$ yield from the freezeout and decay of $X$ is so large that it becomes larger than the critical yield; so $X'$ starts re-annihilating with a yield given by $Y'_{\mathrm{FO\&D}_r}$. From Table 2.1, the contour plots for $Y'_{\mathrm{FO\&D}_r}$ follow a simple power law ($\frac{\langle \sigma v \rangle'}{\langle \sigma v \rangle} \propto \sqrt{\tau}$). The boundary curve between the FO&D and FO&D$_r$ regions is given by:

$$Y'_{\mathrm{FO\&D}_r} = Y'_{\mathrm{FO\&D}} \implies \frac{\langle \sigma v \rangle'}{\langle \sigma v \rangle} = \frac{1}{A_{\mathrm{FO\&D}_r}} \frac{\sqrt{x_{\mathrm{FO\&D}_r}}}{x_{\mathrm{FO}}} \frac{m}{\sqrt{\Gamma M_{\mathrm{Pl}}}} \frac{\langle \sigma v \rangle'}{\langle \sigma v \rangle} \propto \sqrt{\tau}$$

showing that the boundary also follows the same power law as the DM yield contours.

For few $\times 10^{-13}$ s $\lesssim \tau \lesssim 10^{-8}$ s, FI$_r$ is again the dominant mechanism as shown by the *orange* region. It dominates over FO&D$_r$ in particular, since the yield is inversely proportional to the relevant temperatures for FO&D$_r$ and FI$_r$, which are $T_{\mathrm{FO\&D}_r}$ and $T_{\mathrm{FI}_r}$ respectively, and $T_{\mathrm{FO}_r}$ is larger for small lifetimes (large $\Gamma$) compared to $T_{\mathrm{FI}_r}$ from Table 2.1. The boundary curve between these two regions is given by:

$$Y'_{\mathrm{FO\&D}_r} = Y'_{\mathrm{FI}_r} \implies \sqrt{\frac{\Gamma M_{\mathrm{Pl}}}{x_{\mathrm{FO\&D}_r}}} A_{\mathrm{FO\&D}_r} = \frac{m}{x_{\mathrm{FI}_r}} \tau \propto \frac{x_{\mathrm{FI}_r}^2}{x_{\mathrm{FO}_r}} \propto \frac{\left( \ln \left[ \frac{\langle \sigma v \rangle'}{\langle \sigma v \rangle} \frac{1}{\tau} \right] \right)^2}{\ln \left[ \frac{\langle \sigma v \rangle'}{\langle \sigma v \rangle} \frac{1}{\sqrt{\tau}} \right]}$$

which is roughly $\tau \propto$ constant, although more precisely there is a dependence on $\frac{\langle \sigma v \rangle'}{\langle \sigma v \rangle}$ and $\tau$ from the logarithms.

Finally, for $\tau_{\min} < \tau \lesssim$ few $\times \tau_{\min}$, FO$'$ again dominates for the entire range of $\frac{\langle \sigma v \rangle'}{\langle \sigma v \rangle}$ as is shown by the *brown* region in Figure 2.7. To understand this, it has to be compared to the next relevant mechanism, namely FI$_r$. Since the lifetime $\tau$ is short in this region, $\xi_{\mathrm{FO}'}$, which is given by the expression in the top line in Eq. (2.40) in this case, becomes large and close to unity. Hence, in this region, $\xi_{\mathrm{FO}'} > \frac{m'}{m} \frac{x_{\mathrm{FI}_r}}{x_{\mathrm{FO}'}}$, or equivalently $T_{\mathrm{FO}'} < T_{\mathrm{FI}_r} < m$ from Table 2.1. Since $\langle \sigma v \rangle$ has been fixed in Figure

Figure 2.8: Sequence of cosmological phase diagrams with $\langle\sigma v\rangle$ varying. Other parameters are as in Figure 2.7: ($\xi_{\mathrm{UV}} = 0.01$, $m = 100\,\mathrm{GeV}$, $m' = 50\,\mathrm{GeV}$). The black contour corresponds to $\Omega h^2 = 0.11$, the observed DM relic abundance.

2.7, from Table 2.1 and (2.40), the contours for the DM yield in this region have a dependence $\frac{\langle\sigma v\rangle'}{\langle\sigma v\rangle} \propto \tau^{-1/4}$. The boundary curve between the two regions is given by:

$$Y'_{\mathrm{FO}'} = Y'_{\mathrm{FI_r}} \implies \frac{1}{\xi_{\mathrm{FO}'}}\frac{m'}{x_{\mathrm{FO}'}} = \frac{m}{x_{\mathrm{FI_r}}}\tau \propto \frac{1}{\left(\ln\left[\frac{\langle\sigma v\rangle'}{\langle\sigma v\rangle}\frac{1}{\tau}\right]\right)^4}$$

which is again approximately $\tau \propto$ constant, but more pecisely with an additional dependence on $\frac{\langle\sigma v\rangle'}{\langle\sigma v\rangle}$ and $\tau$ in the logarithm.

## 2.2.1 Behavior of Phase Space Diagram

In the cosmological phase space diagram depicted in Figure 7, the parameters $\{m, m', \langle\sigma v\rangle, \xi_{\mathrm{UV}}\}$ were fixed. Let us now examine how each phase region changes as we vary these four parameters. Figures 2.8, 2.9, and 2.10 are cosmological phase diagrams showing the variation of one of these parameters while keeping the remaining three fixed. The effects on the regions can be understood by referring to the formulae in Section 2.2 which define the boundaries between regions. In addition, we would like to examine how the mechanism of DM production is affected. To this end we include in these figures a single "critical DM abundance" contour (black line) corresponding to the $\Omega h^2 = 0.11$.

Figure 2.8 illustrates the effect of varying $\langle\sigma v\rangle$. The most dramatic change is in the contours of total yield. As can be seen from the analytic yield formulas in Section 2.2, when $\langle\sigma v\rangle$ is decreased, $\frac{\langle\sigma v\rangle'}{\langle\sigma v\rangle}$ must increase in order to maintain a constant yield, whether dominated by FO′, FO&D, FO&D$_{\mathrm{r}}$, or FI$_{\mathrm{r}}$. In addition the boundaries of the FI region shift to smaller lifetimes. Thus the yield contours "rise" in the $\tau - \frac{\langle\sigma v\rangle'}{\langle\sigma v\rangle}$ plane. For larger values of $\langle\sigma v\rangle$, as in the left panel of Figure 2.8, the black line corresponding to $\Omega h^2 = 0.11$ can access the FI region but not the FO&D region.
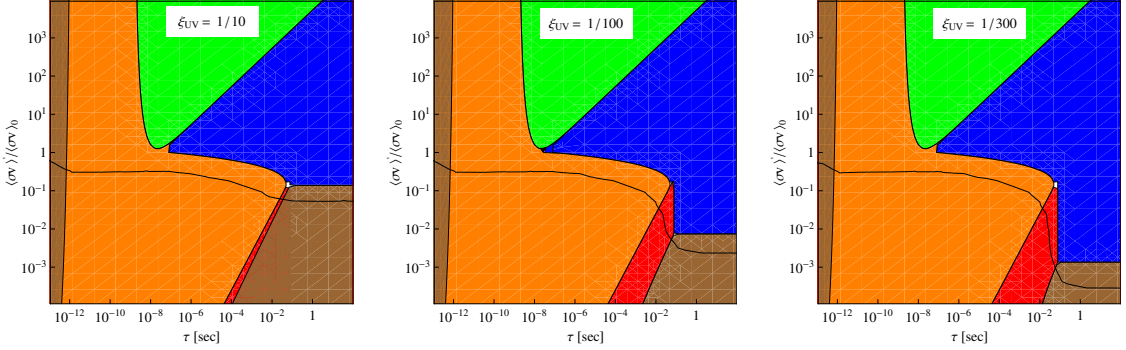
Figure 2.9: Sequence of cosmological phase diagrams with $\xi_{\mathrm{UV}}$ varying. Other parameters are as in Figure 2.7: ($m = 100\,\mathrm{GeV}$, $m' = 50\,\mathrm{GeV}$, $\langle \sigma v \rangle = 3 \times 10^{-26}\,\mathrm{cm^3/s}$). The black contour corresponds to $\Omega h^2 = 0.11$, the observed DM relic abundance.

Once FI dominates it will give the correct DM abundance when:

$$\tau \simeq (3 \times 10^{-15}\,\mathrm{s}) \times M_{\mathrm{Pl}} \frac{m'}{m^2} \frac{g}{g_\star^{3/2}} \simeq \left(4 \times 10^{-2}\,\mathrm{s}\right) \left(\frac{m'}{m}\right) \left(\frac{100\mathrm{GeV}}{m}\right) \left(\frac{228.5}{g_\star}\right)^{3/2} \quad (2.45)$$

this corresponds to a lifetime of $\simeq 10^{-2}$ s in the left panel of Figure 2.8. As $\langle \sigma v \rangle$ is decreased the critical DM contour rises and can start to access the FO&D region. For FO&D to give the correct DM abundance the following relation must hold:

$$\frac{\langle \sigma v \rangle m}{m'} \sim \frac{4 \times 10^{10}}{M_{\mathrm{Pl}} \sqrt{g_\star}} \sim \frac{2 \times 10^{-25}\,\mathrm{cm^3 sec^{-1}}}{\sqrt{g_\star}} \quad (2.46)$$

This is the case for the center panel of Figure 2.8 with $g_\star = 228.5$. Decreasing $\langle \sigma v \rangle$ even further leads to FO&D$_\mathrm{r}$ domination, as shown in the right panel of Figure 2.8.

Figure 2.9 illustrates the effect of varying $\xi_{\mathrm{UV}}$. As is expected from Eq.(46) decreasing $\xi_{\mathrm{UV}}$ results in a smaller large-$\tau$ FO$'$ region. This makes sense since decreasing $\xi_{\mathrm{UV}}$ corresponds to an earlier FO$'$ (for large $\tau$, $\xi_{\mathrm{FO}'} \sim \xi_{\mathrm{UV}}$) and a smaller $Y'_{\mathrm{FO}'}$ which will thus dominate in a smaller region of parameter space. It is clear that the FI region expands as $\xi_{\mathrm{UV}}$ is decreased.

Figure 2.10 illustrates the effect of varying $m'$. From (2.45) it is clear that the lifetime that yields the observed DM abundance from FI is proportional to $m'$. In the left panel of Figure 2.10, $m' = 50$ GeV and the FI lifetime is $\tau \sim 10^{-2}$ s; decreasing $m'$ it is possible to lower this lifetime. This is shown in the center and right panels of Figure 2.10; $m' = 10$ GeV requires $\tau \sim 10^{-3}$ s for FI to dominate. Also note that decreasing $m'$ results in a larger FO$'$ region at small $\tau$, as expected since this boundary is approximately the line $\xi = \frac{m'}{m}$.

Finally we comment on the variation of $m$. The only major effect is the change in the lifetime at the thermalization bound (red line) which corresponds to $\xi(\tau, m) = 1$. Thus as $m$ is increased this lifetime is decreased.
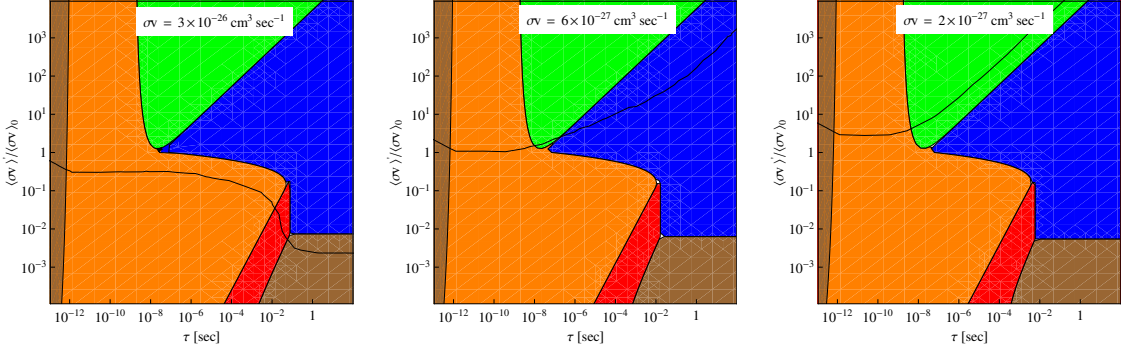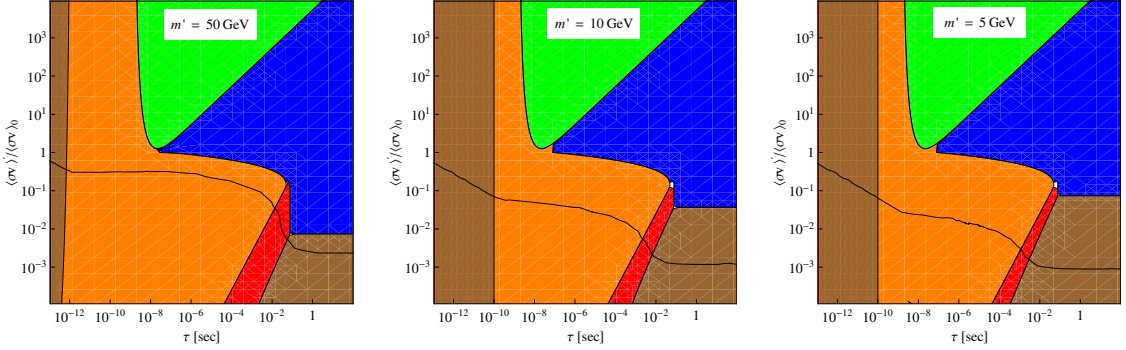
Figure 2.10: Sequence of cosmological phase diagrams with $m'$ varying. Other parameters are as in Figure 2.7: ($\xi_{\mathrm{UV}} = 0.01$, $m = 100\,\mathrm{GeV}$, $\langle \sigma v \rangle = 3 \times 10^{-26}\,\mathrm{cm^3/s}$). The black contour corresponds to $\Omega h^2 = 0.11$, the observed DM relic abundance.

## 2.3  Dark Matter Asymmetry

Until now our discussion has been limited to cases in which the final abundance of the DM, $X'$, is symmetric under the exchange of particles and anti-particles. As such we have implicitly assumed that either $X'$ is its own anti-particle or that the mechanism of DM production dynamically produces equal numbers of $X'$ and $\bar{X}'$. In this section we determine the conditions necessary for DM to arise from a particle anti-particle asymmetry

$$\eta' = \frac{n' - \bar{n}'}{s} \tag{2.47}$$

rather than from a symmetric yield, $Y' = (n' + \bar{n}')/s$. An asymmetric mechanism of DM production requires that the hidden sector possess a global $U(1)$ symmetry, $Q'$. A crucial question is then whether the portal interactions connecting each sector either completely break $Q'$, or whether they preserve some combination of $Q'$, baryon number $B$, and lepton number $L$. We study two possible scenarios in which there exists a global $U(1)$ symmetry $S$ having the properties

- $S_1 = Q'$ rotates only hidden sector fields and is broken by the connector interactions.

- $S_2 = \alpha B + \beta L + \gamma Q'$, with real parameters $\alpha, \beta$ and $\gamma$, is exact, except possibly for anomalies.

### 2.3.1  Asymmetric FI and Asymmetric FO&D

At temperatures well above the weak scale we assume that there does not exist any asymmetry between the DM particles and anti-particles, so $\eta' = 0$. Is it possible for a non-zero asymmetry to be generated by the thermal production mechanisms studied

in the last section? At first sight the answer is no, since each sector is separately in thermal equilibrium. While thermal equilibrium is lost right at the end of FO and FO$'$, these processes involve *total* annihilation cross-sections $\langle\sigma v\rangle, \langle\sigma v\rangle'$ which are the same for anti-particles as for particles, so an asymmetry cannot be generated. However, the sectors are at different temperatures, so processes mediated by the connector interactions are not in thermal equilibrium. This offers new possibilities for generating a DM asymmetry, and indeed for baryogenesis. For the symmetry $S_1$, the connector interactions may generate $\eta'$, but it is unrelated to the baryon and lepton asymmetries, $\eta_{L,B}$. On the other hand, symmetry $S_2$ is exact so any $Q'$ charge that is generated must be compensated by baryon and lepton charges, so that the universe remains neutral under the charge of $S_2$. Asymmetric FI that provides such a correlation between the baryon and DM densities is discussed in [?], and explicit supersymmetric models are constructed.

There are now four Boltzmann equations to be studied for the evolution of $n, \bar{n}, n'$ and $\bar{n}'$. The equations for $n$ and $\bar{n}$ are identical and take the form of Eq. (2.5). The decay rate $\Gamma$ is the total decay rate of $X$, and by CPT the total decay rate of $\bar{X}$ is also $\Gamma$. However, the equations for $n'$ and $\bar{n}'$ become more complicated once we consider multiple decay modes for $X$, which is one of the necessary conditions to generate an asymmetry. We index each decay mode by $i$, with a partial width $\Gamma_i$ corresponding to

$$X \to p_i X' + \bar{p}_i \bar{X}' + (\text{particles with } Q' = 0) \tag{2.48}$$

where $p_i$ and $\bar{p}_i$ are integers denoting the number of $X'$ and $\bar{X}'$ particles produced via the $i$th decay mode. The $X'$ and $\bar{X}'$ may result from a cascade of decays in the hidden sector. In general, there can be modes containing particles other than $X'$ and $\bar{X}'$ (say $Y'$) with $Q' \neq 0$; however we assume that the hidden sector interactions are large enough that $Y'$ rapidly decays into $X'$ and $\bar{X}'$, so that we only need to consider modes of the form in (2.48) above. If $X$ is not equal to its own anti-particle then $\bar{X}$ has a set of decay modes to the corresponding anti-particles with partial widths $\bar{\Gamma}_i$, and by CPT the total decay rates of $X$ and $\bar{X}$ are equal, i.e. defining $\Gamma \equiv \sum_i \Gamma_i$ and $\bar{\Gamma} \equiv \sum_i \bar{\Gamma}_i$, then $\Gamma = \bar{\Gamma}$. On the other hand, if $X$ is real it can decay both via Eq. (2.48) and by the decay to the corresponding anti-particles, so that its total lifetime is $\Gamma = \sum_i \Gamma_i + \sum_i \bar{\Gamma}_i$.

The Boltzmann equations for $n'$ and $\bar{n}'$ are:

$$\frac{d}{dt}n' + 3Hn' = -(n'\bar{n}' - n'_{\text{eq}}\bar{n}'_{\text{eq}})\langle\sigma v\rangle' + n\sum_i p_i\Gamma_i + \bar{n}\sum_i \bar{p}_i\bar{\Gamma}_i \tag{2.49}$$

$$\frac{d}{dt}\bar{n}' + 3H\bar{n}' = -(n'\bar{n}' - n'_{\text{eq}}\bar{n}'_{\text{eq}})\langle\sigma v\rangle' + n\sum_i \bar{p}_i\Gamma_i + \bar{n}\sum_i p_i\bar{\Gamma}_i. \tag{2.50}$$

As with the analysis of the symmetric abundance $Y'$ in the previous section, we omit scattering process contributions to FI. They are UV dominated both for $Y'$ and $\eta'$,

and it is unclear how they can be distinguished experimentally from a high scale initial condition on $\eta'$. Taking sums and differences of these two equations, the source terms for $n' \pm \bar{n}'$ are $\sum_i (p_i \pm \bar{p}_i)(n\Gamma_i \pm \bar{n}\bar{\Gamma}_i)$. The goal of this analysis is to understand how $\eta'$ is generated from these equations starting from *symmetric* boundary conditions, i.e. when $\bar{n} = n$. As such, this mechanism is markedly different from using these equations to transfer a pre-existing asymmetry in $X$ to $X'$, as has been studied in the context of ADM [77]. With $\bar{n} = n$ the source terms become $\Gamma n \sum_i (p_i \pm \bar{p}_i)(r_i \pm \bar{r}_i)$, where we introduced the branching ratios $r_i = \Gamma_i/\Gamma$ and $\bar{r}_i = \bar{\Gamma}_i/\bar{\Gamma}$. This last form is also the correct source term for the case that $X$ is the same as its anti-particle.

Using these source terms, the symmetric and asymmetric contributions to the DM yields are given for FO&D by

$$Y'_{\text{FO\&D}} = \frac{C_{\text{FO}}}{M_{\text{Pl}} T_{\text{FO}} \langle \sigma v \rangle} \sum_i (p_i + \bar{p}_i)(r_i + \bar{r}_i) \qquad \eta'_{\text{FO\&D}} = \frac{C_{\text{FO}}}{M_{\text{Pl}} T_{\text{FO}} \langle \sigma v \rangle} \sum_i (p_i - \bar{p}_i)(r_i - \bar{r}_i),$$

$$(2.51)$$

and for FI by

$$Y'_{\text{FI}} = C_{\text{FI}} \frac{M_{\text{Pl}} \Gamma}{m^2} \sum_i (p_i + \bar{p}_i)(r_i + \bar{r}_i) \qquad \eta'_{FI} = C_{\text{FI}} \frac{M_{\text{Pl}} \Gamma}{m^2} \sum_i (p_i - \bar{p}_i)(r_i - \bar{r}_i). \quad (2.52)$$

The symmetric yields $Y'_{\text{FO\&D}}$ and $Y'_{\text{FI}}$ were studied in great detail in Sections 3.1 and 2.2. Note that these yields do not take re-annihilation into account; this will be discussed soon. On the other hand, the asymmetric yields $\eta'_{\text{FO\&D}}$ and $\eta'_{\text{FI}}$, are new—we denote these DM production mechanisms by Asymmetric Freeze-Out and Decay (FO&D$_{\text{a}}$) and Asymmetric Freeze-In (FI$_{\text{a}}$). As seen from (2.51) and (2.52), generating an asymmetry requires decay modes with $\bar{p}_i \neq p_i$ so that the final state has $Q' \neq 0$, as well as $\bar{r}_i \neq r_i$.

According to Eqs. (2.51) and (2.52), the symmetric and asymmetric mechanisms obey the general relation,

$$\eta' = \epsilon Y', \qquad (2.53)$$

where

$$\epsilon = \sum_i \frac{(p_i - \bar{p}_i)(r_i - \bar{r}_i)}{(p_i + \bar{p}_i)(r_i + \bar{r}_i)}. \qquad (2.54)$$

Here $\epsilon$ is a general measure of CP violation occurring in decays of $X$. If, for example, there are two relevant decay modes such that $p_{1,2}$ and $\bar{p}_{1,2}$ are not large, then $\epsilon$ is roughly given by $r_1 - \bar{r}_1$.

Next, let us determine the typical size of $\epsilon$ for a simple case with two decay modes. We take the two decay modes of interest to be $X \to X' + f_1$ and $X \to Y' + f_2$, where $f_i$ are particles in the final state that have $Q' = 0$, and $Y'$ and $X'$ have different $Q'$ charge. We introduce dimensionless amplitudes $A_i$ to describe these decays, defined by $\Gamma_i = |A_i|^2 m/8\pi$. Furthermore, as mentioned earlier we assume the existence of additional (hidden) interactions which allow for the rapid decay of

$Y'$ via $Y' \to p_2 X' + \bar{p}_2 \bar{X}'$, with $p_2 - \bar{p}_2 \neq 1$. In addition, a vertex allowing for the rescattering process $Y' + f_2 \to X' + f_1$ (with dimensionless amplitude $A_{12}$) is also required. This allows the final state of process 2 above to rescatter into the final state of process 1 at one loop (and vice versa), which is necessary for successful asymmetry production.

If the aforementioned amplitudes are too large, they will cause the two sectors to equilibrate at the era $T \approx m$ and destroy the viability of the FI and FO&D mechanisms. Applying the equilibration condition Eq. (2.33) demands that

$$|A_i| \lesssim 10^{-6} \sqrt{\frac{m}{100\,\text{GeV}}} \sqrt{\frac{g'_*(T \simeq m)/g_X}{100}}. \tag{2.55}$$

A non-zero value for $\epsilon$ results from interference between tree and one loop contributions to the decays

$$\epsilon \simeq \frac{1}{16\pi} \frac{\text{Im}(A_1 A_2^* A_{12})}{|A_1|^2 + |A_2|^2}. \tag{2.56}$$

In general the rescattering involves both visible and hidden sector particles so that, to avoid equilibration of the sectors at $T \approx m$, $A_{12}$ must satisfy the same bound, (2.55), as $A_i$, giving

$$\epsilon \lesssim 10^{-8} \sin\phi \sqrt{\frac{m}{100\,\text{GeV}}} \sqrt{\frac{g'_*(T \simeq m)/g_X}{100}} \tag{2.57}$$

where $\phi = \arg(A_1 A_2^* A_{12})$.

Is it possible to evade this bound? For theories with a global symmetry of type $S_2$ such that a combination of $B$, $L$ and $Q'$ is preserved, the requirement that the two decay modes have different $Q'$ charge implies that the two modes also have different $B/L$ charge so that the set of particles comprising $f_1$ and $f_2$ are different. This further implies that rescattering $A_{12}$ between the final states of the two decay modes involves *both* visible and hidden sector particles so that it is not possible to evade the bound (2.57) above.

However, this bound may be evaded in theories where the global symmetry is of type $S_1$ since then it is possible for $f_1$ and $f_2$ to contain the same set of visible sector particles. Rescattering then only involves the hidden sector and $A_{12}$ can be $\mathcal{O}(1)$ in principle. There is still the requirement that the rescattering amplitude not wash-out the asymmetry once it is produced, but this is highly model dependent since the asymmetry may be produced at $T' \ll m_{X'}$, so that the washout is exponentially suppressed. Hence, in these theories $\epsilon$ can be as large as $10^{-2}$ for $A_{12}$ of $\mathcal{O}(1)$.

Can these new mechanisms generate sufficient DM? This requires $m'\eta' = 4 \times 10^{-10}$ GeV. For Asymmetric FI

$$m'\eta'_{\text{FI}} \simeq \tag{2.58}$$

$$4 \times 10^{-10}\,\text{GeV} \left(\frac{10^{-10}\,\text{s}}{\tau} \frac{|A_{12}|}{10^{-6}}\right) \left(\frac{C_{\text{FI}}}{10^{-3}}\right) \left(\frac{m'}{40\,\text{GeV}}\right) \left(\frac{100\,\text{GeV}}{m}\right)^2 \frac{\sin\phi |A_1 A_2|}{|A_1|^2 + |A_2|^2}$$
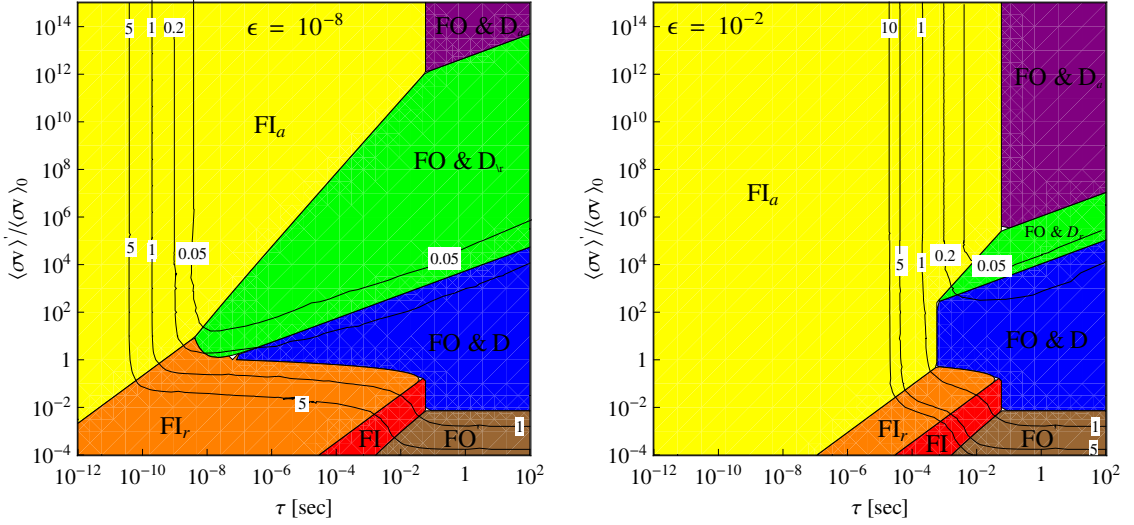
Figure 2.11: Cosmological phase diagrams similar to Figure 2.7, only depicting FO&D$_a$ and FI$_a$ along with other production mechanisms. Here the numerically evaluated contours correspond to $\Omega h^2$ arising from the sum of $Y'$ and $\eta'$. The left and right panels correspond to $\epsilon = 10^{-8}$ and $10^{-2}$, respectively.

while for Asymmetric FO&D

$$m'\eta'_{\text{FO\&D}} \simeq \tag{2.59}$$
$$4 \times 10^{-10} \text{ GeV } \left(\frac{10^{-8}\langle\sigma v\rangle_0}{\langle\sigma v\rangle}\frac{|A_{12}|}{10^{-6}}\right)\left(\frac{C_{\text{FO}}}{10^{-1}}\right)\left(\frac{m'}{40 \text{ GeV}}\right)\left(\frac{100 \text{ GeV}}{m}\right)\frac{\sin\phi|A_1A_2|}{|A_1|^2 + |A_2|^2}.$$

Since the last factor in these equations is always less than unity, Asymmetric FI requires a short lifetime $\tau < 10^{-10}$ s $|A_{12}|/10^{-6}$ and Asymmetric FO&D requires a small annihilation cross-section $\langle\sigma v\rangle < 10^{-8}\langle\sigma v\rangle_0 \, |A_{12}|/10^{-6}$.

The symmetric yields $Y'$ in (2.51) and (2.52) do not take re-annihilation into account. As has been discussed earlier in section 2.1.6, if the (symmetric) yields for FO&D and FI are sufficiently large, then re-annihilation occurs giving rise to much smaller values for the final (symmetric) yields $Y'_{\text{FO\&D}_r}$ and $Y'_{\text{FI}_r}$. This is crucial for the asymmetric yield to dominate the symmetric yield since $\epsilon$ arises at the loop level and is expected to be small. DM will be dominated by the asymmetric component of $X'$ only if $\langle\sigma v\rangle'$ is sufficiently large for re-annihilation to occur, hence reducing the symmetric component $Y'$ while leaving the asymmetric component $\eta'$ unaltered. Thus a DM asymmetry can be the dominant component of DM only in the re-annihilation regions for the symmetric abundance depicted in Figure 2.7. It is interesting that while FI dominates the DM density only in a narrow region of parameters as shown in Figure 2.7, asymmetric FI can dominate over a very wide region of parameters (assuming other conditions for generating the asymmetry are satisfied).

### 2.3.2 Cosmological Phase Diagrams for DM Asymmetries

Cosmological phase diagrams are shown in Figure 2.11 for non-zero values of $\epsilon$. The parameters held fixed are the same as in Figure 2.7, allowing a comparison of the asymmetric and symmetric DM production mechanisms. The contours are of $\Omega h^2$, now arising from the sum of $Y'$ and $\eta'$, and we have included *purple* and *yellow* regions denoting $FO\&D_a$ and $FI_a$ phases, respectively. The left and right panels of Figure 2.11 correspond to $\epsilon = 10^{-8}, 10^{-2}$. Here the lower value of $\epsilon$ arises from the non-thermalization bound in Eq. (2.57) and the upper value arises in theories of type $S_1$ where $\epsilon$ is only bounded from above by the fact that in the perturbative regime, CP violating decays must always be at least a loop factor down from the CP respecting decays.

In Figure 2.11 we see that the regions corresponding to $FO\&D$ and $FI$ are essentially unchanged from Figure 2.7, while the regions for $FO\&D_a$ and $FI_a$ are shown encroaching on the $FO\&D_r$ and $FI_r$ regions. This is reasonable because these asymmetric DM production mechanism are only active when re-annihilation effects are maximal, so the symmetric component of the DM relic abundance is efficiently destroyed. As expected, for larger $\epsilon$, as depicted in the right panel of Figure 2.11, $FI_a$ becomes dominant at larger values of $\tau$, which is reasonable because in this case the CP phase in $X$ decays is larger so the decay rate of $X$ can be smaller while producing the same asymmetric DM abundance. On the other hand, at large $\epsilon$, $FO\&D_a$ can dominate at smaller values of $\langle \sigma v \rangle'/\langle \sigma v \rangle$, since the large CP phase in $X$ decays allows for the abundance of $X$ arising from FO to be smaller while producing the same DM asymmetry from late decays. There are no contours in the $FO\&D_a$ region because this production mechanism gives an abundance independent of $\langle \sigma v \rangle'$ and $\tau$.

Note the behavior of the contours of $\Omega h^2$ depicted in Figure 2.11. In particular, as soon as these curves enter the $FI_a$ region, they turn vertically upward. This is an indication that the abundance of DM contributed by Asymmetric FI is entirely independent of $\langle \sigma v \rangle'/\langle \sigma v \rangle$, and instead only depends on $\tau$—thus, $FI_a$ behaves essentially identically to FI without re-annihilation effects.

Next, let us consider the boundary between Asymmetric FI and Asymmetric FO&D. In particular, the abundance from $FI_a$ dominates the contribution from $FO\&D_a$ when $\eta'_{FI} > \eta'_{FO\&D}$, so

$$\tau < C_{FI} \, \frac{M_{Pl}}{m^2 Y'_{FO\&D}} = \frac{C_{FI}}{C_{FO} x_{FO}} \, \frac{M_{Pl}^2 \langle \sigma v \rangle}{m}. \tag{2.60}$$

Thus $FO\&D_a$ dominates at large $\tau$, since then $FI_a$ is negligible, and for $\langle \sigma v \rangle \ll \langle \sigma v \rangle_0$, so there is a very large FO abundance of $X$. Notice that the right-hand side of Eq. (2.60) depends on quantites which are fixed between the two panels of Figure 2.11, which is why the boundary between $FI_a$ and $FO\&D_a$ is at the same value of $\tau$ in both.

$FO\&D_a$ requires very small $\langle \sigma v \rangle$, especially if $\epsilon$ is small, and also dominates for

large $\tau$ where it might lead to signatures in big bang nucleosynthesis. On the other hand, $FI_a$ is independent of $\langle \sigma v \rangle$ and can successfully account for DM over a very wide range of $\tau$. The challenge for both asymmetric mechanisms is to construct theories where the CP violating phase in $\epsilon$ can be measured in the laboratory.

## 2.4   Conclusions

A popular theoretical justification for the existence of non-graviational interactions of DM is the so-called "WIMP miracle", whereby DM is initially in thermal equilibrium with visible sector particles and undergoes FO, yielding approximately the correct DM relic abundance for weak scale masses and cross-sections. This setup has the advantage that DM generation is "IR dominated", and fixed wholly by the DM annihilation cross-section, which may be directly accessible at colliders. As discussed in this chapter it is clear that the single sector setup required for the WIMP miracle is only a very particular slice within the whole of theory space. In general, extra dimensional and string theoretic constructions motivate the existence of one or more hidden sectors which are very weakly coupled to our own visible sector. The inclusion of a weak-scale hidden sector, complete with its own set of particles, dynamics, and thermal history, substantially expands the allowed space of mechanisms for DM generation. Concretely, single sector FO is extended to two sector FO&D and FI, along with their re-annihilated and asymmetric cousins.

Despite the proliferation of DM production modes, this broad two sector framework retains the IR dominated features of the WIMP miracle. As we have shown, since both the visible and hidden sectors are initially thermalized, the origin of DM and its final abundance are dictated entirely by the handful of quantities shown in Eq. (2.2). Remarkably, many of these quantities, namely $m$, $m'$, $\langle \sigma v \rangle$, and $\tau$ may be measured at particle colliders. This offers the prospect that the origin of DM might be successfully reconstructed from collider physics in this theoretically motivated class of theories. The study of such collider signals is the topic of the Chap. 3.

# Chapter 3

# Hidden Sector Dark Matter at Colliders

In the standard WIMP picture a weak scale DM particle is in thermal equilibrium with a bath of visible sector particles at some high temperature. As is well-known, the thermal DM relic abundance is uniquely determined by the DM annihilation cross-section, a quantity which can in principle be accessed at colliders. Hence, the WIMP paradigm offers the remarkable prospect of reconstructing the cosmological origin of DM at the LHC [16]. In Chap. 2 we discussed the broad class of DM production mechanisms possible in a two sector framework where the DM resides in a hidden sector which is coupled weakly to the visible sector but contains its own set of particles and interactions. In this chapter we discuss the prospects for using colliders to reconstruct the origin of DM in this broader class of models.

As in Chap. 2, we assume that DM is charged under a stabilizing symmetry shared by the visible and hidden sectors and that there exist portal interactions which mediate the decay in Eq. 2.14, leading to a handful of allowed mechanisms that can account for the present day DM abundance. In the present chapter we focus on FI and FO&D, the two potentially reconstructable mechanisms.

$$\Omega_{FO\&D} = 15.1 \frac{\sqrt{g_*}}{g_{*S}} \frac{1}{M_{\mathrm{Pl}} \langle \sigma v \rangle} \frac{m'}{m} \propto \frac{m'}{m \langle \sigma v \rangle}. \tag{3.1}$$

$$\Omega_{FI} = 1.64 \frac{g}{g_{*S} \sqrt{g_*}} \frac{\Gamma M_{\mathrm{Pl}} m'}{m^2} \propto \frac{m'}{m^2 \tau}. \tag{3.2}$$

The above formulas imply that the origin of DM is correlated with a characteristic window in the parameter space defined by $\tau$, the lifetime of $X$, and $\langle \sigma v \rangle$, the thermally averaged annihilation cross-section of $X$ (see Figure 2.1). Remarkably, FO&D and FI depend solely on parameters which might some day be measured at the LHC. In particular, since $X$ is a visible sector field there is a chance that it will be produced directly in high energy collisions. If this is the case then its mass, lifetime, and

annihilation cross-section can in principle be measured. At the same time, the visible decay products in Eq. 2.14 may be analyzed for an event by event reconstruction of the decay process in order to determine the mass of $X'$. If we require that the visible and hidden sectors do not thermally equilibrate at the weak scale, then this implies

$$\tau > 10^{-13} \text{ s } \ \left(\frac{100 \text{ GeV}}{m}\right)^2 \left(\frac{100}{g'_*(T \simeq m)/g_X}\right), \tag{3.3}$$

where $g'_*(g_X)$ are the number of spin degrees of freedom of the hidden sector $(X)$. This implies that the broad class of theories that we consider will typically produce exotic signals such as displaced vertices and kinked tracks [1] from the decay of $X$. How may the origin of DM be reconstructed at the LHC? The connection between a very weakly coupled dark sector and displaced vertices at colliders as well as the possibility of reconstructing the cosmology from such measurements, was first pointed out in [26].

We consider a concrete supersymmetric realization of the scenario described above. Supersymmetry offers the ideal stabilizing symmetry for DM, i.e. R-parity, while gravity mediated supersymmetry breaking provides a compelling theoretical explanation for the existence of weak scale states in both the visible and hidden sectors. In the context of supersymmetry, $X$ is then identified lightest observable sector superpartner (LOSP) while $X'$ is the lightest superpartner (LSP).

In the single sector MSSM, the neutral superpartners $\tilde{b}, \tilde{w}, \tilde{h}$ and $\tilde{\nu}$ are all candidates for DM. However, for masses of interest the FO yields are too high for $\tilde{b}$ and too low for $\tilde{w}, \tilde{h}$ and $\tilde{\nu}$. As discussed in chap. 1, successful DM typically requires the LSP to be a careful mixture of these states or for other states to have accidental degeneracies [7, 85]. However, in two sector cosmologies $\tilde{b}$ becomes an ideal candidate for the LOSP that gives DM via FO&D, while $\tilde{w}, \tilde{h}$ and $\tilde{\nu}$ are ideal LOSP candidates for DM from FI. Furthermore any charged or colored LOSP allows DM to be dominated by FI, while the right-handed slepton also allows FO&D.

A priori, the identity of the LOSP is unknown, as is the nature of its couplings to the LSP. Scanning over all possible LOSP candidates and portal operators, we obtain Table 3.1, which summarizes the circumstances under which FO&D and FI might be fully reconstructed at the LHC. For each mechanism of DM production one requires a specific combination of LOSP candidates and operators. Furthermore, in order to measure the observables designated in Table 3.1, it is necessary to specify the particular decay processes which are relevant for each choice of LOSP and portal operator (see Tables 3.3, 3.4, and 3.5). As we will see, the nature of the LOSP, i.e. whether it is charged or colored, will have a significant impact on whether these observables can truly be probed at the LHC. However, in the event that these observables are successfully measured, we may discover that they lie in the ranges and satisfy the

---

[1]Other exotic (and overlooked) signals may also be possible [97].

|  | Freeze-Out and Decay (FO&D) | Freeze-In (FI) |
|---|---|---|
| LOSP | $\tilde{\chi}_0, \tilde{\ell}$ | $\tilde{q}, \tilde{\ell}, \tilde{\nu}, \tilde{g}, \tilde{\chi}_0, \tilde{\chi}_\pm$ |
| Operators | $\mathcal{O}X'$ | $H_u H_d X', B^\alpha X'_\alpha$ |
| Observables | $m, m', \langle\sigma v\rangle$ | $m, m', \tau$ |
| Range | $10^{-27} \text{ cm}^3/\text{s} < \langle\sigma v\rangle < 10^{-26} \text{ cm}^3/\text{s}$ | $10^{-4} \text{ s} < \tau < 10^{-1} \text{ s}$ |
| Predicted Relation | $\frac{m'\langle\sigma v\rangle_0}{m\langle\sigma v\rangle} = 1$ | $\frac{m'}{m\tau}\left(\frac{100 \text{ GeV}}{m}\right) = 25 \text{ s}^{-1}$ |

Table 3.1: The origin of DM may be fully reconstructed for a specific set of LOSP candididates and portal operators. If the designated observables are measured, we should discover they lie in the ranges listed above, and satisfy the predicted relations given schematically in Eqs. 2.3 and 2.4 and precisely in the last row of the table. Here $\langle\sigma v\rangle_0 = 3 \times 10^{-26} \text{ cm}^3/\text{s}$ and $\mathcal{O}$ denotes an operator of dimension $\leq 4$ comprised of visible sector fields.

predicted relations specified in Table 3.1. If so, the LHC would provide a spectacular verification of the cosmological origin of hidden sector DM.

It is of course possible that $\tau$ and $\langle\sigma v\rangle$ will be measured but found to lie outside the expected ranges for FO&D and FI depicted in Figure 2.1. Such an observation could be consistent with DM arising from variants of FO&D and FI, namely {FO&D$_\text{r}$, FO&D$_\text{a}$, FI$_\text{r}$, FI$_\text{a}$}, discussed in significant detail in Chap. 2. As shown in Chap. 2 these mechanisms are strongly dependent on parameters which are inaccessible to colliders[2], so a smoking gun verification of these cosmologies at the LHC is unlikely. At the same time, these variant DM production mechanisms correspond to a particular set of collider signatures which depend on the portal interaction. For FO&D$_\text{r}$ and FI$_\text{r}$, the relevant signatures include those associated with FO&D and FI, which are contained in Tables 3.3, 3.4, and 3.5. Furthermore, FO&D$_\text{r}$ and FI$_\text{r}$ also include those signatures shown in Tables 3.4 and 3.5. These signature tables also apply to FO&D$_\text{a}$ and FI$_\text{a}$. Similar results were found in an analysis of displaced collider signatures associated with asymmetric DM [26].

## 3.1 Two-Sector Setup

We assume that DM is stabilized by an exact R-parity shared by the visible and hidden sectors. We denote all superfields in upper-case and all component fields in lower-case. Furthermore, all R-parity odd component fields will appear with a tilde, so for instance the quark, squark, and quark superfield will be denoted by $q$, $\tilde{q}$, and $Q$. In this notation, $X$ and $X'$ are the superfields containing the LOSP, $\tilde{x}$, and the LSP, $\tilde{x}'$.

---

[2]In particular, FO&D$_\text{r}$ and FI$_\text{r}$ depend on the annihilation cross-section of $X'$, while FO&D$_\text{a}$ and FI$_\text{a}$ depend on the CP violation in processes that connect the sectors.
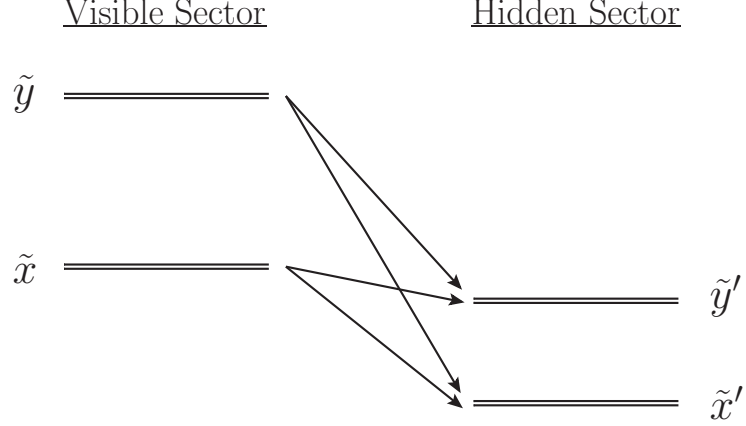
Figure 3.1: Allowed decays among visible and hidden sector states. Here $\tilde{x}$ and $\tilde{x}'$ denote the LOSP and LSP, and $\tilde{y}$ and $\tilde{y}'$ collectively denote the spectator fields. Only $\tilde{x} \to (\tilde{x}', \tilde{y}') + \text{SM}$ can be measured at colliders. The process $\tilde{x} \to \tilde{x}' + \text{SM}$ must be visible in order to measure the LSP mass.

Our discussion will be free from theoretical prejudices on supersymmetry breaking and so the identity of the LOSP will be unconstrained by UV considerations:

$$X \in \{Q, U, D, L, E, H_u, H_d, B^\alpha, W^\alpha, G^\alpha\}. \tag{3.4}$$

Our primary focus will be the interplay between cosmology and collider phenomenology in the cases of FO&D and FI. In order to reconstruct our cosmological history at the LHC it will be necessary to extract several important observables from colliders, as summarized in Table 3.1. For FO&D, we must measure or infer the annihilation cross-section and mass of the LOSP, as well as the mass of the LSP. For FI, we must measure or infer the partial width of every MSSM field into the LSP, as well as the masses of the LOSP and LSP. In both cases, we are interested in the prospect of measuring the LSP mass from the long-lived decay process,

$$\tilde{x} \to \tilde{x}' + \text{SM} \tag{3.5}$$

Along these lines, a subset of LOSP candidates have been studied extensively in the literature. For instance, e.g. the superWIMP for which $\tilde{x} = \tilde{\ell}^{\pm}$ is a charged slepton and $\tilde{x}' = \tilde{G}$ is the gravitino [50, 51]. In these scenarios, the long-lived decay $\tilde{\ell}^{\pm} \to \ell^{\pm} \tilde{G}$ can be probed in colliders to reconstruct the cosmological history of the universe. Others have considered alternative LOSP candidates, such as the bino, as well as other possible LSP candidates, such as an axino [44] or goldstino [36, 34].

The existing literature has been largely focused on measuring decays of the LOSP to the LSP. However, our philosophy is that the hidden sector may be as rich in spectrum and dynamics as our own, and so the visible and hidden sectors actually contain many more fields than just $X$ and $X'$.

First of all, there of course exist numerous additional visible sector superfields which we will denote by $Y$, whose R-parity odd component we denote by $\tilde{y}$. Here $\tilde{y}$ could be a heavy squark or gluino, for example. Secondly, the hidden sector may contain additional superfields which we collectively denote by $Y'$, whose R-parity odd component we denote by $\tilde{y}'$. Given our working premise that visible and hidden sector fields interact weakly, then there in general exist operators which couple $X, Y$ to $X', Y'$, yielding the decay modes (see Figure 3.1)

$$\tilde{x} \to \tilde{x}' + \text{SM} \quad \tilde{x} \to \tilde{y}' + \text{SM} \quad \tilde{y} \to \tilde{x}' + \text{SM} \quad \tilde{y} \to \tilde{y}' + \text{SM} \tag{3.6}$$

At the LHC, MSSM cascades will terminate at $\tilde{x}$, which in turn decays via $\tilde{x} \to (\tilde{x}', \tilde{y}') + \text{SM}$. As long as there is a sufficiently large branching ratio of the LOSP to the LSP via visible decay modes, then the LSP mass may be measured, which is essential for reconstructing the cosmological history of FO&D and FI.

What are the constraints on the gravitino in this two sector cosmology? First, the gravitino must be heavier than the hidden sector LSP, otherwise the gravitino itself would be the LSP. This requires a large scale of supersymmetry breaking, as in gravity or anomaly mediation. If the gravitino is lighter than the LOSP, then it has no effect on our cosmology: LOSP decays to gravitinos are highly suppressed compared to decays to the LSP, and any gravitinos produced at very high temperatures will decay to hidden sector states and not affect nucleosynthesis. On the other hand, if the gravitino is heavier than the LOSP a standard gravitino problem emerges, with decays to visible sector superpartners limiting the reheat temperature to about $10^6$ GeV.

## 3.2 Operator Analysis

We assume that the LSP is a gauge singlet and catalog all dimension $d \leq 5$ gauge-invariant operators that connect it to visible sector fields. These operators in turn dictate the allowed decay modes of the LOSP. We organize our analysis in terms of the symmetry structure of each of these operators, and summarize all of our results for FO&D and FI in tables 3.3 + 3.4 and 3.5, respectively. We will provide a detailed explanation of these tables in Sections 3.3.3 and 3.4.4.

$X'$ couples to the visible sector via $d \leq 5$ operators of the form

$$\mathcal{O} X'^{(\dagger)} \tag{3.7}$$

where $\mathcal{O}$ is a gauge invariant, dimension $\leq 4$ operator comprised of visible sector fields and $\mathcal{O} X'^{(\dagger)}$ appears in the Kahler potential or superpotential depending on the holomorphy properties of this operator. Note that $\mathcal{O}$ need *not* directly contain the LOSP, $X$!

As we will see, whether $\mathcal{O} X'^{(\dagger)}$ appears in the Kahler potential or the superpotential will often dictate whether the portal to the hidden sector is renormalizable or

| | $\mathcal{O}_K$ | $\mathcal{O}_W$ | $H_u H_d$ | $B^\alpha$ | $LH_u$ | $LH_d^\dagger$ | $LLE, QLD$ | $UDD$ |
|---|---|---|---|---|---|---|---|---|
| R-parity | + | + | + | − | − | − | − | − |
| R-charge | 0 | 2 | $R_1$ | 1 | $R_2$ | $R_2 - R_1$ | $2 + R_2 - R_1$ | $R_3$ |

Table 3.2: Table of R-parity and R-charge assignments for various visible sector operators. Here $\mathcal{O}_K$ and $\mathcal{O}_W$ are defined in Eq. (3.9).

not. We will define a dimensionless coupling $\lambda$ which characterizes the strength of the portal interaction in Eq. (3.7). If $d = 4$, then $\lambda$ is simply the coefficient of the marginal portal interaction. However, for $d > 4$ higher dimension operators, we can define

$$\lambda \equiv (m/M_*)^{d-4} \tag{3.8}$$

where $M_*$ is the scale of the higher dimension operator.

Assuming that the visible sector is the MSSM, we can catalog all operators $\mathcal{O}$ according to their transformation properties under R-parity and R-symmetry, as shown in Table 3.2. There we have defined the operators

$$\mathcal{O}_K = \{Q^\dagger Q, U^\dagger U, D^\dagger D, L^\dagger L, E^\dagger E, H_u^\dagger H_u, H_d^\dagger H_d\}$$

$$\mathcal{O}_W = \{B^\alpha B_\alpha, W^\alpha W_\alpha, G^\alpha G_\alpha, QH_u U, QH_d D, LH_d E\}, \tag{3.9}$$

which correspond to operators which appear in the Kahler and superpotential of the MSSM. Note that $\mathcal{O}_K$, $\mathcal{O}_W$, and $B^\alpha$ have fixed R-charge because they are present in the MSSM Lagrangian. In contrast, the remaining operators have unspecified R-charge because they are R-parity odd and are thus absent from the MSSM Lagrangian. Furthermore, $H_u H_d$ has unspecified R-charge because we wish to be agnostic about the origin of the $\mu$ parameter.

The R-parity and R-charge of $X'$ dictates which subset of operators can function as a portal between the visible and hidden sectors. For each group of operators in Table 3.2, we have catalogued the associated decay modes of the LOSP, given various choices for the LOSP. Our results for FO&D are summarized in Tables 3.3 and 3.4, and for FI in Table 3.5. We assume all operators in a group have comparable coefficients, so that some groups have many possible decay modes. Because we are concerned with the measurement of the LSP mass via $\tilde{x} \to \tilde{x}' + \text{SM}$, we have only listed the leading decay mode, as well as any subdominant (three-body) decay modes which are lepton rich and thus more useful in reconstructing the event. For this reason, we do not include subdominant decay modes involving only quarks or Higgs bosons. Moreover, we include the parametric size of each branching ratio as a function of masses, mixing angles, couplings, and three-body phase space factors. In doing that, we have omitted the coefficients of the various connector operators (which can be

different by $\mathcal{O}(1)$) and have assumed that $m \sim v \sim m_{3/2}$ are parametrically the same, so the dependences on these three quantities is just shown as a dependence on $m$.

There is an important difference between Tables 3.3 and 3.4 for FO&D on the one hand and Table 3.5 for FI on the other, which highlights the complementarity of these two cosmological scenarios. In particular, FO&D (Tables 3.3 and 3.4) can be achieved for many different operators but only for two LOSP candidates: a bino-like neutralino or a right-handed slepton. In contrast, FI (Table 3.5) can be achieved for many different LOSP candidates, but only for a restricted subset of operators. The reasons for the asymmetry are discussed in detail in Sections 3.3 and 3.4.

Before concluding our operator analysis, we wish to address a number of related issues. First of all, there is the matter of supersymmetry breaking operators, which we have ignored thus far. In particular, any supersymmetry respecting coupling between the visible and hidden sector can be dressed with supersymmetry breaking spurions yielding a supersymmetry breaking operator. For example, if $\mathcal{O}X'^{(\dagger)}$ is allowed by symmetries, then there can also be operators of the form $f(\Phi, \Phi^\dagger)\mathcal{O}X'^{(\dagger)}$, where $f$ is an arbitrary complex function of a supersymmetry breaking spurion, $\Phi = \theta^2 m_{3/2}$. In general, these supersymmetry breaking operators provide new decay modes for the LOSP which can affect cosmology. We will discuss the effects of these operators on FO&D and FI in Sections 3.3 and 3.4.

Secondly, we note that our discussion has been purposefully general with respect to R-parity and R-charge assignments in the operators listed in Table 3.2. However, particular choices of the ultraviolet physics can be used to fix $R_i$. For instance, if neutrino masses are generated above the supersymmetry breaking scale, then $(LH_u)^2$ is present in the superpotential and so $R_2 = 1$. If the $\mu$ term is generated by the Giudice-Masiero mechanism, which is natural for gravity mediated supersymmetry breaking, then $R_1 = 0$, assuming that all supersymmetry breaking spurions have R-charge zero. With both of these assumptions, all of the R-charges are fixed except $R_3$.

### 3.2.1 Bino Portal

The portal coupling through $B^\alpha X'_\alpha$ in Eq. 3.9 induces a gauge kinetic mixing between $U(1)$ vector superfields in the visible and hidden sector fields [69]. This is the "Bino Portal" which been studied extensively in terms of hidden sector phenomenology [59, 101, 10, 18, 37, 38, 113]. The operator $B^\alpha$ automatically has an R-charge of one and is odd under R-parity. As a consequence, the hidden sector field that can couple to $B^\alpha$ must be a vector field with R-charge one and must be odd under R-parity. The leading gauge invariant operators are

$$\mathcal{L} = \lambda \int d^2\theta \, B^\alpha X'_\alpha + \tilde{\lambda} \int d^2\theta \, B^\alpha X'_\alpha \Phi \qquad (3.10)$$

where $\lambda$ and $\tilde{\lambda}$ are dimensionless coupling constants and again $\Phi = \theta^2 m_{3/2}$ is the supersymmetry breaking spurion. The first term is supersymmetric and was studied in the gauge kinetic mixing scenario [69], which occurs when the hidden sector contains a $U(1)'$ symmetry, with gauge field $X'_\alpha$. The second term is intrinsically supersymmetry breaking and will induce a mass mixing between the gauginos. Both terms will induce couplings between the hidden and visible sector states. Also, note that the supersymmetric kinetic mixing operator, $\lambda B^\alpha X'_\alpha$, is dimension four, so it may be generated from UV dynamics but is non-decoupling in the infrared. Also, since this Lagrangian does not violate any symmetries of the SM, it is not too constrained by existing experiment.

The above portal operators contain a kinetic and mass mixing among gauginos which are gauge invariant, relevant operators given by

$$\mathcal{L} \supset i\lambda\,\tilde{b}\bar{\sigma}^\mu\partial_\mu\tilde{x}' + \tilde{\lambda}\,m_{3/2}\,\tilde{b}\tilde{x}'. \tag{3.11}$$

In Chap. 2 it was shown that the requirement for the FI mechanism to yield the correct dark matter relic abundance fixes a LOSP lifetime which corresponds to $\lambda$ and $\tilde{\lambda}$ of order $10^{-12} - 10^{-11}$ for weak scale masses. The kinetic mixing term is generated from the underlying theory, and so to generate a sufficiently small $\lambda$ and $\tilde{\lambda}$ requires some constraints on the underlying theory.

One possibility is if the $U(1)'$ is embedded in a GUT, then the there will be connector particles with couplings $g$ and $g'$ to $B^\alpha$ and $X'_\alpha$ respectively. So, $B^\alpha$ and $X'_\alpha$ will be connected by a loop of these heavy particles. The kinetic mixing term can be generated by integrating out the connector particles, which results in an induced coefficient for the kinetic mixing term in Eq. (3.11):

$$\lambda = \sum_i \frac{g_i g'_i}{16\pi^2} \mathrm{Log}\left(\frac{\Lambda}{m_i}\right) \tag{3.12}$$

where $\Lambda$ is the UV cutoff and $m_i$ is the mass of the heavy particles in the loop. In this case $\lambda$ may be made small if $g'_i \ll g_i$. A more attractive possibility is if the underlying theory contained some non-Abelian group that was broken down to $U(1)'$. In this case the $U(1)'$ gauge field is not primordial, so a kinetic mixing term can only be generated with the help of a gauge symmetry breaking field $\Sigma$ which acquires a VEV:

$$\int d^2\theta B^\alpha X'_\alpha \frac{\langle\Sigma\rangle}{M_\star} \Rightarrow \lambda = \frac{\langle\Sigma\rangle}{M_\star} \tag{3.13}$$

giving rise to a naturally suppressed $\lambda$ if $\langle\Sigma\rangle \sim M_{\mathrm{EW}} \ll M_\star$. This mechanism will simultaneously suppress $\tilde{\lambda}$.

The gaugino kinetic mixing can be removed from the Lagrangian by a field shift of the gaugino component of $B_\alpha$ superfield: $\tilde{B}_\alpha \to \tilde{B}_\alpha + \lambda\tilde{X}'_\alpha$. However, this field redefinition induces hidden-visible sector couplings in the gauge-chiral interaction

lagrangian:

$$\mathcal{L}_{\text{int}} = \int d^4\theta \left( \Phi_i^\dagger e^{2g_i B_\alpha} \Phi_i + \Phi_j^{\prime\dagger} e^{2g_j' X_\alpha'} \Phi_j' \right)$$

$$\rightarrow \left( \Phi_i^\dagger e^{2g_i(B_\alpha + \lambda \tilde{X}_\alpha')} \Phi_i + \Phi_j^{\prime\dagger} e^{2g_j' X_\alpha'} \Phi_j' \right)$$

$$\supset g_i \phi_i^\star \psi_i \tilde{b} + \text{h.c} + g_i \lambda \, \phi_i^\star \psi_i \tilde{x}' + \dots \tag{3.14}$$

where $\Phi_i$ and $\Phi_j'$ collectively denote charged chiral superfields in the visible and hidden sectors, respectively. Also $\phi_i$ and $\psi_i$ denote the scalar and fermionic components of $\Phi_i$, and so on. Thus, upon shifting $\tilde{b}$, a coupling $\lambda \tilde{x}' \tilde{J}$ is generated where $\tilde{J}$ is the hypercharge supercurrent of the visible sector: $\tilde{J} = \sum_{i=\text{visible}} g_i \phi_i \psi_i$.

In addition, since the bino is massive, the shift in $\tilde{b}$ generates a mass mixing between the bino and the hidden sector fermion $\tilde{x}'$ : $m_{\tilde{b}} \tilde{b}\tilde{b} \rightarrow m_{\tilde{b}} \tilde{b}\tilde{b} + \lambda m_{\tilde{b}} \left( \tilde{b}\tilde{x}' + \text{h.c} \right)$. Moreover, the supersymmetry breaking operator, $\tilde{\lambda} m_{3/2} \tilde{b}\tilde{x}'$, contributes a direct mass mixing term. After removing the gaugino kinetic mixing term and diagonalizing the gaugino mass matrix, the $\tilde{b}$ and $\tilde{x}'$ become maximally mixed since $m_{\tilde{b}} \sim m_{\tilde{x}'} \sim M_{\text{EW}}$. Consequently, this gives rise to a coupling $\lambda \tilde{b}\tilde{J}'$, with $\tilde{J}' = \sum_{i=\text{hidden}} g_i' \phi_i' \psi_i'$. In summary the hidden-visible sector couplings induced by kinetic mixing are given schematically by

$$\mathcal{L}_{\text{int}} \approx \lambda \left( \tilde{x}' \tilde{J} + \tilde{b}\tilde{J}' \right)$$

where there is in actuality a relative $\mathcal{O}(1)$ mixing angle between these two terms fixed by the precise (weak scale) masses of the visible and hidden sector gauginos. Consequently, given comparable visible and hidden sector gaugino masses, which is the case in our scenario of gravity mediated supersymmetry breaking, the total effect of the gauge kinetic mixing is to weakly couple the visible sector gaugino to the hidden sector supercurrent and vice versa.

## 3.2.2  Higgs Portal

In a addition to the Bino Portal, a second noteworthy and well studied portal operator in Eq. 3.9 is $H_u H_d X'$ which, after EWSB, induces a mass mixing between the LSP and the higgsinos. In particular, we are concerned with UV motivations for the presence of the associated operator,

$$\lambda \int d^2\theta \, H_u H_d X' \tag{3.15}$$

where $\lambda$ is a dimensionless coupling. Certainly, if we assign $X'$ to have even R-parity and R-charge $2 - R_1$, then this is the leading supersymmetric operator connecting the visible and hidden sectors. A priori, from an effective field theory point of view one would expect $\lambda \lesssim 1$. However, as shown in Chap. 2 the requirement that the FI

mechanism give rise to the correct relic abundance fixes a lifetime for $X$ corresponding to $\lambda$ of order $10^{-12} - 10^{-11}$ for weak scale $X$ and $X'$ masses. Thus, to generate a value for $\lambda$ which is sufficiently suppressed, we require additional model-building.

For example, this can be accomplished by separating the visible and hidden sectors along an extra dimension. In this case $\lambda$ may be vanishing or exponentially small in the microscopic theory, but nonetheless generated in the IR after integrating out heavy "connector" fields bridging the visible and hidden sectors. This can occur singlet kinetic mixing scenarios in which $X'$ kinetically mixes with a visible sector singlet, as in [35]. Alternatively, $\lambda$ may be small if $X'$ or the MSSM Higgs fields are composite operators, in which case $H_u H_d X'$ will arise from some primordial higher dimension operator suppressed by a high scale $M_*$. In this case $\lambda$ will be proportional the compositeness scale over $M_*$, which may be quite small.

However, it is also possible to naturally generate a suppressed $\lambda$ with supersymmetry breaking operators, assuming a different R-charge assignment of $X'$. This has the advantage of relying only on symmetry arguments. To this effect, we assign $X'$ to be R-parity even with R-charge equal to $-R_1$. We assume the existence of a spurion $\Phi = \theta^2 m_{3/2}$ which is the order parameter for supersymmetry breaking. Since $\int d^4\theta H_u H_d X'$ vanishes by holomorphy, then the leading portal interactions are given by

$$\mathcal{L} = \frac{\kappa}{M_*} \int d^4\theta \, H_u \, H_d \, X' \, \Phi^\dagger + \frac{\tilde{\kappa}}{M_*} \int d^4\theta \, H_u \, H_d \, X' \, \Phi^\dagger \Phi$$
$$= \lambda \int d^2\theta \, H_u \, H_d \, X' + \tilde{\lambda} \, m_{3/2} \, h_u \, h_d \, x' \tag{3.16}$$

where $\kappa$ and $\tilde{\kappa}$ are coefficients of $\mathcal{O}(1)$, and $\lambda, \tilde{\lambda} = \mathcal{O}(1) \frac{m_{3/2}}{M_*}$. Thus, if $\lambda$ is effectively a supersymmetry breaking operator, then it is naturally suppressed for $M_* \gg m_{3/2}$, which is quite small. Note that the Giudice-Masiero mechanism for $\mu$ and $B\mu$ can still operate if there is an additional spurion for supersymmetry breaking with the appropriate R-charge and R-symmetry.

From Eq. (3.16), the leading decays of all superpartners occur through the operator $H_u H_d X'$ with coefficient $\lambda$. Apart from visible sector couplings, masses and mixing angles (which we assume can be measured), all such processes only depend on the coefficient $\lambda$ and the mass of the LSP $m'$, as they only involve the operator in Eq. (3.15). Thus, measuring $(\lambda, m')$ from the decays of the LOSP allows us to infer the decay rates for the heavier superpartners and reconstruct the entire FI contribution to the LSP abundance in the early Universe. Recall that as explained in Section 3.4, all processes $(\tilde{y}, \tilde{x} \to \tilde{y}' + \text{SM})$ are assumed to be absent. This can easily occur if the R-parity and R-charge of $Y'$ forbid such couplings or if such processes are kinematically forbidden.

Note that Eq. (3.15) leads to a mass-mixing between the higgsino and $\tilde{x}'$ when one of the higgs fields gets a vev. This mass mixing allows the neutralino to mix with $\tilde{x}'$ via its higgsino component and decay to hidden sector particles. Also note that both
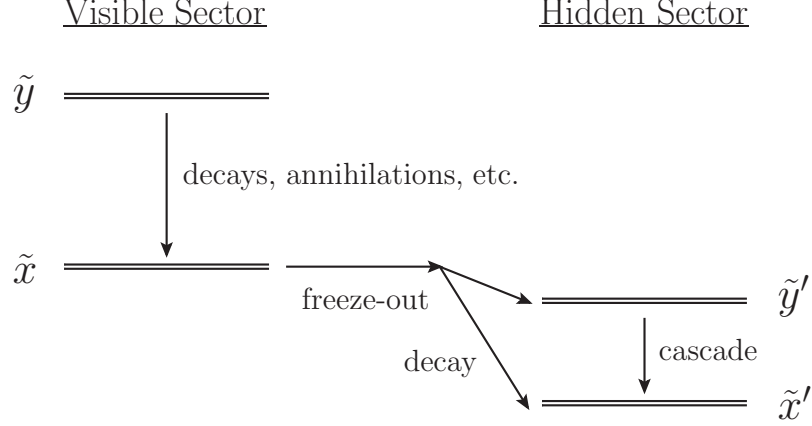
Figure 3.2: Depiction of the cosmological history of FO&D. As the temperature drops below their masses, heavy visible superparters, $\tilde{y}$, are depleted to a negligible level by decay and annihilation. As the temperature falls below the mass of the LOSP, $\tilde{x}$, they annihilate and freeze-out; these relic particles decay much later into the hidden sector. Consequently, direct decays of $\tilde{y}$ to the hidden sector are irrelevant. Also, due to R-parity all decays of $\tilde{x}$ ultimately yield the LSP, $\tilde{x}'$. To reconstuct this cosmology we must measure the annihilation cross-section and mass of $\tilde{x}$ and the mass of $\tilde{x}'$.

the Bino and Higgs portals are distinct from the operator portals shown in Eq. 3.2 in that they induce relevant kinetic and mass mixings, respectively, between $\tilde{x}'$ and MSSM neutralinos.

## 3.3  Freeze-Out and Decay (FO&D)

In the case of FO&D, $\tilde{x}$ undergoes thermal FO and then decays late into the hidden sector. Throughout, we assume that the annihilation cross-section and mass of $\tilde{x}$ can be measured at colliders, and refer the reader to detailed analyses on this topic [16]. Once these quantities are known, the thermal relic abundance of $\tilde{x}$ is straightforwardly inferred. The mass of the LSP can be measured in colliders via $\tilde{x} \to \tilde{x}' + \text{SM}$. Still, what is the effect of the additional decay processes, $\tilde{x} \to \tilde{y}' + \text{SM}$ and $\tilde{y} \to (\tilde{x}', \tilde{y}') + \text{SM}$?

### 3.3.1  Spectator Fields in Freeze-Out and Decay

First of all, since $\tilde{y}$ has no FO abundance, all of its decays are irrelevant to the cosmology of FO&D. This is fortunate because the partial width of $\tilde{y}$ into the hidden sector is too tiny to be measured directly at colliders. Second of all, while $\tilde{x}$ can decay to $\tilde{y}'$, these hidden sector particles ultimately cascade down to $\tilde{y}'$ due to R-parity conservation. Consequently, every $\tilde{x}$ decay yields precisely an odd number of $\tilde{x}'$ particles. In the vast majority of cases, a single $\tilde{x}'$ is produced in each $\tilde{x}$ decay, but

in some instances three or more may be produced. We will elaborate on this possibility later on when we discuss FO&D via the Bino ($B^\alpha X'_\alpha$) and Higgs ($H_u H_d X'$) Portals. As long as there is a non-negligible branching fraction of $\tilde{x}$ to visibly decay into $\tilde{x}'$, then the LSP mass can be measured[3]. Thus, we have argued that the decay processes in Figure 3.2 are largely irrelevant except for $\tilde{x} \to \tilde{x}' + \text{SM}$, which is necessary to measure the LSP mass.

### 3.3.2   Theories of Freeze-Out and Decay

Since FO&D can be verified at the LHC quite model independently, the only constraint on the LOSP candidate for FO&D is that the FO abundance is sufficiently large. As we will explain, this is possible if the LOSP is a bino-like neutralino or a right-handed slepton.

In particular, since yield of LSP particles from FO&D is precisely equal to the abundance of $X$ which arises from visible sector FO, the final energy density of DM arising from FO&D will be $m'/m$ smaller than the FO abundance that would have been produced in a single sector theory with the same annihilation cross-section. This implies that obtaining the observed relic abundance of DM from FO&D requires the LOSP to overproduce by a factor of $m/m'$. Hence the bino is an ideal candidate for the LOSP since in the MSSM a bino LOSP with $m_{\tilde{b}} < 100$ GeV already yields the correct relic abundance $\Omega h^2 \sim 0.11$. Since the bino can annihilate via exchange of a right-handed slepton, the bino cross-section depends on the slepton mass in addition to the bino mass (see Eq. (2) of [7]). Fixing the dark matter abundance and requiring a bino LOSP sets an upper bound on the bino mass. For the bino to overproduce the resulting bound is $m_{\tilde{b}} < 250$ GeV for $m'/m_{\tilde{b}} > 1/20$.

Similarly for the case of the right-handed slepton, a diagram involving t-channel bino exchange results in bino mass dependent cross-section:

$$\sigma v_{\tilde{l}_R} \sim \frac{4\pi\alpha^2}{m_{\tilde{l}_R}^2} + \frac{16\pi\alpha^2 m_{\tilde{b}}^2}{\cos^4\theta_w \left(m_{\tilde{l}_R}^2 + m_{\tilde{b}}^2\right)^2} \tag{3.17}$$

Requiring that the right-handed slepton be the LOSP, and that $\tilde{b}$ is not closely degenerate with $\tilde{l}_R$ results in the lower bound $m_{\tilde{l}_R} > 700$ GeV for $m'/m_{\tilde{l}_R} < 1/2$. This makes $\tilde{l}_R$ a less attractive LOSP candidate then $\tilde{b}$. Other MSSM LOSP candidates would need to be even heavier.

Thus, the primary constraint on theories of FO&D are on the identity of the LOSP. On the other hand, the nature of portal interactions are essentially irrelevant, as long as the decay products from the decay of $\tilde{x}$ are sufficient to reconstruct the LSP mass.

---

[3]In principle, the branching fraction to the LSP can be fairly small, since for instance in $\tilde{\tau} \to \tau\tilde{x}'$, the endpoint in the tau-stau invariant mass distribution indicates the mass of the *lightest* decay product.

| | | $\tilde{\chi}_0$ | | $\tilde{\ell}^{\pm}$ | |
|---|---|---|---|---|---|
| Operator | Charges ($X'$) | Decay | $k$ | Decay | $k$ |
| $\mathcal{O}_K X'$ | $(+,0)$ | $\tilde{\chi}_0 \to \ell^+ \ell^- \tilde{x}'$ | $\frac{1}{(4\pi)^2} g^2_{\tilde{\chi}\tilde{\ell}\ell} \frac{m^4}{m^4_{\tilde{\ell}}}$ | $\tilde{\ell}^{\pm} \to \ell^{\pm} \tilde{x}'$ | $1$ |
| | | $\tilde{\chi}_0 \to (h^0, Z)\tilde{x}'$ | $\theta^2_{\tilde{\chi}\tilde{h}}, \theta^2_{\tilde{\chi}\tilde{h}} g^2_2$ | | |
| $\mathcal{O}_W X'$ | $(+,0)$ | $\chi_0 \to (\gamma, Z)\tilde{x}'$ | $\theta^2_{\tilde{\chi}\tilde{b}}, \theta^2_{\tilde{\chi}\tilde{w}}$ | $\tilde{\ell}^{\pm} \to \ell^{\pm}(\gamma, Z)\tilde{x}'$ | $\frac{1}{(4\pi)^2} m^2 (\frac{g^2_{1\ell}}{m^2_{\tilde{b}}}, \frac{g^2_2}{m^2_{\tilde{w}}})$ |
| | | $\tilde{\chi}_0 \to \ell^+ \ell^- \tilde{x}'$ | $\frac{1}{(4\pi)^2} g^2_{\tilde{\chi}\tilde{\ell}\ell} \frac{m^4}{m^4_{\tilde{\ell}}}$ | $\tilde{\ell}^{\pm} \to \ell^{\pm} \tilde{x}'$ | $1$ |
| $H_u H_d X' (X'^{\dagger})$ | $(+, 2-R_1)$ | $\tilde{\chi}_0 \to (h^0, Z)\tilde{x}'$ | $\theta^2_{\tilde{\chi}\tilde{h}}, \theta^2_{\tilde{\chi}\tilde{h}} g^2_2$ | $\tilde{\ell}^{\pm} \to \ell^{\pm} \tilde{x}'$ | $g^2_{\tilde{h}\tilde{\ell}\ell}$ |
| | or | $\tilde{\chi}_0 \to y' \tilde{y}'$ | $\theta^2_{\tilde{\chi}\tilde{h}} \lambda'^2$ | | |
| | $(+, R_1)$ | $\tilde{\chi}_0 \to \ell^+ \ell^- \tilde{x}'$ | $\frac{1}{(4\pi)^2} g^2_{\tilde{\chi}\tilde{\ell}\ell} g^2_{1\ell} \frac{m^4}{m^4_{\tilde{\ell}}}$ | | |

Table 3.3: Decay modes and decay rates for LOSP candidates $\tilde{\chi}_0$ and $\tilde{\ell}$, relevant for FO&D, with $X'$ R-parity even. The second column lists the R-parity and R-charge of $X'$. Here $g_{\tilde{\chi}\tilde{\ell}\ell} \equiv \theta_{\tilde{\chi}\tilde{b}} g_{1\ell} + \theta_{\tilde{\chi}\tilde{w}} g_2 + \theta_{\tilde{\chi}\tilde{h}} \lambda_\ell$ is the effective coupling between $\tilde{\chi}_0$ and $\tilde{\ell}\ell$ and $g_{\tilde{h}\tilde{\ell}\ell} \equiv \lambda_\ell + v(g_{1\ell} g_{1h}/m_{\tilde{b}} + \theta_{\tilde{\ell}\tilde{\ell}_L} g^2_2/m_{\tilde{w}})$ is the effective coupling between $\tilde{h}$ and $\tilde{\ell}\ell$, with mass mixing calculated using an insertion approximation. Here $k$ characterizes the size of the partial width for each process, as defined in Eq. 3.18.

As we will see in the following sections, and in Tables 3.3 and 3.4, a broad range of portal interactions allow for lepton rich decay channels which are promising for constructing the LSP mass. Next, let us consider the collider signatures of neutralino and slepton LOSP in turn.

### 3.3.3 Collider Signatures of Freeze-Out and Decay

We now consider associated collider signatures for FO&D for the right-handed slepton and bino-like neutralino. Tables 3.3 and 3.4 provide an extensive summary of the decay processes relevant for reconstructing the cosmological history. The structure and notation in these tables require a bit of explanation.

Each row corresponds to a possible choice for the portal operator coupling the visible and hidden sectors. Here Table 3.3 (3.4) corresponds to the R-parity even (odd) $X'$. Along each row in each table, we have presented the (R-parity, R-charge) assignments for $X'$ required for the corresponding portal interaction. Also, along each

| FO&D | | | | | |
|---|---|---|---|---|---|
| | | $\tilde{\chi}_0$ | | $\tilde{\ell}^{\pm}$ | |
| Operator | Charges $(X')$ | Decay | $k$ | Decay | $k$ |
| $B^{\alpha}X'_{\alpha}$ | $(-, 1)$ | $\tilde{\chi}_0 \to y'\tilde{y}'$ | $\theta_{\tilde{\chi}\tilde{b}}^2 g'^2$ | $\tilde{\ell}^{\pm} \to \ell^{\pm}\tilde{x}'$ | $g_{1\ell}^2$ |
| | | $\tilde{\chi}_0 \to \ell^+\ell^-\tilde{x}'$ | $\frac{1}{(4\pi)^2} g_{\tilde{\chi}\tilde{\ell}\ell}^2 g_{1\ell}^2 \frac{m^4}{m_{\tilde{l}}^4}$ | | |
| | | $\tilde{\chi}_0 \to (h^0, Z)\tilde{x}'$ | $\theta_{\tilde{\chi}\tilde{h}}^2, \theta_{\tilde{\chi}\tilde{h}}^2 g_2^2$ | | |
| $LH_u X'$ | $(-, 2-R_2)$ | $\tilde{\chi}_0 \to \nu\tilde{x}'$ | $\theta_{\tilde{\chi}\tilde{h}}^2$ | $\tilde{\ell}^{\pm} \to \ell^{\pm}\nu\tilde{x}'$ | $\frac{1}{(4\pi)^2} g_{\tilde{h}\tilde{\ell}\ell}^2 \frac{m^2}{m_{\tilde{h}}^2}$ |
| | | $\tilde{\chi}_0 \to \ell^{\pm}(h^{\mp}, W^{\mp})\tilde{x}'$ | $\frac{1}{(4\pi)^2} g_2^2 \frac{m^2}{m_{\tilde{h}}^2}(\theta_{\tilde{\chi}\tilde{w}}^2, \theta_{\tilde{\chi}\tilde{h}}^2)$ | $\tilde{\ell}^{\pm} \to (h^{\pm}, W^{\pm})\tilde{x}'$ | $\theta_{\tilde{\ell}\tilde{\ell}_L}^2 (1, g_2^2)$ |
| $LH_u X'^{\dagger}$ | $(-, R_2)$ | " | " | " | " |
| $LH_d^{\dagger} X'^{\dagger}$ | $(-, R_2 - R_1)$ | " | " | " | " |
| $LH_d^{\dagger} X'$ | $(-, R_1 - R_2)$ | " | " | " | " |
| $LLEX'$ | $(-, R_1 - R_2)$ | $\tilde{\chi}_0 \to l^+l^-\nu\tilde{x}'$ | $\frac{1}{(4\pi)^4} g_{\tilde{\chi}\tilde{\ell}\ell}^2 \frac{m^4}{m_{\tilde{l}}^4}$ | $\tilde{\ell}^{\pm} \to \ell^{\pm}\nu\tilde{x}'$ | $\frac{1}{(4\pi)^2}$ |
| $QLDX'$ | " | "," | " | " | " |

Table 3.4: Decay modes and decay rates for LOSP candidates $\tilde{\chi}_0$ and $\tilde{\ell}$, relevant for FO&D, with $X'$ R-parity odd. Here $k$, $g_{\tilde{\chi}\tilde{\ell}\ell}$, and $g_{\tilde{h}\tilde{\ell}\ell}$ are defined as in Table 3.3.

row is the information characterizing the collider signatures for each choice of LOSP, which in the case of FO&D can be $\tilde{\chi}_0$ or $\tilde{\ell}^{\pm}$. For each LOSP, we list the leading decay channel of the LOSP, as well as subdominant decay channels which contain leptons or Higgs and gauge bosons, which may decay leptonically. These lepton–rich channels are more promising for event reconstruction. Note that $y'$ and $\tilde{y}'$ denoted in the neutralino decay via the Higgs Portal operator are used to denote hidden sector particles which are effectively invisible in the collider.

Each decay process is associated with a partial width

$$\Gamma(\tilde{x} \to \tilde{x}' + \text{SM}) = \left(\frac{1}{8\pi}\lambda^2 m\right) k(\tilde{x} \to \tilde{x}' + \text{SM}) \tag{3.18}$$

where $\lambda$ is the coefficient of the portal operator if it is marginal, and otherwise is defined as in Eq. 3.8. Here the dimensionless parameter $k$ is presented for each decay

process in Tables 3.3 and 3.4. In our expressions for $k$, the factors of $1/(4\pi)^2$ arise from three-body phase space, and $g_{abc}$ generically denotes the coupling between the fields $a$, $b$, and $c$, so for instance $g_{\tilde{\chi}\tilde{\ell}\ell}$ is the coupling between a neutralino, slepton, and lepton. The expressions for $g_{abc}$ shown in the caption of Table 3.3 were computed using a mass mixing insertion approximation. Moreover, $g_{1a}$ denotes the hypercharge coupling of the field $a$, while $g_2$ denotes the $SU(2)$ coupling. The symbol $\theta_{ab}$ denotes the mixing angle between the fields $a$ and $b$, so for instance $\theta_{\tilde{\chi}\tilde{h}}$ is the mixing angle between the neutralino and the pure higgsino. Because we are concerned with a primarily bino-like neutralino and mostly right-handed slepton, $\theta_{\tilde{\chi}\tilde{w}}$, $\theta_{\tilde{\chi}\tilde{h}}$, and $\theta_{\tilde{\ell}\tilde{\ell}_L}$ are small while $\theta_{\tilde{\chi}\tilde{b}}$ and $\theta_{\tilde{\ell}\tilde{\ell}_R}$ are order unity. We have also taken the Higgs vev to be of order $m$ for simplicity in this analysis. Lastly, note the factors of $m^2/m_a^2$ $(m^4/m_a^4)$ which arise from three-body decays through an off-shell fermionic (bosonic) field $a$.

Let us now discuss the salient features of the tables. To begin, consider the case of a right-handed slepton LOSP, which is relatively straightforward in terms of collider signals. For the R-parity even operators and the Bino Portal operator, visible sector lepton number is conserved and so the right-handed slepton decays to a charged lepton and an LSP, for example via $\tilde{\ell}^\pm \to \ell^\pm \tilde{x}'$. If the LOSP is a smuon or selectron, then for the fraction of LOSPs which stop inside the detector before decaying, the outgoing charged lepton is monochromatic and offers the best conditions for reconstructing the LSP mass.

For the remaining R-parity odd operators, visible sector lepton number is violated. Thus, the slepton LOSP will invariably decay into an even number of visible sector leptons, for instance via $\tilde{\ell}^\pm \to \ell^\pm \nu \tilde{x}'$. These decays often involve neutrinos, either directly or from decays of charged $W$ and higgs bosons. Because of the inherent challenge of identifying outgoing neutrinos, this scenario may be more difficult to distinguish from the R-parity even collider signals. However, in the case of smuon or selecton LOSP it may be possible to distinguish between $\tilde{\ell}^\pm \to \ell^\pm \tilde{x}'$ and $\tilde{\ell}^\pm \to \ell^\pm \nu \tilde{x}'$, based on whether the outgoing charged lepton is monochromatic in events with stopped LOSPs.

Second, let us consider the case of a bino-like neutralino LOSP. If $X'$ couples via $\mathcal{O}_K$ or $\mathcal{O}_W$, then there is a two-body decay to a $Z$ boson whose leptonic decays may be useful for event reconstruction and eventual LSP mass measurement. Moreover, there is a subdominant three-body decay to di-lepton through an off-shell slepton which might be likewise be employed. Note that it is possible to distinguish $\mathcal{O}_K$ from $\mathcal{O}_W$ at colliders based on the fact that only $\mathcal{O}_W$ allows for a decay to photons via $B^\alpha B_\alpha X'$.

Next, consider the scenario where $X'$ couples via $B^\alpha X'_\alpha$ or $H_u H_d X'$, corresponding to Bino and Higgs Portals, respectively. In both cases, the leading decay process of the neutralino occurs via mixing with the LSP. Specifically, the neutralino two-body decays via its tiny LSP fraction into two hidden sector states, so $\tilde{\chi}^0 \to y' \tilde{y}'$. However, in both cases there is also a subdominant visible decay mode which may be used to reconstruct the LSP mass.

Visible Sector                    Hidden Sector

$\tilde{y}$ ════════

                                                freeze-in

$\tilde{x}$ ════════                    ════════ $\tilde{y}'$

                                                        cascade

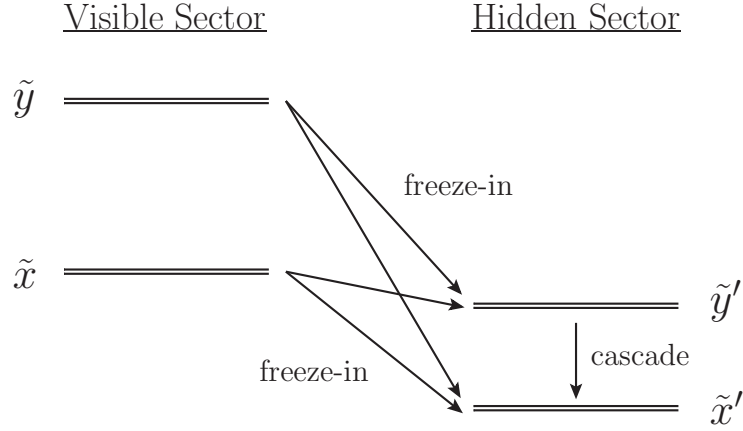                    freeze-in                 ════════ $\tilde{x}'$

Figure 3.3: Depiction of the cosmological history of FI. While the heavy visible superparters, $\tilde{y}$, and the LOSP, $\tilde{x}$, are in thermal equilibrium, they can FI an abundance of the LSP, $\tilde{x}'$, or a hidden sector spectator, $\tilde{y}'$. Due to R-parity each $\tilde{y}'$ ultimately cascades down to $\tilde{x}'$. In order to reconstuct this cosmology we need to be able to measure the lifetime and mass of $\tilde{x}$ and the mass of $\tilde{x}'$.


The invisible neutralino LOSP decays, $\tilde{\chi}^0 \to y'\tilde{y}'$, occur via the Bino and Higgs Portals and can pose a problem for reconstructing FO&D because more than a single $\tilde{x}'$ may be produced from the decay of the LOSP. In general, R-parity only implies that an *odd* number of $\tilde{x}'$ particles are produced. While $\tilde{y}'$ ultimately cascades into $\tilde{x}'$ due to R-parity, $y' \to \tilde{x}'\tilde{x}'$ could yield two additional $\tilde{x}'$ particles. The effects of these unwelcome LSP multiplicities on cosmology may be small for two reasons. First, the coupling controlling the invisible decay may be small. For example in the case of the Bino Portal, one can demand a smallish gauge coupling for the hidden sector $U(1)$. This has no effect on the strength of the visible decays of the LOSP, which are fixed by the MSSM hypercharge gauge coupling, but will reduce the branching ratio to invisible decays. Second, production of multiple LSPs is forbidden by kinematics if $m < 3m'$.

Finally, consider the case where the neutralino LOSP couples to the R-parity odd operators, $LH_u$ and $LH_d^\dagger$. For these operators the LOSP decays through the higgsino fraction of the neutralino. However, the leading two-body decay is $\tilde{\chi}^0 \to \nu\tilde{x}'$, which is invisible, and thus useless for LSP mass reconstruction. The leading visible decay is three-body through an off-shell higgsino-like neutralino, give by $\tilde{\chi}^0 \to h^\pm\tilde{h}^{\mp*} \to h^\pm\ell^\mp\tilde{x}'$, and likewise with $h^\pm$ replaced with $W^\pm$.

Lastly, note that modifying the portal operators by inserting powers of supersymmetry breaking spurions leaves the decay modes and $k$ factors of Tables 3.3 and 3.4 parametrically unchanged if $m \sim m_{3/2} \sim v$.

# 3.4 Freeze-In (FI)

Let us now consider the FI mechanism whereby $\tilde{x}'$ particles are produced from the decays of visible sector particles *before* they undergo thermal FO. In this scenario, the dominant contribution to the abundance of $\tilde{x}'$ arises when visible particles become non-relativistic, which is at temperatures of order their mass.

## 3.4.1 Spectator Fields in Freeze-In

In FO&D, particles other than the LOSP and LSP have essentially no effect on the cosmological history of the universe. In contrast, FI can be substantially affected by spectator fields in the visible and hidden sectors, collectively denoted by $\tilde{y}$ and $\tilde{y}'$. In particular, the decays $\tilde{y} \to (\tilde{x}', \tilde{y}') + \mathrm{SM}$, and $\tilde{x} \to \tilde{y}' + \mathrm{SM}$ may occur while these fields are still in thermal equilibrium but after the LSP has frozen out in the hidden sector. These decays produce additional FI contributions to the final LSP abundance. The rate of these decays cannot be directly measured at colliders, and generically they cannot be inferred from measurements of the LOSP $\tilde{x}$ decay. Therefore, there is no model-independent way to reconstruct FI at the LHC.

Nevertheless, there can easily be situations in which the FI contributions of $\tilde{y}$ particles to the LSP via $\tilde{y} \to \tilde{x}' + \mathrm{SM}$ may be inferred from the visible decays $\tilde{x} \to \tilde{x}' + \mathrm{SM}$. On the other hand, the decays $(\tilde{y}, \tilde{x}) \to \tilde{y}' + \mathrm{SM}$ are invariably model-dependent and thus unknown, as they require information about the entire hidden sector. In certain cases, however, such decays may be either forbidden (for example, by symmetries), or irrelevant (for example, if decays to $\tilde{y}' + \mathrm{SM}$ allowed by symmetries are kinematically inaccessible). Hence, it will be assumed hereafter that the decays $(\tilde{y}, \tilde{x}) \to \tilde{y}' + \mathrm{SM}$ do not provide an important contribution to FI of the LSP.

From above, it is clear that the criterion for reconstructing hidden sector cosmology from measurements at colliders imposes a constraint on theoretical models realizing the FI mechanism. On the other hand, within theoretical models satisfying the above constraint, there are very few constraints on the identity of the LOSP— the only requirement being that the LOSP FO abundance provides a subdominant component to the total relic abundance. This allows almost the entire superpartner spectrum of the MSSM to be the LOSP for sub-TeV masses, with the exception of the bino. Note that the situation is complementary to that for FO&D, where the identity of the LOSP is limited to the bino and right-handed sleptons, but there are no or minimal constraints on theoretical models.

## 3.4.2 Theories of Freeze-In

We now discuss models in which the couplings for all relevant decays for FI such as $\tilde{y} \to \tilde{x}' + \mathrm{SM}$ can be inferred from the measurable decays $\tilde{x} \to \tilde{x}' + \mathrm{SM}$ by using the

R-symmetry and R-parity transformation properties of the MSSM operators listed in (3.9), which can couple to $X'$ at dimension $\leq 5$.

A useful first step in constructing such models is to consider R-parity and R-symmetry assignments of $X'$ which allow only one operator coupling the visible sector to the hidden sector while forbidding others. One could then hope that all couplings between the visible and hidden sector would proceed via this operator, allowing us to infer the couplings for the decays $\tilde{y} \to \tilde{x}' + \text{SM}$. However, as mentioned earlier, we work within the framework of a low energy effective field theory in which supersymmetry breaking is mediated to us by Planck-suppressed operators with unknown coefficients. Thus, any supersymmetric operator allowed by symmetries can be dressed with functions of supersymmetry breaking spurions $\Phi$ with arbitrary coefficients, which complicates the situation.

If $X'$ is assigned to be R-parity even with R-charge zero, then it can couple via $\mathcal{O}_W X'$ and $\mathcal{O}_K X'$ at a supersymmetric level. This is a problem since the different supersymmetric operators have different coefficients in general, only a handful of which may be measured from the decays of the LOSP. Therefore, in order to reconstruct the FI mechanism from measurements at the LHC, it is important to couple an R-parity even chiral superfield $X'$ to a class of operators in the visible sector containing only one operator. There is only one such operator in the list 3.2 — $H_u H_d$, and giving rise to the connector operator $\lambda \int d^2\theta \, H_u H_d X'$, dubbed the Higgs Portal in Section 3.2.

One can try to do the same for an R-parity odd chiral superfield $X'$. A simple example is given by the supersymmetric operator $\lambda_i \int d^2\theta \, L H_u X'$ which could be arranged to be the only supersymmetric operator allowed by R-parity and R-symmetry. Since this operator is linear in lepton fields, its operator coefficient, $\lambda_i$ has a lepton flavor index. Thus, for a slepton LOSP, the prospect of reconstructing all of the operator coefficients is not promising. For example, if the LOSP is a stau, then $\lambda_3$ may be measured, but $\lambda_{1,2}$ will be inaccessible at colliders. On the other hand, for higgsino LOSP, the above operator gives rise to $\tilde{h}_u \to \ell \, \tilde{x}'$. By measuring the branching ratios of decays into each lepton generation, $\lambda_i$ can be fully measured.

Nevertheless, this theory still has a problem since there exist supersymmetry breaking operators derived from the supersymmetric operator which give rise to additional unknown contributions to FI in the early Universe. For example, if the symmetries allow $\int d^2\theta L H_u X'$, then they also allow the supersymmetry breaking operator $\int d^4\theta \, L H_u X' \frac{\Phi^\dagger \Phi}{M_{pl}^2}$. This operator mediates the process $\tilde{\ell} \to h \, \tilde{x}'$. Thus, in this scenario there are at least two active FI processes, each involving a different superpartner, $\tilde{h}$ and $\tilde{\ell}$ with different unknown decay widths. Since there is only one LOSP, only one of these decay processes can be measured at the LHC, making reconstruction of the full FI mechanism difficult. Note that this is not an issue for R-parity even $X'$ which couples to the visible sector, such as via $H_u H_d X'$ above, since then $\tilde{x}'$ is a fermion and the induced supersymmetry breaking operator does not give rise to a

decay to $\tilde{x}'$ from an R-parity odd particle in the visible sector.

Until now, the LSP was assumed to be a chiral superfield. If the LSP is a $U(1)'$ vector superfield $X'_\alpha$, then it can only couple via the operator $B^\alpha X'_\alpha$, consisting of the single operator $B_\alpha$ and giving rise to the Bino Portal operator $\lambda \int d^2\theta \, B^\alpha \, X'_\alpha$. This kinetic mixing can be removed by a shift of the gauge fields, inducing a $U(1)'$ millicharge for MSSM fields. Hence, this single kinetic mixing operator uniquely fixes the couplings of *every* MSSM superpartner to $\tilde{x}'$. As such, from the measurement of the decay of the LOSP, the coupling of $\tilde{x}'$ to the remaining MSSM particles can be inferred. With these couplings, the contribution to FI from all the MSSM fields can be computed, and checked against the FI formula in Eq. 2.4. Thus, the FI mechanism can be fully reconstructed from measurements at the LHC for these models.

### 3.4.3   UV Sensitivity of Freeze-In

If DM is dominantly produced by FI, its abundance will only be reconstructable if the FI process is IR dominated. FI of $X'$ can occur via both decays and scatterings of visible sector particles. While the decay contribution is always IR dominated, the contribution from scattering at temperature $T$ to the FI yield has the behavior $Y_d(T) \propto T^{2d-9}$, where $d$ is the dimension of the portal operator inducing FI. Thus, for the $d = 4$ operators of Table 3.2 all contributions to FI are IR dominated, and this includes both Bino and Higgs Portals. On the other hand, for $d \geq 5$, FI by scattering is UV dominated. However, any production of $X'$ before $X'$ freeze-out is irrelevant to the final yield of DM hence, for the $d = 5$ operators of Table 3.2, the question is whether FI by decay beats FI by scattering after $X'$ freeze-out.

For the $d = 5$ operators $(\mathcal{O}_K, \mathcal{O}_W, LH_d^\dagger, L^\dagger H_d, L^\dagger H_u^\dagger)X'$ there are contributions to FI from 2-body decay modes, and these dominate the scattering contribution provided the temperature of the visible sector when $X'$ freezes out is less than about 10 TeV [63], which is always the case as we have shown in Chap. 2. On the other hand, for the operators $(LLE, QLD, UDD)X'$ the decays are always at least three body, giving phase space suppression relative to scattering, so that FI by scattering can not be ignored even if $X'$ FO$'$ occurs as late as $T \simeq m$. Hence, the FI abundance resulting from these operators is always UV sensitive.

### 3.4.4   Collider Signatures of Freeze-In

Table 3.5 lists the important decay modes for all possible LOSP candidates for the Bino and Higgs Portal models, in which measurements at the LHC can reconstruct the FI mechanism in the early Universe. As mentioned earlier, a variety of LOSP candidates are possible—gluinos, squarks, sleptons, charginos, neutralinos and sneutrinos. Most of them have more than one interesting decay mode, as can be seen from Table 3.5. The table shows all two-body decay modes. Lepton rich three-body modes are also shown, as they are more useful than hadronic modes for determining the

| FI | | | | |
|---|---|---|---|---|
| | Higgs Portal: $H_uH_dX'$ | | Bino Portal: $B^\alpha X'_\alpha$ | |
| LOSP | Decay | k | Decay | k |
| $\tilde{g}$ | $\tilde{g} \to qq\tilde{x}'$ | $\frac{1}{(4\pi)^2}g^2_{\tilde{h}\tilde{q}q}\frac{m^4}{m^4_{\tilde{q}}}$ | $\tilde{g} \to qq\tilde{x}'$ | $\frac{1}{(4\pi)^2}g^2_{1q}\frac{m^4}{m^4_{\tilde{q}}}$ |
| $\tilde{\nu}$ | $\tilde{\nu} \to \ell^{\pm}(h^{\mp},W^{\mp})\tilde{x}'$ | $\frac{1}{(4\pi)^2}g^2_{\tilde{h}\tilde{\nu}\ell}\frac{m^2}{m^2_{\tilde{h}}}(1,g^2_2)$ | $\tilde{\nu} \to \ell^{\pm}(h^{\mp},W^{\mp})\tilde{x}'$ | $\frac{1}{(4\pi)^2}g^2_{1h}g^2_{\tilde{h}\tilde{\nu}\ell}\frac{m^2}{m^2_{\tilde{h}}}(1,g^2_2)$ |
| | $\tilde{\nu} \to \tilde{\nu}\tilde{x}'$ | $g^2_{\tilde{h}\tilde{\nu}\nu}$ | $\nu \to \nu\tilde{x}'$ | $g^2_{1\nu}$ |
| $\tilde{q}$ | $\tilde{q} \to q\tilde{x}'$ | $g^2_{\tilde{h}\tilde{q}q}$ | $\tilde{q} \to q\tilde{x}'$ | $g^2_{1q}$ |
| | $\tilde{q} \to q(h^{0,\pm},W^{0,\pm})\tilde{x}'$ | $\frac{1}{(4\pi)^2}g^2_{\tilde{h}\tilde{q}q}\frac{m^2}{m^2_{\tilde{h}}}(1,g^2_2)$ | $\tilde{q} \to q(h^{0,\pm},W^{0,\pm})\tilde{x}'$ | $\frac{1}{(4\pi)^2}g^2_{1h}g^2_{\tilde{h}\tilde{q}q}\frac{m^2}{m^2_{\tilde{h}}}(1,g^2_2)$ |
| $\tilde{\chi}^{\pm}$ | $\tilde{\chi}^{\pm} \to (h^{\pm},W^{\pm})\tilde{x}'$ | $g^2_2(\theta^2_{\tilde{\chi}\tilde{w}},\theta^2_{\tilde{\chi}\tilde{h}})$ | $\tilde{\chi}^{\pm} \to (h^{\pm},W^{\pm})\tilde{x}'$ | $g^2_{1h}(\theta^2_{\tilde{\chi}\tilde{h}},\theta^2_{\tilde{\chi}\tilde{w}})$ |
| | $\tilde{\chi}^{\pm} \to \ell^{\pm}\nu\tilde{x}'$ | $\frac{1}{(4\pi)^2}g^2_{\tilde{\chi}\tilde{\ell}\nu}g^2_{\tilde{h}\tilde{\ell}\nu}\frac{m^4}{m^4_{\tilde{l}}}$ | $\tilde{\chi}^{\pm} \to \ell^{\pm}\nu\tilde{x}'$ | $\frac{1}{(4\pi)^2}g^2_{\tilde{\chi}\tilde{\ell}\nu}g^2_{1\ell}\frac{m^4}{m^4_{\tilde{l}}}$ |
| $\tilde{\chi}_0$ | $\tilde{\chi}_0 \to (h^0,Z)\tilde{x}'$ | $\theta^2_{\tilde{\chi}\tilde{h}},\theta^2_{\tilde{\chi}\tilde{h}}g^2_2$ | $\tilde{\chi}_0 \to (h^0,Z)\tilde{x}'$ | $\theta^2_{\tilde{\chi}\tilde{h}}g^2_{1h},\theta^2_{\tilde{\chi}\tilde{h}}g^2_2g^2_{1h}$ |
| | $\tilde{\chi}_0 \to y'\tilde{y}'$ | $\theta^2_{\tilde{\chi}\tilde{h}}\lambda'^2$ | $\tilde{\chi}_0 \to y'\tilde{y}'$ | $\theta^2_{\tilde{\chi}\tilde{b}}g'^2$ |
| | $\tilde{\chi}_0 \to \ell^+\ell^-\tilde{x}'$ | $\frac{1}{(4\pi)^2}g^2_{\tilde{\chi}\tilde{\ell}\ell}g^2_{\tilde{h}\tilde{\ell}\ell}\frac{m^4}{m^4_{\tilde{l}}}$ | $\tilde{\chi}_0 \to \ell^+\ell^-\tilde{x}'$ | $\frac{1}{(4\pi)^2}g^2_{\tilde{\chi}\tilde{\ell}\ell}g^2_{1\ell}\frac{m^4}{m^4_{\tilde{l}}}$ |
| $\tilde{\ell}^{\pm}$ | $\tilde{\ell}^{\pm} \to \ell^{\pm}\tilde{x}'$ | $g^2_{\tilde{h}\tilde{\ell}\ell}$ | $\tilde{\ell}^{\pm} \to \ell^{\pm}\tilde{x}'$ | $g^2_{1\ell}$ |

Table 3.5: Summary of LOSP decay modes and rates for FI for interactions corresponding to the Higgs and Bino Portals. Here $g_{\tilde{h}\tilde{q}q} \equiv \lambda_q + vg^2_2/m_{\tilde{w}} + vg_{1q}g_{1h}/m_{\tilde{b}}$ is the effective coupling between the higgsino $\tilde{h}$ and $\tilde{q}q$ and $g_{\tilde{h}\tilde{\nu}\nu} = vg^2_2/m_{\tilde{w}} + vg_{1l}g_{1h}/m_{\tilde{b}}$ is the effective coupling between higgsino and $\tilde{\nu}\nu$. $g_{\tilde{\chi}\tilde{\ell}\nu}$ and $g_{\tilde{h}\tilde{\nu}\ell}$ are defined similarly as $g_{\tilde{\chi}\tilde{\ell}\ell}$ and $g_{\tilde{h}\tilde{\ell}\ell}$ in the caption of Table 3.3. Also, $y'$ and $\tilde{y}'$ denote hidden sector states. The dimensionless branching ratio, $k$, is defined in Eq. 3.18

LSP mass at the LHC. Three-body hadronic modes and those with Higgs and vector bosons are only shown if two body modes are absent or are hard to measure. Table 3.5 uses the same notation as in Tables 3.3 and 3.4, which is discussed in Section 3.3.3.

Some salient features of Table 3.5 are worth mentioning. First, it is striking that in

both the Higgs and Bino portal, the decay modes for all LOSP candidates are exactly the same, albeit with different branching ratios for the various modes in general. This is the case because the basic effect of both the Higgs and Bino portal is to induce mass/kinetic mixings among the neutralinos and $\tilde{x}'$. This will be important in distinguishing the models. Note that many channels can proceed through both gauge couplings $(g_1, g_2)$ and Yukawa couplings $(\lambda_q, \lambda_l)$; hence many of the branching ratios depend on both of them. The slepton LOSP has a two body leptonic mode, so it should be quite easy to measure. Chargino LOSPs have a two-body mode containing $h^\pm$ or $W^\pm$, and the LSP mass could probably be measured through the leptonic decays of $h^\pm, W^\pm$. The leading decays of squark LOSPs are hadronic, but the LSP mass should be measurable since the decay is two-body and the jet is expected to be hard.

For neutralino LOSPs, apart from the two-body decays with $h, Z$ and three-body decays with $l^+l^-$ which should be measurable, there is also a completely invisible mode with both decay products in the hidden sector. This is made possible due to the mixing between $\tilde{\chi}^0$ and $\tilde{x}'$ for both the Bino and Higgs Portals. However, as long as the visible decay width is sufficiently large so as to be measurable, it should be possible to measure the mass of the LSP. The sneutrino LOSP also has a practically invisible two-body decay mode to $\nu \tilde{x}'$; therefore one has to rely on the three-body modes to measure the mass of the LSP in this case.

The completely invisible decay mode for a neutralino LOSP gives rise to some subtleties for the FI mechanism, similar in spirit to those for LOSP FO&D discussed in Section 3.3. The FI abundance from the LOSP depends on the total LOSP decay width, but the LOSP lifetime is typically too long to be measured from the distribution of decay lengths in events at the LHC. Hence, the invisible decay mode induces an *a priori* unknown contribution to the FI abundance since the decay width for this mode depends on hidden sector couplings collectively denoted by $g'$. In addition, the invisible decays could give rise to more than one LSP $\tilde{x}'$, in general an odd number of $\tilde{x}'$ due to R-parity. This could occur via $\tilde{\chi}^0 \to y' \tilde{y}'$, with $\tilde{y}'$ ultimately decaying to one $\tilde{x}'$ and $y'$ decaying to two $\tilde{x}'$ if kinematically allowed.

However, these invisible decays will be subdominant as long as the hidden sector couplings are not too large, for example if $g'$ is comparable to the visible sector gauge couplings. This is because the FI contributions from the other decays of $\tilde{\chi}^0$ as well as from all the decays of other superpartners only depend on the parameter $\lambda$ (and visible masses and mixings) which can be measured from the visible decays of $\tilde{\chi}^0$. Thus, the unknown contribution is one among many known contributions. Assuming for simplicity that $g' \simeq g_{1,2}$, the branching ratio for the invisible decays is given roughly by:

$$B_{\text{invis}} \sim \frac{1}{N_{\text{eff}}} \tag{3.19}$$

where $N_{\text{eff}}$ varies from unity, when the non-LOSP visible superpartners are very heavy and their contributions to FI are negligible, to $N_{\text{eff}} \sim 60$ when these non-LOSPs are

close in mass to the LOSP and each superpartner gives a comparable contribution to FI.[4] Hence, although spectrum dependent, the single unknown contribution to FI from $\tilde{\chi}_0 \to y'\tilde{y}'$ is typically negligible.

Is it possible to distinguish between the two models for LSP FI? The answer is yes. The reason is that in the Higgs and Bino Portals, $\tilde{x}'$ is effectively an additional neutralino which is very weakly coupled to the MSSM. Because the Higgs (Bino) Portal mediates mass/kinetic mixings between $\tilde{x}'$ and the higgsino (bino), the $\tilde{x}'$ is higgsino (bino)-like. This implies an important difference in the branching ratios to various decay modes of the LOSP. For example, consider the example of a chargino LOSP. As shown in Table 3.5, if the chargino is wino-like, then for the Higgs (Bino) Portal the dominant decay mode is to $h^\pm$ ($W^\pm$). On the other hand, if the chargino is higgsino-like, then for the Higgs (Bino) Portal the dominant decay mode is to $W^\pm$ ($h^\pm$). Hence, the branching ratios of the LOSP can be used to infer whether the connector interaction is the Higgs or Bino Portal. More generally, for the decay branching ratios for squark, slepton, neutralino, and gluino LOSP can also be used to determine the connector operator.

Finally, it is worth noting that a gluino LOSP gives a signal very similar to that for split-supersymmetry [8, 9], namely a three-body decay mode, $\tilde{x} \to q\bar{q}\tilde{x}'$. However, it should be easy to distinguish the FI scenario from split-supersymmetry. In split-supersymmetry the LOSP is generically not the gluino, and furthermore the squarks are too heavy to be produced at the LHC. In the FI scenario on the other hand, it is possible to produce squarks and have a long-lived gluino decay signal.

## 3.5 Detection Prospects at the LHC

What are the prospects for detection of these particles at the LHC? This depends crucially on the nature of the LOSP—in particular, whether it is neutral or charged/colored. There is a large body of literature on detecting long-lived charged particles (such as staus) [65] and colored particles (such as gluinos) [11], but relatively very little on long-lived neutral particles, however see [98]. This is because charged and colored long-lived particles (LOSPs in our case) leave tracks in the detector and can be stopped effectively by their interactions with matter. Experimental searches for neutral LOSPs, on the other hand, are quite difficult and depend strongly on the lifetime of the LOSP as the lifetime determines the number of LOSPs decaying inside the detector.

### 3.5.1 Charged or Colored LOSP

Charged and colored LOSPs have lifetimes and decay products that can be measured for a huge range of lifetimes, from $10^{-12}$ s to at least $10^6$ s. Furthermore, charged

---

[4]In passing, we note that Figure 2.1 is drawn for $N_{\text{eff}} = 1$.

sleptons and charginos will produce spectacular and distinctive massive charged tracks at the LHC allowing a measurement of the LOSP mass [98]. Some fraction of LOSPs, emitted with small velocities, will lose their kinetic energy by ionization and stop inside the calorimeter. There have been proposals by both ATLAS and CMS to use the existing detector apparatus to precisely measure LOSP decays in their "inactive" mode [12, 11]. In addition, there have been numerous proposals for stopper detectors which may be built outside the main detector to stop these particles in order to perform precision spectroscopy on their decays [65]. These stopper detectors could perform extremely precise measurements of the lifetime of the LOSP as well as the mass of the LSP, assuming that it is sufficiently heavy, $m' > 0.2\, m$ for a stau LOSP. A similar analysis applies for squark and gluino LOSPs, relevant for FI.

For the FI scenario, it is important to measure the coupling $\lambda$ for the Higgs and Bino Portals, discussed in Section 3.4. In the limit where the hidden sector coupling $g'$ is small, $\lambda$ can be extracted by measuring the total lifetime of the LOSP. If $g'$ is not small, so that the invisible branching ratio is relevant to the extraction of $\lambda$, one can make progress by the following procedure. R-parity implies that all supersymmetric events end up with two LOSPs. One can compare the number of events with one invisible decay and one visible decay of the LOSP with the number of events with both LOSPs decaying visibly. This gives the ratio of the invisible and visible decay widths and, combining with the previous procedure, allows a measurement of $\lambda$.

### 3.5.2   Neutral LOSP

As mentioned earlier, the prospects for neutral LOSPs depend crucially on their lifetime, which has a different range in the FO&D and FI scenarios. Since the FI mechanism gives rise to a relic abundance proportional to the decay width of LOSP (and the partial width of other superpartners to the LSP), requiring that FI gives the total relic abundance of the LSP essentially fixes the lifetime of the LOSP ($\tilde{\chi}^0$ or $\tilde{\nu}$) to be $\sim 10^{-2}\,$s, giving a decay length $L \equiv \gamma c \tau$ of the LOSP of

$$L_{\mathrm{FI}} \sim 10^6 \text{ meters} \times \gamma \left( \frac{m'/m}{0.25} \right) \left( \frac{300 \mathrm{GeV}}{m} \right) \frac{1}{N_{\mathrm{eff}}} \tag{3.20}$$

where $N_{\mathrm{eff}} > 1$ arises from the FI contribution of non-LOSPs, as described by Eq. (3.19).

On the other hand, for FO&D the lifetime of the LOSP (bino-like $\tilde{\chi}^0$) is not relevant for the relic abundance, only its mass. As shown in Figure 2.1 the lifetime for FO&D varies very widely from less than about 100 s from nucleosynthesis to greater than about $\sim 10^{-13}$ s from the requirement that the two sectors *not* be in thermal equilibrium with each other, giving

$$L_{\mathrm{FO\&D}} \sim (10^{10} - 10^{-5} \text{ meters})\gamma. \tag{3.21}$$

Note that for $10^{-8}$ s $< \tau < 10^{-2}$ s, we are in the region where the contribution from FI is above the critical abundance giving rise to reannihilation of LSPs in the hidden sector and that the hidden sector annihilation cross-section is large enough so that LOSP FO&D provides the dominant relic abundance; see Section 3.3 for details.

Given the number of LOSPs produced at the LHC ($N_{\mathrm{produced}}$), the number of LOSPs decaying within the detector ($N_{\mathrm{decayed}}$) is given by:

$$N_{\mathrm{decayed}} = N_{\mathrm{produced}} \left(1 - e^{-d/L}\right) \overset{L \gg d}{\Rightarrow} N_{\mathrm{produced}} \frac{d}{L} \tag{3.22}$$

where $d$ is the size of the detector ($\sim 10$ m). Assuming a typical strong production cross-section of $\mathcal{O}(100)$ pb at the LHC gives $N_{\mathrm{produced}} \approx 10^7$ with an integrated luminosity of 100 fb$^{-1}$. Thus, from (3.22) a signal of $N_{\mathrm{decayed}} \gtrsim 10^2$ requires:

$$L \lesssim 10^6 \text{ meters.} \tag{3.23}$$

Thus, we find that a large fraction of the lifetime range for FO&D from the decay of a bino-like $\tilde{\chi}^0$ can be probed at the LHC. However, the situation for FI with a neutral LOSP, $\tilde{\chi}^0$ or $\tilde{\nu}$, is critical, and is likely to be seen only for high luminosities and high values of $m$, $m/m'$, and $N_{eff}$.

## 3.6 Discussion

Early running at the LHC will test a wide class of weak-scale supersymmetric theories that have unconventional DM: an LSP residing in a hidden sector. Any such two-sector cosmology has a long-lived LOSP, with a lifetime greater than $\tau_{\mathrm{min}} \simeq 10^{-13}$ s so that, for a total superpartner production cross section of 1-10 pb at the LHC with $\sqrt{s} = 7$ TeV, an integrated luminosity of 1 fb$^{-1}$ will yield $10^{3-4}$ events with long-lived LOSPs. If such events are observed, how can we deduce the underlying cosmology?

The visible and hidden sectors have different temperatures, allowing two classes of thermal relic abundance mechanisms: conventional Freeze-Out of the LOSP followed by LOSP decay, and Freeze-In of the LSP from visible superpartners as they become non-relativistic. In this paper we have concentrated on the case that these processes are symmetric between particles and anti-particles, and that the production of the LSP is not so copious as to initiate re-annihilations of LSPs in the hidden sector, giving the cases of FO&D and FI. In these cases the DM abundances are tightly related to measurable parameters, as shown in Figure 2.1, and we summarize our results in the next sub-section. However, in two sector cosmologies both FO&D and FI come in versions with particle anti-particle asymmetries and with re-annihilations. These cases {FO&D$_\mathrm{r}$, FO&D$_\mathrm{a}$, FI$_\mathrm{r}$, FI$_\mathrm{a}$} occur for a wide range of parameters and, although a complete reconstruction of the DM density is difficult, the collider signals are distinctive and are summarized in the second sub-section.

| | $L^\dagger L X'$ $Q^\dagger Q X'$ $H^\dagger H X'$ | $W^2 X'$ | $QUHX'$ $LEHX'$ $QDHX'$ | $H_u H_d X'$ |
|---|---|---|---|---|
| $\tilde{\chi}^0$ | $h^0, Z, \ell^+\ell^-$ | $\gamma, Z$ | $l^+l^-$ | $h^0, Z, l^+l^-$ |
| $\tilde{l}^\pm$ | $l^\pm$ | $l^\pm\left(\gamma, Z, h^0\right), \nu(W^\pm, h^\pm)$ | $l^\pm$ | $l^\pm$ |
| $\tilde{\chi}^\pm$ | $h^\pm, W^\pm, \ell^\pm\nu$ | $h^\pm, W^\pm$ | $l^\pm\nu$ | $h^\pm, W^\pm$ |
| $\tilde{\nu}$ | $\nu(1, h^0, Z), l^\pm(h^\mp W^\mp)$ | $\nu\left(\gamma, Z, h^0\right), \ell^\pm(W^\mp, h^\mp)$ | $l^\pm(h^\mp, W^\mp)$ | $\nu(1, h^0, Z), l^\pm(h^\mp W^\mp)$ |
| $\tilde{q}$ | $j(1, h^0, Z, h^\pm, W^\pm)$ | $j\left(\gamma, Z, h^0, W^\pm, h^\pm\right)$ | $j(1, h^0, Z, h^\pm, W^\pm)$ | $j(1, h^0, Z, h^\pm, W^\pm)$ |
| $\tilde{g}$ | $jj(1, h^0, Z, h^\pm, W^\pm)$ | $jj\left(\gamma, Z, h^0, W^\pm, h^\pm\right)$ | $jj(1, h^0, Z, h^\pm, W^\pm)$ | $jj(1, h^0, Z, h^\pm, W^\pm)$ |

Figure 3.4: Signal topologies at displaced vertices from LOSP decays induced by R-parity even $X'$, for a variety of LOSP candidates. A jet is represented by $j$. All topologies have missing energy carried by the LSP.

### 3.6.1 Signals from Freeze-Out and Decay and Freeze-In

If superpartners are produced at the LHC, standard analyses of cascade chains will allow the determination of both the nature and mass of the LOSP. If the LOSP is a neutralino or charged slepton it will be important to make sufficient measurements to infer the annihilation cross section, $\langle\sigma v\rangle$, to determine whether they are candidates to yield DM by FI or FO&D. Other LOSP candidates accessible to LHC will be candidates for yielding DM by FI.

What operator is relevant for inducing the LOSP decay? In Tables 3.4 and 3.5 we give the topologies for the displaced decay vertices that arise for all LOSP candidates and all decay operators of dimension 4 and 5 when the visible sector is the MSSM. Once the nature of the LOSP is known, one can examine the corresponding row of the tables. Sometimes this gives a unique result: for example a chargino LOSP with a dominant decay to $l^+l^-l^\pm\tilde{x}'$ implies DM by FI via the operator $LLEX'$; a charged slepton LOSP with dominant decay to two jets plus missing energy is decaying via the $QDLX'$ operator. Depending on the properties of the slepton, DM may arise from FO&D or FI. On the other hand, in many cases the decay topology does not select a unique operator, but leaves ambiguities. For example a light charged slepton LOSP, with a two body decay to a charged lepton and the LSP, would be a signal of DM by FI, but could occur via either the Higgs or Bino Portal, or indeed from the $L^\dagger L X'$ or $LEHX'$ operators. In the next subsection we imagine a particular

| | $B^\alpha X'_\alpha$ | $LH_u X'$ $LH_u X'^\dagger$ | $LH_d^\dagger X'$ $LH_d^\dagger X'^\dagger$ | $LLEX'$ | $QDLX'$ | $UDDX'$ |
|---|---|---|---|---|---|---|
| $\tilde\chi^0$ | $h^0, Z, l^+l^-$ | $\nu(1,h^0,Z), l^\pm(h^\mp,W^\mp)$ | $\nu(1,h^0,Z), l^\pm(h^\mp,W^\mp)$ | $l^+l^-\nu$ | $jj\,(l^\pm,\nu)$ | $jjj$ |
| $\tilde l^\pm$ | $l^\pm$ | $h^\pm, W^\pm$ | $h^\pm, W^\pm$ | $l^\pm\nu$ | $jj$ | $jjj\,(l^\pm,\nu)$ |
| $\tilde\chi^\pm$ | $h^\pm W^\pm$ | $l^\pm$ | $l^\pm$ | $l^\pm l^+l^-,\, l^\pm\nu\nu$ | $jj\,(l^\pm,\nu)$ | $jjj$ |
| $\tilde\nu$ | $\nu(1,h^0,Z), l^\pm(h^\mp W^\mp)$ | $h^0, Z$ | $h^0, Z$ | $l^+l^-$ | $jj$ | $jjj\,(l^\pm,\nu)$ |
| $\tilde q$ | $j(1,h^0,Z,h^\pm,W^\pm)$ | $j(l^\pm,\nu)$ | $j(l^\pm,\nu)$ | $j\,(l^+l^-\nu, l^\pm l^+l^-, l^\pm\nu\nu)$ | $j\,(l^\pm,\nu)$ | $jj$ |
| $\tilde g$ | $jj(1,h^0,Z,h^\pm,W^\pm)$ | $jj(l^\pm,\nu)$ | $jj(l^\pm,\nu)$ | $jj\,(l^+l^-\nu, l^\pm l^+l^-, l^\pm\nu\nu)$ | $jj\,(l^\pm,\nu)$ | $jjj$ |

Figure 3.5: Signal topologies at displaced vertices from LOSP decays induced by R-parity odd $X'$, for a variety of LOSP candidates. A jet is represented by $j$. All topologies have missing energy carried by the LSP.

set of measurements at LHC and discuss how this ambiguity could be resolved. A similar analysis would be necessary for any signal of the Higgs and Bino Portals since, no matter what the LOSP, the same decay signatures occur. These portals are distinguished by whether the LSP is dominantly mixed with a Higgsino or bino.

For FO&D, once the LOSP mass and annihilation cross section are known, reconstruction depends on the ability to measure the LSP mass, and this depends on the decay mode, as discussed in section 3.3. The key is to verify the prediction given in the last row of Table 3.1. Although not needed for reconstruction, it may be possible to infer the size of the coefficient of the operator inducing the LOSP decay, $\lambda$ of Eq. 3.8. All possible LOSP decay topologies for FO&D are shown in Tables 3.3 and 3.4, together with the mixing angles and kinematical factors, $k$, that enter the computation of the LOSP decay rate. The quantities in $k$ are all visible sector quantities, and measuring them allows $\lambda$ to be deduced from Eq. 3.18 once the LOSP lifetime is measured.

For reconstructing FI it is critical to measure the LSP mass, as discussed in Section 3.4, as well as the LOSP lifetime. If the dominant contribution to the FI abundance arises from the decay of the LOSP, as might happen if the LOSP is significantly lighter than other superpartners, then the key relation to test is given in the last row of Table 3.1. However, the FI contribution from heavier visible superpartners might dominate, and it is in this case that the Higgs and Bino Portals are important. To compute the FI contribution from the heavier superpartners one must deduce the coefficient $\lambda$ of the portal operator, which can be done with the use of Table 3.5. For the LOSP decay mode under study one must measure the corresponding quantity $k$, then a measurement of the LOSP lifetime allows $\lambda$ to be deduced from Eq. 3.18. Knowing
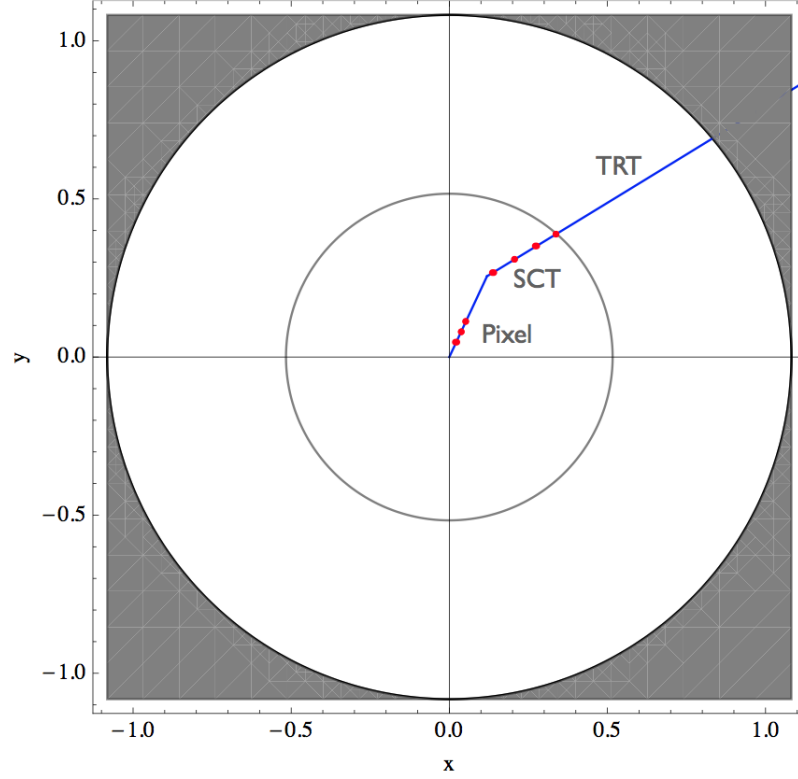
Figure 3.6: Simulation of a kinked track in the geometry of the ATLAS tracker. A charged particle decays to a charged and neutral particle creating a kink in the track. For an example in Sec. 3.6.2. The red dots correspond to hits in the tracker. Here the z-axis is defined along the beamline. Although too large to be visible to the naked eye, the track curvature is taken into account in this simulation so that it may be used for mass reconstruction.

the portal operator and its coefficient one can then compute the FI abundances from all non-LOSP superpartners and reconstruct the cosmology.

## 3.6.2 An example: $\tilde{l}^{\pm} \rightarrow l^{\pm} \tilde{x}'$

To illustrate our ideas, and the challenges involved in reconstructing the DM cosmology, we consider a very specific example. Suppose that LHC discovers a charged slepton LOSP with mass of 200 GeV. Frequently the slepton will get stopped in the detector and we suppose that it is measured to have a lifetime of 0.1 s and that it has a dominant two body decay to $l^{\pm} \tilde{x}'$; further we suppose that $m'$ is reconstructed from these two body decays to be 100 GeV. How would we interpret this within a two sector cosmology?

First, the low mass of the slepton implies that its FO yields a low abundance; one that would not give sufficient DM if it were stable, so that the mechanism of
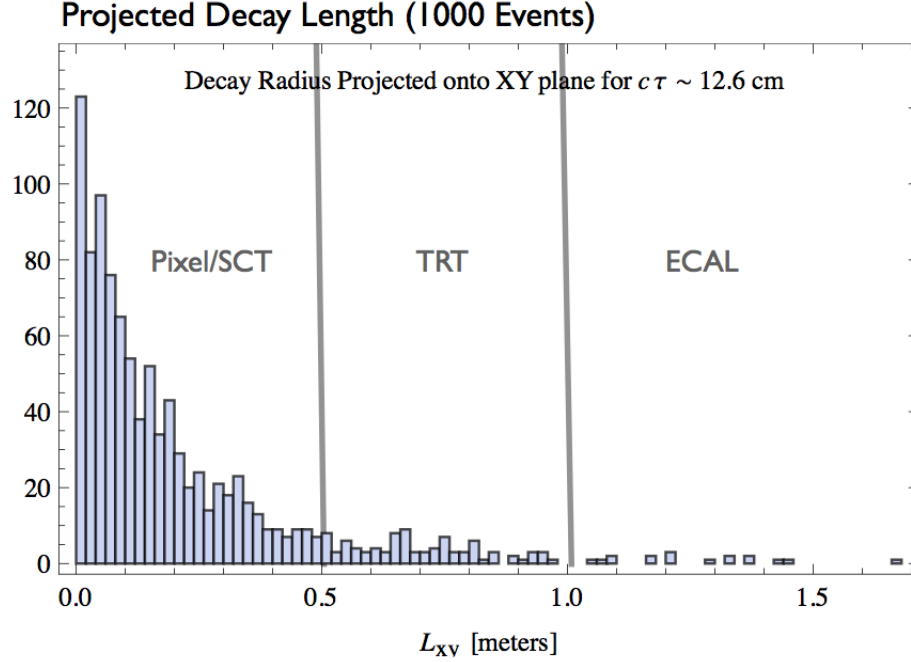
**Figure 3.7:** Projected decay locations for 1000 lepton decay events simulated with Pythia8 [] with decay length of $c\tau = 12.6$cm. In the ATLAS detector geometry the majority of events occur in the silicon layers of the inner tracker. Additional events occur in the TRT lays which have poor track reconstruction along one direction. Some residual decays are also expected to occur in the electronic calorimeter.

interest is FI rather than FO&D. Second, a glance at the second row of Tables 3.4 and 3.5 shows that this signal could result from both Higgs and Bino Portals, and also from the operators $L^\dagger L X'$ and $LEHX'$. Thirdly, if the slepton LOSP decay was solely responsible for DM FI then, from the relation in the last line of Table 3.1, it should have a lifetime of $10^{-2}$ s. Since the measured lifetime is an order of magnitude longer, only 10% of the observed DM abundance arises from FI from LOSP decays. Such a direct experimental verification of the process that generated the DM in the early universe would be an exciting triumph, and using LHC data to infer the DM abundance within an order of magnitude would suggest that FI is the right mechanism. But could further measurements reveal that the remaining 90% of DM production arose from FI via decays of non-LOSPs?

Consider first the Higgs and Bino Portals, where the symmetries of $X'$ imply that there is a single portal operator with a single coupling $\lambda$. In these portals, the LOSP decays via a small mass mixing between the DM and the Higgsino or bino that is proportional to $\lambda$. The crucial coupling $\lambda$ can be extracted from the slepton lifetime by measuring sufficient parameters of the visible neutralino mass matrix. Knowing $\lambda$ one can then compute the yield of DM from FI from decays of other superpartners,

such as the neutralinos, charginos and squarks. These yields will differ in the Higgs and Bino Portals, and the question is whether sufficient measurements of the visible superpartner spectrum can be made to show that in one of these portals the yield from non-LOSP decays accounts for the remaining 90% of DM. If so this would be a remarkable achievement.

It may be that the superpartner spectrum will be sufficiently determined to exclude the Higgs and Bino Portals. In this case it would seem that the observed slepton decays are being induced by $L^\dagger L X'$ or $LEHX'$. It could be that these operators happen to have larger coefficients, $\lambda$, than other operators with the same $R$-parity and $R$ change, so that inferring $\lambda$ from the slepton lifetime allows a successful computation of the full DM abundance from non-LOSP decays. However, it is likely that the total FI abundance from this operator is insufficient, and that other operators with the same $R$-parity and $R$ charge are making important contributions that cannot be reconstructed. For example, the $QUHX'$ operator could yield a substantial FI contribution from squark decays; but the corresponding squark branching ratio would be too small to measure. Such operators would also lead to subdominant decay modes of the LOSP, such as $\tilde{l}^\pm \to l^\pm \bar{q} q \tilde{x}'$, but the branching ratio may be too small to measure.

Until now we have not discussed the flavor structure of the LOSP and its decays. To the extent that the charged lepton Yukawa coupling are small, the Higgs and Bino Portals will have $\tilde{l}_i^\pm \to l_i^\pm \tilde{x}'$; the flavor of the lepton appearing at the LOSP vertex will be the same as the flavor of the slepton LOSP. On the other hand if the LOSP decay arises from $L^\dagger L X'$ or $LEHX'$ then we expect decays $\tilde{l}_i^\pm \to l_j^\pm \tilde{x}'$ that reflect the flavor structure of the corresponding coupling matrix. Thus the flavor structure will be a strong indication of whether the Higgs/Bino Portals are operative or not, since these theories are flavor blind.

For even shorter lifetimes within the range of reconstructability for FI in Table 3.1 the sleptons decay is fast enough to occur in the inner tracker of the LHC detectors; thus producing a "kinked" track [5]. Fig. 3.6 shows a simulated example of such an event in the geometry of the ALTAS detector. Fig. 3.7 shows the projected decay length for 1000 such simulated events. With high enough resolution the mass of $\tilde{x}'$ may be reconstructed from the kinematics of the kink event via $m_{\text{Recon}}'^2 = m_{\tilde{l}}^2 + m_l^2 - 2E_{\tilde{l}}E_l + 2|\vec{p}_{\tilde{l}}||\vec{p}_l|\cos\theta_k$.

---

[5]Current ATLAS and CMS tracking algorithms do not reconstruct kinked tracks, rather kinks appear as poor resolution tracks and are thrown out. Since many models of new physics predict kinks, it is clear that such a signal should not be overlooked. For instance, in gauge mediated susy breaking, a kink event can occur when a slepton fast decays to a lepton and a light gravitino. Other scenarios such as anomaly mediated susy breaking, R parity violation, and even more exotic models are all expected to produce kinked tracks. Not only may new physics be missed if we do not study kinks, but kink studies may also be crucial in distinguishing models of new physics. Additionally kinks and other exotic tracks may be used to learn something truly fundamental such as the scale and source of susy breaking.

### 3.6.3  Signals from Re-Annihilations and Asymmetry

The predicted relation for the FI mechanism in Table 3.1 corresponds to FI arising solely from LOSP decays. In general, there will be FI contributions which arise from heavier superpartners, and in the cases of the Higgs and Bino Portals, the DM abundance from FI can be computed exactly, assuming the mass spectrum has been measured. From this, the LOSP lifetime necessary to account for the measured DM abundance can be determined and checked against collider measurements.

More generally, this predicted relationship among measured quantities for FI, as well as those in the case of FO&D shown in Table 3.1 will be verified if either of these are indeed the dominant mechanisms for DM production in our universe. On the other hand, if these predicted relations are not satisfied, this would be an indication that a different mechanism of DM production is at work. Depending on the values of $\tau$ and $\langle \sigma v \rangle$ measured, Figure 2.1 implies that the origin of DM may be FO&D$_r$, FI$_r$, FO&D$_a$, or FI$_a$. Unfortunately, the re-annihilated variants, FO&D$_r$ and FI$_r$ are not fully reconstructible because in these theories the final abundance of DM depends on $\langle \sigma v \rangle'$, the annihilation cross-section of $X'$, which is not accessible at the LHC. Likewise, the asymmetric variants, FO&D$_a$ and FI$_a$ both depend on a CP phase which may be very difficult to measure at the LHC.

Nonetheless, while these theories are usually not fully reconstructible, it is the case that their associated portal operators may still be probed at the LHC. For example, just like FO&D, FO&D$_r$ and FO&D$_a$ can only function if visible sector FO yields an overabundance of $X$, and so the allowed LOSP candidates for these cosmologies are the bino-like neutralino and the right-handed slepton. FO&D$_r$ and FO&D$_a$ work for a broad range of portal interactions, and the signatures are precisely the same as those for FO&D shown in Tables 3.3 and 3.4 and in the first two rows of Tables 3.4 and 3.5.

The range of LOSP lifetimes for FO&D$_r$ is large, and similar to that for FO&D, as shown in Chap. 2. On the other hand, FO&D$_a$ requires a long lifetime, reducing the number of LOSP decays that can be measured for the case of the neutral bino. Furthermore, as $\epsilon$ is reduced so FO&D$_a$ requires a larger over-abundance from LOSP FO, which will remove the charged slepton LOSP candidate. FO&D$_a$ also requires the interference of two LOSP decay modes with differing hidden sector charges. If the amplitudes for these two modes are very different the asymmetry is suppressed, hence, with a high luminosity both modes may be seen. They could have the same or differing visible sector signatures, but they must have different hidden sector particles; for example $\tilde{x}'$ in one and $\tilde{y}'$, with larger mass, in the other.

What about FI? FI$_r$ and FI$_a$ are similar to FI in the sense that the LOSP can be any MSSM superpartner except for the bino. Depending on the dominant operator, the LOSP decay signatures are as in Tables 3.4 and 3.5. As shown in Chap. 2, a wide range of lifetimes are possible for both re-annihilated and asymmetric cases. While the DM abundance from FI$_r$ can never be reconstructed, since it depends on

the annihilation cross section in the hidden sector, there may be special cases of $FI_a$ that can be reconstructed. As shown in [64], $FI_a$ results from decays of a non-LOSP and the leading contribution typically arises from the interference between a purely visible sector decay and a decay mode involving the hidden sector. If one is lucky, the decay mode to the hidden sector may be dominated by a single interaction, and its coefficient learned from the LOSP lifetime. If $B - L$ is to be created via $FO\&D_a$, or via $FI_a$ [64], the visible part of the portal operator must be R-parity odd so that the signals are those of Table 3.5.

The signals that arise in supersymmetric theories where a pre-existing asymmetry, in either baryons or DM, is shared by equilibration via $R$-parity odd operators [26] have the same topologies as those shown in Table 3.5. However equilibration of an asymmetry can be distinguished from the $FO\&D_a$ and $FI_a$ generation mechanisms as the LOSP requires a shorter lifetime that violates Eq. 3.3.

# Chapter 4

# Gravitino Dark Matter from Freeze-In

As discussed in Chap 1, supersymmetry is an elegant and well-motivated extension of the standard model which potentially alleviates the gauge hierarchy problem and results in extensive phenomenological consequences. However as we have seen SUSY suffers from an assortment of cosmological difficulties which are collectively refereed to as the "cosmological gravitino problem". There are two components:

a) Late decaying superpartners can produce electromagnetic or hadronic radiation that can adversely affect Big Bang Nucleosynthesis (BBN).

b) Relic gravitinos produced by scattering and decaying superpartners can overclose the universe.

The gravitino problem highlights a robust tension between supersymmetry and cosmology. This is so because the existence of the gravitino is required by supergravity, and because the couplings of the gravitino to superpartners are uniquely fixed by soft masses and a single additional parameter, the gravitino mass.

At the same time, there are a number of approaches by which to address these issues. For example, a) may be evaded if the scale of supersymmetry breaking is very high, as in anomaly mediation, in which case the gravitino will decay safely before BBN. Alternatively, superpartner decays to the gravitino can be made sufficiently rapid if the scale of supersymmetry breaking is low or intermediate, as in gauge mediation.

Likewise, b) can be resolved if $m_{3/2} \lesssim$ keV, in which case the gravitino is simply too light to overclose the universe[1]. For $m_{3/2} \gtrsim$ keV, the authors of [99] showed that b) can be avoided if the reheating temperature after inflation, $T_R$, is below a critical value which depends on the superpartner spectrum and is shown in Fig. 4.1. Numerous new physics proposals—for example, ones including new stable charged

---

[1]However, note that this class of theories is in tension with warm dark matter constraints.

particles or superweakly interacting particles—suffer from an analogous overclosure problem which may be evaded by appropriately lowering $T_R$.

The conventional wisdom is that low $T_R$ is disfavored; for example, $T_R \gtrsim 10^9$ GeV for high scale leptogenesis [54]. As a consequence, the vast majority of studies of gravitino cosmology have focused on the portion of Fig. 4.1 at high $T_R$. However, the cosmological baryon asymmetry can be generated at much lower temperatures, for example via soft leptogenesis [61], and in this case gravitinos become a virtue rather than a problem: not only are both a) and b) resolved, but gravitinos can fully account for the observed dark matter for a wide range of masses, as depicted in Fig. 4.1.

In this chapter we investigate a more or less overlooked regime of gravitino cosmology corresponding to the vertical incline in critical $T_R$ shown as a function of $m_{3/2}$ in Fig. 4.1[2]. Here gravitino dark matter arises dominantly from the freeze-in mechanism, which was studied in some generality in [63]. In this setup, a feebly interacting dark matter particle is produced via the decays of particles which are still in thermal equilibrium. Crucially, since the decay rates of these particles fix the final abundance of dark matter, the associated lifetimes are hence constrained by the observed dark matter abundance. Furthermore, because the production is dominated at low temperatures, the freeze-in abundance is largely independent of $T_R$, explaining the vertical incline in critical $T_R$. Applying the general formulae in [63], we find that for the case of gravitino freeze-in, decays of superpartners in thermal equilibrium produce a final yield of

$$Y_{3/2}^{\text{decay}} \simeq \frac{405}{2\pi^4}\sqrt{\frac{5}{2}}\frac{m_{\text{Pl}}}{g_*^{3/2}}\sum_i \frac{\Gamma_i}{m_i^2}, \tag{4.1}$$

where $i$ sums over all superpartners, $m_i$ and $\Gamma_i$ are superpartner masses and partial decay widths to the gravitino, and $m_{\text{Pl}}$ is the reduced Planck mass[3].

As we will see, the freeze-in abundance of gravitino dark matter depends solely on the superpartner spectrum and $m_{3/2}$, a quantity which is straightforwardly inferred from the mass and lifetime of the NLSP when it decays to the gravitino LSP. Thus, for a given superpartner spectrum, the constraint of $\Omega_{3/2}^{\text{decay}} h^2 \simeq 0.11$ entirely fixes the lifetime of the NLSP. Because these quantities are experimentally accessible, we chance upon the rather amazing prospect of reconstructing the origin of gravitino dark matter through collider measurements. For example, demanding that gravitino freeze-in from Eq. (4.1) is dominated by degenerate heavy squarks and gluinos at a mass $m$, the NLSP lifetime is

$$\tau_{\text{NLSP}} \simeq 10^{-7} \text{ sec} \left(\frac{m_{\text{NLSP}}}{300 \text{ GeV}}\right)\left(\frac{m}{m_{\text{NLSP}}}\right)^6, \tag{4.2}$$

---

[2]Based on our work in [30]

[3]Throughout, sums over superpartners will implicitly include a degeneracy factor—for instance, a factor of 8 for gluinos, etc.
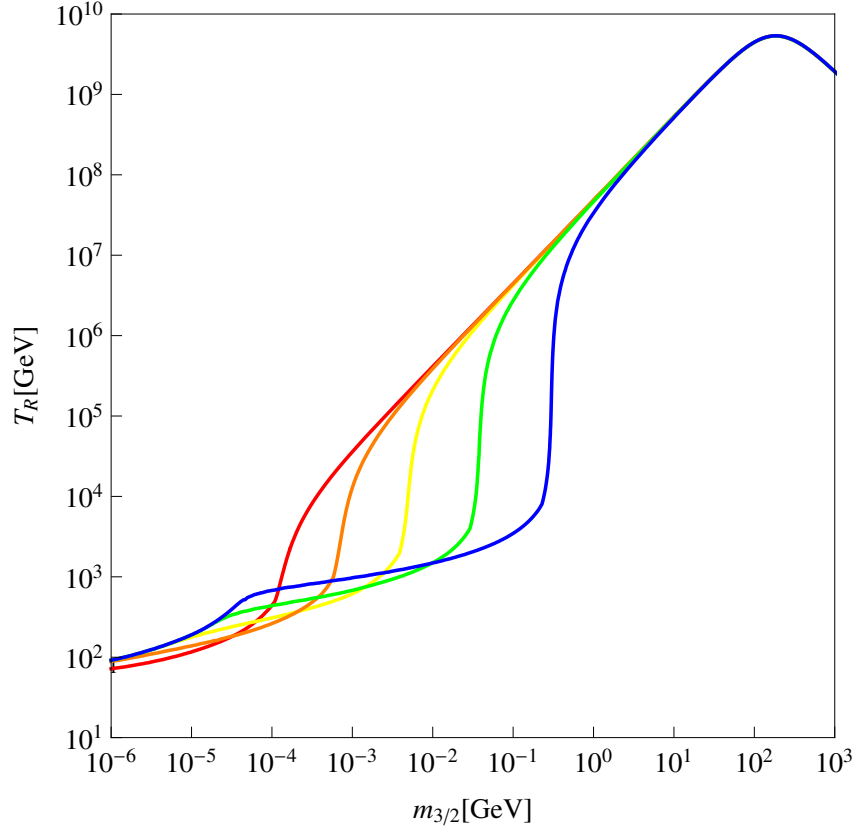
Figure 4.1: Contours of $\Omega_{3/2}h^2 = 0.11$ for gaugino masses fixed to $\{m_{\tilde{b}}, m_{\tilde{w}}, m_{\tilde{g}}\} = \{100, 210, 638\}$ GeV. The {red, orange, yellow, green, blue} contours correspond to universal scalar masses {500 GeV, 1 TeV, 2 TeV, 4 TeV, 8 TeV}.

if gravitino freeze-in accounts for the present day abundance of dark matter. Note that this proposal is a specific instance of the generalized cosmological scenario discussed in [63].

While the lifetime $\tau_{\text{NLSP}}$ indicated by Eq. (4.2) is effectively long-lived on collider time scales, a number of theoretical and experimental collaborations have suggested that the LHC is capable of measuring the long-lived decays of the sizable number of charged or colored metastable NLSPs which will typically slow and eventually stop within the detector material. Sufficiently long lifetimes can easily arise in theories of split supersymmetry [11], as well as theories with very weakly coupled particles like gravitinos [24], axinos [22], goldstini [36, 34], sterile sneutrinos [33], and dark matter [52]. Hence, stopped NLSPs allow for a range of $10^{-9} - 10^6$ sec to be probed in early LHC running, and indeed bounds on stopped gluinos have already been set by the CMS collaboration [82]. At higher luminosities, neutral NLSPs might also be probed if their lifetimes lie in the range $10^{-9} - 10^{-5}$ sec. As such, gravitino freeze-in offers
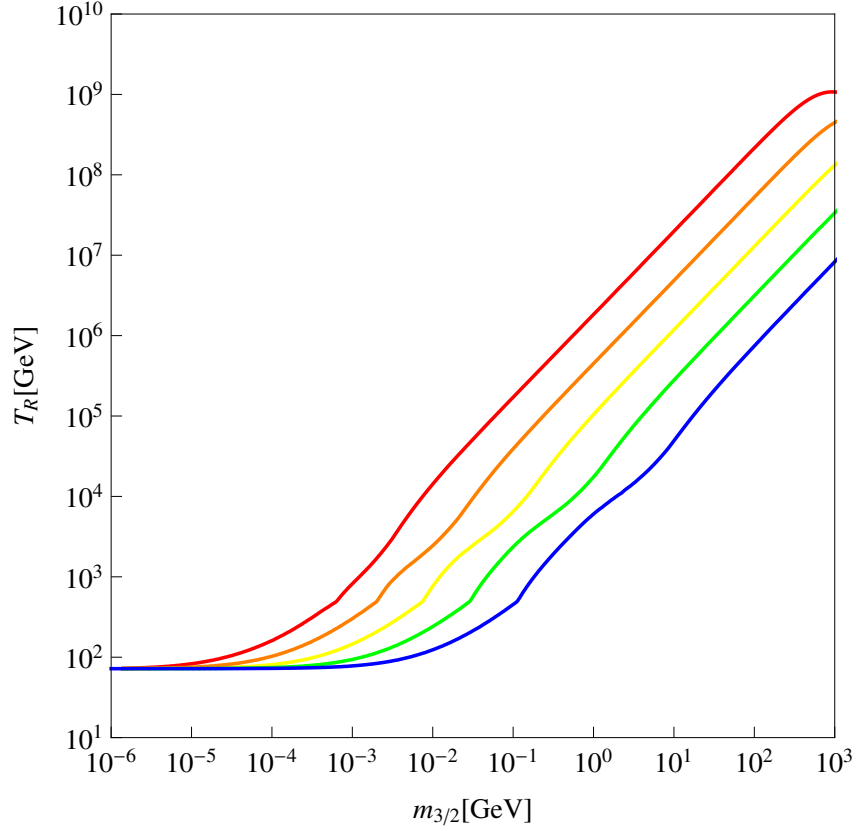
Figure 4.2: Contours of $\Omega_{3/2}h^2 = 0.11$ for universal scalar masses fixed to 500 GeV. The {red, orange, yellow, green, blue} contours correspond to a bino mass $m_{\tilde{b}} = \{500$ GeV, 1 TeV, 2 TeV, 4 TeV, 8 TeV$\}$, where $m_{\tilde{w}}$ and $m_{\tilde{g}}$ are fixed assuming gaugino mass unification at $M_{\text{GUT}} \sim 10^{16}$ GeV.

a novel mechanism of dark matter generation which has direct implications for the LHC in the near term [4].

## 4.1   Gravitino Cosmology

Assuming that the messenger scale of supersymmetry breaking is below the Planck scale, then the gravitino is the lightest of all the superpartners and is thus an attractive R-parity stabilized dark matter candidate. Typically, the gravitino mass is considered in the range keV $\lesssim m_{3/2} \lesssim 1$ GeV, where the lower bound arises from warm dark

---

[4]Here again kinked track studies discussed in Chap. 3 may be used to gain information from colliders on the FI decays

matter constraints and the upper bound arises from tension with BBN[5]. Broadly speaking, gravitinos are produced via three distinct physical mechanisms, each with a much different dependence on the reheating temperature after inflation, $T_R$, and the gravitino mass, $m_{3/2}$.

### 4.1.1 Modes of Production

First, there is a contribution to the gravitino abundance arising from NLSPs which freeze-out and then decay to the gravitino, as in the so-called superWIMP scenario [50]. This contribution is highly model dependent and can easily be negligible since the final relic gravitino abundance is down by a factor of $m_{3/2}/m_{\mathrm{NLSP}}$ relative to the freeze-out abundance of the NLSP, which can itself be small if the NLSP has strong annihilation channels. In addition, BBN is in tension with the superWIMP mechanism as the origin of the dark matter [80]. For these reasons, we will ignore superWIMP contributions and focus on other gravitino production mechanisms.

A second source of gravitino production is the thermal scattering of superpartners in the early universe. Since the goldstino couples to gauginos through a dimension five operator, the associated scattering processes are dominant at high temperatures, and so the final abundance of gravitinos depends linearly on $T_R$. For example, the yield of gravitinos from gaugino scattering goes parametrically as [99]

$$Y_{3/2}^{\mathrm{scatt}} \quad \propto \quad \frac{T_R \sum_a g_a^2 m_a^2}{m_{3/2}^2 m_{\mathrm{Pl}}}, \tag{4.3}$$

where $a = 1, 2, 3$ sums over the gauge group and $m_a$ are the gaugino masses. This scattering contribution has been the primary focus of existing work on gravitino dark matter, and corresponds to the straight, sloped portions of the contours in Figs. 4.1 and 4.2, which depict contours of the total gravitino abundance $\Omega_{3/2} h^2 = 0.11$ in the $(m_{3/2}, T_R)$ plane for different choices for the superpartner spectra.

Lastly, gravitinos may be produced by freeze-in: that is, from the decays of superpartners which are still in thermal equilibrium. The near vertical portions of the curves in Figs. 4.1 and 4.2 correspond to freeze-in, which is infrared dominated and thus independent of $T_R$. Plugging in for $\Gamma_i$ in Eq. (4.1) yields the parametric dependence

$$Y_{3/2}^{\mathrm{decay}} \quad \propto \quad \frac{\sum_i m_i^3}{m_{3/2}^2 m_{\mathrm{Pl}}}, \tag{4.4}$$

where $i$ sums over all superpartners. As $T_R$ drops below the superpartner masses, the superpartners are not efficiently produced from reheating, and hence gravitino

---

[5]The quantitative BBN bound on $m_{3/2}$ varies with the nature and mass of the NLSP. Moreover, in some cases it can be evaded altogether, e.g. with sneutrino NLSP or R-parity violation [73].

production arises from the exponentially tiny Boltzmann tail fixing the abundance of superpartners.

The size of the freeze-in region in Figs. 4.1 and 4.2 is determined by the competition between $Y_{3/2}^{\text{scatt}}$ and $Y_{3/2}^{\text{decay}}$. Thus, let us define $T_R^*$ to be the reheating temperature at which these two quantities are equal. Clearly, the range in $T_R$ in which freeze-in is operative runs from the superpartner masses up to $T_R^*$. Combing Eq. (4.3) and Eq. (4.4) this cross-over value of the reheating temperature goes as

$$T_R^* \quad \propto \quad \frac{\sum_i m_i^3}{\sum_a m_a^2}, \tag{4.5}$$

this implies that the freeze-in region will diminish for larger gaugino masses, and will grow for larger scalar masses.

The trend implied by Eq. (4.5) is verified in Fig. 4.1, which depicts $\Omega_{3/2}h^2 = 0.11$ from a total gravitino yield of $Y_{3/2} = Y_{3/2}^{\text{scatt}} + Y_{3/2}^{\text{decay}}$ in the $(m_{3/2}, T_R)$ plane. We note that requiring a dark matter abundance dominated by freeze-in fixes the value of $m_{3/2}$ which is made clear by the vertical regions of Fig. 4.1. One can see that the freeze-in region grows with increasing scalar masses. This is the case because heavier scalars imply larger decay rates without commensurately larger contributions from thermal scattering at high temperatures. For the allowed region of gravitino masses, $1 \text{ keV} \lesssim m_{3/2} \lesssim 1 \text{ GeV}$, the reheating temperature required for gravitino dark matter varies over $100 \text{ GeV} \lesssim T_R \lesssim 10^7 \text{ GeV}$.

It is key to note that a sizable fraction of this range corresponds to gravitino freeze-in and is thus insensitive to $T_R$, this is fortuitous because $T_R$ is not an experimentally accessible quantity. Hence this allows for the unique possibility of reconstructing the freeze-in origin of gravitino dark matter from LHC measurements. As shown in Fig. 4.1, for squarks accessible at LHC ($m_{\tilde{q}} \lesssim 2 \text{ TeV}$) this occurs in about $30\% - 50\%$ of the logarithmic range of $T_R$, while for heavier squarks the range is even greater. From a theoretical standpoint, it is straightforward to make the scalars quite heavy while keeping the gauginos light with an R-symmetry. Note that while Fig. 4.1 was produced assuming degenerate scalar masses, an almost identical plot results if the top and bottom squarks are pushed down to near the weak scale, as considered in [?].

Fig. 4.2 also verifies the trend indicated by Eq. (4.5), since it shows the freeze-in region diminishing for increasing gaugino masses. This is the case because heavier gauginos imply larger scattering cross-sections at high energies and thus a larger contribution arising from $Y_{3/2}^{\text{scatt}}$. From a top-down viewpoint, theories with very heavy gauginos and light scalars are difficult to accommodate, since very large values of $m_{\tilde{g}}$ tend to drag up $m_{\tilde{q}}$ and exacerbate fine-tuning of electroweak symmetry breaking. Thus, we conclude that it is actually theoretically difficult to obtain theories in which the freeze-in region is small, and so a large freeze-in region is a typical feature of many reasonable models.

Also, let us note that immediately after freeze-in, the produced gravitinos are highly relativistic, but they become non-relativistic as the temperature drops be-
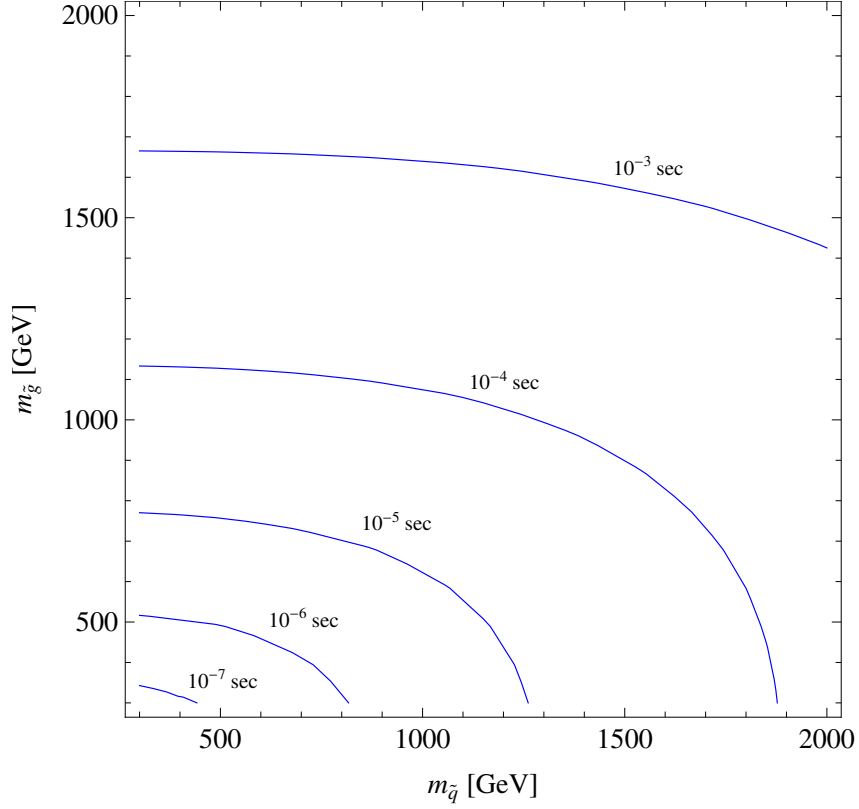
Figure 4.3: Prediction of $\tau_{\mathrm{NLSP}}$ for gravitino dark matter arising from freeze-in, for $m_{\mathrm{NLSP}} = 300$ GeV. The sum over superpartner contributions is assumed to be dominated by gluinos and degenerate squarks as shown in Eq. (4.8).

low their mass, yielding cold dark matter. At the same time, very light gravitinos, $m_{3/2} < 10$ keV, yield warm dark matter, especially since freeze-in arises from decays of superpartners in the exponential tail of their thermal distribution.

## 4.1.2 Reconstructing the Origins of Dark Matter

Let us now consider the extent to which the freeze-in origin of gravitino dark matter might actually be verified at the LHC. Assuming that the present day abundance of gravitinos arises entirely from freeze-in, $Y_{3/2} = Y_{3/2}^{\mathrm{decay}}$, one can rewrite Eq. (4.1) as

$$m_{3/2} Y_{3/2} \;=\; \frac{0.26}{g_*^{3/2}} \sqrt{\frac{m_{\mathrm{NLSP}}}{\tau_{\mathrm{NLSP}}}} \sum_i \left( \frac{m_i}{m_{\mathrm{NLSP}}} \right)^3, \tag{4.6}$$

which is obtained from

$$\tau_{\text{NLSP}}^{-1} \;=\; \frac{1}{48\pi}\frac{m_{\text{NLSP}}^5}{m_{3/2}^2 m_{\text{Pl}}^2} \tag{4.7}$$

while normalizing the partial widths of the superpartners decaying into gravitinos, $\Gamma_i$, with respect to the NLSP decay width, $\Gamma_{\text{NLSP}}$, so $\Gamma_i/m_i^5 = \Gamma_{\text{NLSP}}/m_{\text{NLSP}}^5$. From Eq. (4.6) we see that $m_{3/2}Y_{3/2} \propto \sum_i m_i^3$ is dominated by the very heaviest superpartners. Assuming that the superpartner spectrum is measured, Eq. (4.6) can be inverted to yield a critical prediction for the NLSP lifetime in terms of the superpartner spectrum:

$$
\begin{aligned}
\tau_{\text{NLSP}} \;=\;& 4 \times 10^{17}\ \text{GeV}^{-2} \times \frac{m_{\text{NLSP}}}{g_*^3}\left[\sum_i\left(\frac{m_i}{m_{\text{NLSP}}}\right)^3\right]^2 \\
\simeq\;& 7 \times 10^{-5}\ \text{sec} \times \left(\frac{150}{g_*}\right)^3 \left(\frac{300\,\text{GeV}}{m_{\text{NLSP}}}\right)^5 \\
& \left[\frac{9}{11}\left(\frac{m_{\tilde{q}}}{\text{TeV}}\right)^3 + \frac{2}{11}\left(\frac{m_{\tilde{g}}}{\text{TeV}}\right)^3\right]^2 .
\end{aligned}
\tag{4.8}
$$

The second line corresponds to an approximation in which the gravitinos are produced dominantly by squarks and gluinos. Also, while the value of $g_*$ actually varies substantially with temperature, for this approximate expression we have normalized its value to 150, which lies somewhere between the $g_*$ for the standard model and the minimal supersymmetric standard model. The corresponding prediction obtained by numerically solving the Boltzmann equations is shown in Fig. 4.3.

Thus, $\tau_{\text{NLSP}}$ may be as short as $10^{-7}$ sec for a squashed supersymmetric spectrum and as long as 100 sec, the approximate bound from BBN, for an extremely split spectrum. Note that this entire range of lifetimes is relatively long-lived on the time scales relevant to collider physics.

Fortunately, some fraction of metastable charged or colored NLSPs, such as the squark, slepton, chargino, or gluino, will interact with and eventually stop within the material of the LHC detectors. A number of groups evaluated this stopping efficiency, as well as prospects for performing precision spectroscopic measurements on the ensuing late NLSP decays [1]. Recently a search for stopped gluinos performed by the CMS collaboration placed a bound of $m_{\tilde{g}} < 398$ GeV for a stable gluino [82]. More generally, it is expected that CMS will effectively probe lifetimes of stopped particles in the range of $10^{-6} - 10^6$ sec [1].

In the case of neutral NLSPs, such as the neutralino or sneutrino, stopping will not occur. That said, a sizeable fraction $L/\gamma c\tau_{\text{NLSP}}$ of events may still decay within the length of the detector, $L \simeq \mathcal{O}(1\ \text{m})$, allowing for the possibility of lifetime probes in the range $10^{-9} - 10^{-5}$ sec at high luminosity.

The key point is that there exists a precision correlation between the superpartner spectrum and the NLSP lifetime which, if verified, would provide very strong evidence for gravitino dark matter arising from freeze-in. Also, while $T_R$ cannot be inferred accurately from collider measurements, precisely because freeze-in occurs on the near vertical part of the contours in Fig. 4.1 and Fig. 4.2, the reheating temperature will have a very strong upper bound at the order of magnitude level.

## 4.2   Conclusions

If the messengers of supersymmetry breaking are below the Planck scale, then the gravitino is the LSP and is thus a prime candidate for dark matter. We find that for a large range in $T_R$, gravitino dark matter is predominantly produced by freeze-in and is thus insensitive to $T_R$. Furthermore, there is a direct correlation between the cosmological abundance of dark matter and the decay rate of the NLSP to gravitinos. The NLSP lifetime, given in Eq. (4.8) and shown as contours in Fig. 4.3, allows for a precision test at the LHC of the freeze-in origins of gravitino dark matter. Moreover, the reheat temperature can then be inferred, at least to within a couple of orders of magnitude, from Fig. 4.1. In Chap. 5 we will provide additional motivations for gravitino freeze-in through an investigation of the cosmology of the QCD axino, the supersymmetric partner of the QCD axion. Our discussion will center on a "QCD axino problem" which is entirely analogous to the gravitino problem but which occurs in a complementary region of $m_{3/2}$. Together, the combined axino and gravitino problem completely exclude the possibility of a high $T_R$ and thus much of parameter space in which gravitino production arises from thermal scattering. This indicates a robust tension between the axion solution to the strong CP problem and supersymmetry which strongly favors a low reheating temperature.

# Part II

# The Strong CP Problem

# Chapter 5

# The Cosmological Axino Problem

The QCD axion is an extraordinarily elegant solution to the strong CP problem. Likewise, weak-scale supersymmetry offers a theoretically motivated resolution to the gauge hierarchy problem and a wealth of implications for the LHC. If we embrace both of these theoretical proposals we are lead to the exploration of the supersymmetric QCD axion[1].

By construction, the QCD axion couples to the gluon with a strength inversely proportional to the axion decay constant, $f_a$. Supersymmetry then requires a corresponding coupling of the QCD axino to the gluino. Expressed in superspace, this interaction takes the form

$$\mathcal{L} = \frac{\sqrt{2}\alpha_3}{8\pi f_a} \int d^2\theta A W^a W^a + \text{h.c.,} \tag{5.1}$$

where the superfield containing the saxion, axion, and axino is defined as

$$A = (s + ia)/\sqrt{2} + \sqrt{2}\theta\tilde{a} + \theta^2 F_A. \tag{5.2}$$

In this basis $A$ shifts by an arbitrary imaginary constant under the nonlinearly realized Peccei-Quinn (PQ) symmetry. In this basis the axino is defined to be a PQ singlet. While Eq. (5.1) may be the only axino coupling present, as in the case of the KSVZ [84] axion, there can be additional couplings between the axino and other superpartners, as in the case of the DFSZ [46] axion.

Since the cosmology of these theories depends crucially on the size of the axino mass, it is of utmost importance to ascertain its typical value. On general grounds, one expects supersymmetry breaking to seep into the PQ sector by way of higher-dimensional operators that couple the axion directly to the supersymmetry breaking field,

$$X = x + \sqrt{2}\theta\eta + \theta^2 F, \tag{5.3}$$

---

[1]Based on our work in [31]

where $F$ is the supersymmetry breaking scale. While these contributions may be present in the form of "Planck slop" operators induced by unspecified ultraviolet physics, they also arise irreducibly from the calculable dynamics of supergravity [115]. Since these operators transfer supersymmetry breaking effects of order $m_{3/2} \sim F/m_{\rm Pl}$ into the PQ sector, the axion and the axino acquire a mass difference of this order. In turn, because the axion is ensured to be massless by the nonlinearly realized PQ symmetry, the axino has a mass of order $m_{3/2}$ due to Planck-scale corrections.

Concretely, this simple physical argument can be understood by the existence of a higher-dimensional operator in the effective field theory below $f_a{}^2$,

$$\int d^4\theta \, \frac{(A+A^\dagger)^2(X+X^\dagger)}{m_{\rm Pl}} \quad \sim \quad \frac{1}{2}m_{3/2}\tilde{a}\tilde{a} + \dots, \tag{5.4}$$

which exactly preserves the full PQ symmetry,[3] and is expected from Planck-scale dynamics. Hence, the axino mass has a lower bound of order

$$m_{\tilde{a}} \quad \gtrsim \quad m_{3/2}, \tag{5.5}$$

which provides a theoretical motivation for considering theories of low-scale supersymmetry breaking with gravitino LSP and axino NLSP. Eq. (5.5) embodies our central result: barring fine-tuning, *the axino mass acquires an irreducible contribution of order the gravitino mass which is allowed by all symmetries and is generated by uncontrolled Planck-scale physics.*

A notable exception to this simple argument arises in certain scenarios in which extra dimensions are used to effectively sequester supersymmetric breaking from the PQ sector [103, 58, 3, 39]. Nevertheless, even in these theories, supersymmetry breaking is still mediated through supergravity effects which typically yield the same result as in Eq. (5.4) [40]. In this paper we will assume that these more complicated dynamics are not at play.

As we will see, the bound in Eq. (5.5) has an enormous effect on early universe cosmology. In particular, it implies the existence of a cosmological axino problem which is similar to the well-known gravitino problem [99] but which occurs in a complementary region of $m_{3/2}$.[4] Together, the combined bounds from axino and gravitino production completely exclude the possibility of a high $T_R$, as shown in Fig. 5.1. In turn, this rather unequivocally nullifies the viability of high-scale leptogenesis [54] while still permitting low-scale models of soft leptogenesis [61] and testable theories of asymmetric freeze-in [64].

The outline of this chapter is as follows, first we will present the theoretical rationale for Eq. (5.5), both in general and for a canonical supersymmetric axion model.

---

[2]Recently a similar effective theory has been considered in [67].

[3]Explicit PQ breaking operators can very easily destabilize the axion solution to the strong CP problem, even if they are generated by Planck scale dynamics [76, 75, 70]. See [56, 15, 45, 28] for possible resolutions to this difficulty.

[4]As in the case of the gravitino problem, this axino problem can be evaded if R-parity is broken.
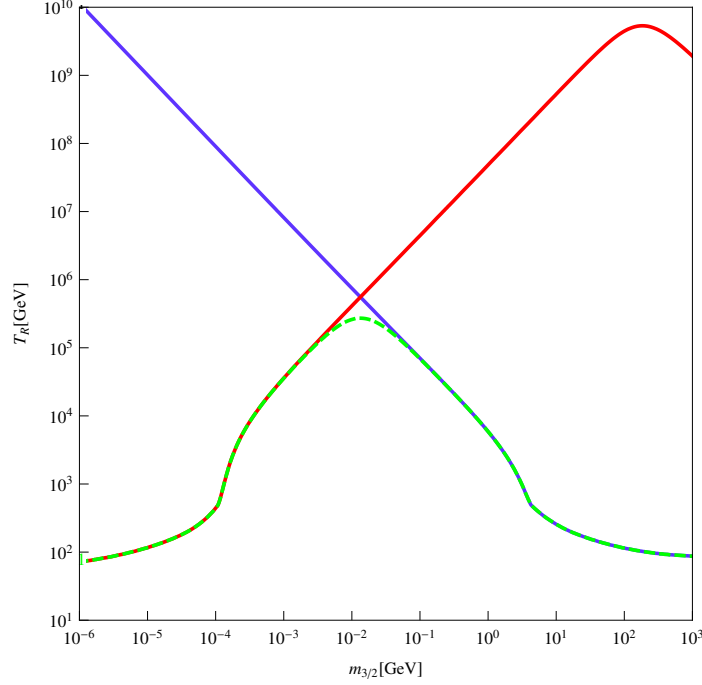
Figure 5.1: The red contour is $\Omega_{3/2}h^2 = 0.11$ from gravitino production alone, and the blue contour is $\Omega_{\tilde{a}}h^2 = 0.11$ for axino production alone with $m_{\tilde{a}} = m_{3/2}$ and $f_a = 10^{12}$ GeV. For larger values of $m_{\tilde{a}}$ and smaller values of $f_a$, the blue contour is translated to the left. The green contour can be interpreted in two ways: (i) as the $(\Omega_{3/2} + \Omega_{\tilde{a}})h^2 = 0.11$ contour for combined gravitino + axino co-dark matter when both are cosmologically stable for $m_{\tilde{a}} = m_{3/2}$; (ii) as the $\Omega_{3/2}h^2 = 0.11$ contour for gravitino dark matter when the axino is unstable and decays sufficiently quickly to gravitinos, for any value of $m_{\tilde{a}} > m_{3/2}$. Observe that a high reheating temperature, $T_R > 3 \times 10^5$ GeV, is unambiguously excluded in both cases. The superpartner spectrum is taken to be $\{m_{\tilde{b}}, m_{\tilde{w}}, m_{\tilde{g}}\} = \{100 \text{ GeV}, 210 \text{ GeV}, 638 \text{ GeV}\}$ and universal scalar masses at the GUT scale equal to 500 GeV.

We then go on to explore the thermal production of axinos in the early universe. Here we take note of a novel regime in which the dominant mode of axino production arises from the decays of superpartners still in thermal equilibrium, i.e. freeze-in [63]. Freeze-in of gravitinos and more generally of hidden sector dark matter was considered in Chaps. 2-4. By combining the bounds on overclosure from gravitino and axino production, we can then precisely quantify the seriousness of the cosmological axino problem. We then go on to consider the mixed cosmology of gravitinos, axinos, and saxions. Applying bounds from overclosure, structure formation, and big bang nucleosynthesis (BBN), we determine the values of $m_{3/2}$, $m_{\tilde{a}}$ and $f_a$ for which the cosmological history is viable.

## 5.1 Supersymmetric Axion Theories

To begin, let us provide a more rigorous justification for the naturalness argument that implies Eq. (5.5). Every supersymmetric axion theory can be described by an ensemble of interacting fields

$$\Phi_i = \phi_i + \sqrt{2}\theta\psi_i + \theta^2 F_i, \tag{5.6}$$

whose dynamics induce vacuum expectation values, $\langle\Phi_i\rangle = f_i$. In the supersymmetric limit, the saxion, axion and axino are linear combinations of Re $\phi_i$, Im $\phi_i$ and $\psi_i$, respectively, and are massless as a consequence of the nonlinearly realized PQ symmetry. The entirety of our discussion will occur in the language of linear fields, $\Phi_i$, so let us briefly note that the field $A$ discussed in the introduction is a linear combination of the fields $A_i = s_i + ia_i + \sqrt{2}\theta\tilde{a}_i + \theta^2 F_{A_i}$ where $\Phi_i = f_i e^{A_i/f_i}$.[5]

Next, let us consider the effect of higher-dimensional operators of the form

$$\int d^4\theta \, \frac{\lambda_i \Phi_i^\dagger \Phi_i (X + X^\dagger)}{\Lambda} = \frac{\lambda_i f_i}{\Lambda}(F_i^\dagger F + F^\dagger F_i) + \ldots, \tag{5.7}$$

which couple supersymmetry breaking to the PQ sector. Here $\lambda_i$ is an order unity dimensionless coupling and $X$ is as defined in Eq. (5.3). The parameter $\Lambda$ is the mass scale of the heavy particles which couple the PQ and supersymmetry breaking sectors and, as discussed in the introduction, it is at most the Planck scale, $\Lambda \lesssim m_{\text{Pl}}$.

It is clear that the only fermion mass terms generated by this operator are a mixing between $\psi_i$ and $\eta$, the fermionic component of $X$. Morally, this can be understood as a rather surprising mixing term between the axino and the goldstino. Such a mixing is strange, but by including a dynamical supersymmetry breaking sector for $X$ and diagonalizing the fermion mass matrix in the presence of Eq. (5.7), one goes to mass eigenstate basis and expectedly finds a massless goldstino and a heavy axino with a mass of order

$$m_{\tilde{a}} \sim \frac{F}{\Lambda}, \tag{5.8}$$

as shown explicitly for the very simple theory described in Appendix A.

One can reach the very same conclusion through a less technical, more physical argument. In particular, the right-hand side of Eq. (5.7) manifestly induces a non-zero value for the auxiliary field $F_i$,

$$F_i = -\frac{\lambda_i f_i F}{\Lambda} + \ldots, \tag{5.9}$$

---

[5]Naively, the $\theta^2$ component of $\Phi_i$ contains a term quadratic in the axino which can produce what appears to be an axino mass in interactions involving only a single $\Phi_i$. However, this quadratic term appears in the combination $(F_{A_i} - \tilde{a}_i^2/2)$, and so can always be removed by a shift of the auxiliary field.

which mediates supersymmetry breaking effects proportional to $F_i$ directly into the scalar potential of the PQ sector. Inserting appropriate powers of the characteristic scale of the PQ sector, $f_i$, we find that the mass scales and vacuum expectation values in the PQ sector shift by an amount which is of order $F/\Lambda$. Hence, one should expect a mass splitting between the axion and the axino of order $F/\Lambda$ which implies Eq. (5.5).

This argument can be restated in another way. In particular, apply a field redefinition

$$\Phi_i \quad \to \quad \Phi_i \left( 1 + \frac{\lambda_i X}{\Lambda} \right), \tag{5.10}$$

which removes the connector interaction in Eq. (5.7) at leading order in $1/\Lambda$ at the expense of introducing $X$ directly into the PQ sector dynamics. The effect of $X$ will be to explicitly generate an axino mass.

For example, consider the canonical supersymmetric axion theory defined by canonical Kahler potential and a superpotential

$$W \quad = \quad \kappa \, \Phi_3(\Phi_1 \Phi_2 - f^2), \tag{5.11}$$

where $\kappa$ is a dimensionless coupling, and a straightforward calculation shows that the vacuum is stabilized at $f_1 f_2 = f^2$ and $f_3 = 0$ in the supersymmetric limit.[6] Consider the effect of the higher-dimensional operators in Eq. (5.7) for the symmetrical case $\lambda_{1,2} = \lambda$ and $\lambda_3 = 0$. After the field redefinition in Eq. (5.10), a simple calculation shows that the vacuum is slightly shifted so that $f_3 = -\lambda F/\kappa \Lambda$. This induces a mass for the axino equal to $\lambda F/2\Lambda$ from the superpotential, which again accords with Eq. (5.5).

Before we continue on to cosmology, let us comment briefly on some of the existing literature on the mass of the axino. While statements are frequently made to the effect that the axino mass is highly model dependent, we disagree. The authors of [40] and [60] computed the axino mass in a variety of settings and verified Eq. (5.5) and Eq. (5.8) in all cases. The only exceptions resulted from the imposition of special relations among disparate and unrelated parameters to yield a lighter axino. We conclude that in generic theories the axino mass is given by Eq. (5.8) and the only model dependence is the value of $\Lambda$, which has an upper bound of $m_{\mathrm{Pl}}$.

### 5.1.1 A Simple Theory

Consider a minimal theory of PQ and supersymmetry breaking defined by

$$\mathcal{L} \quad = \quad \int d^4\theta \, K + \int d^2\theta \, W + \mathrm{h.c.}, \tag{5.12}$$

---

[6]Our results hold irrespective of the precise dynamics which break supersymmetry—indeed, one obtains the correct answer even when treating $X$ as a non-dynamical spurion of supersymmetry breaking.

where the Kahler potential and and superpotential are defined by

$$K = G(\Phi^\dagger\Phi) + H(X^\dagger, X) + \frac{\Phi^\dagger\Phi X}{\Lambda} + \text{h.c.} \tag{5.13}$$

$$W = FX. \tag{5.14}$$

Here $\Phi$ and $X$ are the PQ and supersymmetry breaking fields, respectively, and $G$ and $H$ are as of yet unspecified real functions. Since $\Phi$ is PQ charged, it cannot be present in the superpotential. Also, note that $G$ is purely a function of $\Phi^\dagger\Phi$ so that the PQ symmetry is left unbroken. We interpret the $1/\Lambda$ suppressed operator coupling $\Phi$ and $X$ as something generated by unspecified high-scale dynamics.

Demanding that $G$ and $H$ have a form such that $\langle\Phi\rangle = f_a$ and $\langle X\rangle = 0$ at the minimum of the scalar potential implies that

$$\langle G^{(1)}\rangle = f_a^2\langle G^{(2)}\rangle + f_a^4\langle G^{(3)}\rangle \tag{5.15}$$

$$\langle H^{(1,2)}\rangle = \langle H^{(2,1)}\rangle = -\frac{f_a^2}{\Lambda^3(\langle G^{(1)}\rangle + f_a^2\langle G^{(2)}\rangle)^2},$$

where the superscripts denote derivatives with respect to the function arguments. Plugging these expressions into the action, canonically normalizing the fermion kinetic terms, and then diagonalizing the fermion mass matrix, one discovers that one linear combination of fermions from $\Phi$ and $X$ is massless, as is expected of the goldstino. Meanwhile, the orthogonal axino component acquires a mass

$$m_{\tilde a} = \frac{F}{2\Lambda}\frac{1}{\langle G^{(1)}\rangle + f_a^2\langle G^{(2)}\rangle}\frac{1}{\langle H^{(1,1)}\rangle} + \ldots, \tag{5.16}$$

where the ellipses denote terms higher order in $\Lambda$. Hence, we confirm the result of the simple operator argument in Eq. (5.5).

## 5.2 Axino Cosmology

Given a proper theoretical justification of Eq. (5.5), let us now consider the early universe cosmology of the axino. Like the gravitino, the axino is produced through thermal scattering and decay processes. As observed by Strumia [107], one can trivially compute axino production by translating every equation relevant to gravitino production by the simple replacement [7]

$$\frac{m_{\tilde g}}{F} \leftrightarrow \frac{\sqrt{2}\alpha_3}{4\pi f_a}, \tag{5.17}$$

---

[7]The results of [19] are used in the calculation of the gravitino yield from scattering processes and translated into the analogous result for axinos via Eq. (5.17). The contributions from decay and inverse decay processes from freeze-in were computed as discussed in [63].
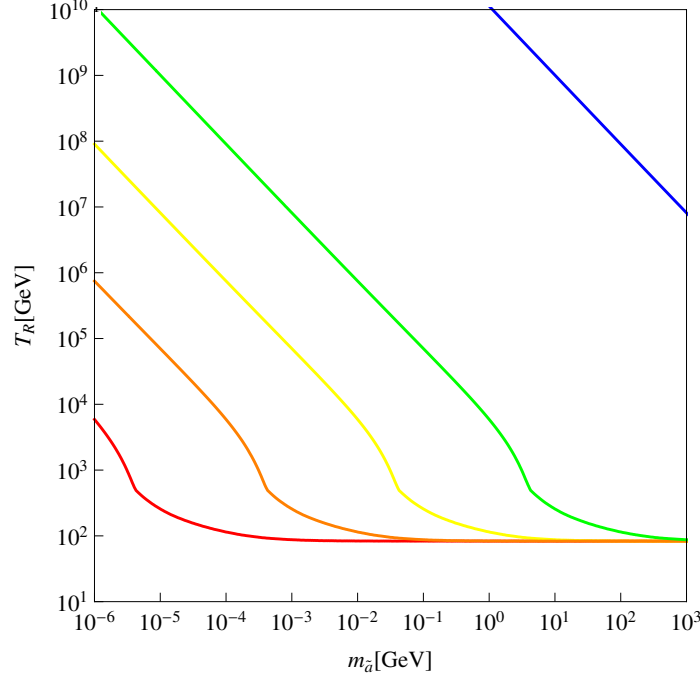
Figure 5.2: Contours of $\Omega_{\tilde{a}}h^2 = 0.11$ for the KSVZ [84] model, where axinos couple minimally, for $m_{\tilde{g}} = 638$ GeV. The {red, orange, yellow, green, blue} contours correspond to $\log_{10} f_a/\text{GeV} = \{9, 10, 11, 12, 15\}$.

while shutting off all scattering and decay processes involving gauginos and scalars not accounted for in Eq. (5.1).

In Fig. 5.2 and Fig. 5.3, we have numerically plotted contours of $\Omega_{\tilde{a}}h^2 = 0.11$ for $m_{\tilde{g}} = 638$ GeV and different values for the axion decay constant, assuming the axino to be cosmologically stable. As one can see, for axion decay constants within the "axion window", $10^9$ GeV $< f_a < 10^{12}$ GeV, the bounds on $T_R$ are quite stringent. For a GUT scale axion decay constant corresponding to the "anthropic window", the bound is weak. Moreover, as in the case of gravitino cosmology, one discovers regions where axino production arises dominantly from freeze-in and scattering, corresponding to the vertical and sloped portions of the contours, respectively. Note that the axino contours in Fig. 5.2 are "flipped" from the usual contours corresponding to gravitino overclosure, simply because the scattering and decay rates for axinos are independent of the axino mass and fixed by $f_a$.

## 5.2.1  Cosmological Axino Problem

The cosmology of gravitinos and axinos has been studied in great detail over many years [83]. Nevertheless, the existence of a serious cosmological axino problem has
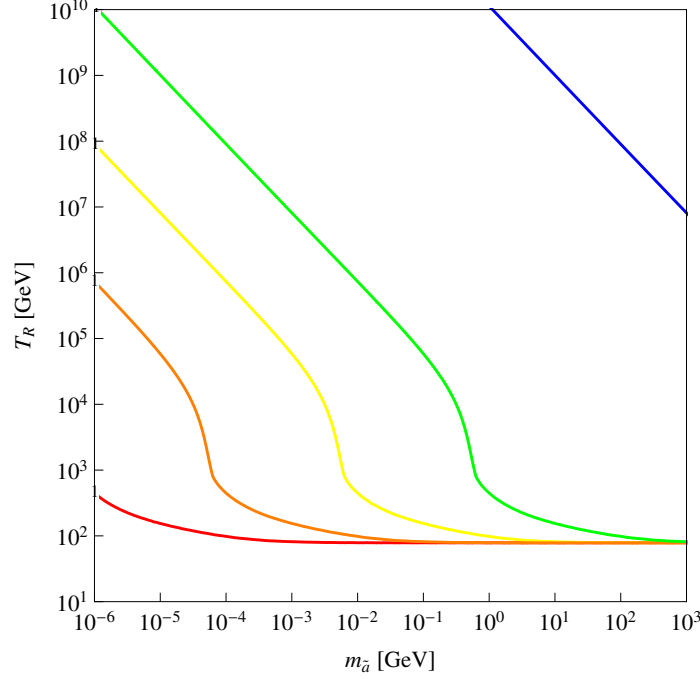
Figure 5.3: Contours of $\Omega_{\tilde{a}} h^2 = 0.11$ for the DFSZ [46] model, where axinos have additional couplings to squarks, for $m_{\tilde{g}} = 638$ GeV and $m_{\tilde{q}} = 500$ GeV. The new decay $\tilde{q} \to \tilde{a} + q$, results in a larger freeze-in region, where the contours are nearly vertical, as compared to Fig. 5.2. The contour colors correspond to the same values of $f_a$ as in Fig. 5.2.

never been clearly discussed. In particular, the red and blue curves in Fig. 5.1 are bounds on $T_R$ from gravitino and axino production overlaid, assuming that they are co-dark matter candidates and $m_{\tilde{a}} = m_{3/2}$. This is a conservative assumption to make because as shown in Eq. (5.4), the axino acquires an irreducible contribution to its mass of order the gravitino mass which cannot be eliminated without arbitrary fine-tuning. On the other hand, if for whatever reason the axino is heavier than the gravitino mass, then this only harshens axino bounds depicted in Fig. 5.1, since the axino contour is translated to the left by a factor $m_{\tilde{a}}/m_{3/2}$.

Fig. 5.1 illustrates our primary claim: *the combined gravitino and axino problems entirely exclude the possibility of a high reheating temperature.* The upper bound on $T_R$ is about $3 \times 10^5$ GeV for $f_a = 10^{12}$ GeV, and is even lower for lower $f_a$. Thus, supersymmetry plus the axion solution to the strong CP problem are strongly at odds with theories of high $T_R$ and high-scale leptogenesis, which typically require $T_R > 10^9$ GeV. The bound on $T_R$ is greatly relaxed for very large $f_a$, as could occur with anthropic selection of a small axion misalignment angle.
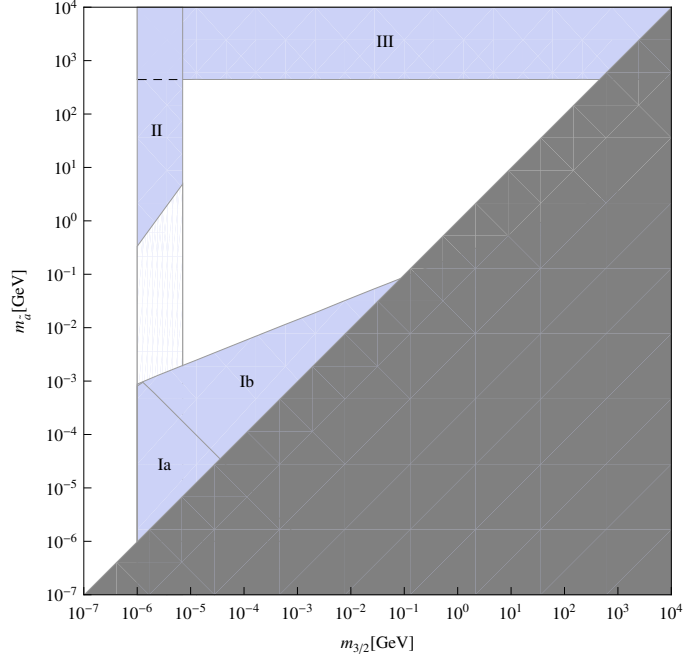
Figure 5.4: Light blue regions in the $(m_{3/2}, m_{\tilde{a}})$ plane have realistic dark matter cosmologies with a gravitino LSP and an axino NLSP for $f_a = 10^9$ GeV. Regions Ia and Ib correspond dark matter comprised of both stable gravitinos and axinos, with gravitinos or axinos dominating the dark matter abundance, respectively. Region II is bounded by warm dark matter constraints and limits on relativistic species. In Region III the axino mass is sufficiently large that the produced gravitinos are cold. The superpartner spectrum is taken to be identical to that of Fig. 5.1.

## 5.3 Gravitino and Axino Cosmology

Finally, let us consider cosmology in theories with gravitino LSP and axino NLSP, keeping careful track of the decays of axinos to gravitinos and cosmological limits on both axinos and saxions. The operator in Eq. (5.4) generates an axino-axion-gravitino coupling of the form

$$\frac{m_{\tilde{a}}}{m_{3/2} m_{\rm Pl}} \tilde{G} \sigma^\mu \tilde{a}^\dagger \partial_\mu a, \tag{5.18}$$

where $\tilde{G}$ is the physical goldstino. Note that this operator respects the PQ symmetry because the axion is derivatively coupled. The above operator mediates the decay of the axino to the gravitino and axion with a lifetime

$$\tau_{\tilde{a}} \simeq 10^9 \text{ sec} \times \left(\frac{m_{3/2}}{\rm MeV}\right)^2 \left(\frac{\rm GeV}{m_{\tilde{a}}}\right)^5. \tag{5.19}$$

This lifetime ranges over many orders of magnitude in the $(m_{3/2}, m_{\tilde{a}})$ plane, yielding a broad spectrum of cosmological histories which we now explore.
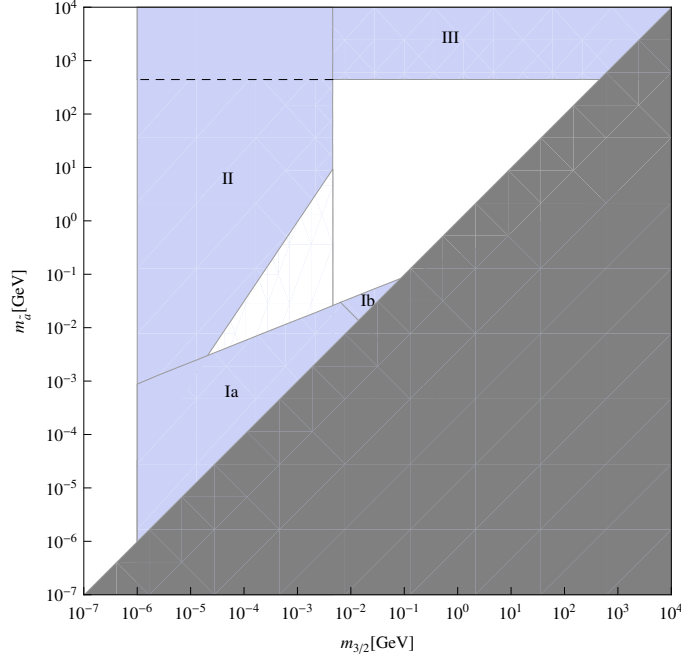
Figure 5.5: Same as Fig. 5.4 but with $f_a = 10^{12}$ GeV. Region II, corresponding to sub-dominant hot gravitino dark matter from axino decay, has increased. The superpartner spectrum is taken to be identical to that of Fig. 5.1.

## 5.3.1 Three Scenarios for Dark Matter

The cosmological history varies substantially in the $\left(m_{\tilde{a}}, m_{3/2}\right)$ plane, as depicted in Fig. 5.4 and Fig. 5.5 for $f_a = 10^9$ GeV and $10^{12}$ GeV respectively. The grey region corresponds to $m_{\tilde{a}} < m_{3/2}$, which is disfavored by the naturalness argument leading to Eq. (5.4), while the blue regions labeled by Ia, Ib, II, and III are consistent with existing experiments.

Region I of these figures, $\tau_{\tilde{a}} \gtrsim 10^{18}$ sec, corresponds to a "Cosmologically-Stable Axino". In this regime, gravitinos and axinos are co-dark matter with $m_{\tilde{a}} Y_{\tilde{a}} + m_{3/2} Y_{3/2} = \rho_0/s_0$, where

$$\frac{\rho_0}{s_0} = 4 \times 10^{-10} \text{ GeV} \tag{5.20}$$

is the observed dark matter relic abundance today. Here $Y_{\tilde{a}}$ and $Y_{3/2}$ are the thermal axino and gravitino yields arising from scattering and decay processes. Provided that $m_{\tilde{a}}, m_{3/2} > \text{keV}$, both components are cold. Region Ia corresponds to the dark matter energy density dominated by gravitinos, while Region Ib corresponds to axino domination.

Meanwhile, as the axino mass increases, the lifetime for the decay $\tilde{a} \to \tilde{G} + a$ decreases, so the axinos become cosmologically unstable. Gravitinos from axino

decay will then contribute to the total gravitino dark matter abundance, requiring $m_{3/2}\left(Y_{\tilde{a}} + Y_{3/2}\right) = \rho_0/s_0$.

If $m_{\tilde{a}} \gg m_{3/2}$ the gravitinos produced in axino decay are highly relativistic, becoming non-relativistic only at a temperature

$$T_{\text{NR}} \sim 10^{-2} \text{ eV} \times \left(\frac{m_{\tilde{a}}}{\text{GeV}}\right)^{3/2}. \tag{5.21}$$

In Region III of Fig. 5.4 and Fig. 5.5, the axino mass $m_{\tilde{a}} \gtrsim \text{TeV}$, so that $T_{\text{NR}} \gtrsim \text{keV}$ and the gravitinos from axino decay are cold. There is little parameter space for this "Fast Decaying Axino" case, since axinos are are no-longer expected to be the NLSP if $m_{\tilde{a}}$ increases much above a TeV.

For cosmologically unstable axinos, $m_{\tilde{a}} \lesssim \text{TeV}$ gives $T_{\text{NR}} \lesssim \text{keV}$ so that the gravitinos from axino decay are warm and will over-deplete sub-Mpc structures unless they constitute less than 3% of dark matter [110]. The right-hand vertical contour that bounds Region II, the "Sub-Dominant Axino" case, corresponds to $Y_{\tilde{a}} < 0.03 Y_{3/2}$, placing an upper bound on $m_{3/2}$ which increases with $f_a$ as seen by comparing Fig. 5.4 and Fig. 5.5.

The lower bound of Region II arises from the adverse effects of relativistic gravitinos arising from axino decay. As discussed in detail in [81], additional relativistic degrees of freedom can adversely affect matter-radiation equality and are thus constrained by observations of the cosmic microwave background, galaxy clustering, and the Lyman-$\alpha$ forest. These bounds apply to axino lifetimes shorter than $10^{13}$ sec, and correspond roughly to an additional effective number of neutrino species less than one. Numerically, this implies [81]

$$m_{\tilde{a}} Y_{\tilde{a}} \lesssim 3.4 \times 10^{-5} \text{ GeV} \times \left(\frac{10}{g_{*s}(T_{\tilde{a}})}\right)\left(\frac{T_{\tilde{a}}}{\text{MeV}}\right), \tag{5.22}$$

where $T_{\tilde{a}}$ is the temperature when the axino decays. Here $T_{\tilde{a}}$ is simply computed by solving for the temperature at which $H = 1/\tau_{\tilde{a}}$, where $\tau_{\tilde{a}}$ is defined in Eq. (5.19). Plugging in the value of $Y_{\tilde{a}}$ from scattering in Eq. (5.22) then yields a substantial limit on $T_R$ given by

$$T_R \quad < \quad 200 \text{ GeV} \times \left(\frac{f_a}{10^{12} \text{ GeV}}\right)^2 \left(\frac{m_{\tilde{a}}}{\text{GeV}}\right)^{3/2} \left(\frac{\text{GeV}}{m_{3/2}}\right)$$

For $m_{\tilde{a}} \sim m_{3/2}$ the above bound on $T_R$ is much more stringent than the one depicted in Fig. 5.1 from overclosure from gravitinos and axinos. However, by fixing $T_R$ to lie on the green contour of Fig. 5.1, such that gravitino dark matter from thermal production equals the measured value today, then the above inequality for $T_R$ can be reinterpreted as a lower bound on $m_{\tilde{a}}$ as a function of $m_{3/2}$. This constraint is what produces the slanted lower-right boundary of Region II.

In Fig. 5.6 contours of $\Omega_{3/2}h^2 = 0.11$ have been plotted for several values of $f_a$ and a fixed superpartner spectrum. These are contours of $m_{3/2}\left(Y_{\tilde{a}} + Y_{3/2}\right) = \rho_0/s_0$ and therefore corresponds to gravitino dark matter in the "Sub-Dominant Axino" case. The contours become dashed when the values of $m_{3/2}$ are excluded by the warm dark matter bound $Y_{\tilde{a}} < 0.03Y_{3/2}$; this corresponds to the rightmost boundary of Region II in Fig. 5.4 and Fig. 5.5. Examining Fig. 5.6 it is clear that while the angled gravitino scattering region is further excluded, the vertical gravitino freeze-in region is relatively unaffected. For $f_a = 10^{11}$ GeV and $10^{12}$ GeV the axino and gravitino yields in the bound $Y_{\tilde{a}} < 0.03Y_{3/2}$ are both dominated by the scattering contributions. Thus the $T_R$ dependence cancels and the resulting upper bound on $m_{3/2}$ is dependent only on $f_a$. As $f_a$ decreases the $m_{3/2}Y_{\tilde{a}}$ contours move to left as seen in Fig. 5.2. Therefore the gravitino yield that is to be compared with the axino scattering yield becomes dominated by freeze-in, forcing $T_R$ to smaller values. Since $Y_{\tilde{a}}^{\text{scatt}}/Y_{3/2}^{\text{decay}} \propto m_{3/2}^2 T_R/f_a^2$ the upper bound on $m_{3/2}$ relaxes whenever we cross over into the freeze-in dominated region.

Fig. 5.4 and Fig. 5.5 depict cosmological restrictions on $(m_{3/2}, m_{\tilde{a}}, f_a)$ which limit the range of collider signals resulting from the decay of the lightest observable-sector superpartner (LOSP)—that is, the lightest R-parity odd superpartner of a standard model particle. Assuming an axion model in which the LOSP couples directly to the axino (for instance a gluino LOSP in the KSVZ model) the ratio of LOSP decay rates to axinos and gravitinos is proportional to $(m_{3/2}/f_a)^2$, then branching ratio to axinos (gravitinos) dominates at large (small) $m_{3/2}$[8]. Hence in Region III at large $m_{3/2}$ the LOSP lifetime is fixed by $f_a$ and the dark matter is produced via axino production. At some intermediate values of $m_{3/2}$ the LOSP has sizable branching ratios to both axinos and gravitinos, and if the axino mass is sufficiently heavy these modes can be distinguished by kinematics. Hence in parts of regions I and II it may be possible to measure $(m_{3/2}, m_{\tilde{a}}, f_a)$. At a particular value of $m_{3/2}$, for instance around $m_{3/2} \sim 0.3$ MeV for squark masses of 500 GeV, the dark matter is produced by gravitino freeze-in. This value of $m_{3/2}$ is sufficiently small that the LOSP decays dominantly to gravitinos and has a lifetime directly correlated with the freeze-in production mechanism. For the charged slepton LOSP, decay signals to gravitinos and axinos have been studied in [22], examining the degree to which axino and gravitino modes can be distinguished.
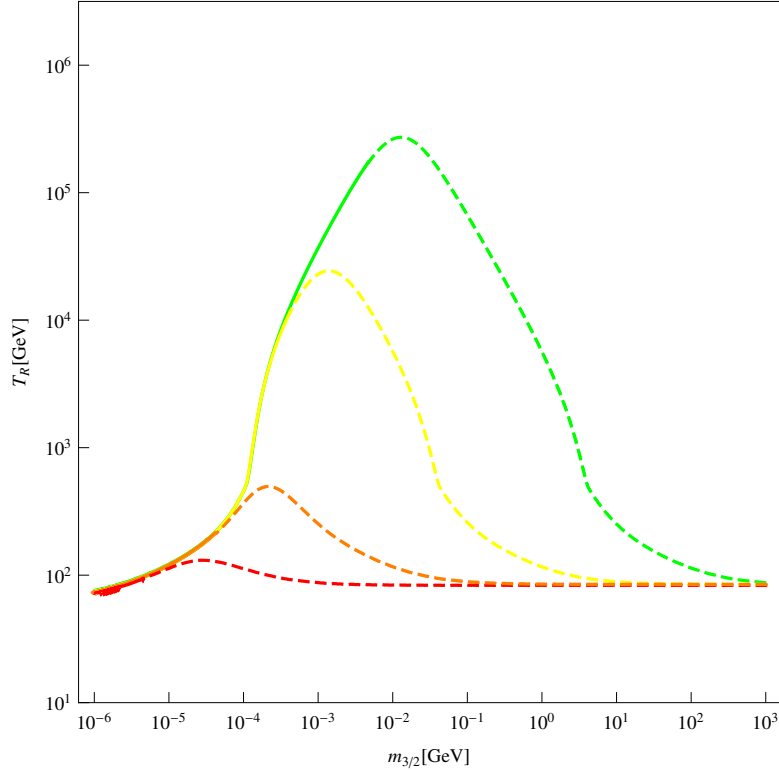
Figure 5.6: Gravitino dark matter in Region II, with contours of $m_{3/2}\left(Y_{\tilde{a}} + Y_{3/2}\right) = \rho_0/s_0$. Here the {Red, Orange, Yellow, Green} contours correspond to $\log_{10} f_a/\text{GeV} = \{9, 10, 11, 12\}$. The dotted portion of each contour shows values of $m_{3/2}$ that are disallowed by hot dark matter, where hot gravitinos from axino decay constitute more than 3% of the total abundance. The transition from solid to dashed contour corresponds to crossing from Region II into the white region of Fig. 5.4 and Fig. 5.5. The superpartner spectrum is taken to be identical to that of Fig. 5.1.

## 5.3.2 Cosmological Bounds from Saxions

So far we have ignored the saxion component of the axion supermultiplet. With communication between the supersymmetry breaking and PQ sectors mediated at mass scale $\Lambda$, the saxion picks up a mass at the same order as the axino mass, $m_s \sim F/\Lambda$. This follows from very similar arguments to those of Section 2—in particular, by inserting one power of $F_i$ of Eq. (5.9) into the operator of Eq. (5.7), or more directly from the dimension 6 operator $\Phi_i^\dagger \Phi_i X^\dagger X/\Lambda^2$ in the Kahler potential.

---

[8]Regardless of the choice of axion model any ultraviolet physics which generates the operator in Eq. (5.4) will typically induce axino/goldstino kinetic mixing via $\int d^4\theta \, \epsilon(A + A^\dagger)(X + X^\dagger)$, where $\epsilon \sim f_a/m_{\text{Pl}}$. In components, $\epsilon \tilde{G}\sigma^\mu \partial_\mu \tilde{a}^\dagger$ is removed by shifting $\tilde{G} \to \tilde{G} + \epsilon \tilde{a}$, which induces a coupling of the axino to the supercurrent of the form $\epsilon \tilde{a} \tilde{J}$. Therefore, the LOSP typically decays to $\tilde{a}$ with a branching fraction suppressed by a factor of $\epsilon^2$ relative to the branching fraction to $\tilde{G}$.

In the effective theory beneath $f_a$, Planck-scale dynamics induce the operator

$$\int d^4\theta \, \frac{X^\dagger X (A^\dagger + A)^2}{m_{\rm Pl}^2} \quad \simeq \quad \frac{1}{2} m_{3/2}^2 ss + {\rm h.c.} + \dots, \tag{5.23}$$

so that the gravitino mass provides a lower bound for the saxion mass.

The cosmological bounds imposed by saxions have been studied in detail in [81]. We find that under the assumption $m_s > m_{3/2}$ these bounds on $T_R$ are typically less stringent than those coming from axino cosmology. In particular supersymmetric axion models must satisfy constraints on

- Saxion overclosure,

- Saxion decays influencing BBN,

- Relativistic degrees of freedom.

The saxion abundance receives a contribution from scattering in the early universe which is identical to the axino scattering yield $Y_s^{\rm scatt} = Y_{\tilde{a}}^{\rm scatt}$, as can be seen from the supersymmetric interaction of Eq. (5.1). We assume a negligible contribution to the saxion abundance from coherent oscillations. Unlike the axino and gravitino, saxion overclosure does not pose a threat because saxions decay rapidly; to photons through the electromagnetic analogue of Eq. (5.1) and to axions through the kinetic term of the axion supermultiplet.

Since the saxion will rapidly decay to photons one may worry that these photons might ruin the predictions of BBN unless the saxion is made heavy enough. However, this is not the case, since decays to photons are suppressed by a loop factor and so will always be subdominant to decays to axions

$$\frac{\Gamma\left(s \to aa\right)}{\Gamma\left(s \to \gamma\gamma\right)} \sim \frac{64\pi^2}{\alpha^2}, \tag{5.24}$$

where $\alpha$ is the fine structure constant. While the branching fraction of the saxion to axions can in principle be small, this requires a delicate and unnatural cancellation in the underlying theory.

Finally, let us consider the issue of relativistic degrees of freedom. In complete analogy with the axino, the saxion will decay and produce relativistic energy in axions which is subject to the bound in Eq. (5.22) taken from [81] except with $m_{\tilde{a}} Y_{\tilde{a}}$ and $T_{\tilde{a}}$ replaced with $m_s Y_s$ and $T_s$. Plugging in for $Y_s$, the saxion yield from thermal scattering (which is essentially equal to the axino yield from thermal scattering), and plugging in for $T_s$, the temperature at the time of saxion decay where $\tau_s^{-1} \sim m_s^3/64\pi f_a^2$, one acquires a bound on $T_R$ given by

$$T_R \quad < \quad 5 \times 10^8 \text{ GeV} \times \left(\frac{f_a}{10^{12} \text{ GeV}}\right) \left(\frac{m_s}{\text{GeV}}\right)^{1/2},$$

which is generally weaker than the $T_R$ bound from overclosure depicted in Fig. 5.1.

## 5.4 Conclusions

If supersymmetry and the QCD axion coexist, then a large range of parameter space will include a gravitino LSP and axino NLSP. In this case the axino plays an important role in determining viable cosmological histories. In particular, the overclosure constraint alone provides a very powerful limit on the reheat temperature that can be approximated by

$$T_R < 3 \times 10^5 \, \text{GeV} \, \left( \frac{f_a}{10^{12} \, \text{GeV}} \right). \qquad (5.25)$$

We identify three very different phases of combined gravitino and axino cosmology which we label according to the nature of the axino:

(I) **"Cosmologically-Stable Axino"** is the case where axinos and gravitinos are co-dark matter.

(II) **"Sub-Dominant Axino"** production leads to gravitino dark matter from decays, with an upper bound on $m_{3/2}$ that depends on $f_a$.

(III) **"Fast-Decaying Axino"** has a TeV scale mass and thus decays sufficiently early that gravitino dark matter is cold.

The regions of gravitino and axino masses that yield these three cosmologies are shown in Fig. 5.4 and Fig. 5.5 for $f_a = 10^9$ GeV and $10^{12}$ GeV. In all three cosmologies, dark matter may be dominantly produced by gravitino freeze-in.

The required ranges of $T_R$ for cases (II) and (III) are shown in Fig. 5.6 for several values of $f_a$. They give an upper bound on $T_R$ that is much lower than for the case of gravitino dark matter without axinos, and is also lower than the bound of Eq. (5.25). Thus the presence of the axinos increases the likelihood that the production mechanism for gravitino dark matter is freeze-in from decays, strengthening the possibility that LHC will provide strong evidence for gravitino dark matter by measuring the LOSP lifetime. Finally, let us note that our conclusions are unaltered by cosmological considerations of the saxion for any value of its mass greater than $m_{3/2}$.

# Part III

# Origins of the Matter - Antimatter Asymmetry

# Chapter 6

# Bubble Baryogenesis

What is the dynamic origin of the observed baryon asymmetry? In this chapter we discuss a proposal a new mechanism of baryogenesis, in which a complex scalar baryon undergoes a percolating first-order phase transition in the early Universe. Tunneling from a metastable vacua is described by Colemans instanton solution, and in Minkowski space corresponds to a bubble nucleation event. In our mechanism Baryon number and Charge-Parity violating terms in the scalar baryons potential act to torque the instanton in field space. The corresponding bubbles will carry an asymmetry in their walls, ultimately resulting in a spatially inhomogeneously distributed asymmetry. The bubbles nucleate expand and eventually collide, percolation occurs, and the entire universe is converted to true vacua. Bubble collision dynamics will also add to the asymmetry yield. After the collision, the bubbles thermalize; the asymmetry spreads and can migrate to the SM via decays. We conduct a detailed model building analysis, and used numerical simulations to study the model-dependent evolution of the baryon asymmetry through bubble nucleation and growth, bubble collisions, and washout.

## 6.1   Introduction

The standard model is incomplete: it does not accommodate the observed baryon asymmetry and therefore new physics is required. Substantial effort has been devoted to constructing theories that dynamically generate this asymmetry and some prominent contenders include electroweak baryogenesis [109], thermal leptogenesis [54], and Affleck-Dine baryogenesis [71, 92]. This paper proposes a new mechanism, which we dub 'bubble baryogenesis'.

Like the Affleck-Dine mechanism, our setup employs a complex scalar baryon $\phi$, represented in a polar decomposition as

$$\phi(x) \;\; = \;\; R(x)e^{i\theta(x)}, \tag{6.1}$$

where $R(x)$ and $\theta(x)$ are four-dimensional real scalar fields. Under baryon-number transformations $U(1)_B$, $\phi$ rephases, $R$ is invariant, and $\theta$ shifts. The charge density of $\phi$ is identified with the number density of baryons

$$n_B \equiv \mathrm{Im}(\phi^* \dot{\phi}) = R^2 \dot{\theta}, \tag{6.2}$$

so a baryon asymmetry is present in field configurations that have 'angular momentum' in field space. Constraints on $B$ violation today imply that $\phi$ is currently at the origin of field space—so as not to spontaneously break $B$—and that the potential there has approximate $U(1)_B$—so as not to explicitly break it. In the early Universe, however, we take $\phi$ to be displaced from this minimum, to a place in the potential where $B$ violation is more substantial. The observed baryon asymmetry is dynamically generated during the field's journey towards the origin.

In the Affleck-Dine mechanism $\phi$ evolves *classically*, relaxing uniformly towards the $B$-symmetric minimum. $B$-violating potential terms torque $\phi$ during its evolution, and so instead of moving in a straight line through field space, $\phi$ takes a curved trajectory; $\phi$ develops non-zero $\dot{\theta}$ and consequently non-zero $B$. The phase transition from the $B$-violating vacuum in the past to the $B$-symmetric vacuum today is *second-order* or higher-order, and the end result is a *spatially homogeneous* condensate carrying a non-zero baryon asymmetry.

But what if there is no classical trajectory connecting $\phi$ to the symmetric minimum? Bubble baryogenesis occurs when $\phi$ evolves via *bubble nucleation*—either through quantum tunneling or thermal excitation. Spherical bubbles of true, $B$-symmetric vacuum nucleate inside the false $B$-violating background. The bubbles expand, collide, and eventually percolate; the phase transition completes when the entire Universe is in the $B$-symmetric phase. During this process, baryons are produced through two distinct mechanisms. First, just as $\phi$ receives a torque in Affleck-Dine, the instanton that mediates bubble nucleation also receives a torque from $B$-violating interactions. Consequently, the bubble wall takes a curved trajectory through field space, and it therefore accumulates $B$ as it expands. Second, when the bubble walls collide, $\phi$ can be excited back into a region of the potential where $B$-violating terms are large, generating additional baryon asymmetry. In bubble baryogenesis, the phase transition is *first-order*, and the end result is a *spatially inhomogeneous* distribution of baryons. After percolation, the baryon asymmetry is assimilated into the thermal plasma of the early Universe.

Like bubble baryogenesis, electroweak baryogenesis also relies on a first-order phase transition in the early Universe. In that case, however, the tunneling scalar is the Higgs field, and baryon number is generated indirectly through scattering off bubble walls.
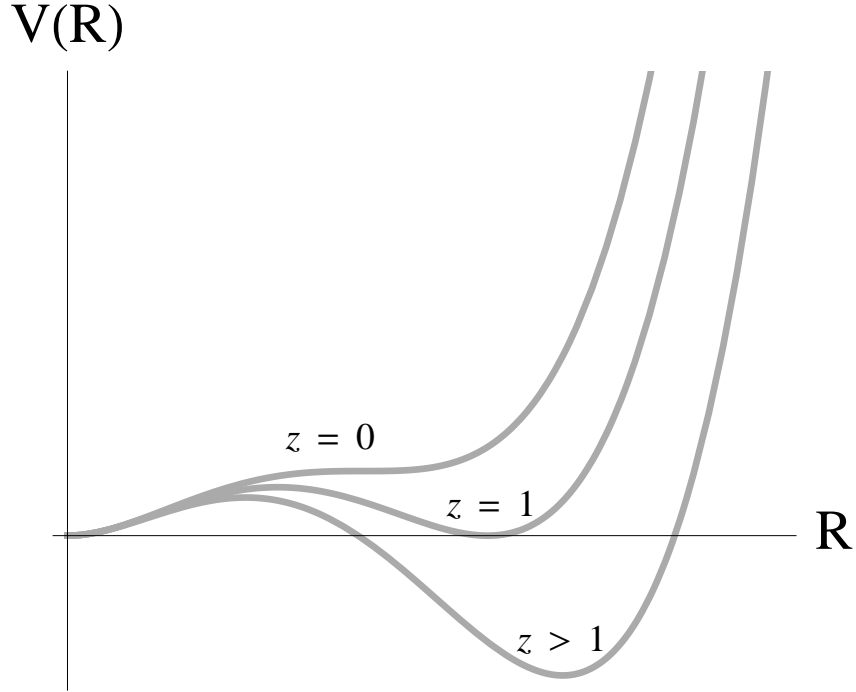
Figure 6.1: A potential that evolves with time so as to give a percolating first-order phase transition; the radial part of our potential has this behavior. We define a 'clock' parameter $z$ that indexes the shape of the potential. At early times, $z > 1$ and the true minimum is $B$-violating and at $\phi \neq 0$. At late times, $z < 0$ and the only minimum is $B$-symmetric and at $\phi = 0$. Vacuum decay is possible in the interval $1 > z > 0$.

## 6.2   General Considerations

Of the potential for the scalar baryon $V(\phi)$, we require two features: first, that it vary with time in such a way as to yield a percolating first-order phase transition in the early Universe; and second, that the potential accommodate explicit $B$- and $CP$-breaking dynamics. We discuss how these two criteria can be accommodated in Sec. 6.2.1 and Sec. 6.2.2, respectively. Afterwards, we tackle the dynamics of baryon production, which occurs at two times: first, at nucleation, which we discuss in Sec. 6.2.3; and second, at collision, which we discuss in Sec. 6.2.5. Once generated, the baryon asymmetry must persist, and migrate into the standard-model sector; we discuss the washout and decay of $\phi$ particles in Sec. 6.2.6.

### 6.2.1   Vacuum Structure and Tunneling

A potential that achieves a first-order phase transition must evolve with time as in Fig. 6.1. In the early Universe, the stable minimum is $B$-violating and at $\phi \neq 0$. As time evolves, the energy density of this $B$-breaking vacuum increases until it is

no longer the true vacuum; the lowest energy vacuum is now $B$-symmetric and at $\phi = 0$, and bubble nucleation begins. At even later times, the energy density in the $B$-breaking vacuum increases so much that the minimum disappears entirely, ensuring that no region of the Universe remains stuck there. For the transition to be first-order, the bubbles must percolate before this time.

It is convenient to introduce a dimensionless 'clock' parameter $z$ that characterizes the evolution of the potential. The two most important events—when the minima become degenerate and when the $B$-breaking minimum disappears—are taken to be at $z = 1$ and $z = 0$, respectively, as in Fig. 6.1. So,

$$
\begin{array}{rcll}
z & \geq 1 & \text{stable vacuum at } \phi \neq 0 \\
1 > & z & > 0 & \text{metastable vacuum at } \phi \neq 0 \\
0 \geq & z & & \text{no vacuum at } \phi \neq 0.
\end{array} \tag{6.3}
$$

In bubble baryogenesis, $z$ decreases monotonically; it is a reparameterization of time.

Bubble nucleation occurs in the window $1 > z > 0$. Tunneling is mediated by an instanton, a solution to the Euclidean equations of motion with a single negative mode. The rate per unit volume per unit time is given by

$$
\Gamma(z) \;=\; K(z)e^{-\Delta S(z)}, \tag{6.4}
$$

where $K$ is a determinant factor of order the characteristic mass scale of the potential to the fourth power, and $\Delta S$ is the difference in Euclidean action between the instanton and the false vacuum [42]. At $z = 1$, tunneling is forbidden, $\Delta S$ is divergent, and $\Gamma$ is zero. At $z = 0$, $\Delta S$ is zero and semiclassical tunneling through the barrier is overcome by classical evolution down the potential.

After nucleation, the energy difference across the bubble wall causes it to accelerate outward, rapidly approaching the speed of light. Bubbles nucleate, expand, and collide until—at percolation—the entire Universe is in the true vacuum. When does percolation occur?

Pick a point in space at time $z$. The expected number of bubbles $N$ that have overlapped this point is

$$
N(z) \sim \int_1^z V(z, z')\Gamma(z')\frac{dt}{dz'}dz', \tag{6.5}
$$

where $V(z, z')$ is the three-volume at time $z'$ of the past lightcone that emerged from our point in space at time $z$, and $dt/dz'$ is a Jacobian factor. The integrand therefore is the probability that a bubble nucleates at a time $z$ in the right position to convert our point to the true vacuum, and it is integrated over all past $z$. Percolation occurs at a time $z_*$ satisfying

$$
1 \sim N(z_*), \tag{6.6}
$$

so that at least one bubble has nucleated in the past lightcone of every point in space.
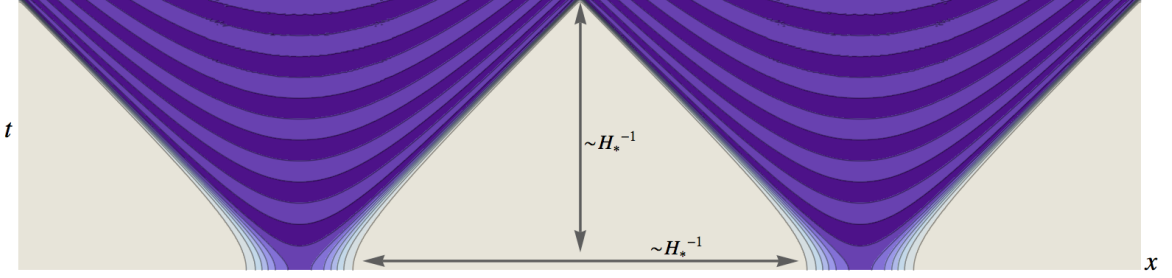
Figure 6.2: Depiction of a simplified bubble collision geometry. At percolation, there is typically one bubble per Hubble volume and the bubbles nucleated one Hubble time earlier. Since the surface area of a bubble scales as $H_*^{-2}$ and the volume scales as $H_*^{-3}$, the baryon number density scales as $H_*$.

As long as $z$ is changing slowly enough with time, then $N(z_*) \sim \Gamma_* H_*^{-4}$, where throughout the $*$ subscript will denote a quantity evaluated at $z = z_*$. The integral is dominated by values of $z$ close to $z_*$ and the percolation condition can be approximated by

$$\Gamma_* \sim H_*^4. \tag{6.7}$$

This means that bubbles typically nucleate one Hubble time before percolation, with roughly one bubble per Hubble volume at percolation, as shown in Fig. 6.2. Though some bubbles do nucleate before this time, the rate is too small to induce percolation.

A time-varying potential of the form in Fig. 6.1 can arise naturally in two ways, depending on whether percolation completes before or after reheating. If the phase transition occurs before reheating, then a direct coupling of the scalar baryon $\phi$ to the inflaton field will give rise to a time-dependent effective potential. This is the same type of coupling that is used to generate the evolving potential in the Affleck-Dine mechanism [93]. From an effective-field-theory standpoint, such couplings are mandatory unless forbidden by a symmetry, and while they are often non-renormalizable they can nonetheless play an essential role in the physics. In this scenario, the phase transition takes place between the end of inflation—so as not to dilute the baryons— and reheating. During this matter-dominated period the inflaton is oscillating about its minimum, but has not yet decayed to standard model particles.

If the phase transition occurs after reheating, then a direct coupling of $\phi$ to the big bang plasma will give rise to a time-dependent thermal correction to the effective potential. The same couplings that allow $\phi$ to decay—so that the baryon asymmetry can migrate to the standard model sector—can generate such terms. Note that similar thermal effects give rise to the first-order phase transition in electroweak baryogenesis [55], with the crucial difference that the relevant scalar field there, the Higgs boson, is not charged under $U(1)_B$. In electroweak baryogenesis the purpose of the first-order phase transition is merely to provide an out of equilibrium environment for particle and anti-particle scattering processes.

While bubble baryogenesis can occur in either scenario, the models we study in Sec. 6.3 and Sec. 6.4 are in the former category, where it is easier to suppress thermal washout.

## 6.2.2 $B$ and $CP$ Violation

The Sakharov conditions [104] state that successful baryogenesis requires both $B$- and $CP$-violating dynamics. Under $B$ and $CP$ transformations the angular field component transforms as

$$\theta \quad \xrightarrow{B} \quad \theta + \text{const} \tag{6.8}$$

$$\theta \quad \xrightarrow{CP} \quad -\theta. \tag{6.9}$$

By Eq. (6.8), $B$ violation requires a potential that violates the shift symmetry on $\theta$, i.e. carries explicit dependence on $\theta$. Such terms are necessary for asymmetry generation because in their absence the field has no reason to move in the $\theta$-direction of field space, so by Eq. (6.2) no asymmetry is produced. In the Affleck-Dine mechanism, these $B$-violating terms torque the field in the $\theta$-direction on its journey back to the origin; in bubble baryogenesis, they force the instanton, which solves the Euclidean equations of motion, to arc in the $\theta$-direction as a function of spacetime.

By Eq. (6.9), $CP$-violation requires either potential couplings with complex phases or spontaneous breaking by an initial $\phi$ localized at a $CP$-odd minimum. $CP$ violation is necessary for asymmetry generation because in its absence, though the potential can exert a torque, $\phi$'s trajectory is just as likely to curve in the $+\theta$-direction as it is to curve in the $-\theta$-direction. That is, in a $CP$-conserving theory, two $CP$-conjugate instantons contribute equally to the path integral. The percolating transition would therefore be comprised of an equal number of bubbles with positive and negative $B$, which average out to a $B$-symmetric Universe.

In general, it is useful to characterize the degree of $B$- and $CP$-violating effects with a dimensionless 'efficiency' parameter $\epsilon$ which is proportional to $B$- and $CP$-violating parameters in such a way that $n_B \propto \epsilon$. From an effective-field-theory perspective, $\epsilon \ll 1$ is technically natural, but $\epsilon \simeq 1$ is also allowed.

Bubble baryogenesis generates baryon asymmetry in two ways. First, the instanton itself is asymmetric, which manifests itself as a surface density of baryons on the bubble walls. Second, bubble collisions excite the field back into the $B$-violating region of the potential. The net number density of baryons is given by a sum

$$n_B \quad = \quad n_{B,\text{instanton}} + n_{B,\text{collision}}. \tag{6.10}$$

We will discuss the two contributions in detail in Sec. 6.2.3 and Sec. 6.2.5, respectively, and show that, for a broad class of models, both of these contributions scale as

$$n_{B,\text{instanton}} \sim n_{B,\text{collision}} \sim \epsilon R_{\text{F}}^2 H_*, \tag{6.11}$$
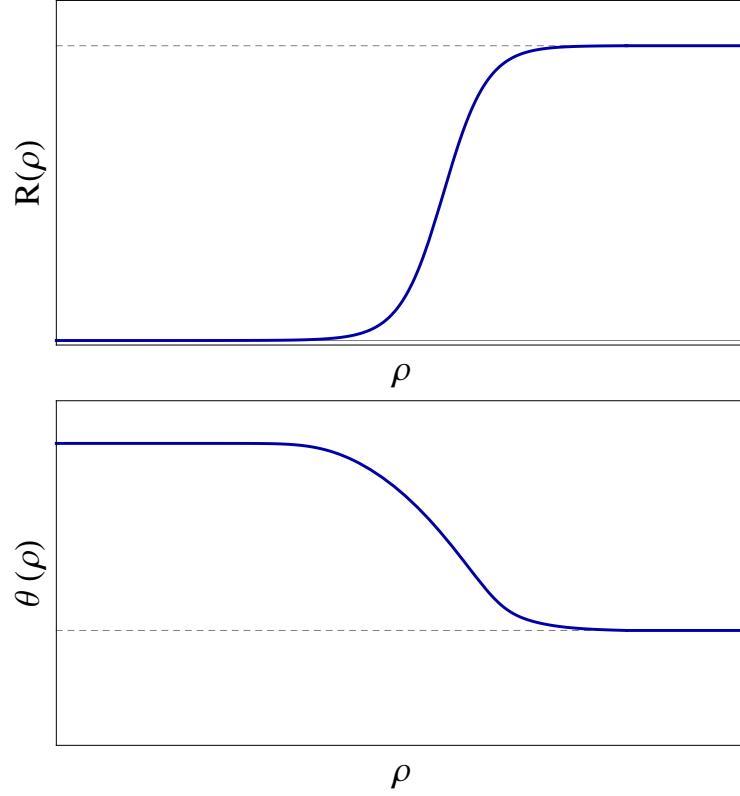
Figure 6.3: Sample instanton profiles for the fields $R$ and $\theta$ as a function of radial coordinate $\rho$ in a potential that breaks $U(1)_B$. False vacuum values for the fields are indicated with dashed gray lines; the true vacuum is at $R = 0$. The center of the bubble ($\rho = 0$) is on the left.

where $\epsilon$ is the dimensionless measure of $B$ and $CP$ violation, $R_{\rm F} = |\phi_{\rm F}|$ in the false vacuum, and $H_*$ is Hubble at the time of percolation.

## 6.2.3 Asymmetry Generation: Instanton

In the presence of $B$- and $CP$-violating potential terms, the instanton will arc in the $\theta$-direction. We are interested in computing both the net torque, which fixes the baryon asymmetry in the walls, and the bubble nucleation rate, which sets the percolation time $z_*$. For both reasons, we need to find the instanton, since it characterizes the most likely bubble configuration to nucleate, and gives the rate via Eq. (6.4). Assuming $SO(4)$ symmetry of the instanton, then the field components $R(\rho)$ and $\theta(\rho)$ are functions of the Euclidean radial variable $\rho$ alone, and the equations of motion
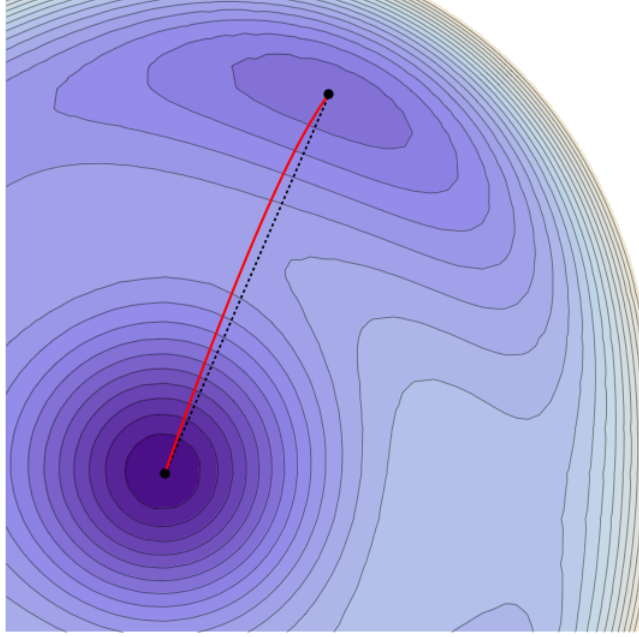
Figure 6.4: The trajectory (red) in field space taken by the Euclidean instanton solution of Fig. 6.3 overlayed on equipotential contours (purple) of the sample $U(1)_B$-violating potential. To guide the eye, we have drawn a straight dashed line connecting the true and false vacua. The trajectory taken by the field is not straight; it curves in the $\theta$-direction.

for the instanton are

$$R'' + \frac{3}{\rho}R' - R\theta'^2 = \frac{1}{2}\partial_R V \qquad (6.12)$$

$$\theta'' + \frac{3}{\rho}\theta' + 2\frac{R'}{R}\theta' = \frac{1}{2R^2}\partial_\theta V. \qquad (6.13)$$

Boundary conditions are regularity at the origin, so $R'(0) = \theta'(0) = 0$, and that far from the bubble the fields settle into their false vacuum values, so $R(\infty) = R_{\rm F}$ and $\theta(\infty) = \theta_{\rm F}$, where $\phi_{\rm F} = R_{\rm F}e^{i\theta_{\rm F}}$. Here, we are assuming that bubble nucleation happens by quantum tunneling through the potential barrier, as would be the case if percolation occurs before reheating. If instead, bubble nucleation occurs primarily by thermal activation over the potential barrier, then the Euclidean time coordinate is periodic, the $SO(4)$ symmetry becomes $SO(3) \times U(1)$, and the equations of motion change correspondingly [91].

The field value at the center of the bubble is near, but not exactly at, the true vacuum. Solutions are found by adjusting the field value at $\rho = 0$ so that the boundary conditions are satisfied at $\rho \to \infty$. A sample instanton, and its curved trajectory through field space, are shown in Figs. 6.3 and 6.4.

To estimate the extent of the curving, consider a simple potential set by only two parameters: $m$, the characteristic mass scale of the potential in the $R$-direction,
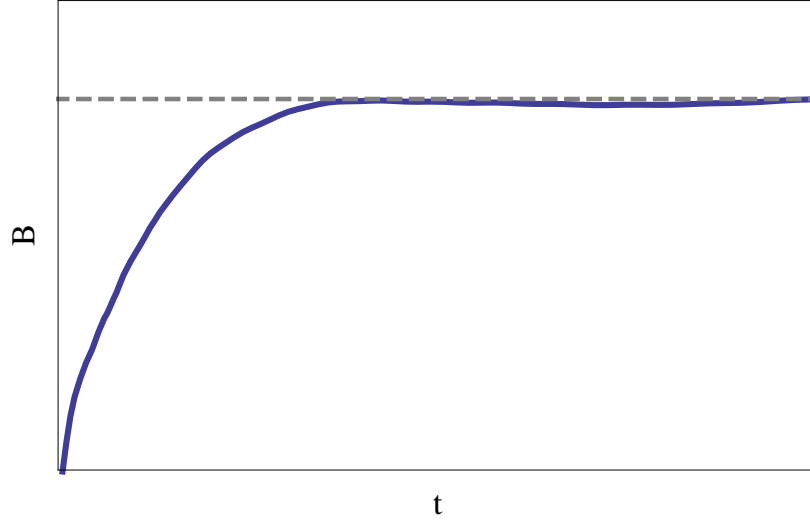
Figure 6.5: The total $B$ that results from a numeric simulation of an expanding 1+1-dimensional domain wall. At nucleation, the bubble wall has $B = 0$; but as the wall accelerates, $B$ rapidly asymptotes to $\mu^2$, indicated by the dashed gray line. In higher dimensions than 1+1, total $B$ would grow with the surface area of the bubble, but in 1+1-dimensions, 'surface area' is constant. The simulation was run in an expanding FRW background; gravitational expansion does not affect the value of $\mu^2$.

and $\epsilon$, a dimensionless parameter that characterizes the degree of the $B$-violation. Parametrically,

$$\epsilon \sim \frac{\partial_\theta V}{V}. \tag{6.14}$$

Because $m$ is the only dimensional parameter, $R_{\mathrm{F}} \sim m$, and the instanton solution varies in $\rho$ on scales of order $\rho \sim m^{-1}$. The parametric scaling of Eq. (6.13) is then such that

$$\theta'(\epsilon \sim m^{-1}) \quad \sim \quad \epsilon m \tag{6.15}$$
$$\Delta\theta \equiv \theta(\infty) - \theta(0) \quad \sim \quad \epsilon. \tag{6.16}$$

To determine the $\mathcal{O}(1)$ factors here requires finding the instantons numerically as above.

Given instanton profiles $R(\rho)$ and $\theta(\rho)$, the evolution of the bubble post nucleation follows from analytic continuation of the instanton from Euclidean to Minkowski signature. The typical size of a bubble at the time of nucleation is much smaller than Hubble, so we can ignore the expansion of the Universe and simply continue $\rho \to \sqrt{r^2 - t^2}$, where $r$ is the radial coordinate away from the center of the bubble, and $t$ is time. At nucleation, $t = 0$ and so $\rho = r$, and the field profile that nucleates is a slice through the center of the instanton.

Because the bubble nucleates at rest, $\dot{\theta} = B = 0$. However, as the wall accelerates outwards, spacetime points in the wall traverse an angle in field space $\Delta\theta$ in less and less time, so the baryon density inside the wall grows and grows. At the same time, as the bubble expands, the thickness of the wall becomes Lorentz contracted, so the baryon density is supported on a smaller and smaller region. As we will now show, these two effects cancel at late times, and the accelerating bubble wall asymptotes to a constant surface density $\mu^2$ of baryons.

To compute the baryon asymmetry contained in a single bubble wall, we integrate Eq. (6.2) on a fixed time slice $t = \tau$ long after nucleation

$$B_{\text{instanton}} = \int_{t=\tau} R^2 \dot{\theta} \, d^3 x. \tag{6.17}$$

Plugging in the analytically continued instanton profile $R(\rho)$ and $\theta(\rho)$, and using spherical symmetry, this becomes

$$
\begin{aligned}
B_{\text{instanton}} &= 4\pi \int_{\tau}^{\infty} R\left(\sqrt{r^2 - \tau^2}\right)^2 \dot{\theta}\left(\sqrt{r^2 - \tau^2}\right) r^2 dr \\
&= 4\pi \int_{0}^{\infty} -R(\rho)^2 \theta'(\rho) \tau \sqrt{\rho^2 + \tau^2} \, d\rho,
\end{aligned}
\tag{6.18}
$$

where the prime indicates a derivative with respect to $\rho$. In the first line, the integral is taken from $\tau$ to $\infty$ because analytic continuation of the instanton only gives the field profile outside of the light-cone; inside the light-cone, the field relaxes towards the $B$-symmetric minimum, producing negligible baryons. The second line is obtained by changing integration variable from $r$ to $\rho = \sqrt{r^2 - \tau^2}$. Lastly, we add the approximation that $\tau$ is a long time after nucleation, considerably bigger than the size of the bubble at nucleation. Since $R^2 \theta'$ dies off exponentially at large $\rho$, $\tau \gg \rho$ over the region where the integrand has support, and.

$$B_{\text{instanton}} \sim 4\pi\tau^2 \times \int_{0}^{\infty} -R(\rho)^2 \theta'(\rho) d\rho, \tag{6.19}$$

which is the bubble surface area at late times ($4\pi\tau^2$), multiplied by the number of baryons per surface area

$$\mu^2 \equiv \int_{0}^{\infty} -R(\rho)^2 \theta'(\rho) d\rho = \int_{F}^{T} R^2 d\theta, \tag{6.20}$$

Because it is a line integral along the instanton field trajectory, $\mu^2$ is constant in time. In the spirit of Eq. (6.15), a parametric estimate is that

$$\mu^2 \sim \epsilon R_{F}^2. \tag{6.21}$$

Note that the sign of $\mu^2$ depends on the direction in which $\theta$ arcs, which in turn depends on the imaginary phases in the potential.

Fig. 6.5 shows the total baryon number of a 1+1-dimensional expanding bubble. The stationary bubble wall carries zero baryon asymmetry, but as it accelerates up to the speed of light the number of baryons per surface area of the bubble wall grows and quickly asymptotes to $\mu^2$. The integrated number of baryons scales with the surface area; in 1+1 dimensions the 'wall' is point-like, and its 'surface area' is constant.

Though we derived Eq. (6.20) in flat space, it remains true in an FRW background. Expansion acts globally on the bubble, affecting the growth of proper surface area with time, but it does not act locally—because the bubble wall is much thinner than $H^{-1}$, the field profile is not significantly affected, and so $\mu^2$ remains as in Eq. (6.20). Though the scale factor $a(t)$ does modify the equation of motion, its effect is far smaller than the gradient and potential terms, which set the shape of the wall [17].

Because the baryon asymmetry scales with the surface area of the bubble wall rather than the volume, the baryon number density from a single bubble dilutes with time, vanishing as $\tau \to \infty$. The baryon asymmetry that is produced is carried away to infinity by the accelerating bubble walls. Thus, to explain the observed asymmetry, there must be many bubbles, and the bubbles must percolate—not only to ensure that $\phi$ is in the $B$-symmetric minimum today, but also to preserve the asymmetry we have generated from escaping to infinity.

At percolation, there is on average one bubble wall stretched across each Hubble volume. The expected number of baryons per Hubble volume at percolation, therefore, is the surface area of that wall $(\sim H_*^{-2})$ times the baryon surface density $(\mu^2)$. The number density of baryons right before collisions, therefore, scales like

$$n_{B,\text{instanton}} \sim \mu^2 \times H_* \sim \epsilon R_\text{F}^2 H_*. \tag{6.22}$$

In the next subsection, we will argue that these baryons are approximately conserved by the collision, so that this $n_{B,\text{instanton}}$ contributes directly to the total $n_B$ in Eq. (6.11).

## 6.2.4   Approximating the Instanton

Calculating the instanton for an arbitrary complex field potential is simplified given two simplifying assumptions. The first approximation is to take $\epsilon \ll 1$, in which case the potential takes the form

$$V(R,\theta) \;\; = \;\; V_0(R) + \epsilon V_1(R,\theta), \tag{6.23}$$

where $\theta$-dependence (and thus $B$-violation) enters only in $V_1$. As a result, Eqs. 6.12 and 6.13 admit a series solution

$$R(\rho) \;\; = \;\; R_0(\rho) + \epsilon R_1(\rho) + \cdots \tag{6.24}$$
$$\theta(\rho) \;\; = \;\; \theta_0(\rho) + \epsilon \theta_1(\rho) + \cdots, \tag{6.25}$$

where $\theta_0 = \theta_F$ is a constant. Then, $R_0(\rho)$ is the bubble wall profile in the symmetric potential, and its action sets the decay rate. The $R_0(\rho)$ profile can be plugged directly into Eq. (6.13) to give an equation for $\theta_1(\rho)$, and if necessary the process can be iterated. This is already a big simplification: the problem of finding one two-field instanton solution is replaced by the problem of finding two one-field instanton solutions.

Further simplification can be achieved by making a second approximation, the thin-wall approximation, which is valid when the two minima are nearly degenerate. In this case, the bubble wall profile becomes a step function: the interior is exactly in the true vacuum, the exterior is exactly in the false vacuum, and the transition happens sharply at a critical value of $\rho = \rho_0$. Because the wall is a localized object in the thin-wall approximation, we can define a surface tension for it,

$$\sigma = \int \sqrt{2V(\phi)}d\phi, \tag{6.26}$$

where the line integral is taken along a trajectory through field space connecting the true and false vacua; because $\epsilon \ll 1$, $\sigma$ is reasonably insensitive to the trajectory. The size of the bubble at nucleation is $3\sigma/\Delta V$, where $\Delta V = V_F - V_T$. The Euclidean action of the instanton (minus the Euclidean action of the false vacuum) is

$$\Delta S = \frac{27\pi^2}{2} \frac{\sigma^4}{\Delta V^3}. \tag{6.27}$$

Though the precise value of $\sigma$ is reasonably independent of the field trajectory, there is an optimal path, and it represents the bubble configuration most likely to nucleate. And even though the field profiles of $R$ and $\theta$ are both step functions in the thin-wall approximation, resolving the step with even infinitesimal thickness reveals that the field takes precisely this optimal trajectory $\theta(R)$ through field space. It can be found either by minimizing $\sigma$ in Eq. (6.26), or by plugging the series expansion into Eq. (6.12) and Eq. (6.13) with the added assumption that $R$ and $\theta$ only start to vary once $\rho$ is large. The resulting equation is

$$\theta''(R) - \frac{1}{R}\theta'(R) = \frac{1}{2}\left(R^2\frac{\partial_\theta V_1}{V_0} - \theta'(R)\frac{\partial_R V_0}{V_0}\right), \tag{6.28}$$

which is easy to integrate to give an approximate field trajectory through field space for any $V$.

## 6.2.5 Asymmetry Generation: Collisions

To gain insight into the dynamics of bubble collisions, we have run numeric simulations for a variety of different models. Specifically, we have studied the collisions of 1+1-dimensional bubble walls in an expanding, matter-dominated, FRW background
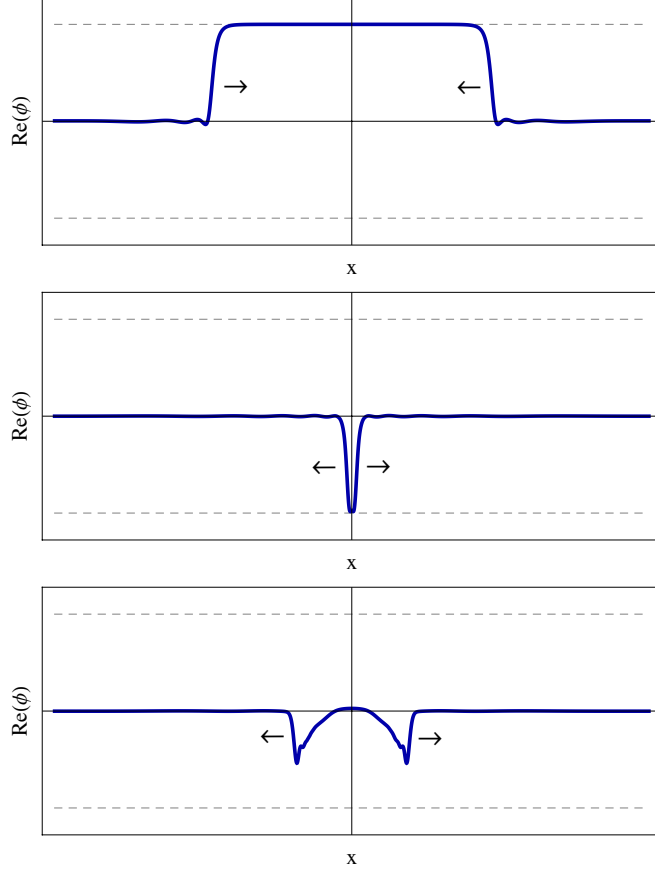
Figure 6.6: Sample field profiles of a collision event at three different times. The gray dashed lines indicate the value of $\pm\phi_{\mathrm{F}}$. Top panel: two boosted domain walls approach one another. Middle panel: as the walls pass, they solve the *free* wave equation, and so linearly superimpose; the walls pass through each other unimpeded and the field between is deposited at $-\phi_{\mathrm{F}}$. Bottom panel: on time scales of order $m^{-1}$, the field begins to respond to the potential. The field between the walls evolves back towards the true minimum, corresponding to behavior I in the text.

with scale factor $a(t)$ for an array of different potentials. The equation of motion for $\phi$, ignoring gravitational backreaction, is

$$\ddot{\phi} + 3H\dot{\phi} - \frac{\phi''}{a(t)^2} = -V'(\phi). \tag{6.29}$$

As initial conditions, we used the exact 1+1-dimensional instanton profiles.

The dynamics of Eq. (6.29) are complicated, but the moment of collision is simple. The colliding walls are relativistic—they are moving very fast and are very thin, by Lorentz contraction. This means that the time scale on which they cross is far smaller than both $H^{-1}$ (the time scale on which FRW expansion acts) and $m^{-1}$ (the time scale on which the potential acts). Gravity and the potential, therefore, can both be ignored, and the field approximately obeys the *free* wave equation $\ddot{\phi} - \phi'' = 0$, where

we have rescaled $x$ by $a(t)$ the time of collision. Linear superposition of waves is an exact solution to the free wave equation, so the impinging walls merely pass through one another, and the field in between is deposited at $-\phi_{\rm F}$, as shown in Fig. 6.6. This behavior is generic: as long as the walls are moving fast enough, the field value at the intersection of the walls is $-\phi_{\rm F}$, independent of the precise shape of the bubble wall or the structure of the potential.

On longer time scales, of order $m^{-1}$, linear superposition is no longer a good approximation and the field begins to evolve under the force of the potential. The field in between the crossed walls rolls down the potential and begins to oscillate around a local minimum. There are two behaviors, depending on which local minimum.

*I. Oscillation about the true minimum.* The field between the walls, deposited on the other side of the potential at $-\phi_F$, is no longer in a vacuum state; under the force of the potential, it evolves back towards the origin, as shown in the bottom panel of Fig. 6.6. By the time the field reaches the true minimum, it has lost enough kinetic energy to gradients and Hubble friction that it cannot escape; it oscillates, Hubble friction damps the oscillations, and eventually the field settles into the true minimum. Fig. 6.7 shows a collision that illustrates this behavior, and Fig. 6.8 depicts the corresponding baryon number density.

As the field at the collision site evolves back towards the origin, it moves through a $B$-violating region of the potential, so a second wave of baryon generation is taking place. Fig. 6.9 shows the integrated baryon number as a function of time, which in $d+1$-dimensions is

$$B(t) = a(t)^d \int n_B(t, x) \, d^d x. \tag{6.30}$$

Before the collision $B(t)$ was constant, as in Fig. 6.5, but it makes an abrupt jump upwards at the moment of collision. The evolution of the field from $-\phi_{\rm F}$ generates new baryons inside the collision lightcone, visible in Fig. 6.8. A simple estimate can be made for the baryon number generated during this evolution.

The process in which the field in the collision region evolves from $-\phi_{\rm F}$ to the origin can be thought of as a localized Affleck-Dine condensate forming and dissolving at the collision site. If the field takes a time $\Delta t$ to evolve from $-\phi_{\rm F}$ to 0, then the spatial width of this condensate is of order $\Delta t$, since the bubble walls propagate at nearly the speed of light. The Affleck-Dine mechanism, were it to occur in this potential, would generate a number density of baryons which scales like $R^2 \dot{\theta} \sim \epsilon R_{\rm F}^2 m$. Multiplying this by the width of the condensate and by the surface area of the collision site per unit volume at percolation $H_*$ gives the expected number density of baryons generated by the collision as

$$n_{B,\text{collision}} \sim \epsilon R_{\rm F}^2 m \times \Delta t H_* \sim \epsilon R_{\rm F}^2 H_*, \tag{6.31}$$

where $\Delta t \sim 1/m$ since $m$ is the characteristic scale of the potential. The contribution to $n_B$ from bubble collisions has the same parametric dependence as the contribution from the instanton.
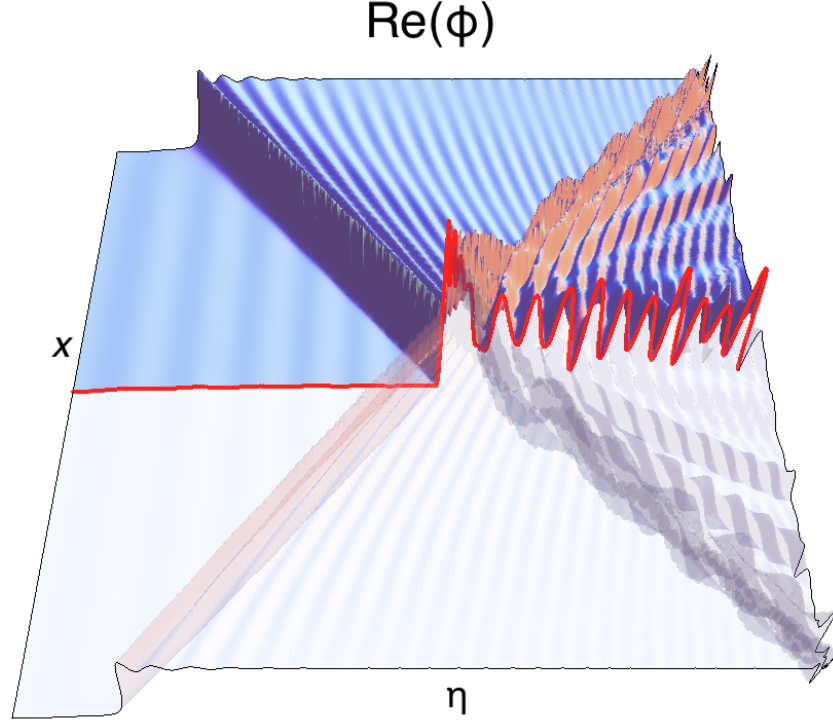
Figure 6.7: Re($\phi$) as function of space and conformal time $\eta$ during a bubble collision showing behavior I. Using conformal time ensures lightcones travel at 45 degrees. Domain walls separating the false and true vacua emerge from the top and bottom of the plot and collide at $x = 0$. The walls cross and the field is locally deposited at $-\phi_\mathrm{F}$, from which it evolves back toward the true vacuum. The value of Re($\phi(x = 0)$) is shown in red. Several localized field excitations related to oscillons are visible at late times.

After the collision, the energy in the field and the walls dissipates, and the asymmetry spreads; the way in which this happens is potential-dependent. Potentials which grow more slowly than quadratically at the origin, admit two related non-topological solitons that can temporarily trap energy and baryon number [72, 74]. Field excitations that move solely in the $\theta$-direction, locally orbiting the origin, are called $Q$-balls [43, 90]; their charge contributes a centrifugal term to their effective potential that makes them absolutely stable. Field excitation that move solely in the $R$-direction, locally oscillating along a line through the origin, are called oscillons [105]; these excitations are long-lived, but not eternal. Our collisions produce a hybrid: it oscillates predominantly in the $R$-direction, and can therefore be seen in Fig. 6.7, but it also carries non-zero baryon number, and can therefore be seen in Fig. 6.8. In other words, the field is locally executing very elliptical orbits about the origin. A number of these hybrids are visible: a stationary one emerges from the collision site, and several boosted ones fall off the wall as it propagates. Because these non-topological field configurations probe larger field amplitudes, they are still
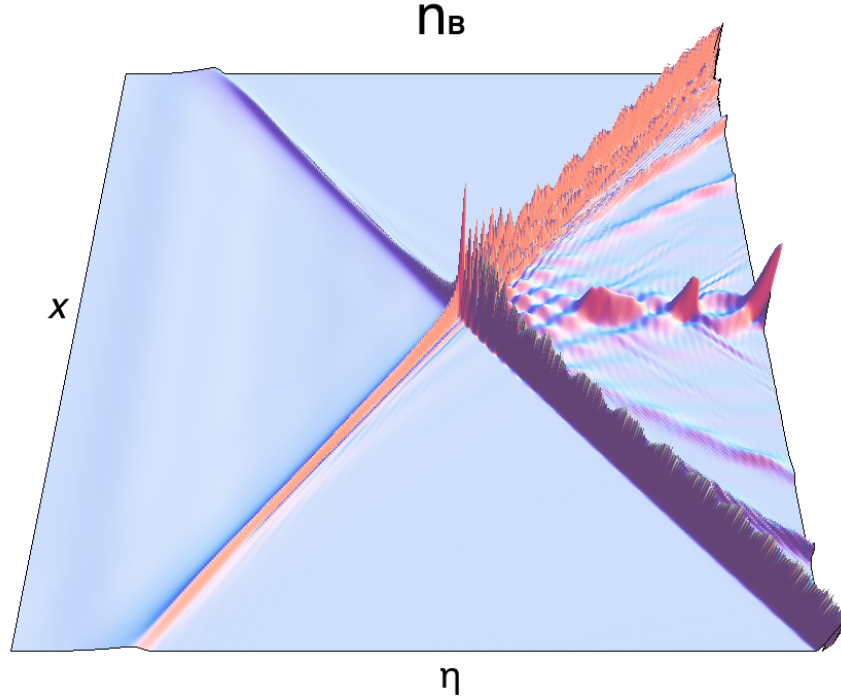
Figure 6.8: The baryon number density as a function of space and conformal time $\eta$ for the same collision as Fig. 6.7. Initially, the asymmetry is carried entirely on the walls; as they accelerate the baryon density at the center of the wall grows and the thickness of the wall shrinks. At the collision, the walls move through each other, roughly conserving baryon number, and the evolution of the field from $-\phi_{\mathrm{F}}$ back to the origin generates new baryons around $x = 0$. The oscillons of Fig. 6.7 carry non-zero $B$.

sensitive to $U(1)_B$ violation, as we discuss in the next subsection.

*II. Pockets of a false vacuum.* For certain potentials instead of oscillating around the true vacuum, the field at collision site ends up in a false vacuum. This can happen in two ways. First, if the potential at $-\phi_{\mathrm{F}}$ is very sloped, then the field can overshoot the true minimum and land back in the original false vacuum, as was noticed in the earliest simulations of bubble collisions [66]. Second, if the potential happens to have an additional local minimum at $-\phi_{\mathrm{F}}$, then the field never has to evolve anywhere, since it is already in a false vacuum [57]. The presence of an additional minimum at $-\phi_{\mathrm{F}}$ does not necessarily require tuning; potentials with approximate $U(1)_B$ have this feature automatically.

The false vacuum provides a locally stable state for the field, around which it can execute small oscillations. Though locally stable, the field does not remain in the false vacuum forever. The walls, moving away from the collision, now have true vacuum on the outside and false vacuum on the inside. This induces a pressure that pushes the walls back towards the collision site, so the walls eventually slow, turn around,
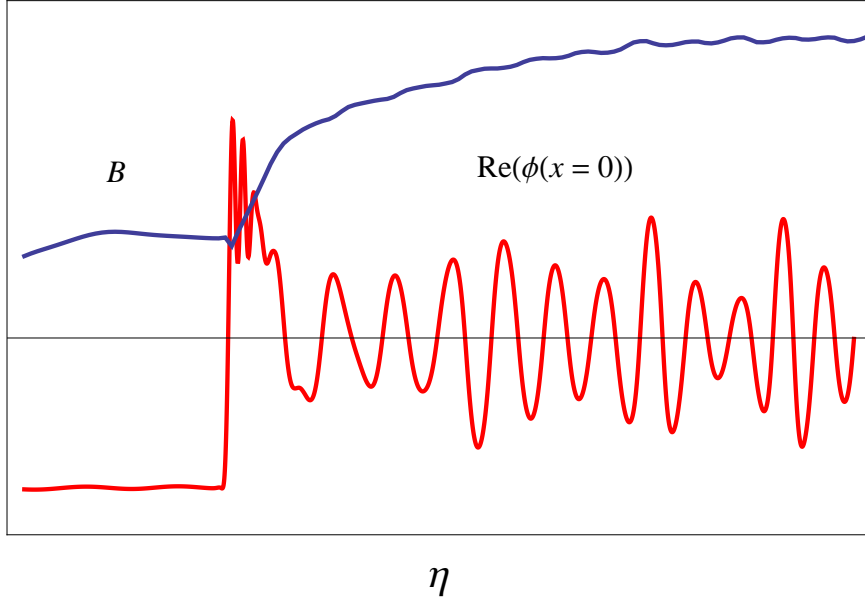
Figure 6.9: The total baryon number $B$ as a function of conformal time for the same collision as Fig. 6.7. Superimposed, in red, is a plot of $\text{Re}(\phi(x = 0))$ during the collision. $B$ is flat before the collision, as in Fig. 6.5. At the collision, the field is deposited at $-\phi_{\text{F}}$ and evolves back towards the origin; during that evolution, $B$ surges.

and re-cross on a time scale of order $H_*^{-1}$, which is far longer than the time scale of oscillations about the minimum. The formation and collapse of long-lived pockets of false vacuum is shown in Fig. 6.10. While the field lingers in the false vacuum, $B$ is not conserved, and the fact that the field is oscillating around the false vacuum can yield large fluctuations in the baryon asymmetry. In this case, the asymmetry is presumably still non-zero, but it is difficult to get an analytic handle on it, and numerical simulations are required.

For potentials with broken $U(1)_B$, there is no reason for $-\phi_{\text{F}}$ to be a local minimum, and the steepness of the potential at $-\phi_F$ determines which behavior occurs. For potentials with approximate $U(1)_B$, the physics depends on the nature of the false vacuum. When $-\phi_{\text{F}}$ has a strong basin of attraction, which happens at larger $z_*$, collisions tend to exhibit behavior II; when $-\phi_{\text{F}}$ has a weak basin of attraction, which happens at smaller $z_*$, collisions tend to exhibit behavior I. In the toy model of Sec. 6.3, percolation tends to happen at smaller $z_*$.

## 6.2.6   Washout and Decay

After percolation, a baryon asymmetry density of order $\sim \epsilon R_{\text{F}}^2 H_*$ is inhomogeneously distributed throughout the Universe in the form of the $\phi$ field. In order to explain observation, this asymmetry must persist and it must migrate to the standard-model sector.
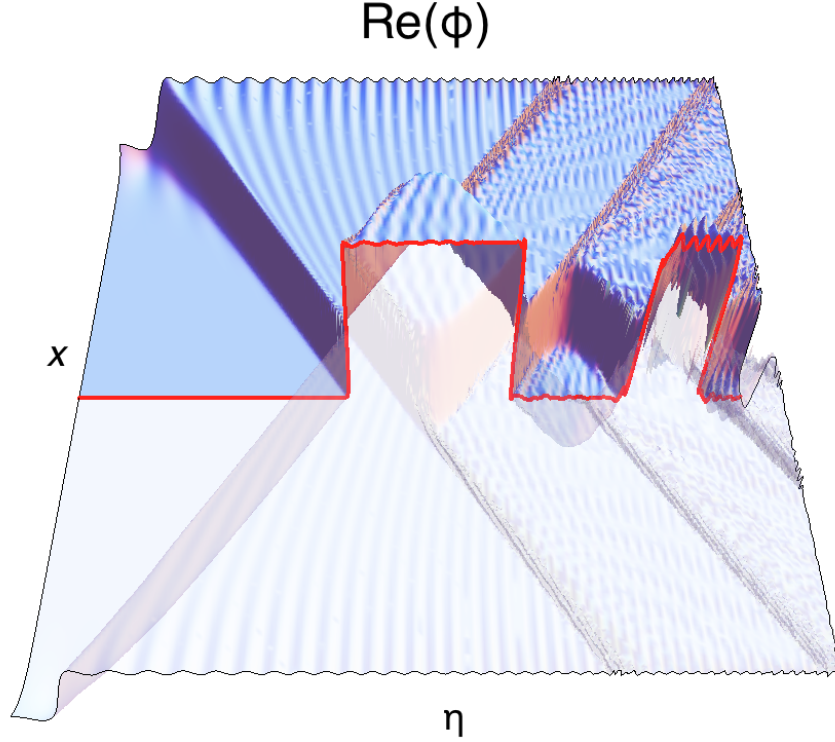
Re(φ)



Figure 6.10: Re($\phi$) as function of space and conformal time $\eta$ during a bubble collision showing behavior II. As in Fig. 6.7, domain walls separating the false and true vacua emerge from the top and bottom of the plot and collide at $x = 0$. At the collision, the field is deposited at $-\phi_{\mathrm{F}}$, which is another false vacuum of the theory. The field oscillates about this vacuum, while the bubble walls move outward, slow, turn around and re-cross. This process can occur several times.

For the asymmetry to persist, we must avoid two types of washout: classical and thermal. Classical washout refers to depletion of the asymmetry by evolution under the classical equations of motion from $B$-violating operators present in the early Universe. The dynamics of classical washout depend on the dimensionality of these operators. In the case of higher-dimension operators, washout can only be effective at large field values. But, since the expansion of the Universe and the growth of the bubble both tend to damp field excitations toward the origin, classical washout from higher-dimension interactions is typically evaded, as is true in the Affleck-Dine mechanism. In the case of marginal or super-renormalizable operators, classical washout may be active even as the fields damp to origin. Consider, for instance, the case in which the potential for $\phi$ near the origin is of the form $m^2(|\phi|^2 + \epsilon\phi^2 + \mathrm{h.c.})$, where $\epsilon$ is a dimensionless measure of $B$ violation. The $\epsilon$ term induces an 'ellipticity' to the potential that splits the mass eigenstates, causing the field to precess as it orbits the origin. The total baryon asymmetry, therefore, oscillates around its initial value. The frequency of these oscillations scales like $\sim (\epsilon m)^{-1}$. Whether the baryon number is spread out evenly, or localized in non-topological solitons, the effect

of classical washout is to make it oscillate.

For small $\epsilon$, this precession frequency is far lower than the characteristic oscillation time of the field $m^{-1}$; the field must sit at the origin through many oscillations if the asymmetry is to appreciably change. As long as the $\phi$ condensate decays before this time, the asymmetry is preserved. Besides, even if it does not decay in time, the asymmetry oscillates around its initial value, it does not damp; unless there is a conspiracy between the decay time and the oscillation time, the final asymmetry will be an $\mathcal{O}(1)$ fraction of the initial asymmetry. Alternatively, in certain models $B$-violation is $\mathcal{O}(1)$, in which case numerical simulation is necessary to evaluate the degree of washout.

Thermal washout refers to depletion of $B$ that occurs after the asymmetry is absorbed into the plasma of the early Universe, through scattering processes which involve $B$-violating interactions. Such scattering tends to restore chemical equilibrium and therefore deplete the asymmetry. Even if these interactions arise from higher-dimension operators, they can still be significant since the associated scattering rates grow with temperature. However, as we will discuss in Sec. 6.3, our models evade thermal washout because $B$-violation is sourced by interactions between $\phi$ and the inflaton. $B$-violation occurs when the temperature is small, before the inflaton has decayed; when the inflaton decays and the temperature becomes large, the $B$-violating interactions have shut off and the asymmetry is frozen in. Thermal washout is avoided because $B$-violating interactions and the thermal plasma are never present at the same time.

Finally, for the baryon asymmetry to migrate to the standard-model sector, the $\phi$ condensate must decay. A direct coupling of $\phi$ to some operator comprised of standard-model fields suffices to transfer the asymmetry; the decay rate of $\phi$ depends on the strength of this coupling. For homogenous fields, the decay rate of a condensate is more or less the same as the decay rate of $\phi$ quanta in the vacuum [96]. In bubble baryogenesis, however, the field configuration is highly inhomogeneous. In particular, because the bubble walls are boosted to near the speed of light shortly after nucleation, one might worry that these field fluctuations will be long-lived due to a Lorentz boost factor. However, as discussed earlier, after the collision these boosted field configurations are not solutions to the equations of motion so they broaden and dissolve. As the quanta become softer, they can decay. In certain models of bubble baryogenesis, the decay of $\phi$ can be very fast—much faster than the Hubble parameter at the time of percolation. In such cases, the $\phi$ condensate decays to particles nearly instantaneously after the nucleation event. Afterwards, there is no classical field, meaning classical washout is straightforwardly evaded.

# 6.3   Toy Model

Our discussion in Sec. 6.2 was framed rather broadly, so in this section we now study a concrete setup. A working model of bubble baryogenesis must accommodate the following criteria:

- Percolation. The Universe must efficiently transit from the false to true vacuum.

- Asymmetry. The theory parameters must accommodate the observed baryon asymmetry.

- Perturbativity. The effective couplings cannot blow up and all energy scales are bounded by the cutoff.

- No Washout. $B$-violating effects, classical or thermal, must be under control.

In this section we present a toy model which satisfies these criteria. As we will see, despite its simplicity the toy model may actually be phenomenologically viable.

## 6.3.1   Model Definition

Our toy model is defined by a potential of the form

$$V(R, \theta) = V_0(R) + \epsilon V_1(R, \theta), \tag{6.32}$$

where $\epsilon$ is a small parameter characterizing $B$- and $CP$- violating interactions. The $B$-symmetric part of the potential is

$$V_0 = m^2|\phi|^2 - A|\phi|^3 + \lambda|\phi|^4. \tag{6.33}$$

In general, the shape of the potential will vary in time due to couplings between $\phi$ and the inflaton $\chi$, whose vacuum expectation value is time-dependent. This occurs in Affleck-Dine models of baryogenesis, where such couplings induce Hubble-dependent parameters in the action. For simplicity, we take $\lambda$ and $A$ to be constant, but

$$m^2 = \tilde{m}^2 - \frac{\rho}{\Lambda^2}, \tag{6.34}$$

where $\rho = 3H^2 m_{\text{Pl}}^2$ is the energy density of the Universe. Here we require $\Lambda^2 > 0$ and $\tilde{m}^2 > 0$ so that $B$ is spontaneously broken at early times but restored in the present day. In a supersymmetric context, such a $\rho$ dependence would originate from $|\chi|^2|\phi|^2/\Lambda^2$ in the Kahler potential.

If the couplings between $\phi$ and $\chi$ are $B$- and $CP$-violating, then $V_1$ will also contain time-dependent terms. At least two $B$-breaking operators are required—otherwise all $CP$ phases can be removed by a field redefinition. As discussed in Sec. 6.2.6, if $B$ violation is higher-dimensional, e.g. $\phi^5$ and $\phi^6$, then explicit breaking is localized
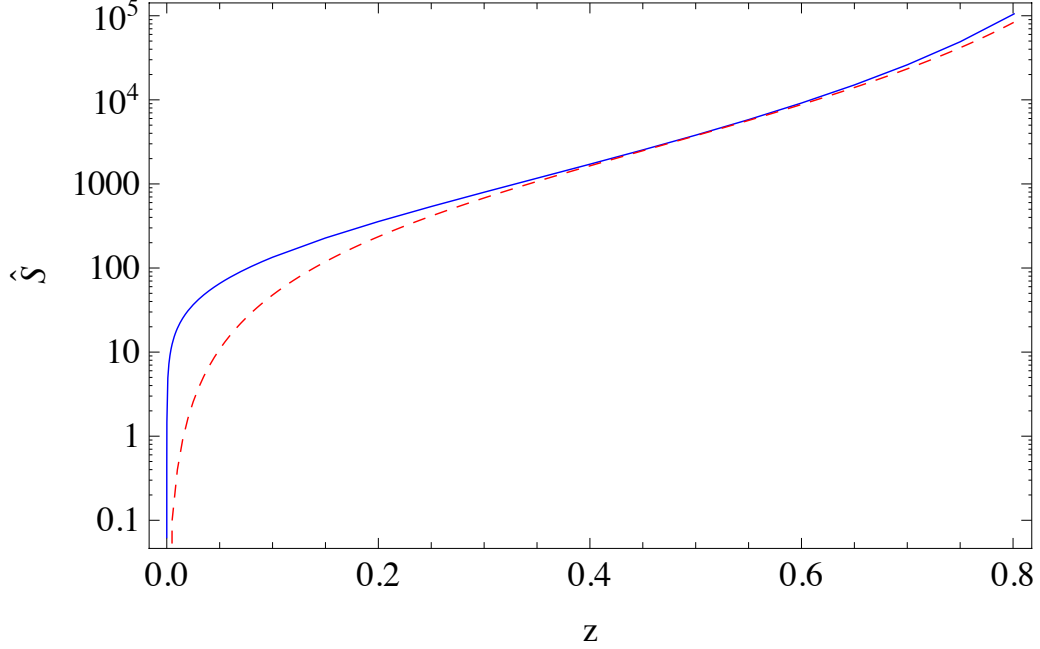
Figure 6.11: $\Delta\hat{S}(z)$ for the potential in Eq. (6.33), computed numerically (blue solid) and analytically in the thin-wall approximation (red dashed).

far from the origin and classical washout is ameliorated by Hubble damping of the field. In contrast, renormalizable $B$-violating operators, e.g. $\phi^2$ and $\phi^3$, typically mediate classical washout with model-dependent effects. Importantly, we assume that $B$-violating interactions are sourced by the inflaton alone, so $B$ is restored after reheating—thus, thermal washout is evaded. This setup can be easily engineered by invoking additional symmetries under which both $\phi$ and $\chi$ transform.

Let us outline the cosmological history of this model. We begin during inflation, when $H$ and therefore all model parameters are constant in time. During this epoch, $m^2 < 0$ and the field resides at $\phi \neq 0$. After inflation ends, the inflaton starts to oscillate around its minimum and the Universe shifts from vacuum-energy domination to matter domination. As $H$ decreases, $m^2$ eventually becomes positive, growing monotonically until the $\phi \neq 0$ vacuum becomes metastable. Once the nucleation rate rises sufficiently, percolation occurs. The $B$- and $CP$-violating interactions in the potential cause the nucleated bubble walls to accumulate baryons; subsequent bubble collisions yield an additional asymmetry component.

In the subsequent sections, we will analyze the vacuum structure, nucleation rate, and asymmetry generation in this model.

## 6.3.2   The Instanton

Neglecting effects proportional to $\epsilon$, the Euclidean action for this theory is

$$S \;=\; 2\pi^2 \int \rho^3 d\rho \left[ \left( \frac{\partial R}{\partial \rho} \right)^2 + m^2 R^2 - AR^3 + \lambda^2 R^4 \right].$$

(6.35)

While the model parameters vary in time, they do so on scales $H \ll 1/m$, so we treat them as constant in our analysis of the instanton. It is convenient to transform to dimensionless variables,

$$\begin{aligned}
S &= \hat{S}/\lambda^2 \\
R &= \hat{R}m/\lambda \\
A &= \hat{A}m\lambda \\
\rho &= \hat{\rho}/m,
\end{aligned}$$

(6.36)

where

$$\hat{S} \;=\; 2\pi^2 \int \hat{\rho}^3 d\hat{\rho} \left[ \left( \frac{\partial \hat{R}}{\partial \hat{\rho}} \right)^2 + \hat{R}^2 - \hat{A}\hat{R}^3 + \hat{R}^4 \right].$$

(6.37)

As a result of our change of variables, the rescaled Euclidean action $\hat{S}$ is a function of $\hat{A}$ alone.

As discussed in Sec. 6.2.1, the variable $z$ is a convenient reparametrization of time in which $1 > z > 0$ corresponds to the epoch in which tunneling is allowed. We can express $\hat{A}$ in terms of $z$ as

$$\hat{A}(z) \;=\; \sqrt{32/9} + z(2 - \sqrt{32/9}),$$

(6.38)

where $1 > z > 0$ maps onto the range $2 > \hat{A} > \sqrt{32/9}$. Within this interval, there is a true and false vacuum located at

$$\hat{R}_{\mathrm{T}} = 0 \quad , \quad \hat{R}_{\mathrm{F}} = \frac{3\hat{A}}{8} \left( 1 - \sqrt{1 - \frac{32}{9\hat{A}^2}} \right).$$

(6.39)

Next, we evaluate $\Delta\hat{S}$ by solving the associated Euclidean equation of motion for an $SO(4)$ symmetric ansatz $\hat{R}$ subject to the initial condition $\partial\hat{R}/\partial\hat{\rho} = 0$ at $\hat{\rho} = 0$. Solving for $\Delta\hat{S}$ numerically, we find that for $z \lesssim 0.25$, $\Delta\hat{S}$ is very well fitted by the function

$$\Delta\hat{S} \;=\; 431.5 z^{0.679} + 8139.4 z^{2.27}$$

(6.40)

As $z \to 0$ the phase transition shifts from first-order to second-order. As $z \to 1$ the bubble becomes thin-walled. From Fig. 6.11, it is clear that our numerics agree with analytic expressions in this regime.

The determinant prefactor can also be straightforwardly estimated. From [25] we can compute the $K$ factor in Eq. (6.4)

$$K = \frac{\Delta S^2}{4\pi^2} \left| \frac{\det'(-\Box + V''(\phi(\rho)))}{\det(-\Box + V''(\phi_{\mathrm{F}}))} \right|^{-1/2} \tag{6.41}$$

$$\sim \frac{\Delta \hat{S}^2 m^4}{4\pi^2 \lambda^4}, \tag{6.42}$$

where $\phi(\rho)$ is the instanton solution and $\det'$ indicates the determinant with zero modes removed. In the second line we used that $\rho$ varies on scales of order $m^{-1}$ to estimate the determinant factors.

Up till now we have neglected $B$- and $CP$-violating effects proportional to $\epsilon$. Employing our numerical code, we have generated instanton profiles for the potential at finite $\epsilon$. Given these numerical solutions, we can compute $\mu^2$, defined in Eq. (6.20) as the measure of the baryon asymmetry in the bubble wall. As shown in Fig. 6.12, at small $\epsilon$, these numerical results match the simple estimate for $\mu^2$ described in Eq. (6.21).

### 6.3.3 Before Percolation

Consider the cosmological history of this model leading up to percolation. As shown in Sec. 6.3.2, the vacuum structure of the theory depends solely on $\hat{A}$, which varies in time with the energy density, $\rho$. Shortly after inflation, $m^2 < 0$ and the potential has a single minimum at large field values. As the universe cools, eventually $m^2 > 0$ and an additional local minimum forms at the origin—at this point $\hat{A}$ is divergent. As $m^2$ continues to increase, $\hat{A}$ monotonically decreases, and a first-order phase transition becomes possible in the window $2 > \hat{A} > \sqrt{32/9}$.

Plugging $\rho = 3H^2 m_{\mathrm{Pl}}^2$ into Eq. (6.38) and Eq. (6.34), we obtain expressions for the important physical quantities as a function of $z$,

$$m(z) = \frac{A}{\lambda \hat{A}(z)} \tag{6.43}$$

$$H(z) = \frac{\Lambda \sqrt{\tilde{m}^2 - m(z)^2}}{\sqrt{3} m_{\mathrm{Pl}}}, \tag{6.44}$$

where $\hat{A}(z)$ is defined in Eq. (6.38). Given the parametric dependences in Eq. (6.44), it is clear that during the first-order phase transition, the dimensionful parameters, $H$, $m$, and $A$ are all well below the cutoff $\Lambda$ and so the effective theory description remains valid.
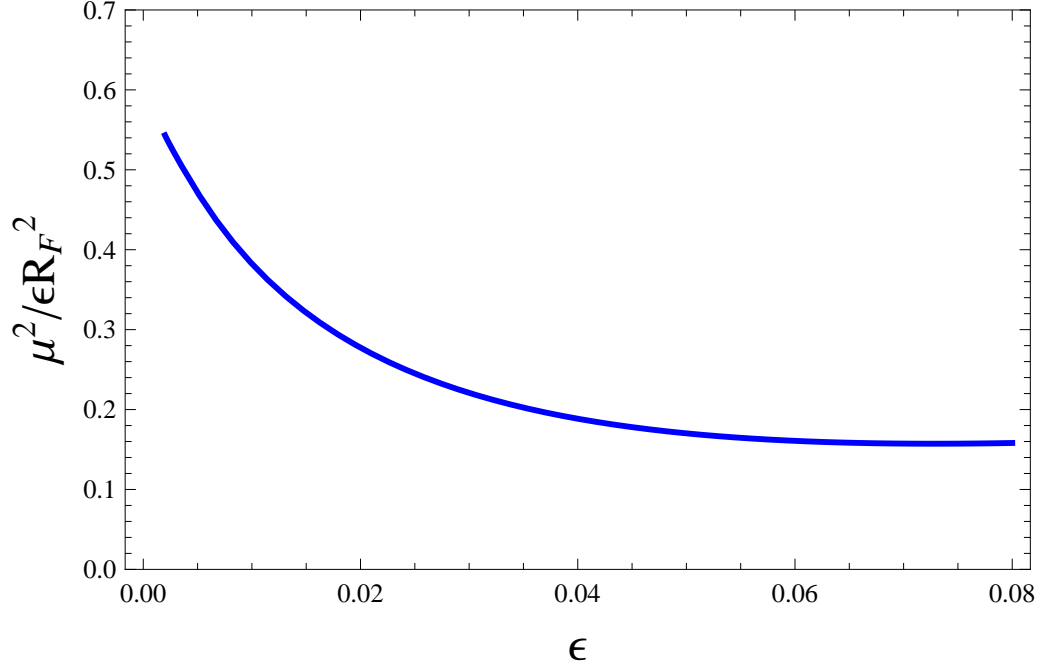
Figure 6.12: Plot of the exact value for $\mu^2$ divided by our parametric estimate, $\epsilon R_{\mathrm{F}}^2$—the answers agree within $\mathcal{O}(1)$ factors. Here we used $V_0$ corresponding to $z = 0.2$ and $V_1 = R^2 \cos(2\theta + \pi/4) + R^3 \cos(3\theta)$.

Eventually, the universe cools sufficiently that Hubble decreases enough that there is a first-order phase transition. Percolation occurs when Eq. (6.6) is satisfied, which is roughly when $\Gamma_* \simeq H_*^4$; in the context of our model this approximation is accurate to $\lesssim 15\%$. Recall that $\Gamma_*$ implicitly depends on $z_*$ through the model parameters in Eq. (6.44). The criterion for percolation can be rewritten as

$$H_*^4 \;=\; \frac{\Delta S_*^2 m_*^4}{4\pi^2} e^{-\Delta S_*}. \tag{6.45}$$

The exponential factor essentially fixes the solution to this equation, and so the prefactors are only logarithmically important. Solving for $S_*$ yields

$$\Delta S_* \;=\; \log\left(\frac{9 m_{\mathrm{Pl}}^4 \Delta S_*^2}{4\pi^2 \Lambda^4 (1 - \tilde{m}^2/m_*^2)^2}\right) \tag{6.46}$$

$$\sim\; 4\log\left(\frac{m_{\mathrm{Pl}}}{\Lambda}\right), \tag{6.47}$$

where the ellipses denote logarithms of $\mathcal{O}(1)$ numbers. If $S_* \ll 1$, then the nucleation rate is very high at the onset of percolation, indicating that the phase transition is bordering on second order. While this is not necessarily bad in and of itself, in this regime $\phi$ evolves like a slow roll Affleck-Dine condensate. Of course, we will be

interested in the first-order regime, whereby tunneling is the dominant mode of the phase transition. To achieve this, we require a modestly sized instanton action, so $\Lambda \ll m_{\text{Pl}}$, which is to say that the higher dimension operators coupling the inflaton to $\phi$ cannot be Planck slop operators, and must be suppressed by a lower scale.

In this toy model $z_\star$ is typically small and we are in the weakly first-order regime. Allowing both $A$ and $\lambda$ to also vary with time can yield any value of $z_\star$ between 0 and 1.

## 6.3.4 After Percolation

Once percolation occurs, bubbles of true vacua nucleate and soon fill the volume of space. Using Eq. (6.21), which applies for $\epsilon \ll 1$, we find that the surface density of baryons on the walls is

$$\mu_*^2 \sim \frac{\epsilon m_*^2 \hat{R}_{\text{F}*}^2}{\lambda^2}. \tag{6.48}$$

The total baryon number density $n_B$ arising from the initial instanton plus the subsequent bubble collisions is given in Eq. (6.11). To compute the observed baryon asymmetry today, we need to consider the remainder of the cosmological history. Because the inflaton sources the $B$- and $CP$- violating interactions of $\phi$, we require that the decay of the inflaton, and thus reheating, occur after the percolating phase transition. Consequently, the asymmetric yield at the time of reheating is given by

$$\eta_B \;\equiv\; \frac{n_B}{s_R} \frac{H_{\text{R}}^2}{H_*^2} \tag{6.49}$$

$$\sim \; \frac{\sqrt{3}\epsilon m_* T_{\text{R}} \hat{R}_{\text{F}*}^2}{4\lambda^2 m_{\text{Pl}} \Lambda \sqrt{\tilde{m}^2/m_*^2 - 1}}, \tag{6.50}$$

where $H_{\text{R}}$ and $T_{\text{R}}$ are the Hubble parameter and the temperature, respectively, at the time of reheating. The above estimates neglect the effects of classical washout, but as discussed in Sec. 6.2.6 these effects are expected to change the asymmetry by an $\mathcal{O}(1)$ fraction and are model-dependent.

To accommodate the present day observed baryon asymmetry, we require that $\eta_B \sim 6 \times 10^{-10}$. The energy density of the Universe at reheating is bounded from above by the energy density at percolation, so $T_{\text{R}}^4 \sim \rho_{\text{R}} \lesssim \rho_*$. In turn, this places an absolute upper limit on $\eta_B$ from Eq. (6.50). Given the observed baryon asymmetry, this upper bound can be rephrased as a lower bound on $\tilde{m}$ in terms of the other fundamental parameters

$$\tilde{m} \;\gtrsim\; \Lambda \left( \frac{10^{10} \text{ GeV} \times \lambda^2}{\epsilon \Lambda} \right)^{2/3}, \tag{6.51}$$
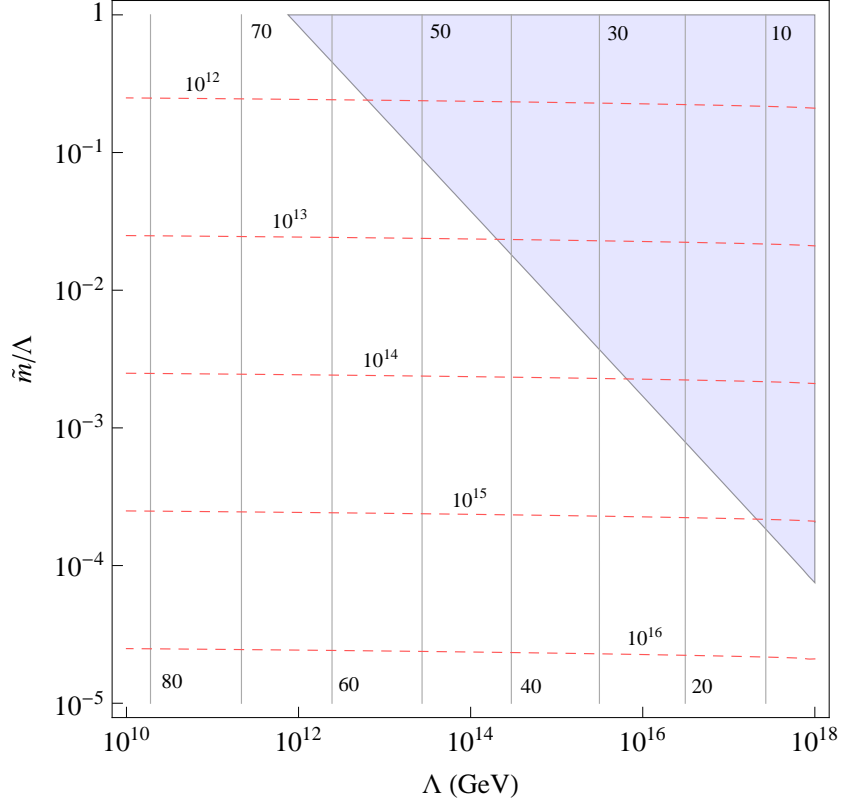
Figure 6.13: Parameter space for the toy model, fixing $\eta_B$ to the observed baryon asymmetry today. The blue region depicts the allowed region after requiring that reheating occurs after percolation, $\rho_{\rm R} \lesssim \rho_*$. The red dotted lines are contours of $T_{\rm R}$ and the solid gray lines are contours of $\Delta S_*$. We have fixed $\lambda = 1$, $\epsilon = 0.1$, $\tilde{m} = A$.

where for simplicity we have dropped the $\mathcal{O}(1)$ factors from the $z_*$ dependence. This limit is a substantial constraint on $\tilde{m}$ in this toy theory, and is depicted in the blue region of Fig. 6.13.

Next, we briefly discuss how the asymmetric yield in Eq. (6.50) is actually transferred from $\phi$ into standard model fields. In a supersymmetric context this is achieved, for example, by the operator $UDD/M$ in the superpotential, where $M$ is the mass scale of some connector field which has been integrated out. This is the lowest-dimension operator which can link standard model $B$ to a gauge singlet field $\phi$. Given this operator, the field $\phi$ has a decay rate of

$$\Gamma(\phi \to qqq) \quad \sim \quad \frac{1}{128\pi^3} \frac{m^3}{M^2}, \tag{6.52}$$

which can be much greater than $H_*$, the Hubble parameter at the time of percolation. In this case the $\phi$ field within each bubble of nucleated true vacuum decays very shortly after percolation. Classical washout from $B$-violating interactions are thus minimized since $\phi$ decays so fast into particle quanta. Alternatively, fast decays

can occur if $\phi$ decays promptly to additional non-gauge-singlet particles which in turn decay to standard model fields. Finally, while our discussion thus far has been framed within the context of $B$, the asymmetry can of course be converted into $L$ via the operators $\phi L H_u$, $\phi L L E$, or $\phi Q L D$, or into a dark matter asymmetry via similar interactions.

## 6.4  More Realistic Models

In this section we discuss possible realizations of bubble baryogenesis in more realistic contexts. The examples here are supersymmetric, but we emphasize that this is not a requirement for bubble baryogenesis.

### 6.4.1  Neutrino Seesaw

Consider the MSSM augmented by a supersymmetric neutrino seesaw. The superpotential is

$$W \;=\; \lambda L H_u N + \frac{1}{2} M N^2, \tag{6.53}$$

where $N$ denotes the sterile neutrinos and we have suppressed all flavor indices. Explicit violation of $U(1)_L$ is present in the form of the mass parameter, $M$. Integrating out the heavy $N$ fields yields the active neutrino masses, whose sum is bounded by cosmological measurements to be less than 0.17 eV [106]. Requiring that $\lambda \lesssim 1$ implies that $M \lesssim 10^{14}$ GeV.

The supersymmetric $F$-term and $D$-term contributions to the potential are

$$\begin{aligned}
V_F &= |\lambda H_u N|^2 + |\lambda L N|^2 + |\lambda L H_u + M N|^2 \\
V_D &= \frac{g'^2 + g^2}{8}(|H_u|^2 - |L|^2)^2. 
\end{aligned} \tag{6.54}$$

If supersymmetry breaking approximately preserves $L$, then the corresponding contributions to the potential are of the form

$$\tilde{V} \;=\; \tilde{V}_0 + \epsilon \tilde{V}_1 \tag{6.55}$$

where $\epsilon$ is small and

$$\begin{aligned}
\tilde{V}_0 &= m_L^2 |L|^2 + m_N^2 |N|^2 + m_{H_u}^2 |H_u|^2 \\
&\quad + A L H_u N + \text{h.c.} 
\end{aligned} \tag{6.56}$$

Because the parameters in $\tilde{V}$ acquire contributions from both zero-temperature supersymmetry breaking and Hubble-induced supersymmetry breaking, they are in general

time-dependent. Which specific contributions arise depends on the symmetry structure of the ultraviolet theory, which dictates the coupling between the MSSM fields, the inflaton, and the supersymmetry breaking sector. For instance, if the inflaton carries $R$-parity, then $L$-violating terms like $LH_u$ or $N^3$ could be present in $\tilde{V}_1$.

The scalar potential is complicated, and contains a large number of fields and parameters. However, it is clear that all the required features of bubble baryogenesis are present. First, the $A$ parameter may be large in the early Universe and produce global minima far from the origin of field space. Second, these $B$-breaking vacua are stabilized by the quartic $\lambda$ which can be $\mathcal{O}(1)$ in order to achieve a sufficiently large nucleation rate. Third, $L$- and $CP$-violating interactions can torque the Euclidean instanton solution during a first-order phase transition. Hence, we do not expect bubble baryogenesis in this potential to differ in any qualitative way from the toy model in Sec. 6.3.

A complete analysis of the multi-field potential of the supersymmetric neutrino seesaw would be non-trivial. However, we take note of certain simplifications to the theory which can reduce the potential to a solvable one. In particular, the lepton flavor indices serve largely to complicate the analysis, so the potential is greatly simplified by taking a single flavor of $L$ and $N$ to be the only fields active in the dynamics. Furthermore, the $D$-term contribution in Eq. (6.54) tends to fix $|L| = |H_u|$, which effectively eliminates another set of field directions.

## 6.4.2   Color-Breaking Minima

Bubble baryogenesis may also be possible within the context of tunneling from color-breaking minima [4] to the electroweak vacuum within the MSSM. If supersymmetry-breaking $A$-terms are too large, then deep minima can form at field values away from the origin, inducing an instability for the electroweak vacuum. The vacuum dynamics are dominated by the field directions of the top squark and the Higgses, where the superpotential is dominated by the usual top quark Yukawa coupling,

$$W = \lambda_3 Q_3 H_u U_3. \tag{6.57}$$

Given approximately $B$-symmetric supersymmetry breaking, the corresponding terms in the potential are as in Eq. (6.55) but with

$$\begin{aligned} \tilde{V}_0 &= m_{Q_3}^2 |Q_3|^2 + m_{U_3}^2 |U_3|^2 + m_{H_u}^2 |H_u|^2 \\ &\quad + A_3 Q_3 H_u U_3 + \text{h.c.} \end{aligned} \tag{6.58}$$

Considering the $D$-flat field direction $|Q_3| = |U_3| = |H_u|$, then the absence of color-breaking minima implies that

$$A_3^2 \le 3\lambda_3^2 (m_{Q_3}^2 + m_{U_3}^2 + m_{H_u}^2), \tag{6.59}$$

if the electroweak vacuum is to be absolutely stable.

For our purposes we take the opposite tack—we want the electroweak vacuum to be unstable in the early Universe. Couplings to the inflaton can be easily arranged so that Eq. (6.59) fails in the early Universe, so that the fields reside in the true, color-breaking vacuum. As the Universe cools, Eq. (6.59) is eventually satisfied, and the fields can tunnel from the color-breaking minimum to the electroweak vacuum.

Of course, to generate a baryon asymmetry, this phase transition requires $B$- and $CP$-violating interactions. The natural candidate for this is the Hubble-induced cubic term, $U_i D_j D_k$, whose coupling can carry non-zero $CP$ phases. Because this operator involves multiple squark flavors, we are then required to understand the tunneling from the color-breaking minimum in other squark directions besides the stop. We leave a proper analysis of this scenario for future work.

## 6.5   Observational Consequences

The byproduct of bubble baryogenesis is a frothy mixture of standard model baryons, inhomogeneously distributed in the early Universe. This inhomogeneity provides a potentially dangerous relic, since the observed baryon density is known to be homogeneous at the epoch of big bang nucleosynthesis (BBN). *On average*, inhomogeneities are small at BBN: the percolating bubbles have a length scale set by $H_*^{-1}$, which is far smaller than $(a_*/a_{\mathrm{BBN}})H_{\mathrm{BBN}}^{-1}$, the size of an inhomogeneity at percolation that would grow to be Hubble size at BBN. The potentially dangerous relic doesn't come from the average bubble, it comes from the rare bubble that nucleates early enough and avoids enough collisions to grow big by percolation. Constraints from big bubbles were studied in [94] in the context of extended inflation [89], which also features a first-order transition around the end of inflation. Though the context was different, the constraints are purely geometrical, so the analysis in [94] carries over. Big bubbles constrain the decay rate considerably before percolation to be small, so that big bubbles are exceedingly unlikely. Bubble baryogenesis is aided in avoiding this constraint by the fact that the nucleation rate can be completely shut off at early times.

Constraints aside, the first-order phase transition also opens up new observational signatures, like gravitational waves. Bubble collisions are an efficient producer of gravitational waves; numeric estimates in [87] show that as much as .1% of the energy released in the transition can end up in gravitational waves. Unfortunately, the energy for us is small—most of the energy density of the Universe is in the inflaton—but the gravitational waves have a distinct signature which may make observation feasible. Because the colliding bubbles at percolation have roughly the same size, the gravitational wave spectrum has a spike at $H_*$ [108]. This observational signature is distinct from Affleck-Dine.

Additionally, black holes might form at the collision sites. This is an intriguing possibility, because a current tension in the data of the mass distribution of early

quasars would be alleviated by a source of primordial 'seed' black holes [112]. Also, because these black holes form with a characteristic size, there could be a second bump in the gravitational wave spectrum from their coincident evaporation.

Lastly, as we discussed in Sec. 6.2.5, bubble collisions can spawn non-topological solitons, like oscillons and $Q$-balls. Oscillons, though long-lived, are not typically stable on present Hubble time-scales [49, 6, 5]; they radiate energy and dissociate. $Q$-balls, on the other hand, can be stable and persist since they are charge-stabilized [41, 88]. In Affleck-Dine baryogenesis, $Q$-balls typically form in gauge-mediated theories [79], and may or may not form in gravity-mediated theories, depending on the supersymmetric spectrum [78]. Analogous statements are likely true for bubble baryogenesis. If $Q$-balls form, their subsequent evolution is model-dependent: $Q$-balls that carry $B$ will be absolutely stable if their mass-to-baryon-charge ratio is smaller than that of a proton; $Q$-balls that carry $L$, however, typically decay, since the mass-to-lepton-charge ratio of the neutrino is so small.

## 6.6 Future Directions

Bubble baryogenesis is a novel scheme for the generation of the cosmological baryon asymmetry. A scalar baryon undergoes a first-order phase transition in the early Universe, and a baryon asymmetry is generated by the process of bubble nucleation and the subsequent bubble collisions. We have presented an explicit toy model to illustrate the basic features of the mechanism, and introduced a handful of realistic models. In addition to fleshing out these more realistic theories, there exists a variety of interesting directions for future work.

First, in Sec. 6.2.3, we argued that a single bubble could never explain the observed baryon asymmetry because the baryons are carried away to infinity. This is not strictly true: a loophole is provided in theories with large extra dimensions—the same loophole that boom-and-bust inflation [23] exploits to provide a graceful exit to old inflation. If a bubble nucleates smaller than the size of the extra dimensions, then as it grows, it wraps the extra dimension and collides with itself on the other side. The bubble wall no longer runs off to infinity; the self-collision preserves the baryons in the wall, and distributes them uniformly throughout the interior of the bubble.

Second, as we discussed in Sec. 6.2.1 there is the possibility of bubble baryogenesis after reheating. Thermal effects from the big-bang plasma can induce time-dependent couplings which give rise to a first-order phase transition; the thermal plasma also assists the transition by enhancing the nucleation rate. To achieve such a scenario requires engineering the appropriate thermal potential and avoiding thermal washout.

Third, models considered in this paper had only a single instanton mediating decay, which imposed a relationship between the efficiency of the phase transition and the resulting asymmetry. This need not be the case. Consider a true and false vacuum connected by two instantons: a dominant one that is purely radial so that it

generates zero baryons, and a subdominant one that arcs so that it alone is responsible for generating baryons. Physically, this would correspond to a percolating phase transition in which the vast majority of nucleated bubbles are $B$-symmetric, but some small fraction are asymmetric. The smallness of the asymmetry in such an example would arise not from small $\epsilon$, but from the exponential suppression of the subdominant instanton. Such a model may suffer from fine-tuning issues because the baryon asymmetry would be so sensitive to the Euclidean action of the subdominant instanton.

Finally, in recent years there has been a resurgence of interest in so-called asymmetric dark matter, where the dynamics of baryogenesis and dark matter genesis are linked. Such a linkage can arise naturally in hidden-sector theories in which dark matter has a $U(1)_{\rm DM}$, and can have phenomenological signatures distinct from standard weakly interacting dark matter. A modification of bubble baryogenesis can achieve simultaneous generation of baryons and dark matter by extending the symmetry structure to $U(1)_B \times U(1)_{\rm DM}$.

# Bibliography

[1] Searching for Stopped Gluinos during Beam-off Periods at CMS. CMS-PAS-EXO-09-00, 2009.

[2] Georges Aad et al. Combined search for the Standard Model Higgs boson using up to 4.9 fb$^{-1}$ of $pp$ collision data at $\sqrt{s} = 7$ TeV with the ATLAS detector at the LHC. *Phys.Lett.*, B710:49–66, 2012.

[3] Nobutaka Abe, Takeo Moroi, and Masahiro Yamaguchi. Anomaly mediated supersymmetry breaking with axion. *JHEP*, 0201:010, 2002.

[4] S.A. Abel and Carlos A. Savoy. Charge and color breaking constraints in the MSSM with nonuniversal SUSY breaking. *Phys.Lett.*, B444:119–126, 1998.

[5] Mustafa A. Amin, Richard Easther, Hal Finkel, Raphael Flauger, and Mark P. Hertzberg. Oscillons After Inflation. *Phys.Rev.Lett.*, 108:241302, 2012.

[6] Mustafa A. Amin and David Shirokoff. Flat-top oscillons in an expanding universe. *Phys.Rev.*, D81:085045, 2010.

[7] N. Arkani-Hamed, A. Delgado, and G.F. Giudice. The Well-tempered neutralino. *Nucl.Phys.*, B741:108–130, 2006.

[8] N. Arkani-Hamed, S. Dimopoulos, G.F. Giudice, and A. Romanino. Aspects of split supersymmetry. *Nucl.Phys.*, B709:3–46, 2005.

[9] Nima Arkani-Hamed and Savas Dimopoulos. Supersymmetric unification without low energy supersymmetry and signatures for fine-tuning at the LHC. *JHEP*, 0506:073, 2005.

[10] Nima Arkani-Hamed and Neal Weiner. LHC Signals for a SuperUnified Theory of Dark Matter. *JHEP*, 0812:104, 2008.

[11] A. Arvanitaki, S. Dimopoulos, A. Pierce, S. Rajendran, and Jay G. Wacker. Stopping gluinos. *Phys.Rev.*, D76:055007, 2007.

[12] Shoji Asai, Koichi Hamaguchi, and Satoshi Shirai. Measuring lifetimes of long-lived charged massive particles stopped in LHC detectors. *Phys.Rev.Lett.*, 103:141803, 2009.

[13] T. Asaka and T. Yanagida. Solving the gravitino problem by axino. *Phys.Lett.*, B494:297–301, 2000.

[14] Takehiko Asaka, Koji Ishiwata, and Takeo Moroi. Right-handed sneutrino as cold dark matter of the universe. *AIP Conf.Proc.*, 903:16–23, 2007.

[15] K.S. Babu, Ilia Gogoladze, and Kai Wang. Stabilizing the axion by discrete gauge symmetries. *Phys.Lett.*, B560:214–222, 2003.

[16] Edward A. Baltz, Marco Battaglia, Michael E. Peskin, and Tommer Wizansky. Determination of dark matter properties at high-energy colliders. *Phys.Rev.*, D74:103521, 2006.

[17] R. Basu and A. Vilenkin. Evolution of topological defects during inflation. *Phys.Rev*, D50:7150, 1994.

[18] Matthew Baumgart, Clifford Cheung, Joshua T. Ruderman, Lian-Tao Wang, and Itay Yavin. Non-Abelian Dark Sectors and Their Collider Signatures. *JHEP*, 0904:014, 2009.

[19] M. Bolz, A. Brandenburg, and W. Buchmuller. Thermal production of gravitinos. *Nucl.Phys.*, B606:518–544, 2001.

[20] Raphael Bousso, Roni Harnik, Graham D. Kribs, and Gilad Perez. Predicting the Cosmological Constant from the Causal Entropic Principle. *Phys.Rev.*, D76:043513, 2007.

[21] Raphael Bousso, Stefan Leichenauer, and Vladimir Rosenhaus. Light-sheets and AdS/CFT. *Phys.Rev.*, D86:046009, 2012.

[22] A. Brandenburg, L. Covi, K. Hamaguchi, L. Roszkowski, and F.D. Steffen. Signatures of axinos and gravitinos at colliders. *Phys.Lett.*, B617:99–111, 2005.

[23] Adam R. Brown. Boom and Bust Inflation: a Graceful Exit via Compact Extra Dimensions. *Phys.Rev.Lett.*, 101:221302, 2008.

[24] Wilfried Buchmuller, Koichi Hamaguchi, Michael Ratz, and Tsutomu Yanagida. Supergravity at colliders. *Phys.Lett.*, B588:90–98, 2004.

[25] Jr. Callan, Curtis G. and Sidney R. Coleman. The Fate of the False Vacuum. 2. First Quantum Corrections. *Phys.Rev.*, D16:1762–1768, 1977.

[26] Spencer Chang and Markus A. Luty. Displaced Dark Matter at Colliders. arXiv:0906.5013 [hep-ph].

[27] Serguei Chatrchyan et al. Combined results of searches for the standard model Higgs boson in $pp$ collisions at $\sqrt{s} = 7$ TeV. *Phys.Lett.*, B710:26–48, 2012.

[28] Clifford Cheung. Axion Protection from Flavor. *JHEP*, 1006:074, 2010.

[29] Clifford Cheung, Alex Dahlen, and Gilly Elor. Bubble Baryogenesis. *JHEP*, 1209:073, 2012.

[30] Clifford Cheung, Gilly Elor, and Lawrence Hall. Gravitino Freeze-In. *Phys.Rev.*, D84:115021, Copyright 2011 by the American Physical Society.

[31] Clifford Cheung, Gilly Elor, and Lawrence J. Hall. The Cosmological Axino Problem. *Phys.Rev.*, D85:015008, Copyright 2012 by the American Physical Society.

[32] Clifford Cheung, Gilly Elor, Lawrence J. Hall, and Piyush Kumar. Origins of Hidden Sector Dark Matter II: Collider Physics. *JHEP*, 1103:085, 2011.

[33] Clifford Cheung, Lawrence J. Hall, and David Pinner. Seesaw Spectroscopy at Colliders. arXiv:1103.3520 [hep-ph].

[34] Clifford Cheung, Jeremy Mardon, Yasunori Nomura, and Jesse Thaler. A Definitive Signal of Multiple Supersymmetry Breaking. *JHEP*, 1007:035, 2010.

[35] Clifford Cheung and Yasunori Nomura. Singlet Portal to the Hidden Sector. *JHEP*, 1011:103, 2010.

[36] Clifford Cheung, Yasunori Nomura, and Jesse Thaler. Goldstini. *JHEP*, 1003:073, 2010.

[37] Clifford Cheung, Joshua T. Ruderman, Lian-Tao Wang, and Itay Yavin. Kinetic Mixing as the Origin of Light Dark Scales. *Phys.Rev.*, D80:035008, 2009.

[38] Clifford Cheung, Joshua T. Ruderman, Lian-Tao Wang, and Itay Yavin. Lepton Jets in (Supersymmetric) Electroweak Processes. *JHEP*, 1004:116, 2010.

[39] Kiwoon Choi, Kwang Sik Jeong, Wan-Il Park, and Chang Sub Shin. Thermal inflation and baryogenesis in heavy gravitino scenario. *JCAP*, 0911:018, 2009.

[40] E.J. Chun and A. Lukas. Axino mass in supergravity models. *Phys.Lett.*, B357:43–50, 1995.

[41] Andrew G. Cohen, Sidney R. Coleman, Howard Georgi, and Aneesh Manohar. THE EVAPORATION OF Q BALLS. *Nucl.Phys.*, B272:301, 1986.

[42] S. Coleman. Fate of the false vacuum: Semiclassical theory. *Phys.Rev.*, D15:10, 1977.

[43] S. R. Coleman. Q balls. *Nucl.Phys*, B262:263, 1985.

[44] Laura Covi. Axinos as Cold Dark Matter. *AIP Conf.Proc.*, 878:145–151, 2006.

[45] Alex G. Dias, V. Pleitez, and M.D. Tonasse. Naturally light invisible axion and local Z(13) x Z(3) symmetries. *Phys.Rev.*, D69:015007, 2004.

[46] Michael Dine, Willy Fischler, and Mark Srednicki. A Simple Solution to the Strong CP Problem with a Harmless Axion. *Phys.Lett.*, B104:199, 1981.

[47] Michael Dine and John D. Mason. Dynamical Supersymmetry Breaking and Low Energy Gauge Mediation. *Phys.Rev.*, D78:055013, 2008.

[48] C. Amsler et al. Review of particle physics. *Phys.Lett*, B667:1, 2008.

[49] E. Farhi, N. Graham, Alan H. Guth, N. Iqbal, R.R. Rosales, et al. Emergence of Oscillons in an Expanding Background. *Phys.Rev.*, D77:085019, 2008.

[50] Jonathan L. Feng, Arvind Rajaraman, and Fumihiro Takayama. SuperWIMP dark matter signals from the early universe. *Phys.Rev.*, D68:063504, 2003.

[51] Jonathan L. Feng, Shu-fang Su, and Fumihiro Takayama. SuperWIMP gravitino dark matter from slepton and sneutrino decays. *Phys.Rev.*, D70:063514, 2004.

[52] Jonathan L. Feng, Shufang Su, and Fumihiro Takayama. Supergravity with a gravitino LSP. *Phys.Rev.*, D70:075019, 2004.

[53] Jonathan L. Feng, Huitzu Tu, and Hai-Bo Yu. Thermal Relics in Hidden Sectors. *JCAP*, 0810:043, 2008.

[54] M. Fukugita and T. Yanagida. Baryogenesis without grand unification. *Phys.Lett.*, B174:45, 1986.

[55] L. J. Hall G. W. Anderson. Electroweak phase transition and baryogenesis. *Phys.Rev.*, D44:8, 1992.

[56] Howard M. Georgi, Lawrence J. Hall, and Mark B. Wise. GRAND UNIFIED MODELS WITH AN AUTOMATIC PECCEI-QUINN SYMMETRY. *Nucl.Phys.*, B192:409, 1981.

[57] Jr Giblin, John T., Lam Hui, Eugene A. Lim, and I-Sheng Yang. How to Run Through Walls: Dynamics of Bubble and Soliton Collisions. *Phys.Rev.*, D82:045019, 2010.

[58] Gian F. Giudice, Markus A. Luty, Hitoshi Murayama, and Riccardo Rattazzi. Gaugino mass without singlets. *JHEP*, 9812:027, 1998.

[59] S.L. Glashow. POSITRONIUM VERSUS THE MIRROR UNIVERSE. *Phys.Lett.*, B167:35, 1986.

[60] Toru Goto and Masahiro Yamaguchi. Is axino dark matter possible in supergravity? *Phys.Lett.*, B276:103–107, 1992.

[61] Yuval Grossman, Tamar Kashti, Yosef Nir, and Esteban Roulet. New ways to soft leptogenesis. *JHEP*, 0411:080, 2004.

[62] Alan H. Guth. Eternal inflation. astro-ph/0101507.

[63] Lawrence J. Hall, Karsten Jedamzik, John March-Russell, and Stephen M. West. Freeze-In Production of FIMP Dark Matter. *JHEP*, 1003:080, 2010.

[64] Lawrence J. Hall, John March-Russell, and Stephen M. West. A Unified Theory of Matter Genesis: Asymmetric Freeze-In. arXiv:1010.0245 [hep-ph].

[65] Koichi Hamaguchi, Yoshitaka Kuno, Tsuyoshi Nakaya, and Mihoko M. Nojiri. A Study of late decaying charged particles at future colliders. *Phys.Rev.*, D70:115007, 2004.

[66] S.W. Hawking, I.G. Moss, and J.M. Stewart. Bubble Collisions in the Very Early Universe. *Phys.Rev.*, D26:2681, 1982.

[67] Tetsutaro Higaki and Ryuichiro Kitano. On Supersymmetric Effective Theories of Axion. *Phys.Rev.*, D86:075027, 2012.

[68] G. Hinshaw, D. Larson, E. Komatsu, D.N. Spergel, C.L. Bennett, et al. Nine-Year Wilkinson Microwave Anisotropy Probe (WMAP) Observations: Cosmological Parameter Results. 2012.

[69] Bob Holdom. Two U(1)'s and Epsilon Charge Shifts. *Phys.Lett.*, B166:196, 1986.

[70] Richard Holman, Stephen D.H. Hsu, Thomas W. Kephart, Edward W. Kolb, Richard Watkins, et al. Solutions to the strong CP problem in a world with gravity. *Phys.Lett.*, B282:132–136, 1992.

[71] M. Dine I. Affleck. A new mechanism for baryogenesis. *Nucl.Phys.*, B249:361, 1985.

[72] M. Khlopov I. Dymnikova, L. Koziel and S. Rubin. Quasilumps from first order phase transitions. *Grav.Cosmol*, 6:311, 2000.

[73] Alejandro Ibarra. Indirect Signatures of Gravitino Dark Matter. *AIP Conf.Proc.*, 1078:122–127, 2009.

[74] Matthew C. Johnson, Hiranya V. Peiris, and Luis Lehner. Determining the outcome of cosmic bubble collisions in full General Relativity. *Phys.Rev.*, D85:083516, 2012.

[75] Renata Kallosh, Andrei D. Linde, Dmitri A. Linde, and Leonard Susskind. Gravity and global symmetries. *Phys.Rev.*, D52:912–935, 1995.

[76] Marc Kamionkowski and John March-Russell. Planck scale physics and the Peccei-Quinn mechanism. *Phys.Lett.*, B282:137–141, 1992.

[77] David E. Kaplan, Markus A. Luty, and Kathryn M. Zurek. Asymmetric Dark Matter. *Phys.Rev.*, D79:115016, 2009.

[78] S. Kasuya and M. Kawasaki. Q Ball formation in the gravity mediated SUSY breaking scenario. *Phys.Rev.*, D62:023512, 2000.

[79] S. Kasuya and M. Kawasaki. Q ball formation: Obstacle to Affleck-Dine baryogenesis in the gauge mediated SUSY breaking? *Phys.Rev.*, D64:123515, 2001.

[80] Masahiro Kawasaki, Kazunori Kohri, Takeo Moroi, and Akira Yotsuyanagi. Big-Bang Nucleosynthesis and Gravitino. *Phys.Rev.*, D78:065011, 2008.

[81] Masahiro Kawasaki, Kazunori Nakayama, and Masato Senami. Cosmological implications of supersymmetric axion models. *JCAP*, 0803:009, 2008.

[82] Vardan Khachatryan et al. Search for Stopped Gluinos in $pp$ collisions at $\sqrt{s} = 7$ TeV. *Phys.Rev.Lett.*, 106:011801, 2011.

[83] Jihn E. Kim. The Axino - gravitino cosmology. astro-ph/9711310.

[84] Jihn E. Kim. Weak Interaction Singlet and Strong CP Invariance. *Phys.Rev.Lett.*, 43:103, 1979.

[85] S.F. King and J.P. Roberts. Natural implementation of neutralino dark matter. *JHEP*, 0609:036, 2006.

[86] E.W. Kolb and M.S. Turner. *The Early Universe*. Addison-Wesley, Reading, Massachusetts, 1990.

[87] Arthur Kosowsky, Michael S. Turner, and Richard Watkins. Gravitational radiation from colliding vacuum bubbles. *Phys.Rev.*, D45:4514–4535, 1992.

[88] Alexander Kusenko and Mikhail E. Shaposhnikov. Supersymmetric Q balls as dark matter. *Phys.Lett.*, B418:46–54, 1998.

[89] Daile La and Paul J. Steinhardt. Extended Inflationary Cosmology. *Phys.Rev.Lett.*, 62:376, 1989.

[90] T.D. Lee. Nontopological Solitons. CO-2271-76, 1976.

[91] A. D. Linde. Fate of the false vacuum at finite temperature: Theory and applications. *Phys.Lett*, B199:37–40, 1981.

[92] A. Kusenko M. Dine. The origin of the matter - antimatter asymmetry. *Rev.Mod.Phys.*, 76:1, 2004.

[93] S. D. Thomas M. Dine, L. Randall. Supersymmetry breaking in the early universe. *Phys.Rev.Lett*, 75:398–401, 1995.

[94] L. M. Widrow M. S. Turner, E. J. Weinberg. *Phys.Rev*, D46:2384, 1992.

[95] Stephen P. Martin. A Supersymmetry primer. hep-ph/9709356.

[96] Shigeki Matsumoto and Takeo Moroi. Decay of scalar condensation in quantum field theory. *Phys.Rev.*, D77:045014, 2008.

[97] Patrick Meade, Michele Papucci, and Tomer Volansky. Odd Tracks at Hadron Colliders. *Phys.Rev.Lett.*, 109:031801, 2012.

[98] Patrick Meade, Matthew Reece, and David Shih. Long-Lived Neutralino NLSPs. *JHEP*, 1010:067, 2010.

[99] T. Moroi, H. Murayama, and Masahiro Yamaguchi. Cosmological constraints on the light stable gravitino. *Phys.Lett.*, B303:289–294, 1993.

[100] R.D. Peccei and Helen R. Quinn. CP Conservation in the Presence of Instantons. *Phys.Rev.Lett.*, 38:1440–1443, 1977.

[101] Maxim Pospelov, Adam Ritz, and Mikhail B. Voloshin. Secluded WIMP Dark Matter. *Phys.Lett.*, B662:53–61, 2008.

[102] Lisa Randall and Raman Sundrum. A Large mass hierarchy from a small extra dimension. *Phys.Rev.Lett.*, 83:3370–3373, 1999.

[103] Lisa Randall and Raman Sundrum. Out of this world supersymmetry breaking. *Nucl.Phys.*, B557:79–118, 1999.

[104] A. D. Sakharov. *JETP.Lett*, 6:24, 1967.

[105] H. Segur and M.D. Kruskal. NONEXISTENCE OF SMALL AMPLITUDE BREATHER SOLUTIONS IN PHI**4 THEORY. *Phys.Rev.Lett.*, 58:747–750, 1987.

[106] Uros Seljak, Anze Slosar, and Patrick McDonald. Cosmological parameters from combining the Lyman-alpha forest with CMB, galaxy clustering and SN constraints. *JCAP*, 0610:014, 2006.

[107] Alessandro Strumia. Thermal production of axino Dark Matter. *JHEP*, 1006:036, 2010.

[108] Michael S. Turner and Frank Wilczek. Relic gravitational waves and extended inflation. *Phys.Rev.Lett.*, 65:3080–3083, 1990.

[109] V. A. Rubakov V. A. Kuzmin and M. E. Shaposhnikov. On the anomalous electroweak baryon number nonconservation in the early universe. *Phys.Lett.*, B155:36, 1985.

[110] Matteo Viel, Julien Lesgourgues, Martin G. Haehnelt, Sabino Matarrese, and Antonio Riotto. Constraining warm dark matter candidates including sterile neutrinos and light gravitinos with WMAP and the Lyman-alpha forest. *Phys.Rev.*, D71:063534, 2005.

[111] Alexander Vilenkin. Global structure of the multiverse and the measure problem. *AIP Conf.Proc.*, 1514:7–13, 2012.

[112] Marta Volonteri, Francesco Haardt, and Piero Madau. The Assembly and merging history of supermassive black holes in hierarchical models of galaxy formation. *Astrophys.J.*, 582:559–573, 2003.

[113] Devin G.E. Walker. Dark Matter Stabilization Symmetries and Long-Lived Particles at the Large Hadron Collider. 2009.

[114] Steven Weinberg. The Cosmological Constant Problem. *Rev.Mod.Phys.*, 61:1–23, 1989.

[115] J. Wess and J. Bagger. Supersymmetry and supergravity. 1992.